UNIVERSITY OF LONDON THESIS

Degree PhD Year 2006 Name of Author SEARLE Samantha Claire

Spectroscopic analysis of the winds and atmospheres of Galactic B supergiant stars

Samantha Claire Searle

Thesis submitted for the Degree of Doctor of Philosophy
of the University of London

Department of Physics & Astronomy
UNIVERSITY COLLEGE LONDON

July 2006

ProQuest LLC
789 East Eisenhower Parkway
P.O. Box 1346
Ann Arbor, MI 48106-1346

I, Samantha Searle, confirm that the work presented in this thesis is my own. Where information has been derived from other sources, I confirm that this has been indicated in the thesis.

To my parents

"I ask you to look both ways. For the road to a knowledge of the stars leads through the atom; and important knowledge of the atom has been reached through the stars"

Arthur Eddington: Stars and Atoms (1928)

"There are more things in heaven and earth, Horatio, than are dreamt of in your philosophy"

William Shakespeare: Hamlet

"Tis the witching hour of night, Or bed is the moon and bright, And the stars they glisten, glisten, Seeming with bright eyes to listen For what listen they? "

John Keats

"The stellar universe is not so difficult of comprehension as the real actions of other people "

Marcel Proust

The impact of massive stars on their environment: The Hubble Space Telescope Image above shows the hot, luminous star η Carinae, which is unstable and undergoes violent episodes of mass loss. It is surrounded by a shell of material that is still rapidly expanding from the last explosion that occurred in 1841, seen as the glowing, red material in the above image. The bright, yellow-white gas nearer the star comes from ejected stellar material that has formed two, distinct lobes moving in opposite directions. Knots seen in this material in the inner part of the shell are similar in size to our Solar System. which puts the vastness of the nebular structure around this star into context. η Carinae provides a challenge to our current understanding of hot, massive stars as its existence cannot be well explained by current theories of stellar evolution. Image credit: J. Hester/Arizona state University NASA.

ABSTRACT

Uncertainties in the post main sequence evolution of B supergiant stars exist because their evolution is controlled by variable mass loss from the star as well as rotation, binarity and convection processes in the core. The latter effect leads to surface enrichment as the products of nuclear burning (carbon, nitrogen and oxygen) are brought to the surface. However, current stellar evolution models fail to predict the correct amount of CNO processing in massive stars. Accurate mass loss rates are essential for underpinning the Wind-momentum Luminosity Relation (Kudritzki *et al.*, 1999) and also for improving stellar evolution calculations. Existing discrepancies between B star mass loss rates obtained from observations and those from theoretical predictions (e.g. Vink et al. 2000) also emphasise the need for a better understanding of structured stellar winds. Recent improvements in stellar atmosphere models to include full nLTE effects & line blanketing also provide us with the mean to derive more accurate temperatures & luminosities, leading to a reduction in OB star temperature scales.

An optical and ultraviolet quantitative spectroscopic analysis of the atmospheres and winds of Galactic B supergiants is presented here. Fundamental parameters such as temperature, luminosity, mass loss rate and CNO abundances are derived for individual stars using the non-LTE, line-blanketed model atmosphere code of Hillier & Miller (1998). We present detailed temperature scales for B supergiants and discuss their implications. Additionally we discuss the derived mass loss rates and CNO abundances for our sample of Galactic B supergiants and compare them to other results.

Empirical analysis of the ionisation conditions of early B supergiant winds has also been

carried out (based on SEI modelling) and compared to model predictions from the stellar atmosphere code of Hillier & Miller (1998). This allows us to undertake a critical comparison of observed and predicted ionisation behaviour in the wind, focusing on trends of the ionisation fraction, q_i, with velocity, relative ionisation strengths and whether ions tend to increase or decrease further out in the wind. Values of $\dot{M}q_i$ (the product of the mass loss rate times the ionisation fraction) have been obtained from UV line synthesis modelling and, using our derived mass loss rates, values of q_i are acquired from $\dot{M}q_i$ for our sample of Galactic B supergiants. Our studies show that values of q_i are much lower than expected and furthermore none of the ions (e.g. Al III, Si IV, C IV, N V) are dominant in the wind, a surprising result since the highest values of q_i occur in the B spectral range. We discuss our most recent findings and their implications for clumping and structure in the wind. Most importantly these results provide strong evidence for a downward revision of mass loss rates by *at least* an order of magnitude. This evidence demonstrates a clear need to review mass loss rate determinations and the role of clumping in massive star winds.

ACKNOWLEDGEMENTS

My thanks go to a large number of people who have helped along the way to make this journey possible. First of all, I would like to thank my supervisors Raman and Ian for their guidance throughout my time as both an undergraduate and postgraduate at UCL. Their teaching and advice has been a great benefit to me and the completion of this thesis would have not been possible without them. I am also grateful to Allan Willis and Pete Storey for financial support; to Callum Wright, John Deacon and Jeremy Yates for assistance in running codes and to John Hillier for advice in running CMFGEN.

I would like to thank my family for their continuous love and support throughout my life, encouraging and enabling me to achieve so much. It would have been a lot harder to get where I am without their support and am greatly indebted to them. A special thanks my go to my mum and late grandad for encouraging me to pursue an interest in all matters scientific from an early age. A huge thanks also goes to Ben for supporting the whole way through my PhD and always being there for me when things got tough.

Another huge thanks goes to all my friends at UCL, both past and present, who have made the last eight years so memorable. I am very grateful to my friends that make up the current G14 crew; Jo, Fab and Dugan (and your infinite computing wisdom!), Adam, Matt and Simon for their support and laughs whilst I was on the 'last leg' (quite literally at times!). An important mention also goes to all those that I previously shared an office with: Sam, Anais, Alex, Jay and Richard for their companionship and many interesting discussions (astronomical and otherwise!) as well as putting up with my incessant, high-speed talking! I would also like to give an enormous thanks to Tom, Chris L., Nick,

Antonio, Will, Mark, Matt, Chris K. and Sarah for their friendship and support over the last few years. As well as making a huge difference to the interactions of the astronomy group, we've all shared a large number of cultural experiences ('sometimes' alcohol-related) that have definitely enriched my time at UCL and certainly broadened my horizons - an important part of the overall educational experience!

Finally I would like to congratulate all my UCL undergraduate friends who have already succeeded in getting their PhDs and the best of luck to those of you who are getting there - there is an end I promise! Last but certainly not least I'd like to mention my non-astronomical friends (just to prove I have them really!), in particular Yvonne, Roza, Sinead and all the members of my french group (LFM) who have also played an important role in getting me out of 'work-mode' when things became stressful!

Contents

List of Figures

List of Tables

CHAPTER 1

Introduction

This thesis involves a quantitative spectroscopic investigation of the fundamental parameters and stellar wind properties of Galactic B supergiants. B supergiants are a class of hot, massive star that are among the most luminous objects seen in the night sky. This is due to their large luminosities ($\sim 10^5\ L/L_{\odot}$) and surface brightness, which allows them to be seen with the naked eye even at great distances. The study of all types of stars is crucial to astrophysics since there are billions of stars in the universe, which influence the environment of their host galaxy and control its formation and evolution. In turn, the formation and evolution of galaxies hold the key to understanding the formation of our universe.

First of all, this chapter presents the general classification scheme used for stars, explaining the different sub-types, after which the properties and importance of B supergiants is discussed. The derivation of fundamental parameters for B supergiants (and hot, massive stars in general) from spectroscopic data sets, using the current generation of stellar atmosphere codes available will be presented. Next, the techniques available for deriving mass loss rates from hot, massive stars are explored, as the determination of *accurate* mass loss rates is a crucial issue in this thesis work. A review is given of recent research on hot, massive stars (but focusing on B supergiants) and the current, unresolved problems that have arisen from this research. The chapter closes by stating the aims of this thesis.

1.1 The classification of stars

Given the vast number and diversity of stars that exist in our universe, it is essential to find a way of describing them, so that a clear distinction is made between their different properties. By grouping stars with similar properties together, we can improve our understanding of the physics that drives their evolution. This is also fundamental to understanding stellar evolution in general. Gazing at a clear night sky, there are obvious differences between the brightness and colour of stars visible to the naked eye. These attributes can be exploited in order to devise a classification system by which any star can be 'labelled' according to these visible properties. It is important that any such classification scheme provides a solid 'frame of reference', so that any object to be studied can fit into the classification scheme. Trends between objects then become clear and consequently any peculiar stars are easily identifiable, providing a useful test to our existing knowledge of stars as we know them.

The first general stellar classification scheme was developed by a Jesuit astronomer, Father Angelo Secchi, who worked at the Vatican Observatory during the 1860s. He observed thousands of stars using a visual spectroscope and small telescopes, ranging from 15 – 25 cm in aperture. However, since the human eye is less sensitive to the blue-violet region of the electromagnetic spectrum ($\sim$ 400 nm), his classification scheme displays a small bias towards cooler stars, which appear to be the brightest at visible wavelengths and exhibit the most visually exciting spectra due to the presence of molecular bands. The scheme was constructed in reference to the solar spectrum, with stars being grouped according to whether they were hotter, cooler or similar to the Sun. Towards the end of the 19th century, astronomers such as Edward C. Pickering (amongst others) realised the potential for using photographic spectra and objective-prism telescopes to classify large numbers of stars and construct a uniform classification scheme based on consistent criteria. The 'HD' project was subsequently established at Harvard College Observatory, sponsored by Henry Draper. By the mid-1920s, over a quarter of a million stars had been classified, with the majority of the work having been done by Annie Jump Cannon. This initial *HD system* classified stars according to the strength of their hydrogen lines, so it was essentially a temperature scale, where spectral types were denoted alphabetically i.e. A, B, C... etc. It was noticed later that the hydrogen lines reach a maximum strength along the temperature scale, so the sequence was rearranged to suit the temperature reference frame. It now exists

in the following form, known as the 'Harvard sequence': OBAFGKM(SRN) where OBA are the hotter stars, GKM represent the cooler stars and SRN refer to stars that are in the same temperature range as GKM stars but display a very different chemical composition in their spectra. The generally accepted version of the stellar classification scheme was finalised by Morgan *et al.* (1943) and is known as the 'MK system'.

1.1.1 The MK system

The advantage of this classification scheme is that it is solely reliant on spectra, which are an easy and directly observable quantity, rather than being dependent on photometric or theoretical calibrations. Stars that are classified according to the scheme can then be used as 'spectral standards', by which other unclassified stars can be compared. It is then merely a question of comparing the line strengths of a spectral standard with an unclassified star in order to determine its spectral type. The criteria used in the MK system is as follows:

1. Stars are assigned a letter (indicating their temperature) based on the 'Harvard sequence' (OBAFGKMSRN). O denotes the hottest stars and M the coolest stars. RN stars are a similar temperature to GK stars but are carbon rich, whereas S stars are as cool in temperature as M stars, but exhibit ZrO absorption bands in their spectra.

2. Each letter is sub-divided by the numbers 0-9, with 0 indicating the hottest spectral sub-type.

3. A luminosity class is included to indirectly express the absolute brightness of the star and is constrained by spectral lines that are sensitive to surface gravity. Roman numerals are used to denote the luminosity class with I meaning supergiant, II–III meaning giant, V referring to a dwarf/main-sequence star and VI a sub-dwarf star. The supergiant class is sub-divided further into Ia, Iab & Ib, with Ia representing the most luminous supergiant.

4. Any additional interesting features or peculiarities observed in the star can be denoted after the spectral type. A chemical peculiarity is shown by the elemental symbol (e.g. C, Fe) and a number 1–5 that is positive for overabundance and negative for depletion. Stars displaying hydrogen lines in emission are denoted with an

'e' and rapid rotators are denoted by 'n' or 'nn', depending on how fast they rotate. The letter 'f' represents O stars with helium, carbon, nitrogen or oxygen in emission. Finally any stars with peculiarities that do not fit into the afore-mentioned categories are denoted 'p'. An atlas of peculiar OB optical spectra is presented by Walborn & Fitzpatrick (2000).

An example of spectral type is G2 V, which is the spectral type of the Sun, a relatively cool dwarf star that is still converting hydrogen into helium on the main sequence. Alternatively, the hottest and most luminous B stars would be denoted B0 Ia. Sometimes if a large number of stars are found to show the same peculiaries, a separate sub-group is created for them. An example of this is a Wolf-Rayet (WR) star, which is a highly-evolved O star that possesses such a strong stellar wind that its spectrum is dominated by strong, broad emission lines. Wolf-Rayets are sub-divided further into two groups; WN stars that show spectra dominated by strong helium and nitrogen lines, with little or no hydrogen and WC stars that show strong helium, carbon and oxygen lines but no nitrogen. Luminous Blue Variables are another well-known group of stars that undergo extreme and often violent episodes of mass loss. This results in variations in their visual brightness as well as significant changes in their spectral appearance. There are two important sub-groups of B stars that should also be noted; Be stars, which are non-supergiant B stars that display their hydrogen lines in emission and B[e] stars, that exhibit forbidden lines in emission. Such phenomena are directly related to physical differences in the star; Be stars are known to have disks around their equator that are not present in normal B stars. Thus in describing stars by their spectral type, one can immediately have an idea of their approximate temperature and luminosity and the appearance of their spectra.

A detailed classification of OB digital optical spectra is given by Walborn & Fitzpatrick (1990). This clearly demonstrates the difference between the strengths of various lines, illustrating the temperature sequence from early O to late B stars, as well as highlighting spectral differences between luminosity classes. Additionally, a spectral atlas dedicated to O9 – B9 Galactic supergiants is presented by Lennon *et al.* (1992). O star spectra are clearly distinguished by the presence of strong H, He I & He II lines, together with weaker lines of N II, N III, C II, C III, O II, Si II, Si III Si IV & Mg II. The O star spectral sequence originally began at O4, but Walborn (1971) introduced O3 to mark the absence of He I

4471 Å in some O stars and more recently O2 & O3.5 sub-types have been added; all 3 sub-types are defined by the relative strengths of N III & N IV lines, rather than the relative strengths of He I & He II lines as for O4 – O9.7 stars (Walborn *et al.*, 2002). The interpolated O9.7 sub-type is defined by the equal strengths of He II 4541 Å and Si III 4552 Å (Walborn, 1971). He II lines reach a maximum around O7, after which they weaken and disappear by B1. The relative strengths of He II 4686 Å and N III 4634–4640–4642 Å define the O star luminosity classes. In contrast to O star spectra, B star spectra display weaker He I lines and stronger metal lines e.g. Si II, Si III, Si IV & Mg II. Walborn (1971) introduced the B0.2 and B0.7 sub-types to make a clearer distinction between the large temperature differences and corresponding line changes from B0 – B1. B star spectral types are primarily defined by the relative strengths of Si II, Si III & Si IV and are discussed in greater detail in §3.1.1. The distinction between luminosity classes is made from the ratio of the He I 4471 Å & Mg II 4481 Å line strengths. Classification schemes are not limited solely to the optical; spectral atlases at UV and infra-red wavelengths have also been published. Walborn & Nichols-Bohlin (1987) produced an atlas of OB supergiant *IUE* spectra, covering the wavelength ranges 1320 – 1580 Å and 1620 – 1880 Å. This atlas highlighted the main stellar wind characteristics that appear in the O3 – B8 spectral range: O V, N V, N IV, C IV, He II, Si IV, Al III, C II & Al II. The O star sequence is clearly defined by the ratio of the line strengths of Si IV $\sim$ 1400 Å & C IV $\sim$ 1550 Å, with O3 – O5 stars displaying O V, N IV & He II 1640 Å, which weaken and disappear at O6 – O9.7. On the other hand, B star UV spectra are marked by the weakening Si IV and C IV lines, as well as the introduction of Al III and C II at B0.5, which reach a maximum around B1 – B2. N V and C IV are at maximum strengths for O3 – O4 and O3 – O6 respectively, after which Si IV attains its maximum strength for O6 – O9.7. This means that these lines are usually saturated in O stars and no longer sensitive to changes in $T_{\rm eff}$ and mass loss, limiting the amount of information that can potentially be obtained from them. B stars are therefore more useful for stellar wind studies compared to O stars, since they display a wide range of different ionisation stages that are mostly *unsaturated*, including N V, C IV & Si IV.

1.2 Modelling OB stars

The sensitivity of these spectral diagnostics to temperature and luminosity can be exploited in order to constrain these parameters for an individual star. Stellar atmosphere models provide a convenient method by which to determine stellar parameters from different diagnostic lines in a spectrum. Such models are *ab-initio*, meaning that they are based on certain assumptions regarding the structure of the stellar atmosphere. The basic assumptions adopted by a stellar atmosphere code are *hydrostatic equilibrium*, which requires a balance between radiation pressure and the star's gravity, *radiative equilibrium*, which states that there is no net flow of energy in or out of the stellar region and *radiative transfer*, which describes the transport of flux from the star via the processes of absorption, emission and scattering. This allows the model to calculate the stellar atmosphere structure and produce a synthetic spectrum that can then be compared to the observed spectrum. The model line profiles can be compared to the observed line diagnostics to see if they match, confirming that the stellar parameters adopted in the model i.e. temperature, luminosity, stellar radius and the surface gravity ($\log g$) are correct. One of the first, most widely-used codes for modelling stars is that of Kurucz (1979), which assumes *local thermodynamic equilibrium* (LTE) i.e., an absolute temperature and total particle density is used to describe the local conditions of the gas. It also accounts for the effects of *line blanketing*, which is the suppression of flux due to the presence of hundreds/thousands of very weak absorption lines (usually Fe lines) that are very close together and therefore unresolved. However, the assumption of LTE is not valid in hot stars, where the radiative processes dominate and the local gas conditions can no longer be described in terms of an absolute temperature and total particle density, and the star is now described as being in *non-local thermodynamic equilibrium* (nLTE). Developments in stellar atmosphere codes over the last decade or two have included the effects of nLTE, as well as improving the treatment of line blanketing. In fact, the thorough treatment of line blanketing in stellar atmosphere codes has lead to a significant reduction in O star temperatures of up to 7 000 K (e.g., Martins *et al.*, 2002; Repolust *et al.*, 2004; Martins *et al.*, 2005), whereas results for B supergiants indicate more modest temperature reductions of 1000 – 2000 K (e.g., Trundle *et al.*, 2004; Trundle & Lennon, 2005; Crowther *et al.*, 2006). One of the purposes of deriving fundamental parameters for Galactic B supergiants in this thesis is to examine whether this trend is confirmed by the temperature scale obtained here. Ac-

curate stellar temperatures are crucial for determining the stellar luminosity and radius, parameters that describe the star's evolutionary path across the HR diagram. Further details of the physics incorporated in stellar atmosphere codes is given in §2.1, and nLTE stellar atmosphere codes are discussed at greater length in §2.1.2.

1.3 Introducing B supergiants

At first appearance O and B supergiants display similar properties. O supergiants are hotter and luminous, with typical values of 30 000 - 60 000 K in temperature and of the order of 10^5 – 10^6 $L_\odot$in luminosity. B supergiants are next in line with temperatures ranging from 30 000 K for a B0 down to around 10 000 K for a B9 and luminosities of $\sim 10^5$ $L_\odot$. B supergiants also possess less dense and strong stellar winds in comparison with O supergiants. The spectra of both stars are dominated by hydrogen and helium lines, but O supergiant spectra feature lines of ionised helium (He II) that are barely discernible in B supergiant spectra, disappearing around B1. In B supergiant spectra, He I increases in strength up to B2, after which it weakens, whereas the H lines increase throughout B0-B9 spectra, eventually reaching a maximum for early A stars (A2). A more detailed discussion of the spectral features of B supergiants is given in §3.1.3, where the sample of 20 Galactic B0 – B5 supergiants, upon which this thesis work is based, is presented. It is of general interest to compare the properties and behaviour of OB supergiants as there are some obvious similarities between the two types and understanding the behaviour of one can help to improve our understanding of the other. An example of well-known B supergiants is shown in Fig. 1.1, where 3 B supergiants can be seen in the constellation of Orion. The first is known as ϵ Ori (B0 Ia) and is located in the middle of 'Orion's Belt', the second is κ Ori (B0.5 Ia) and is found at the left foot of the hunter Orion and lastly the third is called Rigel (B8 Ia) and marks the right foot of the hunter.

One of the most important features of OB supergiants is their stellar wind, a continuous emission of particles driven from the star into the ISM by radiation pressure. This means that OB supergiants lose mass constantly during their lifetime, which has a significant impact on their evolution. The ionising flux that they output to the interstellar medium (ISM) is also very important, since it has a huge impact on the star's local environment. Both these features are discussed further in §1.4 and §1.5.2.

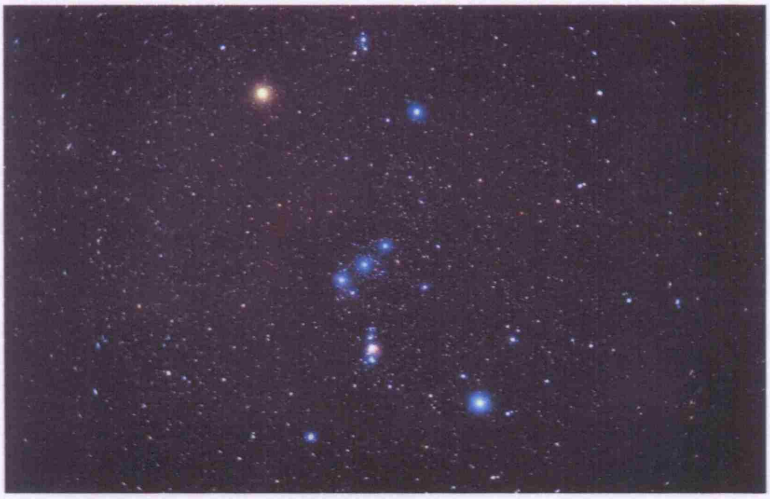

Figure 1.1: B supergiants in the constellation of Orion. The star ϵ Ori is the middle star in the belt of Orion whereas κ Ori and Rigel make up the left and right feet of the hunter respectively.

1.3.1 The evolution of hot, massive stars

Stars form from the condensation of interstellar clouds, where gravitational energy generated under contraction heats the stellar interior as it forms. Once a sufficiently high temperature is reached to enable nuclei to overcome the Coulomb repulsion, nuclear fusion can begin, converting hydrogen into helium. The evolution of the star is strongly influenced by the amount of energy lost through radiation from the stellar surface (causing the star to contract under gravity) and the amount of energy generated by nuclear burning. When the energy produced through nuclear burning balances the energy loss from the stellar surface, the star ceases to contract until all the hydrogen in the core has been consumed, leaving helium and other heavier elements in the core. At this point, the region outside the stellar core is still hot enough to allow hydrogen fusion to continue, producing a *shell source*. The result of this is that more helium is added to the core, causing it to contract and release more gravitational energy. This has the benefit of heating up the core again until it reaches an even higher temperature needed to burn the next set of nuclear reactions, this time fusing three helium nuclei into a carbon nucleus until all the helium available in the core is exhausted. Nuclear evolution in any star follows this general pattern of core contraction generating gravitational energy until the temperature is high enough to start the next nuclear reaction, which may be accompanied by shell sources

burning outside the core. The process of nucleosynthesis (nuclear burning) in stars is fundamental to astrophysics, since it is an important source of heavier elements in the universe. These elements are distributed to the interstellar medium (ISM) via the stellar wind and supernovae explosions, where they form an essential part of the new material from which the next generation of stars and planets will form.

The overall evolution of stars is clearly illustrated by the Hertzsprung-Russell diagram shown in Fig. 1.2. This diagram, constructed independently by Ejnair Hertzsprung and Norris Russell, plots the stellar temperature against luminosity or magnitude of brightness, charting the evolutionary phases of a star as these parameters vary during its evolution as a function of the star's mass and chemical composition. Stars that have only just begun core hydrogen burning are found at the *zero age main sequence* and evolve along the main sequence toward higher temperature and luminosity. The star reaches its post-main-sequence evolution phase as a blue supergiant once core hydrogen burning ends, signalling the start of helium core burning. Hot, massive stars with $M_* \geq 10\ M_\odot$ manage to generate enough heat through core contraction to sustain the fusion of carbon and heavier elements (Ne, O & Si). Those stars in the range $10\ M_\odot \leq M_* \leq 40\ M_\odot$ should pass through a red supergiant phase, which leads to further mixing of the products of nuclear burning in the core. It is therefore straightforward to identify which stars have passed through a red supergiant phase from their highly enriched nitrogen abundances. Eventually an iron core forms and it is no longer possible for the star to generate any more energy via nuclear reactions, since iron possesses the maximum binding energy and fusion of iron nuclei would require further energy that is not available. The core contracts in order to compensate for energy loss through radiation, leading to further core heating. This results in the dissociation of iron nuclei to protons and neutrons, which produces further core contraction in an attempt to provide more energy for dissociation. The core density increases to such an extent as the star undergoes dynamical collapse that it becomes more energetically favourable for each proton to capture an electron and form a neutron, emitting a neutrino. The dynamical collapse reaches an abrupt halt when the neutron core becomes degenerate, causing shock waves to rebound off the core and transfer energy into the stellar envelope. The envelope is ejected in a huge explosion of energy, mostly in the form of neutrinos, known as a supernova explosion. Stars with an initial mass of $\leq 25\ M_\odot$ become a neutron star after exploding as a supernova, whereas those with initial masses $\geq$

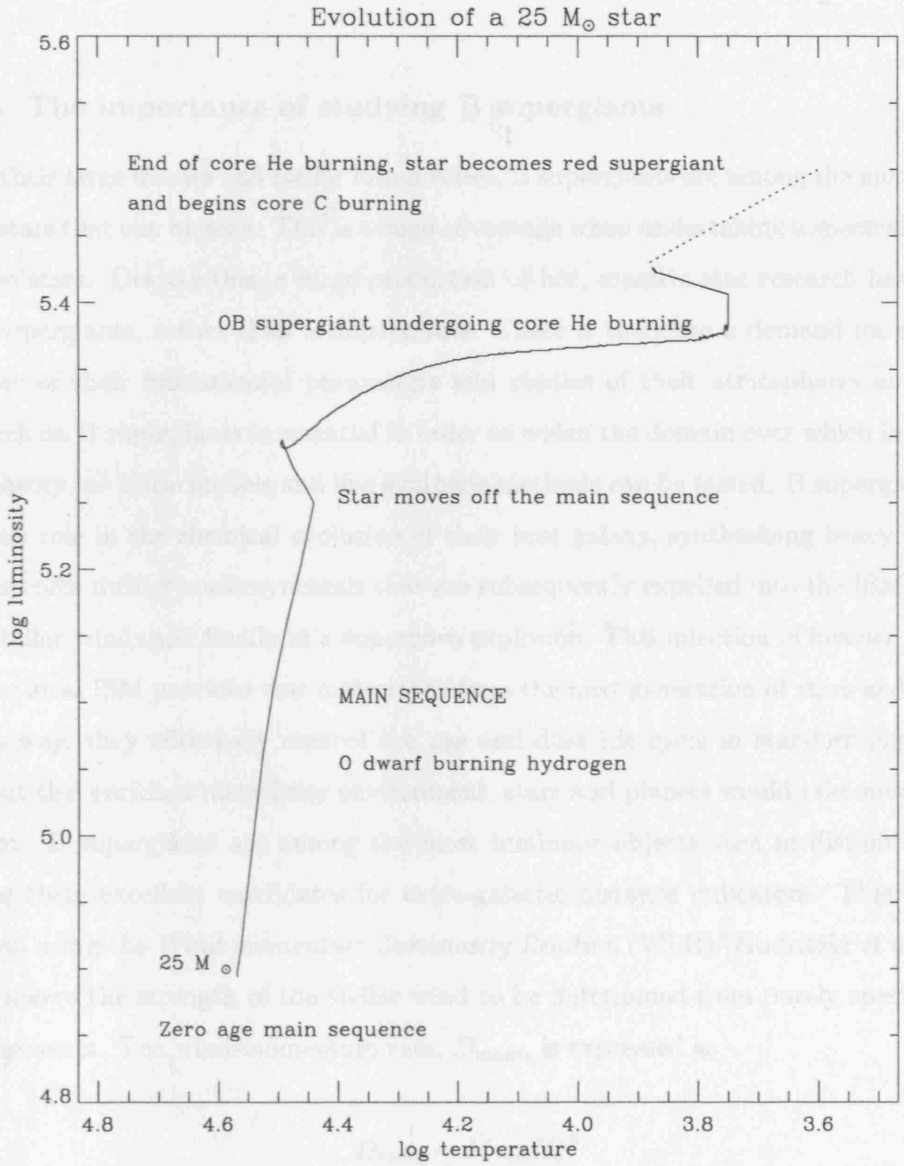

Figure 1.2: An example of a Hertzsprung-Russell Diagram showing the early evolutionary phases of a hot, massive star with an initial mass of 25 $M_{\odot}$. See text for full description. Based on the Meynet & Maeder (2000) evolutionary tracks, which calculate the evolutionary path of massive stars up to the end of core He burning.

25 $M_{\odot}$ end up as black holes (Heger *et al.*, 2003). The type of supernova usually produced from a red supergiant is known as a Type II supernova.

1.3.2 The importance of studying B supergiants

Given their large masses and stellar luminosities, B supergiants are among the most distant single stars that can be seen. This is a huge advantage when undertaking a spectral analysis of these stars. Despite this, a large proportion of hot, massive star research has focused on O supergiants, rather than B supergiants. There is therefore a demand for extensive analyses of their fundamental parameters and studies of their atmospheres and winds. Research on B supergiants is essential in order to widen the domain over which line-driven wind theory, *ab initio* models and line synthesis methods can be tested. B supergiants play a crucial role in the chemical evolution of their host galaxy, synthesising heavy elements in their cores during nucleosynthesis that are subsequently expelled into the ISM through their stellar winds and finally in a supernova explosion. This injection of heavier elements into the local ISM provides new material to form the next generation of stars and planets. In this way, they effectively control the gas and dust life cycle in star-forming regions. Without this enriched metallicity environment, stars and planets would take much longer to form. B supergiants are among the most luminous objects seen in distant galaxies, making them excellent candidates for extra-galactic distance indicators. This could be achieved using the *Wind-momentum Luminosity Relation* (WLR) (Kudritzki *et al.*, 1999), which allows the strength of the stellar wind to be determined from purely spectroscopic measurements. The wind-momentum rate, $D_{\rm mom}$, is expressed as

$$D_{mom} = \dot{M} v_{\infty} R_{*}^{0.5} \tag{1.1}$$

where R_{*} is given in units of $R_{\odot}$, $\dot{M}$ in g/s and v_{∞} in cm/s. The success of such a method is strongly dependent on establishing a reliably-calibrated WLR using hot, massive stars that have well-known distances. It would then be possible to observe hot, massive stars in other galaxies, measure the strength of their stellar wind from spectra and use it to infer a reliable estimate of the distance to the host galaxy. The WLR will be discussed further in §1.5 and 3.2.8.

Whilst B supergiants are responsible for the chemical enrichment of their host galaxy, along with O supergiants and WR stars, they play an equally important role in starburst galaxies. These stars are usually grouped into young clusters and the combined effect of their powerful stellar winds and supernova explosions form 'superbubbles' around the clusters. Images from the Hubble Space Telescope (HST) have shown that these 'superbubbles' are excellent sites for further star formation. In producing 'superbubbles', hot, massive star winds feed the galactic energy outflows (referred to as galactic winds) observed in starbursts and starburst galaxies, effectively shaping the dynamical evolution of the ISM. Furthermore, the key to understanding the various processes that result in continuous star formation lies in the examination of these 'superbubbles'. Spectra of star-forming galaxies are dominated by the presence of OB stars, demonstrating that a solid understanding of the physics of these stars is vital to understanding the physics of star-forming regions.

B supergiants are also intriguing since they are the progenitor stars of supernovae. The surprise discovery that the progenitor of supernova 1987A was a B3 supergiant (Walborn *et al.*, 1989) sparked renewed interest in them, as well as providing another test for stellar evolution models. It is expected that a blue-supergiant would go through a red-supergiant phase before exploding as a supernova; in the case of supernova 1987A there is evidence of a large nitrogen enhancement (typical of that which accompanies a star that has passed through a red-supergiant phase) in the nebula surrounding the progenitor. It is also possible that through their final supernova explosion, B supergiants become sources of gamma ray bursts.

1.4 The stellar winds of B supergiants

As seen in the previous sections, stellar winds of B supergiants have a huge impact on their local environment. It is therefore imperative that we understand the physics that drives them in order to improve our knowledge of their effect on, and contribution to, the ISM. The stellar wind of a star is described as a continuous outflow of material from the star. It is described generally by two parameters: the terminal velocity v_∞, meaning the speed of the stellar wind at a large distance from the star and the mass loss rate $\dot{M}$, expressed in units of $M_\odot$ yr^{-1}. One of the aims in studying B supergiants is to constrain these quantities as precisely as possible because:

- The mass loss rate of a star indicates how much material is lost from the star in a given time interval. Stars with higher mass loss rates will evolve differently than those with lower mass loss rates, so precise measurements of mass loss are crucial in obtaining a more accurate description of the B supergiant evolution.
- Reliable measurements of these quantities can test the validity of stellar wind theory and the assumptions upon which it is based.
- The stellar wind carries a huge amount of momentum into the ISM; in order to quantify this amount, knowledge of v_∞ & $\dot{M}$ are required. This information is also useful for the calibration of the WLR.

The following sections will outline the methods available for measuring v_∞ and $\dot{M}$ from stellar spectra. The theory of stellar winds is presented in §2.2.1. The stellar winds of hot, massive stars emit the majority of their flux in the UV & FUV, but flux is also observed over a range of other wavelengths besides the optical part of the spectrum. The process of free-free emission (or *bremsstrahlung*) in the stellar wind leads to the production of an excess of continuum emission at radio and infra-red wavelengths. This excess flux is defined relative to the flux that would be expected from the photosphere of a star with no stellar wind. Non-thermal emission can also be produced at radio and infra-red wavelengths. The launch of the Einstein Observatory in November 1978 led to the discovery that hot star winds emit soft X-rays. In June 1990, the ROSAT X-ray satellite was launched and was used to carry out the first all-sky survey at the soft X-ray band (0.1-2.4 keV). Since then, various authors have analysed X-ray observations of hot, massive stars (Feldmeier *et al.*, 1997; Cassinelli *et al.*, 2001) and constructed models (Lucy, 1982; Owocki *et al.*, 1988) in an attempt to explain their origin. The basis of the Owocki *et al.* (1988) model proposes that instabilities at the base of the stellar wind grow into shocks that generate high enough energies to produce X-rays and in general, this is the currently excepted explanation.

1.4.1 Spectral signatures of stellar winds

The spectral signatures seen in stellar winds are very distinctive in comparison to photospheric lines due to their observed wavelength shift arising from the outflow of gas in the wind. B supergiant winds present the opportunity to study P Cygni profiles that represent the various ionisation stages of carbon, nitrogen, silicon and aluminium over a wide range

in temperature ($\sim$ 15 000 – 30 000 K). Since B supergiants have weaker winds than O supergiants, the observed P Cygni profiles are less likely to be saturated, meaning that are more useful for analysis since they are still sensitive to changes in temperature, density and mass loss from the wind. The overall profile shape of each spectral line is controlled by the efficiency of the wind in absorbing or emitting photons in the line of sight. There are four line formation processes that exist in the winds of hot, massive stars:

- *Line scattering*: — This occurs when an atom absorbs a photon, leading to photo-excitation of an electron in the atom. Very soon after, the electron de-excites down to its original energy level, resulting in the emission of another photon and producing a spectral line. The frequencies of the absorbed and emitted photons are almost equal, giving the illusion that the photon was merely *scattered*, rather than absorbed and re-emitted, hence the term 'line scattering'. When the resulting line transition is from the ground state, it is known as a *resonance line* and the scattering is referred to as *resonance scattering*. This is the principle mechanism responsible for the formation of 'P Cygni' profiles, which will be discussed shortly.

- *Recombination*: — The collision of an ion in the stellar wind with an electron can result in recombination, normally to the ground state. However, an ion can recombine to an excited state then go through a series of de-excitations, cascading down the energy levels. A line photon is produced from each de-excitation, meaning that recombination is an important source of line photons in the wind. In fact, spectral lines that are dominated by this process may well be observed in emission, examples being the Hα line and infra-red emission lines in the winds of hot, massive stars.

- *Collisional- & Photo de-excitation*: — Collisional-excitation is a process by which an atom gains energy through a collision and switches from ground state to an excited state. It can then de-excite to a lower energy level, producing a line photon as it has converted kinetic energy into photon energy. This process is often seen in hot, low density plasmas, where it is highly efficient due to the high frequency of collisions taking place there. As a result, it leads to the production of emission lines in hot chromospheres and coronae.

- *Pure absorption*: — Here an excited atom is photo-excited into a higher excited state and immediately de-excites to a lower level spontaneously. The photon resulting from

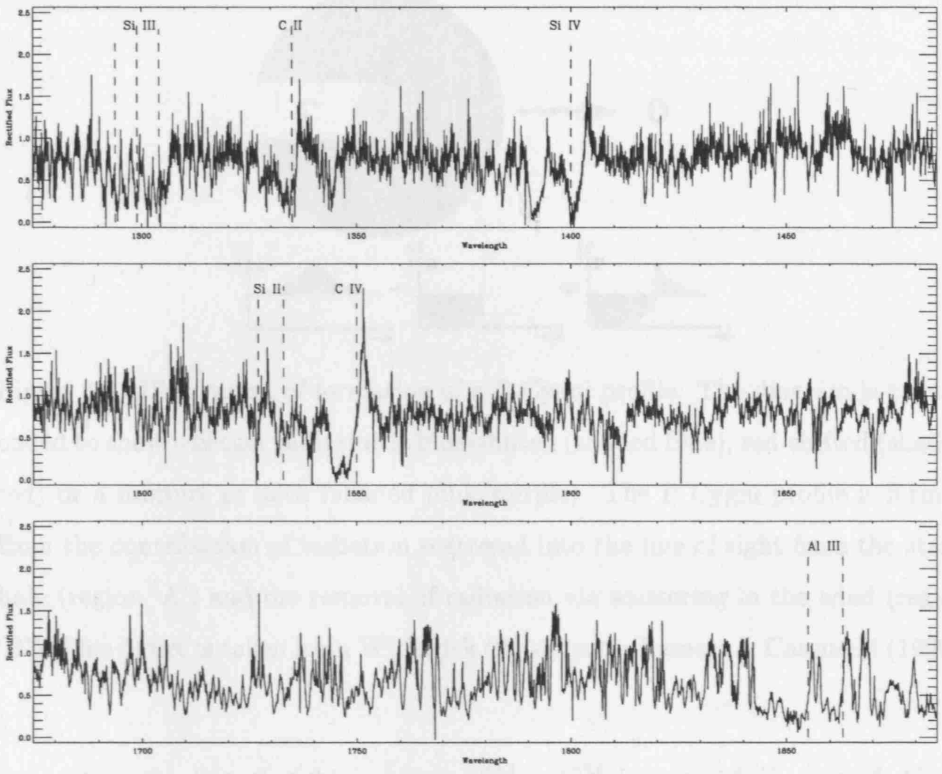

Figure 1.3: *IUE* spectrum of the B1 Iab star HD 13854

the first transition is destroyed but a second photon is created from the de-excitation. In reality, this process is not very important in stellar winds, since the majority of atoms are in their ground state.

The most striking spectral features observed in the stellar winds of hot, massive stars are 'P Cygni' profiles, named after the star in which they were first noticed (e.g., Beals, 1951). They are also highly sensitive to mass loss from the stellar wind, and thus provide excellent diagnostics for constraining the mass loss rate of a star (see §1.4.2). Examples of UV resonance lines in B supergiants are N V, C IV and Si IV as shown as Fig. 1.3 for the star HD 13854. In O supergiants, their higher temperatures allow resonances lines in higher ionisation stages e.g., P V and O VI in the FUV, whereas in the cooler temperature regime of mid-to-late B supergiants and A supergiants, C II and Mg II are important resonance lines. All these resonance lines are usually present as an observable absorption line, showing some evidence of broadening. This occurs in situations where the number of absorbing

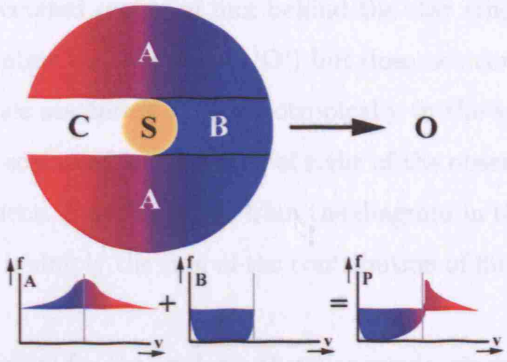

Figure 1.4: Illustration of formation of a P Cygni profile. The diagram is colour-coded to show whether radiation is blue-shifted (shaded blue), red-shifted (shaded red) or a mixture of both (shaded pink/purple). The P Cygni profile is formed from the contribution of radiation scattered into the line of sight from the star's halo (region 'A') and the removal of radiation via scattering in the wind (region 'B'). This figure is taken from Witherick (2004), after Lamers & Cassinelli (1999).

ions present in the line of sight is about 10^{13} – 10^{14} ions cm^{-2} (Lamers & Cassinelli, 1999). The absorption line is Doppler shifted to shorter wavelengths (or *blue-shifted*) because the line forms in a part of the stellar wind that is moving *away* from the star and *toward* the observer. Conversely, if the number of absorbing ions in the line of sight is greater than 10^{15} cm^{-2}, then a 'P Cygni' profile is observed, this time with a *red-shifted* emission component that has been Doppler-shifted to longer wavelengths. Note that the terms *blue-shifted* and *red-shifted* refer to the Dopper shift of a line to shorter and longer wavelengths respectively, but *in reference to the rest velocity of the line.* In other words, these terms do *not* refer to the location of the spectral line in the electromagnetic spectrum.

The formation of a P Cygni profile is illustrated in Fig. 1.4, showing the different regions of the stellar wind that contribute flux to the overall profile shape. The star (labelled 'S' in Fig. 1.4) is emitting a continuum flux that results in a photospheric absorption component. In the area of flux in front of the star (the region labelled 'B'), radiation is scattered (via resonance scattering in the wind) out of the line of sight to the observer. This results in the characteristic blue-shifted absorption component of the P Cygni profile, since this radiation has been prevented from reaching the observer. However, some radiation can be scattered back into the line of sight, so the absorption component may not reach zero

intensity. There is an occulted region of flux behind the star (the white region 'C') that also does not reach the observer (marked as 'O') but does not contribute to the P Cygni profile. Further resonance scattering occurs isotropically in the stellar halo (region 'A'), where some radiation is scattered into the line of sight of the observer, producing the red-shifted emission component. It is then clear from the diagram in the lower half of Fig. 1.4 that the P Cygni profile is simply the sum of the contribution of flux from regions A and B.

P Cygni profiles are essential for the analysis of stellar winds, since (as stated earlier) they are highly sensitive to mass loss from the wind as long as the line remains *unsaturated.* Once a line is strongly saturated, it becomes mostly sensitive to the velocity law. Hence the value of the terminal velocity v_∞ can be accurately measured from the edge of a blue absorption trough, the highest accuracy being achieved when the line is *fully* saturated and known as a black absorption trough, meaning the amount of flux removed from the continuum by this component has reached zero intensity. For the purpose of stellar wind models, the wind is usually described by a velocity law. The 'steepness' of this velocity law is controlled by a parameter called β, and the value of β can also be constrained by fitting a model profile to the emission part of the saturated P Cygni profile.

1.4.2 Techniques for deriving mass loss rates

In principle, the UV wind resonance lines appear to be ideal diagnostic lines from which to estimate the mass loss rate, given their distinctive P Cygni profile shape. Their formation is well understood and they can be accurately modelled using a UV line synthesis code (usually the 'SEI method' (Lamers *et al.*, 1987), introduced in §5.1.1). In brief, a predicted model profile that assumes a certain radial distribution of ions in the wind, $n_i(r)$, is compared to the observed profile to see if the assumed $n_i(r)$ can reproduce it accurately, thereby confirming or disproving the adopted values of $n_i(r)$. However the situation is complicated by a couple of caveats. As previously mentioned, P Cygni profiles have a tendency to saturate (e.g., C IV in B0 – B3 supergiants) once a large number of absorbing ions are present in the line of sight, and consequently are no longer sensitive to density changes in the wind and mass loss. Therefore it is only possible to obtain an upper limit estimate for the mass loss rate in these cases. A more serious issue is that in order to extract a value of $\dot{M}$ from modelling a P Cygni profile, a detailed knowledge of the ionisation structure of the wind is required. More precisely, the *fractional population*

of each ion, q_i, must be known and despite several attempts at constraining q_i for OB stars Massa *et al.* e.g. 2003; Prinja *et al.* e.g. 2005, currently these values are unexpectedly low. Once a solution is found to this problem, then the analysis of UV wind resonance lines can provide an excellent method for determining mass loss rates. For a more in-depth discussion of the analysis of P Cygni profiles and obtaining values of q_i, please refer to Chapter 5.

An alternative method of determining mass loss from massive star winds is to use the optical Hα line at 6562 Å. The amplitude of the line gives an indication of the amount of mass loss occuring in the wind, whereas the line profile shape can be used to constrain the shape of the velocity law (β). Due to the thermal nature and large emitting region of the wind, Hα is often seen strongly in emission and very broad. The line is formed primarily by recombination and the line formation, controlled by the number of absorbing ions in the line of sight, shows a strong dependence on ρ^2, where ρ is the wind density. This suggests that high-density regions in the wind are responsible for Hα emission, located at the base of the wind where much of the wind acceleration occurs. A strong, underlying photospheric component, produced from the continuum, also contributes to the formation of the Hα line profile, and accurate photospheric input is needed in Hα modelling codes to account for its affect on the Hα line. In stars with weak winds and consequently small mass loss rates, this photospheric component dominates the Hα line profile, which is still 'filled-in' by emission from the stellar wind such that the resulting line profile is shallower in absorption than the actual photospheric component. Although an estimate of $\dot{M}$ can still be obtained from Hα when in absorption as it is still influenced by the wind, the accuracy of this value is reduced. It is not however possible to constrain β in this situation, since rotational broadening in the absorption component destroys any details of wind emission in the line profile structure. In mid-to-late B supergiants and A supergiants, line scattering becomes dominant and the Hα line can assume a P Cygni profile shape. In this case, an accurate value of β can still be obtained but some models (e.g., CMFGEN, Hillier & Miller 1998; FASTWIND, Puls *et al.* 2005) might struggle to reproduce the observed P Cygni profile. The Hα line provides a very useful diagnostic for deriving the mass loss rate since it is easily observable and the line profile should be reliably reproduced by a model. However problems arise from the variability of the line, not just due to variations in the stellar wind but also in the photosphere. In early B supergiants and O stars, the line can suffer from contamination from a blend with He II on the blue-ward side of the profile,

making it difficult for a model code to reproduce. If this problem occurs, then priority is given to fitting the red-ward side of the profile when generating model profiles to match the observed line. The presence of rotation also needs to be accounted for; this is normally done by convolving the model Hα profile with a rotationally broadened profile, which is a very simplistic approach. A more realistic approach would involve including the effects of *differential* rotation, as shown in the Hα code developed by Petrenz & Puls (1996). Finally, the He II 4686 Å line is sometimes observed in emission in early B supergiants and O stars, so can be used as an additional constraint for mass loss in stars earlier than B1.

Another method for determining mass loss rates of hot, massive stars makes use of the infra-red, sub-mm and radio continua, which allow the stellar wind plasma to be analysed. This consitutes the most reliable method for deriving $\dot{M}$, since it is based on the well-understood physics of atomic processes and radiation transfer, without the complications of nLTE effects and line broadening. The principle of the method is to measure the excess flux produced by bound-free and free-free emission in the wind and compare it to the amount of flux predicted by photospheric model atmospheres. However this method depends on the assumption that all wind emission is thermal. Two groups of authors, Wright & Barlow (1975) and Panagia & Felli (1975), independently discovered that the continuum flux, $S_\nu \propto \nu^{0.6}$, for an optically thick, spherically symmetric and isothermal envelope expanding at a constant velocity. They also showed that the observed radiation at infra-red and radio wavelengths depends strongly on the distance to the star, the mass loss rate and the terminal velocity but only weakly on the electron temperature in the wind. In summary,

$$S_\nu \propto \left(\frac{\dot{M}}{v_\infty}\right)^{\frac{4}{3}} \frac{\nu^{0.6}}{d^2} \tag{1.2}$$

Obtaining measurements of the infra-red or radio excess from OB stars is a problem, since many of the objects emit weakly at these wavelengths. This excludes this method from being applied to extra-galactic OB stars or stars with weak winds. However, Barlow & Cohen (1977) succeeded in analysing the IR excess of 34 OBA supergiants using this method. Bieging *et al.* (1989) made radio measurements for a large sample of OB stars, but concluded that a radio flux had not been detected for a number of sources. More

recently, Runacres & Blomme (1996) confirmed consistency between observed radio fluxes and IR excess and current theoretical predictions for OB stars.

1.5 Recent research on B supergiants

In this section important advances in research focused on B supergiants is presented. Improvements in stellar atmosphere codes have enabled astronomers to derive increasingly accurate stellar parameters for hot, massive stars and this is discussed in Chapter 2. This had led to revisions of the O star temperature scale and an important part of this thesis work is dedicated to revising the temperature scale for Galactic B supergiants (presented in Chapter 3). It has also provided a simple method for accurate abundances to be derived using these models, enabling precise determinations of the amount of nitrogen enrichment and carbon/oxygen depletion. Recent analyses of B supergiants in the Small Magellanic Cloud (SMC) by Trundle *et al.* (2004); Trundle & Lennon (2005) have produced revised temperatures, abundances and mass loss rates that are complementary to this thesis work and also provide insight into how these parameters are affected by the low-metallicity environment of the SMC. Crowther *et al.* (2006) have also presented an analysis of Galactic B0 – B3 Ia stars, showing evidence of a modest reduction of 1000 – 2000 K in the B supergiant temperature scale. The availability of *FUSE* and *IUE* spectra for a large number of OB supergiants has enabled stellar atmosphere codes to be applied to the UV & FUV to test their validity in this region. Again this forms part of the research presented here (see Chapter 4). Hanson & Conti (1994); Hanson *et al.* (1996) have explored the possibility of deriving stellar parameters from the infra-red and found that the stellar temperature and surface gravity can be derived from K-band spectroscopy. This proves to be an indispensable tool for determining the parameters of hot, massive stars that are embedded in star-formation regions or the Galactic centre, where they are obscured by large amounts of dust. In the last year, a near-infrared spectral atlas of early OB stars has been published (Hanson *et al.*, 2005) that includes 7 B supergiants, allowing the accuracy of these stellar atmosphere models to be tested at near-infrared wavelengths. An initial analysis of the near-infrared spectra of 25 Galactic OB stars has already been carried out by Repolust *et al.* (2005), who found that stellar parameters derived from the near-infrared are generally in good agreement with those obtained from the analysis of optical spectra.

There has been renewed interest in hot, massive stars in general in the last few years for several reasons. First is the possibility that B supergiants might be the progenitors of Type II supernovae, given the surprise discovery that the progenitor of SN1987A was a B3 supergiant. Analyses of other Type II supernovae (e.g., Maund *et al.*, 2005; Hendry *et al.*, 2005) appear to suggest that the progenitors of Type II supernovae are low-to-intermediate mass red supergiants, which have of course evolved from blue supergiants. This makes the progenitor of SN1987A of even greater interest as there is currently no explanation why it may have exploded 'early' in its lifetime, rather than waiting to evolve into a red supergiant before exploding as a Type II supernova. However the idea that OB supergiants going through a red supergiant phase might produce a gamma-ray burst is not supported by Woosley & Heger (2006). These authors point out that the production of gamma ray bursts depend strongly on the mass loss rate and rotation rate of the progenitor star. In general, OB supergiants do not possess a high enough initial rotation to be rotating fast enough towards the end of their lifetime to produce a gamma ray burst, since they lost too much angular momentum through mass loss. This may not be the case if mass loss rates were smaller than those they adopted for this work, either because gamma ray bursts are of lower metallicity than originally thought or too much angular momentum loss was used in the models. The idea is interesting as in the next section, current evidence suggesting that observed mass loss rates are over-estimate is presented. Finally, it has also been shown by Bromm *et al.* (2001); Matteucci & Calura (2005) that massive stars play a key role in the chemical evolution and reionisation of the early Universe.

1.5.1 Clumping in B supergiant winds

The issue of clumping in the stellar winds of B supergiants and other hot stars is a highly topical one. The term 'clumping' refers to the inhomogeneous distribution of material in the stellar wind, where material is grouped into 'clumps' rather than distributed evenly throughout the wind. There are increasing amounts of both observational and theoretical evidence to support the idea that stellar winds are not smooth and homogeneous as assumed by the standard model. Observationally, the effects of clumping can be seen in the form of large and small scale structure in the wind that causes line profile variations (Prinja *et al.*, 2002). Discrepancies between mass loss rates derived from the Hα line profile and the infra-red excess have also been attributed to the inhomogeneous nature of the stellar wind. Similarly early indications of the unexpectedly low values of ionisa-

tion fractions in OB star winds (Massa *et al.*, 2003; Prinja *et al.*, 2005; Fullerton *et al.*, 2006) suggest that the presence of clumping might be the cause. When using stellar atmosphere models that include the presence of a stellar wind, Bouret *et al.* (2005); Hillier *et al.* (2003) claim that the inclusion of clumping is required in the model to fit certain UV wind lines. Using a purely theoretical approach, Dessart & Owocki (2003, 2005) have shown that the instabilities generated at the base of the wind can grow to produce an inhomogeneous wind that can explain the observed line profile variations in OB star spectra.

There is a vast amount of evidence available in the literature for both photospheric and wind variations in OB stars, revealing the extent to which B supergiant winds are clumped and structured, but here the most important results for B supergiants are presented. Kaufer *et al.* (1996, 1997), for example, carried out an extensive monitoring campaign of optical spectroscopic variability in late B and early A supergiants, which gave valuable insight into the complexity of the structure of the circumstellar envelope. Time-series analysis of Hα revealed asymmetry in the envelope morphology, whilst observations of recurring absorption features were attributed to rotation. Examination of line-profile variations in the photospheric spectrum imply that non-radial pulsations in the photosphere are responsible. A detailed study of the optical variations of the B0 Ia star ϵ Ori by Prinja *et al.* (2004) found evidence of periodic variations in *both* Hα and Hβ i.e. lines affected by the stellar wind and photospheric He I and metal lines. This result is unprecedented in showing a connection between photospheric variations and perturbations in the stellar wind.

The study of B supergiant winds is vital in revealing information on the presence of small-scale and large-scale structure in the wind. Examples of small-scale structure are the presence of extended black absorption troughs in P Cygni profiles, X-ray emission (e.g., Feldmeier *et al.*, 1997) and non-thermal radio emission. It is thought to originate from instabilities in line-driven winds (e.g., Owocki *et al.*, 1988). UV analysis of stellar wind variability in B supergiants has been carried out by Prinja *et al.* (2002), which is important in outlining the main characteristic features of time-series data of B supergiants that correspond to large-scale structure in the wind. The observed spectral variations appear as the result of organised, spatially-extended perturbations in the wind, possibly caused by magnetic or pulsational processes at the stellar surface. An example of large-scale

structure is the presence of *discrete absorption components* (DACs), localised absorption enhancements that migrate blue-wards in line profiles. Another example is the presence of bowed structures that appear due to optical depth changes that occur suddenly over a wide velocity range. Fig. 1.5 illustrates a grey-scale representation of variability in the B0 Ia star HD 37128 (ϵ Ori), showing examples of these structures.

1.5.2 Current issues in stellar astrophysics

In this section important, unresolved problems concerning B supergiants and hot, massive stars is general are summarised, following on from the previous section. The most urgent issue concerning hot, massive stars is the discrepancy between observed mass loss rates obtained from different methods and the role of clumping in contributing to this discrepancy. Earlier work by Lamers & Leitherer (1993); Lamers *et al.* (1999*a*) for O stars that claimed good agreement between $\dot{M}_{\rm H\alpha}$ & $\dot{M}_{\rm radio}$ and this has been confirmed for Galactic B supergiants by Crowther *et al.* (2006). Blomme *et al.* (2002) measured the thermal radio flux of ϵ Ori (the only B supergiant for which this has been achieved) and found that the derived value of $\dot{M}_{\rm radio}$ was in good agreement with $\dot{M}_{\rm H\alpha}$. The exception to the general agreement between $\dot{M}_{\rm H\alpha}$ and $\dot{M}_{\rm radio}$ is ζ Pup, where Blomme *et al.* (2003) measured $\dot{M}_{\rm radio} = 3.5 \pm 0.1 \times 10^{-6}\ M_{\odot}\ {\rm yr}^{-1}$ compared with $\dot{M}_{\rm H\alpha} = 5.9 \times 10^{-6}\ M_{\odot}\ {\rm yr}^{-1}$ (Puls *et al.*, 1996). The remaining results that *do* show agreement between $\dot{M}_{\rm H\alpha}$ & $\dot{M}_{\rm radio}$ remain a puzzle since it implies that the same amounts of structure and material are present in very different regions of the stellar wind. It also contradicts the results of hydrodynamical simulations (e.g., Runacres & Owocki, 2002) that imply that clumping/filling factor should increase with increasing distance from the star. It is also useful to test the validity of line driven wind theory by comparing observational and theoretical mass loss rates. The mass loss prescription written by Vink *et al.* (2000) provides a convenient method of determining the theoretical mass loss rate of a star. Trundle & Lennon (2005) have compared their values of $\dot{M}$ (derived for a sample of Small Magellanic Cloud B supergiants) with those predicted by the Vink *et al.* (2000) formula and found that theoretical $\dot{M}$ are larger than the observed $\dot{M}$ of early B supergiants, whereas for cooler B supergiants the reverse is true. Interestingly this discrepancy does not correlate with the shape of the Hα profile i.e. whether it is in absorption, emission or assumes a P Cygni morphology.

The discrepancy between observed and theoretical WLRs for B supergiants also points

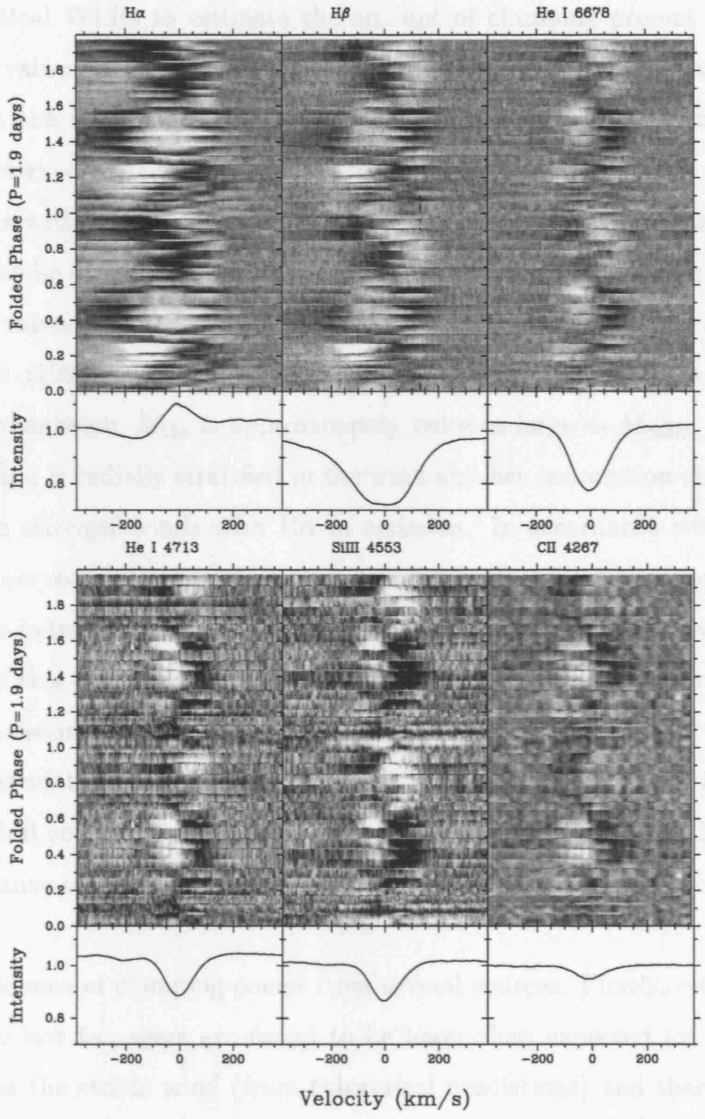

Figure 1.5: Grey-scale representation of variability in HD 37128. The weak metal lines display a clear 'S-wave' pattern, which is also present in Hα & Hβ, superimposed with another 'S-wave' pattern half-a-cycle out of phase with the original one.

toward a discrepancy in mass loss. The WLR shows a dependency on spectral type so it is probable that the problem lies with the sensitivity of $\dot{M}$ to both luminosity and metallicity. Markova *et al.* (2004) discussed the possibility of using the offset between observed and theoretical WLRs to estimate the amount of clumping present in O star winds by comparing values of $\dot{M}_{\mathrm{H}\alpha}$ and $\dot{M}_{\mathrm{radio}}$. Following evidence put forward by Owocki *et al.* (2000) that the clumping factor is radially stratified in the wind, it should then follow that the observed $\dot{M}_{\mathrm{H}\alpha}$ should be large for stars with stronger winds i.e. Hα in emission, *but* for stars with *weaker* winds displaying Hα in absorption, an equal or higher value of $\dot{M}_{\mathrm{radio}}$ might be expected. Markova *et al.* (2004) then tested out this hypothesis by comparing the values of $\dot{M}_{\mathrm{H}\alpha}$ that she had derived with those of $\dot{M}_{\mathrm{radio}}$ obtained by Lamers & Leitherer (1993) and Scuderi *et al.* (1998). For 3 O supergiants in her sample that show Hα in emission, $\dot{M}_{\mathrm{H}\alpha}$ is approximately twice as large as $\dot{M}_{\mathrm{radio}}$, supporting the idea that clumping is radially stratified in the wind and her assumption that it can only really be 'seen' in stronger winds with Hα in emission. In accordance with the disagreement between observed and theoretical mass loss rates, Trundle & Lennon (2005) also find a discrepancy between observed and theoretical WLRs. In order to investigate the effect of clumping in this discrepancy, Repolust *et al.* (2004) modified their derived $\dot{M}$ with clumping factors, assuming a constant clumping factor in the Hα-emitting region of the stellar wind. Recalculating the observed WLR using these 'clumped' mass loss rates, they subsequently find consistency between the observed and theoretical WLRs. This emphasises the importance of the influence of clumping when determining stellar wind parameters.

Further evidence of clumping comes from several sources. Firstly, estimates of q_i for OB stars in the last ten years are found to be lower than expected for ions assumed to be dominant in the stellar wind (from theoretical predictions) and therefore approaching a value of unity (Lamers *et al.*, 1999*a*; Massa *et al.*, 2003; Prinja *et al.*, 2005). Since the estimated value of q_i is affected by the adopted mass loss rate, an over-estimation of $\dot{M}$ due to the presence of clumping would lower q_i. The estimates of $\dot{M}q_i$ are derived from sampling the optical depth of each wind resonance line directly, so it is *highly* unlikely that this is the source of the discrepancy. As mentioned in the previous section, much evidence exists of photospheric and stellar wind variability of B supergiants, indicating that deep-seated instabilities in the highly structured and inhomogeneous winds. The same is true for O supergiants (e.g., Prinja *et al.*, 2006; Prinja *et al.*, 1996; Massa *et al.*, 1995*a*),

demonstrating that the explanation of the exact mechanisms behind such variations and their link with clumping is an essential step in improving our understanding of the nature of OB stellar winds.

Another unresolved issue in massive, hot star is research is the *mass discrepancy*. First noted by Herrero *et al.* (1992), this refers to the difference between stellar masses derived *spectroscopically* from measured values of the surface gravity, $M_{\rm spec}$, and those estimated from stellar evolutionary tracks, $M_{\rm evol}$, where $M_{\rm spec}$ was systematically smaller than $M_{\rm evol}$. It was thought that the discrepancy could be attributed to the omission of sphericity and mass loss from the analysis, so Herrero *et al.* (2002) revisited the problem and found that, with the inclusion of sphericity and mass loss, a smaller discrepancy still existed for stars with $M_* \leq 15\ M_\odot$. This result has also been confirmed by Repolust *et al.* (2004).

1.5.3 Aims of this thesis work

The main focus of this thesis work is an optical-UV analysis of the stellar atmosphere and wind properties of Galactic B0 – B5 supergiants. The first aim is to derive accurate fundamental parameters (including $T_{\rm eff}$, log g and luminosity) for a sample of 20 Galactic B supergiants that includes B Ia, B Iab, B Ib & B II stars. CMFGEN, a line-blanketed, nLTE stellar atmosphere code that incorporates the effects of the stellar wind (Hillier & Miller, 1998) is selected for this work and is introduced in §2.4. This is the first analysis of its kind to use an *ab initio* model atmosphere code to obtain parameters for B stars *over a range of luminosity classes* (i.e., B Ia – II) and produces a unique Galactic B supergiant temperature scale. Such a temperature scale is highly useful as the temperatures are constrained from *individual* stars, rather than being based on spectral type. A distinction is made between different luminosity classes, making an improvement on previous temperature scales such as Humphreys & McElroy (1984). These temperatures scales made the assumption that all stars of e.g., spectral type B0.5 were the same temperature regardless of luminosity class, which is not necessarily true especially between B Ia & B Ib stars. This consequently led to a 'spectral-bin effect' when examining trends of stellar parameters with temperature, potentially masking any clear trend. It is also possible to derive luminosities, stellar radii, surface gravities (and therefore stellar masses) from this analysis. Given the improved reliability of stellar atmosphere codes in recent years, accurate CNO abundances can also be obtained. This provides vital clues to the precise

evolutionary status of each star by examining how much CNO processing has occurred.

An important part of this analysis is to constrain mass loss rates from fits to the Hα profile and investigate the effects of clumping, again using the stellar atmosphere code of Hillier & Miller (1998). The method of deriving $\dot{M}$ from Hα was chosen in this case for several reasons. Firstly, CMFGEN has been proven to derive reliable mass loss rates for O supergiants by Hillier *et al.* (2003); Evans *et al.* (2004*a*). Secondly, the *majority* of B supergiants do not emit strongly at radio and infra-red wavelengths, making it impossible to derive $\dot{M}_{\rm radio}$ for the whole sample of 20 B supergiants. Also since we have optical data readily available and can model the Hα profiles using CMFGEN, this seems to be the more efficient way to derive mass loss rates for the purpose of this thesis work. This is complemented by extending the stellar atmosphere code into the UV, to investigate whether the same mass loss rate is implied at a different wavelength in a region that is affected differently by clumping ($\dot{M}_{\rm H\alpha} \propto \rho^2$ whereas $\dot{M}({\rm UV}) \propto \rho$).

Using these derived mass loss rates, the aim is then to investigate the ionisation structure of B supergiant winds using the SEI method to obtain estimates of empirical q_i. This information, along with that obtained through stellar atmosphere modelling, permits us to make a unique comparison of empirical and theoretical predictions of the ionisation structure for B supergiants. The aim is then to investigate which ions are predicted to be dominant in B supergiant winds and what corresponding value of q_i is given by the model in comparison with the empirically derived q_i, as well as how the theoretical and empirical q_i depend on temperature and velocity. The main purpose of this work is to confirm or disprove the unexpectedly low q_i values found so far by Lamers *et al.* (1995); Massa *et al.* (2003); Prinja *et al.* (2005) & Fullerton *et al.* (2006), which suggest a reduction in observed mass loss rates is required to resolve this problem. Additionally, the available information should enable us to examine whether B supergiants can exist in a bi-stable state, as suggested by Pauldrach *et al.* (1994); Lamers *et al.* (1995) and predicted by Vink *et al.* (2000). More recent research Prinja & Massa 1998; Crowther *et al.* 2006 implies a more gradual trend.

In summary, this thesis aims to provide some answers to the following questions:

- How does the new B supergiant temperature scale compare to previous temperature scales, especially those recently revised for O stars?
- How much CNO processing is observed in Galactic B supergiants?
- Is there a mass discrepancy for Galactic B supergiants?
- How reliable are mass loss rates derived from Hα? What method for estimating mass loss rates is most appropriate and reliable for B supergiants?
- How well can CMFGEN reproduce both optical and UV spectral diagnostics over an extended temperature domain?
- How do results obtained from *ab initio* and empirical line synthesis models used to analyse stellar winds compare?
- How can we constrain the amount and extent of clumping in B supergiant winds?
- What is the ionisation structure of B supergiant winds and how is it affected by inhomogeneities?
- Does the bi-stability jump observed around B1 stars still exist observationally?

CHAPTER 2

The stellar atmosphere codes CMFGEN & TLUSTY

This chapter will first of all review our current theoretical understanding of the atmospheres and winds of hot stars, then focus on describing the stellar atmosphere codes CMFGEN and TLUSTY, which have been used in this thesis work. An overview of the nLTE stellar atmosphere codes that are available for use at present, the physical processes incorporated in them and the computational methods used to run them will be included in this section. Many of these codes have been written to describe the atmospheres of O stars and can be successfully applied to B stars.

2.1 The physics of stellar atmospheres

The physics involved in generating a star's atmosphere must incorporate the processes of nucleosynthesis, radiation and convection within the photosphere. The photosphere of the star is defined as its visible surface, where the outflow velocities are smaller than the local speed of sound and can be considered to be negligible. This allows us to approximate the photosphere to a static region that can be described by the equation of hydrostatic equilibrium (see equation 2.2 below). The photosphere forms part of the stellar atmosphere, the low density outer region of the star that is transparent to light at all wavelengths except those which it absorbs. Beyond the region of the photosphere then lies the stellar wind, where by definition the outflow velocities must be at least equivalent to, if not greater than, the local sound speed. Fig. 2.1 outlines the structure of a stellar atmosphere (not

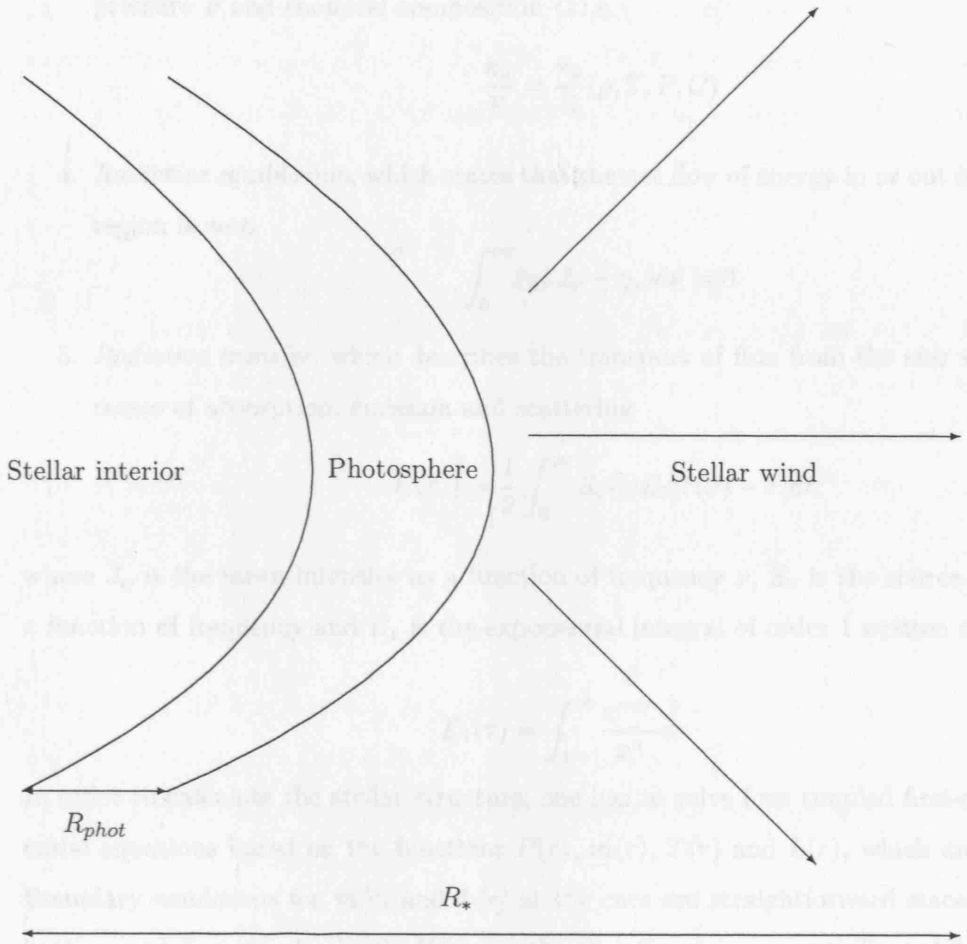

Figure 2.1: A stellar atmosphere consists of the stellar interior, stellar photosphere and stellar wind. Note that the radius of the photosphere $R_{phot} \ll R_*$.

to scale). The structure of a stellar atmosphere in LTE (see §2.1.1 for definition) can be described by the following conditions:

1. *The equation of state (describing charge & particle conservation)*, which states that the pressure is a function of density ρ, temperature T and chemical composition C.

$$P = P(\rho, T, C) \tag{2.1}$$

2. *Hydrostatic equilibrium*, which describes the internal pressure gradient required to prevent the star from collapsing under gravity.

$$\frac{dP}{dr} = -\frac{Gm(r)\rho(r)}{r^2} \tag{2.2}$$

3. *Definition of opacity*, where the opacity is a function of density ρ, temperature T, pressure P and chemical composition C i.e.

$$\frac{\kappa_\nu}{\overline{\kappa}} = \frac{\kappa_\nu}{\overline{\kappa}}(\rho, T, P, C) \tag{2.3}$$

4. *Radiative equilibrium*, which states that the net flow of energy in or out of the stellar region is zero

$$\int_0^\infty (\chi_\nu J_\nu - \eta_\nu) d\nu = 0 \tag{2.4}$$

5. *Radiative transfer*, which describes the transport of flux from the star via the processes of absorption, emission and scattering

$$J_\nu(\tau_\nu) = \frac{1}{2}\int_0^\infty S_\nu(t) E_1|\tau(\nu) - \tau| dt \tag{2.5}$$

where J_ν is the mean intensity as a function of frequency ν, S_ν is the source function as a function of frequency and E_1 is the exponential integral of order 1 written as

$$E_1(\tau) = \int_1^\infty \frac{e^{-x\tau}}{x^n} dx \tag{2.6}$$

In order to calculate the stellar structure, one has to solve four coupled first-order differential equations based on the functions $P(r)$, $m(r)$, $T(r)$ and $L(r)$, which are unknown. Boundary conditions for *m(r)* and *L(r)* at the core are straightforward since when r=0, both m and L must also be 0. However the situation is more complicated for *P(r)* and *T(r)* in the stellar atmosphere and requires a more precise knowledge of the atmospheric properties. Most stellar atmosphere codes consider a hydrostatic photosphere in radiative equilibrium, which for a spherically symmetric star can be mathematically expressed as

$$\frac{dP}{dr} = -\frac{\rho G M_*}{r^2} \approx -\frac{\rho G M_*}{R_*^2} = -\rho g \tag{2.7}$$

where P is the total pressure (i.e. the sum of the effects of gas, radiation and turbulent pressure) as a function of r, the radial coordinate, M_* represents the stellar mass, $R_*$the stellar radius, ρ is the mass density and g is the gravitational acceleration. This expression merely describes the total pressure gradient through the photosphere, held in balance by the local gravitational acceleration, which can be assumed to be constant on account of its small radial extent. Gas pressure in hot star winds is negligible (except at the base of

the wind) because extremely high temperatures are needed to generate a sufficiently large gas pressure force to drive the wind beyond the sonic point. When radiative equilibrium is used in stellar atmosphere codes for hot stars, the stars are assumed to be convectionally stable. Using this assumption, we can then write the equation of radiative equilibrium as:

$$\int_0^\infty (\chi_\nu J_\nu - \eta_\nu) d\nu = 0 \tag{2.8}$$

where χ_ν is the absorption coefficient, η_ν is the emission coefficient and J_ν is the mean intensity of the radiation field. All terms are a function of frequency and will be explained further shortly. From the above equation we can derive the equation of radiative transfer to describe how the radiative energy from the stellar interior interacts with the surrounding matter:

$$(\frac{1}{c}\frac{\delta}{\delta t} + n.\Delta)I(\nu, r, n, t) = \eta(\nu, r, n, t) - \chi(\nu, r, n, t)I(\nu, r, n, t) \tag{2.9}$$

which expresses the radiation in terms of the specific intensity, I, dependent on the frequency per solid angle, per unit area, per time interval. This intensity can be represented by the Planck function when a star is in thermodynamic equilibrium:

$$B(\nu, T) = \frac{2h\nu^3}{c^2}\frac{1}{e^{\frac{h\nu}{kT}} - 1} \tag{2.10}$$

where $B(\nu, T)$ is the Planck function as a function of frequency ν and gas temperature T, (equivalent to the specific intensity I under thermodynamic equilibrium), h is the Planck constant, c is the speed of light and k is the Boltzmann constant. In thermodynamic equilibrium the condition $I = \frac{\eta}{\chi}$ holds true i.e. equal amounts of radiation energy are absorbed and emitted in the same volume and freqeuncy interval. The role of the absorption and emission coefficients in the equation of radiative transfer can now be seen as they represent the removal and addition of radiation and its subsequent effect on the net emergent radiation from the star. We can then write the absorption coefficient χ_v as:

$$\begin{aligned}\chi_v = &\sum_i \sum_{j>i} [n_i - \frac{g_i}{g_j} n_j]\sigma_{ij}(\nu) \\ &+ \sum_i (n_i - n_i^* e^{-\frac{h\nu}{kT}})\sigma_{i\kappa}(\nu) \\ &+ \sum_\kappa n_e n_\kappa \sigma_{\kappa\kappa}(\nu, T)(1 - e^{-\frac{h\nu}{kT}}) + n_e \sigma_e\end{aligned} \tag{2.11}$$

and similarly the emission coefficient η_ν can be written as:

$$\begin{aligned}\eta_\nu = &\frac{2h\nu^3}{c^2}(\sum_i \sum_{j>i} n_j (\frac{g_i}{g_j})\sigma_{ij}(\nu)) \\ &+ \sum_i (n_i^* \sigma_{i\kappa}(\nu) e^{-\frac{h\nu}{kT}}) \\ &+ \sum_\kappa (n_e n_\kappa \sigma_{\kappa\kappa}(\nu, T) e^{-\frac{h\nu}{kT}})\end{aligned} \tag{2.12}$$

the population density of state i (or to a transitional state j) and g_i is the corresponding statistical weight; n_i^* describes the population in statistical equilibrium; σ is the cross-section of the atom at frequency ν where subscript κ represents the continuum. All terms are consistent for both the absorption and the emission coefficients. In the above equations 2.11 and 2.12, the first three terms of each equation represent bound-bound transitions (responsible for spectral lines), bound-free transitions (produce continua) and free-free absorption (or *bremsstrahlung*); any negative contributions are due to stimulated emission. The scattering term has no correction for stimulated emission as it cancels out precisely with absorption. Electron scattering can be approximated to coherent (i.e. Thomson scattering) in stellar atmospheres since there is no change of photon frequency. The bound-bound cross-section $\sigma_{ij}(\nu)$ for a bound transition is described by the following expression:

$$\sigma_{ij}(\nu) = \frac{h\nu_0}{4\pi} B_{ij} \phi(\nu) \tag{2.13}$$

where B_{ij} is the Einstein coefficient for photoexcitation and $\phi(\nu)$ is the absorption profile coefficient and is normalised to unity such that $\int \phi(\nu) d\nu = 1$. Alternatively this expression gives the conditional probability density of a photon being absorbed in the frequency

range $(\nu, \nu + d\nu)$ if it has been absorbed in the transition i to j. For further details on these equations please refer to Hubeny (1999).

2.1.1 A brief history of LTE stellar atmosphere codes

A model atmosphere can be described as the specification of all the atmospheric state parameters as a function of position. The first stellar atmosphere codes used the assumption of LTE (Local Thermodynamic Equilibrium), meaning that local conditions (i.e. atom, ion & molecule level populations) of the gas can be described by an absolute temperature and total particle density i.e. a Saha-Boltzmann distribution:

$$N_n = \frac{g_n}{Z_0(T)} e^{\frac{-E_n}{kT}} [1 + \frac{2Z_i}{n_e Z_0} \frac{(2\pi m_e kT)^{\frac{3}{2}}}{h^3} e^{\frac{-\chi_0}{kT}}]^{-1} N_H \tag{2.14}$$

where N_n is the population of state n, g_n is the statistical weight of state n, Z_0 and Z_i are the partition functions for neutral atoms and ions respectively, E_n is the energy of state n, n_e is the electron density, m_e is the mass of an electron, χ_0 is the ionisation energy of an electron in ground state and $N_H = N_0 + N_i$. LTE is only valid if collisional processes dominate in the atmosphere (as opposed to radiative processes), *detailed balance* holds (i.e. each microscopic process of excitation or ionisation is statistically balanced by its precise inverse process of de-excitation or recombination) and/or if the mean-free path of a photon in the star's atmosphere is small and therefore localised. It tends to be appropriate for cooler, low mass stars such as A, F & G-type stars.

Hot stars such as OB, Wolf Rayet and Luminous Blue Variable stars all possess strong stellar winds and extended atmospheres. In such conditions, radiative processes dominate and the assumption of LTE breaks down, so the star is now in non-local thermodynamic equilibrium (nLTE). Since the condition of radiative equilibrium no longer holds, radiation from the star cannot be described by the Planck function as it is when LTE is valid. In addition to this, the level populations begin to diverge from those specified by the Saha-Boltzmann distribution. This effect leads to over- or under-population of atomic levels and such an effect is observed in hot stars. It is therefore necessary for stellar atmosphere codes to account for this departure from LTE conditions, by allowing level populations to

differ from the local Saha-Boltzmann equilibrium values. The code can construct model atoms and ions, reproduce individual line transitions and define departure coefficients to quantify how much a given population deviates from LTE in order to calculate the level populations directly. This is the basic principle of handling nLTE conditions in nLTE stellar atmosphere codes.

In order to reduce the complexity of calculating a model atmosphere, a simplified geometry can be assumed. The geometrical approximation used for a model atmosphere needs to fulfil the requirements of reducing computation time whilst including enough numerical calculations to produce a sufficiently realistic model atmosphere. The aim of these geometrical simplifications is to avoid the complexity of a spatially three-dimensional problem by replacing it with a one or two-dimensional problem. The most frequently used geometries are listed below, starting with the simplest:

1. *Plane parallel geometry* assumes horizontally homogeneous layers in a one-dimensional model where atmospheric depth is the only dimension. This approximation holds well for stellar photospheres since they are several orders of magnitude thinner than the stellar radius, meaning that curvature effects are negligible.

2. *Spherical symmetry* is another one-dimensional approximation employed for *extended atmospheres*, where atmospheric thickness is significant compared to the stellar radius. This simplification is applied in models used for early type giants and supergiants.

3. *Multi-dimensional geometry* involves numerical simulations calculated in two or three-dimensional geometry that are highly demanding in terms of computational time and resources. However two-dimensional simulations of early type stellar winds (see Dessart & Owocki (2005) and solar model atmospheres based on two and three-dimensional geometry have been achieved.

Dynamical approximations can also be made regarding the treatment of the macroscopic velocity fields in the model, again to alleviate the complexity of numerical calculations and minimise computation time. The following simplifications are usually adopted:

1. *Static models* where the macroscopic velocity field is zero, corresponding to a stellar photosphere model with no influence of a stellar wind.

2. *Models with an 'a priori' given velocity field.* Here the velocity field is treated explicitly along with a detailed study of its effect on other state parameters e.g. the emergent radiation. There are two different models that employ this approximation; *core halo models* which assume the incoming photospheric radiation as *a priori* and only treat the stellar wind and *unified models* that treat both the photosphere and the wind.

3. *Self-consistent velocity field models* where the solution of the relevant hydrodynamical equations determines the macroscopic velocity field. These solutions are derived in conjunction with a rough treatment of radiative transfer in spectral lines to deal with the complexity of the wind driving force, produced by photon absorption in thousands to millions of metal lines.

The inclusion of opacities in stellar atmosphere models can prove to be another vastly complex function of frequency. It is impossible to provide a detailed account for all the opacity sources, especially since elements such as Fe and Ni have the order of $10^6 - 10^7$ spectral lines per ion. Therefore one of the following approximations is normally made in a stellar atmosphere model:

1. *Grey models* where frequency-averaged opacities are constructed. The assumption made is that these frequency-averaged opacities can reasonably describe the behaviour of the frequency-averaged intensity of the radiation. The most widely used frequency-averaged opacity is the *Rosseland mean opacity*, given by:

$$\frac{1}{\chi_R} \equiv \frac{\int_0^\infty (\frac{1}{\chi_\nu}) \frac{dB_\nu}{dT}\, d\nu}{\int_0^\infty \frac{dB_\nu}{dT}\, d\nu} \tag{2.15}$$

   where χ_ν represents the opacity (per gram of stellar material). The Rosseland mean opacity describes the total radiation flux well as it is averaged using $\frac{1}{\chi}$, giving the most weighting to the lowest opacity regions where energy flux transport is the most efficient. Grey models are not a realistic assumption and are therefore not used for spectroscopic analysis anymore, but they are still used in stellar atmosphere codes as an initial estimate for an iterative method to solve for radiative transfer.

2. *The multi-frequency/multi-grey method* involves the use of stepwise frequency averages for a number of frequency bins. This approach is usually applied in other as-

trophysical and laboratory radiative transfer codes but rarely in stellar atmosphere codes.

3. *Metal line-blanketed model atmospheres* which attempt to account for the opacity of all metal lines. In LTE, this calculation is simplified by the fact that the opacity and emissivity only depend on the local temperature and electron density, leaving only the more complicated situation of describing the frequency dependence of the opacity. However in nLTE, this becomes a highly complex problem since all the atomic level populations and temperatures need to be determined self-consistently with the radiation field. Despite this, most current nLTE stellar atmosphere codes adopt this approach with success.

One of the first widely used LTE model atmosphere codes was that of Kurucz (1979), whose code included treatment of line blanketing. Models were now founded on the concept that the essential tool for understanding the physics of a stellar atmosphere was the (non-local) coupling of physical quantities (e.g. temperature, radiation field, level populations). During the 1980's, it was soon realised that not all varieties of coupling are equally important, only the essential parts need to be treated explicitly and the rest could be solved via iteration. This lead to the development of 'ALI', accelerated lambda iteration Scharmer (1982), based on ideas originally put forth by Cannon (1973*a*,*b*) and Rybicki (1972). The basic principle of this technique was to use a lambda operator to represent the radiation intensity and allow it to act on the source function plus a correction term provided from a previous iteration, such that radiation intensity is actually eliminated from a set of unknown variables. Werner (1986, 1987, 1989) was the first to apply the ALI method to model stellar atmospheres. Another important concept (known as *the multifrequency/multigray algorithm*, see the opacity approximations above) was introduced during this time allowing all frequency points to be grouped into a small set of frequency blocks, instead of treating them individually ((Anderson, 1985, 1987, 1989)). Despite these improvements, these models were still limited to treating hundreds to thousands of lines (mostly elements such as C,N,O) and were not therefore fully blanketed. The main reason for this limitation was that each energy level was treated individually, making it impossible to include iron-peak elements that possess a highly complex energy level structure. Anderson (1989) found a solution to this problem by introducing a statistical method that allowed him to group many energy levels with similar 'behaviour' into a small number of

superlevels (see §2.3.4 & §2.4.1) and succeeded in calculating the first properly line blanketed stellar atmosphere model.

2.1.2 Introduction to nLTE stellar atmosphere codes

Developments in the last 20 years to nLTE stellar atmosphere codes have lead to a resurgence of interest in obtaining accurate fundamental parameters for hot stars. Significant improvements have been made to the codes such as including more complex atoms e.g. C, N, O, Si, S, Mg & Fe (rather than just H & He as before), extending the geometry from plane-parallel to spherical (to allow for extended atmospheres and stellar winds) and more recently incorporating the effects of line blanketing. The last effect is complex since it involves computing thousands of level populations of metal atoms in order to solve both statistical equilibrium and radiative transfer equations in an expanding atmosphere but also very important since these metal lines have a profound effect on the star's atmospheric structure and emergent spectrum. In the case of O stars, the use of nLTE models with a thorough treatment of the effect of line blanketing lead to a reduction in O star temperature scales (Martins *et al.*, 2002; Herrero *et al.*, 2002; Bianchi, 2002; Repolust *et al.*, 2004; Massey *et al.*, 2004), ranging from 2000 K in dwarfs to 8000 K in supergiants (Martins *et al.*, 2005). Given the complexity of including line blanketing, various nLTE stellar atmosphere codes employ different methods for the task. There are 5 main nLTE stellar atmosphere codes currently in use which vary in their assumptions, computation time and means of solving the equation of radiative transfer:

- *TLUSTY* (Hubeny & Lanz, 1995; Lanz, 2003) is based on the assumption of a plane-parallel atmosphere, meaning that it calculates a horizontally homogeneous atmosphere that is in hydrostatic and radiative equilibrium. The code also uses opacity distribution functions to incorporate a full treatment of line blanketing and includes very detailed calculations of the nLTE rate equations. Very good results have been achieved using TLUSTY to model hot stars (Lanz, 2003).

- *CMFGEN* (Hillier & Miller, 1998) is a unified wind-atmosphere code (meaning it is a code that combines the effects of a dynamic stellar wind with those of the star's radiation field) that solves the nLTE rate equations in a co-moving frame using super-levels. In other words, a single super-level groups together levels with similar atomic

properties such as energies and transition rates. It assumes a spherically symmetric atmosphere that is extended, expanding and in steady state. It incorporates a full treatment of line blanketing as well as the inclusion of many atomic species including all the Fe-group elements. Finally the code also has the capacity to include the effects of X-rays and clumping in the stellar wind. The only real disadvantage is that computation time can be lengthy (i.e. 12-50 hours using a system with a 2.8 GHz processor) and the code does not calculate self-consistent dynamics.

- *WM-BASIC* (Wind Momentum - (VISUAL) BASIC) (Pauldrach *et al.*, 2001) is also a unified wind-atmosphere code that makes a complete hydrodynamical calculation of the atmospheric structure. This is done by treating the stellar wind in the observer's frame to solve the nLTE rate equations whilst using the Sobolev plus continuum approximation. One disadvantage is that it does not include line broadening terms, which could lead to a poorer reproduction of the H & He lines, especially in the profile wings. It does however treat line blanketing via by employing the opacity sampling method and has a reasonably fast computation time on a normal desktop PC.

- *ISA-WIND* (de Koter *et al.*, 1997) is another unified wind-atmosphere code, which uses an approximate lambda iteration method to solve the equations of statistical equilibrium and radiative transfer. The code includes a full treatment of the diffuse radiation field by using the improved Sobolev approximation (ISA) (Puls, 1988) to treat line transfer.

- *FASTWIND* (Santolaya-Rey & Puls, 1997; Puls *et al.*, 2005) ,as its name suggests, is designed for fast computation, employing a consistent photospheric stratification. The code has the option to deal with line transfer either in a co-moving frame or by using the Sobolev approximation with continuum. It also includes an approximate treatment of line blocking and blanketing. The main difference between this code and the other nLTE codes is that it allows for a consistent treatment of incoherent electron scattering via the use of a fast solution algorithm. FASTWIND has been used to model OB stars with very good results (e.g., Herrero *et al.*, 2002; Repolust *et al.*, 2004; Trundle *et al.*, 2004; Trundle & Lennon, 2005).

All these codes are useful for modelling hot stars since they all adopt nLTE and include the effects of metal line blanketing with the exception of ISA-WIND. However when modelling B supergiants, we require not only nLTE and a full treatment of line blanketing, but also a reliable treatment of the star's expanding, extended atmosphere and wind. This narrows our choice of code down to CMFGEN or WM-BASIC, since FASTWIND only uses an approximate method to treat line blanketing and did not compute a UV spectrum until very recently (2005). On the other hand, WM-BASIC does not include line broadening, which could be a potential problem when obtaining estimates of the surface gravity (log g) from Balmer line wings (see §3.2.1). Therefore we decided to use CMFGEN to derive fundamental parameters for our sample of B supergiants. However, CMFGEN has the drawback that it does not compute the hydrodynamical structure itself, so the hydrostatic structure from TLUSTY models was used as input to improve the photospheric structure of the CMFGEN models (refer to §3.2 for more details).

2.2 The theory of stellar winds

The first attempts to develop a theory for how material is driven from the star were based on the concept of absorption through spectral lines in its wind (Abbott, 1977, 1982; Castor *et al.*, 1975). Their radiatively driven wind theory forms the basis for our present day theories on the propagation and physical properties of stellar winds and will be discussed further in §2.2.1. The wind of a star is normally described as a continuous outflow of material that moves away from the star. This results in the ejection of material from the star via its wind, a phenomenon known as mass loss. Most stars possess a stellar wind and undergo mass loss, hot massive stars however have dense winds that become opaque at certain wavelengths and suffer a considerable amount of mass loss, which has a profound effect on their post-main sequence evolution.

2.2.1 Radiatively driven wind theory

The current accepted theory to describe the propagation of stellar winds explains the phenomenon by radiatively driven processes, where the wind can gain momentum from intercepting material in the wind, generating a radiative force. A stellar wind is parameterised by its terminal velocity, v_∞, the velocity of the outflowing wind, and its mass loss

rate (in $M_{\odot}$ yr^{-1}). Assuming a spherically symmetric and stationary wind, we can use the equation of mass continuity to relate mass loss to the velocity and density of the stellar wind:

$$\dot{M} = 4\pi r^2 \rho(r) v(r) \tag{2.16}$$

If we consider a highly simplified case, the radiative force can be described by grey scattering i.e. the scattering of free electrons (this is unrealistic of course since line driving must be frequency dependent). Since there is no frequency dependence in this case, the star's luminosity is not affected, so we can express the radiative flux energy as $\frac{L}{4\pi r^2}$, where r is the stellar radius. The radiative momentum flux can then be expressed as $\frac{L}{4\pi r^2 c}$, where c is the speed of light. We can define the opacity as a constant, $\kappa_e = \frac{\sigma_e}{\mu_e}$, where σ_e is the classical Thompson cross section and μ_e is the mean atomic mass per free electron (varying as a function of mass and mass fraction of hydrogen). Then by combining the equations for wind opacity and radiative momentum flux we can express the radiative acceleration in the wind due to free electron scattering as:

$$g_e(r) = \frac{\kappa_e L}{4\pi r^2 c} \tag{2.17}$$

Now we can compare Equation 2.17 with the equation for the star's gravitational acceleration, $g = GM/r^2$, where M is the mass of the star and G is the gravitational constant. By eliminating the r^2 term (since both accelerations depend on this term), we obtain the *Eddington parameter*:

$$\Gamma_e = \frac{\kappa_e L}{4\pi G M c} \tag{2.18}$$

which expresses the maximum stellar luminosity possible before the radiative forces overcome the force of gravity, rendering the star unstable. Once this limit, called the *Eddington limit*, is reached, the star's gravity can no longer withstand the inner radiation pressure and the star will be blown apart. This corresponds to the Eddington parameter approaching a value of 1. Hot, massive stars tend to have a value of about 0.5 for this ratio, whereas for lower mass stars like a Sun it is much smaller, usually around the order of 2 x 10^{-5}.

The fact that hot stars have $\Gamma_e = 0.5$, which is quite close to the Eddington limit, is of interest, as it implies that gravity can be overcome with a reasonably small opacity in order to produce an outflow.

In reality, the more complicated picture is that hot star winds are driven by absorption and scattering in spectral lines. Line scattering can prove to be an extremely efficient way of producing the radiative force for two reasons. Firstly, bound electrons moving between two discrete energy levels are able to amplify the interaction cross section with photons of the correct energy by creating a *resonance cavity*. The second and more important effect is that, due to the star's expanding outer atmosphere, the outer regions can redshift the local line resonance via the Doppler effect. The line is then able to resonate with previously unattenuated flux and with higher energies, leading to a positive feedback effect.
In order to solve the equations of radiative acceleration due to line scattering, we would require a full evalution over a non-local spatial integral. However the situation is simplified if we adopt the *Sobolev approximation* (Sobolev, 1960), which states that the interaction region of the local line resonance is infinitely narrow. Given the almost homogeneous conditions within the resonance layers, this allows us to consider the *local* density and velocity gradient at any given radius. We can also define a *Sobolev length*, $l_{Sob} = v_{th}/(dv/dr)$, which depends on the velocity gradient and thermal broadening of the line. Then the optical depth of the radiation at a given line resonance can be written as a fraction of l_{Sob}:

$$\tau = \frac{\kappa \rho v_{th}}{dv/dr} \tag{2.19}$$

where κ is the line opacity and ρ is the local density. By considering the amount of flux that passes through the *Sobolev region*, an expression for the line acceleration g_{line} in the stellar wind can be derived:

$$g_{line} \approx g_{thin}(\frac{1 - e^{-\tau}}{\tau}) \tag{2.20}$$

allowing us to calculate the total line force by summing up the contributions of all the line forces from all individual lines. The radiation is also assumed to originate directly from the photosphere and any contribution of diffuse line radiation in the wind from multiple

line scattering are ignored since this radiation is mostly isotropic. In addition, the *point source limit* (see Castor *et al.* 1975 approximation, equivalent to assuming that the star is a point source) has been used to treat the photospheric radiation absorbed at a point r in the wind is moving radially outward from the star. Such an approximation holds well at large distances from the star but breaks down closer to the star where the radiation may propagate at a large angle to the radial direction. If we consider the optically thin limit where $\tau << 1$, Equation 2.20 reduces to:

$$g_{thin} = \frac{\kappa v_{th} \nu_0 L_\nu}{4\pi r^2 c^2} \approx g_e \frac{\kappa}{\kappa_e} \frac{v_{th}}{c} \tag{2.21}$$

where we have approximated the first expression to the second by assuming that the line frequency is close to the peak luminosity, such that $\nu_0 L_\nu \approx L$. To derive the optically thick limit (i.e. $\tau \geq\geq 1$) where a line can absorb all the flux (close to ν_0) from a stellar source and is dependent on the optically thin result so can therefore be written as:

$$g_{thick} \approx \frac{g_{thin}}{\tau} = \frac{L}{4\pi r^2 \rho c^2} \frac{dv}{dr} \tag{2.22}$$

In deriving these equations, we have assumed that the radiating source emits in a radial direction from the stellar photosphere and also used the Sobolev approximation. However the effect of diffuse line radiation, resulting from multiple scatterings, has not been accounted for. Some authors have tried to improve the situation by removing the assumption that the star is a point source e.g. the finite disk correction (Owocki & Puls 2002), since this particular approximation becomes invalid close to the star. It is important to note that from equation 2.22 that the optically thick line driving force depends on the velocity gradient $\frac{dv}{dr}$ and not the opacity. This implies that the line driving force in the optically thick case is proportional to the advective rate of wind acceleration , $v\frac{dv}{dr}$, which is interesting since Newton's second law is normally interpreted as saying that a force causes an acceleration of an object rather than an acceleration producing force as in this example.

2.2.2 CAK Theory

In reality, a stellar wind is driven by a huge number of optically thick lines, so a more realistic equation to describe the propagation of a hot star wind must include a more accurate treatment of this mechanism. Castor *et al.* (1975) achieved this with their formalism for a radiatively driven wind. It provides a self-consistent solution of the stellar wind properties, which is useful since the number of optically thick lines to drive the wind depends on the mass loss rate and therefore is not known *a priori*. Their formalism makes use of the following important simplification - to use a power law to represent the flux-weighted number distribution of lines in the line opacity κ i.e.

$$\frac{dN}{d\kappa} = \frac{1}{\kappa_0}\left(\frac{\kappa}{\kappa_0}\right)^{\alpha-2} \tag{2.23}$$

where the value of the power law index must satisfy $0 < \alpha < 1$ and κ_0 is a constant defined such that $\kappa_0 \frac{dN}{d\kappa} \equiv 1$. Then in order to obtain the total force from these lines, we need to integrate equation 2.20 over the opacity distribution, giving a kind of 'geometric mean' between the optically thin and thick limits for a single line (equations 2.21 and 2.22)

$$g_{cak} = \frac{g_{thin,0}}{\tau_0^{\alpha}} \tag{2.24}$$

where τ_0 is the Sobolev optical thickness and $g_{thin,0}$ is the optically thin acceleration for a single, spectral-peak line of opacity κ_0. According to the steady state equation of motion, the wind acceleration must balance the line acceleration minus the inward accleration due to gravity (neglecting any contribution from gas pressure), in other words

$$v\frac{dv}{dr} = g_{cak} - \frac{GM(1-\Gamma_e)}{r^2} \tag{2.25}$$

where the effective reduction in gravity due to the free-electron scattering factor Γ_e is included in the above expression. Then if we define the flow acceleration in units of gravity, we can rewrite equation 2.25 in the following dimensionless form

$$w = Cw^{\alpha} - 1 \tag{2.26}$$

where C is a constant given by

$$C = \left(\frac{Q\Gamma_e}{1-\Gamma_e}\right)^{1-\alpha}\left(\frac{L}{\dot{M}c^2}\right)^{\alpha} \tag{2.27}$$

Fig. 2.2.1 shows the solutions to this equation, which represent various assumed mass loss rates given fixed stellar and opacity distribution parameters. There is no solution for $\dot{M} > \dot{M}_{cak}$ (see Equation 2.32 for definition of $\dot{M}_{cak}$), but 2 solutions can be found for $\dot{M} < \dot{M}_{cak}$. The maximum mass loss can be evaluated by considering the *critical case* where $f = Cw^{\alpha}$ and $f = 1+w$ intersect at a tangent. Combining this with Equation 2.26, we obtain the following critical conditions:

$$w_c = \frac{\alpha}{1-\alpha} \tag{2.28}$$

$$C_c = \frac{1}{(\alpha^{\alpha}(1-\alpha)^{(1-\alpha)}} \tag{2.29}$$

Equation 2.26 is dimensionless and therefore has no spatial dependence, so these solutions are valid at all stellar radii. The critical acceleration w_c can be integrated from R_* to get the CAK velocity law:

$$v(r) = v_{\infty}\left(1 - \frac{R_*}{r}\right)^{\frac{1}{2}} \tag{2.30}$$

where the terminal velocity v_{∞} is defined as

$$v_{\infty} = v_{\rm esc}\left[\frac{\alpha}{1-\alpha}\right]^{\frac{1}{2}} \tag{2.31}$$

where $v_{\rm esc}$ is the effective escape velocity from the surface. The maximum mass loss rate is then predicted by the following relation:

$$\dot{M}_{cak} = \alpha\left(\frac{(1-\alpha)\bar{Q}\Gamma_e}{1-\Gamma_e}\right)^{\frac{(1-\alpha)}{\alpha}}\frac{L}{c^2} \tag{2.32}$$

where $\bar{Q}$ is the line resonance amplification factor. The analytical solution above can provide good predictions of hot star mass loss rates, despite using several somewhat invalid

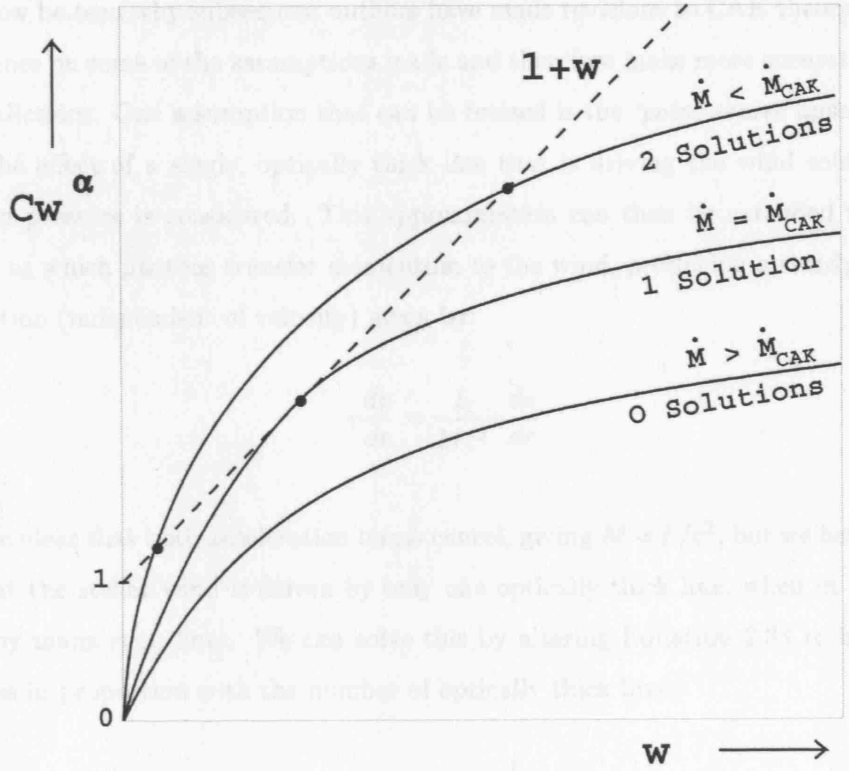

Figure 2.2: Solutions to Equation 2.26 corresponding to different, assumed mass loss rates. A description of the significance of the solutions is given in the text.

assumptions. Examples of such assumptions are that it neglects line blanketing effects in the wind and the assumption that line interactions occur only once in the wind. Additionally, the above relation is only valid when the force multiplier parameters K and α are constant.

2.2.3 More accurate methods for predicting mass loss

It can now be seen why subsequent authors have made revisions to CAK theory to remove dependence on some of the assumptions made and therefore make more accurate mass loss rate predictions. One assumption that can be revised is the *'point source approximation'*, where the effect of a single, optically thick line that is driving the wind solely through radiation pressure is considered. This approximation can then be extended to consider the rate at which photons transfer momentum to the wind, producing a steady state flow acceleration (independent of velocity) given by:

$$v\frac{dv}{dr} \approx \frac{L}{\dot{M}c^2}v\frac{dv}{dr} \tag{2.33}$$

It is then clear that both acceleration terms cancel, giving $\dot{M} \approx L/c^2$, but we have assumed here that the stellar wind is driven by only one optically thick line, when in reality it is driven by many such lines. We can solve this by altering Equation 2.33 to increase the mass loss in proportion with the number of optically thick lines:

$$\dot{M} \approx N_{thick}\frac{L}{c^2} \tag{2.34}$$

Now we can define the parameter η to describe the efficiency of the stellar wind i.e. how efficiently radiative momentum is transferred into wind momentum:

$$\eta = \frac{\dot{M}v_\infty}{L_*/c} \approx N_{thick}\frac{v_\infty}{c} \tag{2.35}$$

Normally $\eta \leq 1$ for OB stars, whereas for WR stars with their powerful stellar winds, η can reach 50.

2.3 TLUSTY

As mentioned in §2.1.2, TLUSTY is one of several nLTE fully line-blanketed stellar atmosphere codes available, written by Ivan Hubeny and Thierry Lanz (see Hubeny & Lanz (1995); Lanz (2003) for more details). This code has been used for the derivation of log g values and to provide a hydrostatic structure for CMFGEN in this thesis work (see §3). It differs from other available codes as it approximates the stellar atmosphere to a plane-parallel and horizontally homogeneous one kept in hydrostatic and radiative equilibrium. Despite the fact that a spherical geometry is more appropriate when modelling hot stars, especially those with a significant stellar wind, TLUSTY has proven to give accurate results when the analysis is based on photospheric lines uncontaminated by any wind contribution. The code also includes line blanketing, using opacity distribution functions (ODFs) to represent a resampled total opacity in any given frequency interval. It involves using the ALI method (see §2.3.3) to treat the radiation intensity at certain frequency points rather than explicitly linearising them. The advantages of such a method are exploited further to ease the problems of calculating a fully line-blanketed model by introducing the concepts of superlevels and superlines (Anderson, 1989).

2.3.1 Solving the equation of radiative transfer

The equation of radiative transfer can also be expressed in terms of the specific intensity I:

$$\mu \frac{dI_{\mu\nu}}{d\tau_{\mu\nu}} = I_{\mu\nu} - S_\nu \tag{2.36}$$

where $\mu = \cos\theta$. The formal solution to this equation is given by:

$$I_{\mu\nu} = \Lambda_{\mu\nu}[S] \tag{2.37}$$

if complete frequency redistribution and no overlapping in the continuum is assumed. Alternatively this solution can be given in terms of the frequency-averaged mean intensity J i.e.

$$\bar{J} = \Lambda[S] \tag{2.38}$$

where

$$\bar{J} = \int J_\nu \phi_\nu \, d\nu \tag{2.39}$$

and

$$\Lambda = \int \Lambda_\nu \phi_\nu \, d\nu \tag{2.40}$$

where ϕ_ν is the normalised absorption profile. Equation 2.39 can then be rewritten as a finite matrix that operates on a vector of source function values at different depth index points d

$$J_d = \sum_{d'}^{D} \Lambda_{dd'} S_{d'} \tag{2.41}$$

This treatment makes the practical assumption that the lambda operator can be represented by a finite matrix, whereas in theory it should be expressed by an infinite one as it operates on a continuous function of position i.e. the source function, which has been treated as discrete in this case. Finally, using this assumption Mihalas (1978) rewrote the equation of statistical equilibrium for a two level atom as

$$S = (1 - \epsilon)\bar{J} + \epsilon B \tag{2.42}$$

where ϵ is the collisional destruction probability and B is the Planck function.

2.3.2 Lambda iteration

The technique of lambda iteration was developed as an improvement on the complete linearisation (CL) method, first developed by Auer & Mihalas (1969), in order to retain the positive attributes of CL method whilst reducing computation time. One of the

achievements of the CL method was to develop a set of equations that was capable of not only detailing how material would respond at each point in the radiation field given any frequency and any depth, but also describing the response from the radiation field to a change in material properties at any point at all frequencies and depths. The main challenge in solving the radiative transfer equation lies in dealing with the coupling between physical parameters e.g. the coupling of depth with frequency and angle. The lambda iteration method attempts to tackle this problem as follows. If we consider the simplest case, by combining Equations 2.38 and 2.42, the source function S_ν can be written as

$$S = (1 - \epsilon)\Lambda[S] + \epsilon B \tag{2.43}$$

If we define Λ as linear, the above equation can be solved in one step

$$S = [1 - (1 - \epsilon)\Lambda]^{-1}\epsilon B \tag{2.44}$$

In reality though Λ is more probably a large matrix (due to the coupling between various parameters) so an iterative is more appropriate than attempting to find a direct solution. The most straightforward iteration method is the *ordinary* lambda iteration, where the user supplies an initial guess S^0 and a solution is found through a series of improved source functions S^n to be determined by the iteration formula

$$S^{n+1} = (1 - \epsilon)\Lambda[S^n] + \epsilon B \tag{2.45}$$

then formal solutions of the radiative transfer equation can be performed for each frequency point in turn. However when applying this technique to stellar atmosphere codes, many iterations are required to achieve convergence since scattering effects become important (meaning high optical depth and small ϵ).

2.3.3 ALI - Accelerated Lambda Iteration

To alleviate the problem of needing a large number of Λ iterations in order to reach a converged solution, Scharmer (1981) and Olson *et al.* (1986) developed the idea of an

accelerated Λ iteration. It involves splitting Λ by specifying a suitable approximate Λ operator Λ^*

$$\Lambda = \Lambda^* + (\Lambda - \Lambda^*) \tag{2.46}$$

so that the iteration scheme given in Equation 2.45 becomes

$$S^{(n+1)} = (1-\epsilon)\Lambda^*[S^{(n+1)}] + (1-\epsilon)(\Lambda - \Lambda^*)[S^n] + \epsilon B \tag{2.47}$$

To solve this requires a matrix inversion of Λ^* such that

$$S^{(n+1)} = [1-(1-\epsilon)\Lambda^*]^{-1}[S^{(n+1)}] + (1-\epsilon)(\Lambda - \Lambda^*)[S^n] + \epsilon B \tag{2.48}$$

where $[1-(1-\epsilon)\Lambda^*]^{-1}$ acts as an acceleration operator to speed up the iteration in comparison to Equation 2.45. Putting $\Lambda^* = 0$ reduces the scheme back to an ordinary Λ iteration, conversely putting $\Lambda^* = \Lambda$ reverts to the exact method which is time-consuming. It is therefore essential, when choosing Λ^*, to strike a balance between an operator that is easy to invert yet retains the crucial properties of the exact operator, a balance that has been well achieved by Scharmer (1981) and Olson *et al.* (1986).

2.3.4 The definition of superlevels

When attempting to calculate the populations of highly complex atoms such as the iron peak elements, the code is required to treat about 10^4 - 10^5 energy levels and correspondingly 10^6 - 10^7 transitions. The immense calculations needed to deal with such a huge number of levels and transitions exceed the resources of even the most powerful computers today. We therefore need to employ some kind of statistical approach to reduce the size of these calculations and, as previously mentioned, Anderson (1989) introduced the concept of *superlevels* for this very purpose. A superlevel can consist of several or even many energy levels grouped together, such that all real levels j that form superlevel J have the same nLTE departure coefficient i.e. each component j is in Boltzmann equilibrium with

respect to the other components. There are two opposing constrictions in choosing how to group separate energy levels into superlevels:

1. firstly levels grouped together should have similar physical properties, more specifically they should belong to the same spectroscopic multiplet and have the same parity. Additionally, separate components should have energies close to each other.

2. a sensible number of superlevels should be used, else too many would defeat the point of the exercise.

For the reasons given above, Hubeny & Lanz (1995) decided to refine the criteria for partitioning levels into superlevels by assuming that firstly, individual components must have the same parity and secondly, small energy differences between levels are allowed. The method they use is to compare the distributions of individual excitation energies for all levels for even and odd parity systems and identify clusters of energies. They find that on average, they choose 10-15 superlevels per system, corresponding to 20-30 superlevels per ion. It is worth noting that these calculations are only based on individual levels that have *measured* energies, rather than predicted ones, which means that some higher energy levels are treated differently via the appropriate partition functions (see Hubeny (1988) for more details).

2.3.5 Using TLUSTY to model stellar atmospheres

TLUSTY can be used to produce accurate stellar atmosphere output that includes a thorough treatment of nLTE and line blanketing in a reasonable computation time of a few hours. In this work version 200 of the TLUSTY code was used. The decision to use TLUSTY models in this work was based on the fact that TLUSTY can provide a hydrostatic structure that can be included in CMFGEN models and that more reliable estimates of log g and $v_{\rm turb}$ could be obtained from TLUSTY models compared to CMFGEN models. For a summary of how the TLUSTY models were incorporated into this work see Fig. 2.4. The grid of TLUSTY models used in this thesis work is based on the grid produced by Dufton *et al.* (2005) with some extensions and refinements included such that this grid explored the same parameter space as the CMFGEN grid. Fig. 2.3 shows the exact parameter space covered by the models in terms of $T_{\rm eff}$ and log g. In order to create a TLUSTY stellar atmosphere model, a standard input file, a file specifying the

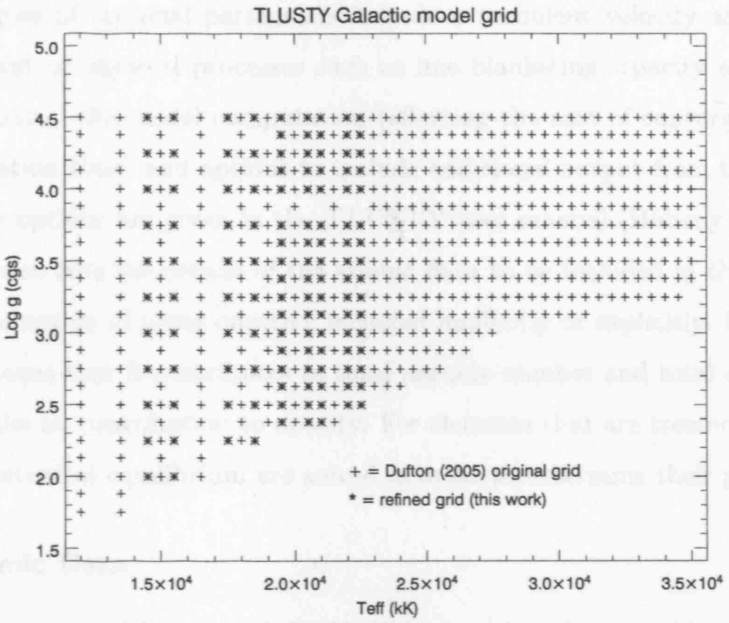

Figure 2.3: The grid of TLUSTY models used in this thesis is based on the initial TLUSTY B star grid constructed by Dufton *et al.* (2005), with extra models added to match the parameter space of the CMFGEN model grid. The grid is shown in terms of $T_{\rm eff}$ and log g but for each grid point, there is a choice of 5 abundances and $v_{\rm turb}$ values.

non-default values of optional parameters (if required), a initial model atmosphere and the relevant atomic data are required. The details of each of these files are as follows.

2.3.5.1 Standard Input

The standard input file gives TLUSTY the stellar parameters, physical processes and control parameters to use for the model to be computed. Examples of control parameters are the number of Λ iterations that the model must undergo and the number of depth points at which the model is calculated. For each model, the standard input file requires the user to state $T_{\rm eff}$ and log g values and choose a LTE/nLTE model and whether they would like to begin with an LTE-grey model for an initial approximation at the start of the calculation. It is only necessary to start the calculation with an LTE-grey model if no initial model atmosphere is available as input. Next a file containing the values of optional parameters can be included if the user requires values other than the default

values. Examples of optional parameters include a turbulent velocity assumed for the model, treatment of physical processes such as line blanketing, opacity and convection, options that control the model computation (affecting the rate of convergence and total model computation time) and options to include additional output from the model. Full details of these options are given in the TLUSTY user manual (Hubeny & Lanz, 2003) The input file also lists the details of the atomic data to be included in the model. Each element has the option of being omitted, included implicitly or explicitly. If an element is implicit this means that it contributes to total particle number and total charge but it is assumed to make no contribution to opacity. For elements that are treated explicitly, the equations of statistical equilibrium are solved in order to determine their populations.

2.3.5.2 Atomic Data

The atomic data required for use with TLUSTY is based on data provided by the Opacity Project Team (1995, 1997). Through *ab initio* calculations, this team have constructed extensive data sets of values of *gf*-values, photoionisation cross-sections etc. for radiative transitions for the most abundant species (i.e. $Z \leq 14$; S, Ca & Fe). However the energies quoted in these data sets show a difference of a few per cent when compared to values measured in a laboratory, despite the sophistication of the Opacity Project Team calculations. To alleviate this problem, Hubeny & Lanz have consulted the Atomic and Spectroscopic Database at NIST (Martins *et al.*, 1999) and updated the level energies with experimental energies where possible. However a different atomic database is needed for the iron peak elements. The Kurucz (1994) extensive semi-empirical calculations list thousands of energy levels for Fe & Ni ions, making them an appropriate source for obtaining values of energy levels and line oscillator strengths. Including such a large number of energy levels in model calculations would hugely increase the total model computation time, therefore the superlevel approximation is used here to group individual levels into superlevels, based on the assumption that the population of each level in a superlevel can be described by a Boltzmann distribution (as previously discussed in §2.3.4).

2.3.5.3 Initial model

The inital model for a new TLUSTY model can be taken from a previous TLUSTY model or a Kurucz model atmosphere. In each case both the initial and new models must

Atomic No.	Element	Z($Z_\odot$)	Ion	Levels
1	H	1.00	H I	16
			H II	1
2	He	1 00	He I	24
			He II	14
			He III	1
6	C	0.30	C II	39
			C III	23
			C IV	1
7	N	0.95	N II	51
			N III	32
			N IV	1
8	O	0.59	O II	74
			O III	29
			O IV	1
12	Mg	0.52	Mg II	31
			Mg III	1
14	Si	0.55	Si II	46
			Si III	74
			Si IV	23
			Si V	1
16	S	1.00	S II	14
			S III	20
			S IV	1
26	Fe	1.00	Fe II	35
			Fe III	50
			Fe IV	43

Table 2.1: Elements included in the TLUSTY models, their assumed abundances, the corresponding ions and the energy levels considered for each element. All elements are treated explicitly. References for the adopted Galactic abundances are Gies & Lambert (1992); Cunha & Lambert (1992, 1994); McErlean (1999)

have the same values of $T_{\rm eff}$ and log g as well as both being either LTE or nLTE. The code then needs to know the number of depth points given in the initial model as well as the input model parameters $T_{\rm eff}$, electron density and mass density at each depth point.

2.3.6 SYNSPEC

In order to convert the model atmosphere output from TLUSTY into a synthetic spectrum, it must be run through another program called SYNSPEC, a general spectrum synthesis program. SYNSPEC reads in a full line list (using data from Kurucz 1979, 1990) of each species included in the TLUSTY model. It then select lines that make a contribution to the total opacity in order to solve the equation of radiative transfer wavelength by wavelength within a predetermined resolution and range. A Voigt profile is assumed for the intrinsic line profiles but SYNSPEC also incorporates the effects of natural, Stark and thermal Doppler broadening into the line profile formation.

2.4 CMFGEN

CMFGEN is a unified wind-atmosphere nLTE radiative transfer code written by John Hillier (see Hillier 1990; Hillier & Miller 1998 for more details). The 1998 version includes a full treatment of line blanketing and assumes a spherically symmetric geometry in order to deal with the the presence of a stellar wind. The latter assumption is the main reason for using CMFGEN as well as TLUSTY for our optical stellar modelling since it incorporates the effects of the stellar wind into the models, which is essential when analysing B supergiants. Additionally, CMFGEN possess the capacity to include millions of spectral lines of varying species such as H, He, C, N, O, S, Si, Mg, Ni, Ph and, like TLUSTY, also adopts the superlevel approximation first proposed by Anderson. Significant improvements were also made to the 1998 version of the code in the form of including the effects of level dissolution, Auger ionisation and resonances on photoionisation cross sections. The principal method employed by the code is to solve for the equation of radiative transfer via the Sobolev approximation or a full solution of the co-moving frame radiative transfer equation, whilst assuming an object with a spherically extended radial flow. A partial linearisation method is required to treat the equations of transfer and statistical equilibrium simultaneously, to resolve the problem of attempting to solve the equation of radiative transfer with the equations of statistical and radiative equilib-

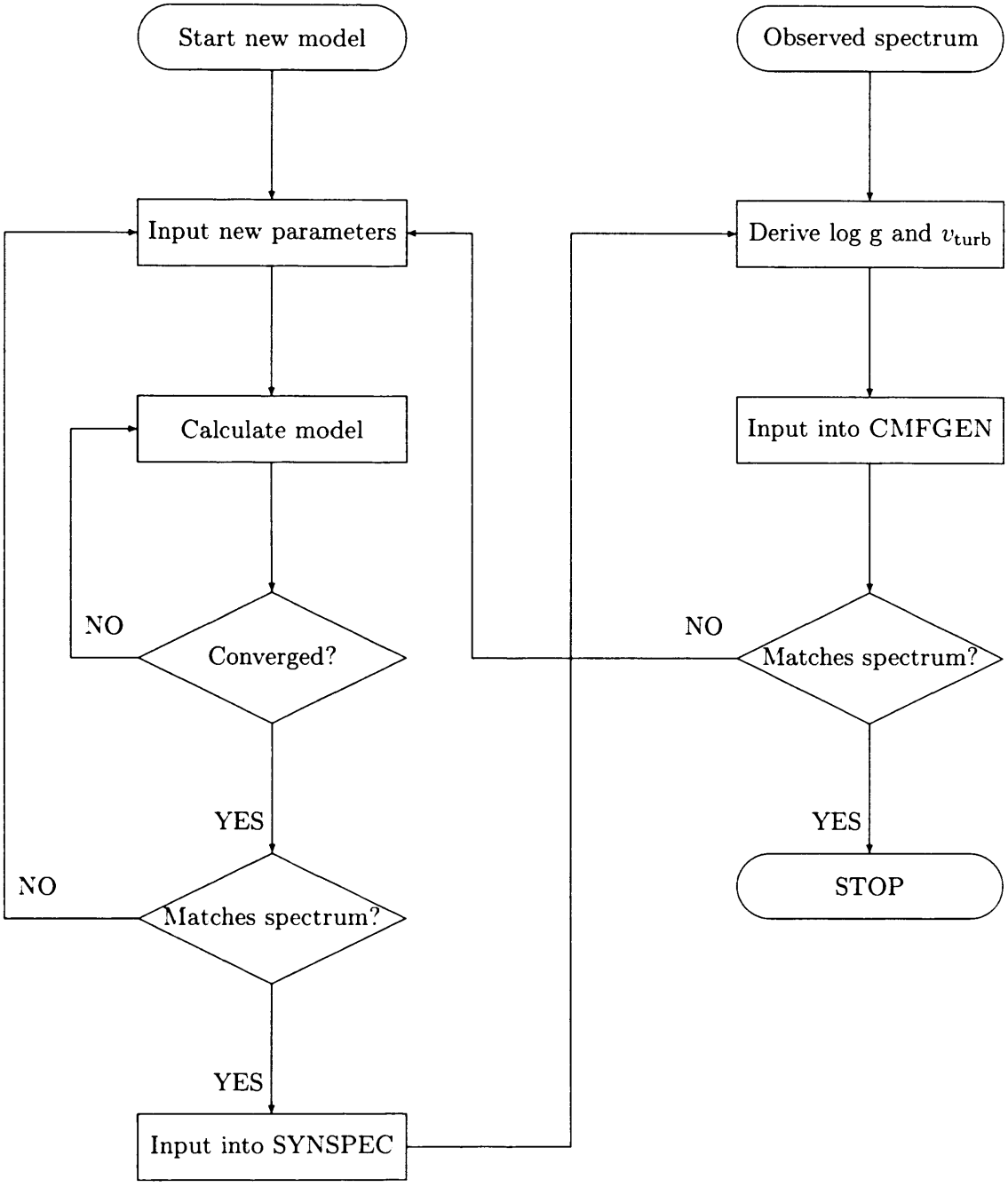

Figure 2.4: outlines the technique applied when using TLUSTY models in this work

rium. Such a method is similar to those using approximate lambda operators (like the "ALI" method used in TLUSTY) and the convergence properties of both procedures are roughly the same. As previously discussed in §2.3, it is crucial to strike a balance between including the transitions of as many lines as possible to fully reproduce the effects of line blanketing and reducing the number of explicitly solved level populations. Hillier & Miller (1998) adopt the following choices and assumptions in order to produce a full nLTE line blanketed version of CMFGEN:

1. No opacity redistribution or sampling methods are used to deal with radiative transfer in the lines, it is treated "exactly".

2. In order to minimise the number of level populations needing to be solved explicitly, levels are grouped into superlevels.

3. The technique of *level dissolution* is employed.

Such assumptions give flexibility to the code e.g. it is relatively straightforward for the user to alter the groupings of superlevels. In choosing the first two assumptions the code is able to recover LTE radiative transfer at depth. Further information on the precise treatment of superlevels and level dissolution will be discussed in §2.4.1 and §2.4.2 respectively.

2.4.1 The treatment of superlevels

As discussed in the previous section, it is advantageous to reduce model computation time by reducing the number of populations N_C that have to be treated during linearisation. However it is important to remember when choosing the number of populations to be included in the model, the numerical accuracy of the solutions may be affected. The application of superlevels in CMFGEN is implemented in much the same way as Hubeny & Lanz did with TLUSTY i.e. based on the original concept by Anderson (1989, 1991). In other words, energy levels with similar energies and properties are grouped together to form a single superlevel in order to reduce the number of statistical equilibrium equations needing to be solved by the code. It can then be stated that the solution of the rate equations only incorporate populations from superlevels (S^n), using the assumption that individual atomic level populations in the full model atom (F^n) have the same departure coefficients as their designated superlevel. The following additional assumptions are also made

$$\sum_i {}^F n_{ij} = {}^S n_j \tag{2.49}$$

and

$$\sum {}^F n^*_{ij} = {}^S n^*_j \tag{2.50}$$

with

$$b = \frac{{}^F n_{ij}}{{}^F n^*_{ij}} = \frac{{}^S n_j}{{}^S n^*_j} \tag{2.51}$$

where an asterisk denotes LTE population, ${}^S n_j$ represents the population density of superlevel j, while F^n_{ij} represents the population density of full level i, which belongs to superlevel j. Hence the above expressions describe the relationship between separate atomic levels in the full atom and their corresponding superlevels. In order to linearise these expressions, the following substitution can be made

$${}^F n_{ij} = {}^S n_j (\frac{{}^F n^*_{ij}}{{}^S n^*_j}) \tag{2.52}$$

such that ${}^F n_{ij}$ is temperature dependent (as it depends on ${}^F n^*_{ij}$ / ${}^S n^*_j$). The authors emphasise that the use of superlevels here is a "natural extension" of LTE, since in LTE all levels of all ionisation stages can basically be described by one superlevel, however in their method many levels represent each ionisation stage.

2.4.2 Level dissolution

In stellar atmosphere codes, the problem of line overlapping and merging near series limits can arise, potentially affecting the reliability of the final synthesised spectrum. This particular problem has been discussed thoroughly by Hubeny & Lanz (1994), where they found the most useful procedure to be a combination of opacity distribution functions and the Hummer (1988) occupation probability formalism, however such a method needs to make generalisations from LTE to nLTE. Hillier & Miller (1998) employ a similar approach to Hubeny & Lanz (1994), but the former adopt an alternate definition of the occupation probability, based on the assumption that if a lower energy state is dissolved, the higher state should be dissolved as well since it is nearer the continuum than the lower state.

2.4.3 Using CMFGEN to model hot stars

As stated at the beginning of this section, CMFGEN is a unified wind-atmosphere code that is capable of coupling the dynamics of the outflowing stellar wind with the radiation field, an important effect for supergiant stars with considerable mass loss i.e. $\dot{M} > 10^{-8}$. In order to compute a new model, a previous model (preferably with a similar stellar radius) is required as input. New model parameters, physical processes to be included and computation options are specified in the input parameter file. Fig. 2.5 shows the method adopted for analysing B supergiants with CMFGEN. A model with new parameters is calculated, using an existing model as input for the temperature structure. The user then verifies if the model has converged by determining whether the maximum and minimum corrections to the tridiagonal operator are less than 1% at various depths in the model atmosphere. The use of a tridiagonal operator is employed since it yields a much higher rate of convergence than approximate diagonal operators (see Hillier (1990) for details). The principal difference is that the tridiagonal operator fully accounts for the derivative term of the diffusion approximation $J = S + \frac{1}{3}\frac{d^2S}{d\tau^2}$. This method should also be more stable since the radiative transfer equation couples the optically thin outer atmospheric layers with the deeper photospheric regions, unlike other linearisation methods where all depth coupling is considered.

The model should also have been calculated with $\tau_{Ross} > 50$ (ideally 100) in the innermost photosphere to ensure that LTE and the diffusion approximation are still valid. The synthetic spectrum produced by CMFGEN is then compared to the observed spectrum of the star to see how well they match in terms of important diagnostic lines (see §3.2 for details) and the overall spectrum. If the model synthetic spectrum is not a satisfactory fit to the observed spectrum, then the input parameters are readjusted accordingly and a new model spectrum is computed. Since the observed spectra upon which our analysis is based (see §3.1) are not flux calibrated, the absolute visual magnitude must be determined independently. This is done by dereddening a combination of IUE spectra and optical photometry to match the unreddened model.

2.4.3.1 Input parameters

Unlike other nLTE stellar atmosphere codes which input $T_{\rm eff}$ and log g in order to calculate the model spectrum, CMFGEN specifies a stellar radius and luminosity and then iterates on the temperature distribution in the radiation field. A stellar mass, mass loss rate, velocity law (see §2.4.3.3) and abundances of elements to be included in the model are also required. There are many options available to alter how certain physical processes such as electron scattering are treated, to improve convergence in the model and to decrease model computation time. For all models we use the following options. The assumptions that the diffusion approximation holds and that electron scattering is coherent are made. Two photon transitions are also included. The temperature is set to the grey temperature T_{grey} when the model optical depth > 0.2 to assist the temperature iterations in converging and values of T_{grey} are read in from the existing input model. In terms of iteration and computation options, a Λ iteration is performed if the percentage change in the tridiagonal operator is > 400 and a maximum of 2 Λ iterations are performed during each full linearisation. All models are calculated with $50 < ND < 80$, where ND is the number of depth points in the model. A variable Doppler profile that is dependent on both depth and species is adopted for spectral line formation.

2.4.3.2 Atomic data

The models computed in this work have included the following elements: H, He, C, N, O, Al, Mg, Si, S, Ca & Fe. Table 2.2 gives the details of the atomic models assumed for each species included in the models. Species marked * are only included in the higher temperature models for B0-B2 supergiants since those ions are not present at lower temperatures. The main sources used to obtain atomic data for CMFGEN are the Opacity Project (Team, 1995, 1997), the Iron Project (Pradhan *et al.*, 1996; Hummer *et al.*, 1993), Kurucz (1995) (also see http://cfa-www.harvard.edu/amdata/ampdata/amdata.shtml) and the Atomic Spectra Database at NIST Physical Laboratory. Again CMFGEN makes extensive use of the superlevel approximation and details of full level and superlevel groupings are also given in Table 2.2.

Ion	Full Levels	Superlevels	b-b transitions
H I	30	20	435
He I	59	41	590
He II	30	20	435
C II	53	30	323
C III	54	29	268
C IV*	18	13	76
N I	22	10	59
N II	41	21	144
N III*	70	34	430
O I	75	18	450
O II	63	22	444
O III*	45	25	182
Mg II	45	18	362
Al II	44	26	171
Al III	65	21	1452
Si II	62	23	365
Si III	45	25	172
Si IV	12	8	26
S II	87	27	786
S III	41	21	177
S IV*	92	37	708
Ca II	12	7	28
Fe II	510	100	7501
Fe III	607	65	5482
Fe IV	272	48	3113
Fe V*	182	46	1781

Table 2.2: The table above gives the number of full levels and superlevels treated as well as the number of bound-bound transitions considered for each ion included in a CMFGEN model.

2.4.3.3 Velocity Law

CMFGEN includes three different velocity law options in the code. All are based on a β-type velocity law that is modified to approach a hydrostatic structure. The first type is a standard β-type velocity law of the form:

$$v(r) = \frac{v_0 + (v_\infty - v_0)(1 - R_*/r)^\beta}{1 + \frac{v_0}{v_{core}} e^{\frac{R_* - r}{h_{\rm eff}}}} \tag{2.53}$$

where v_0 is the photospheric velocity, v_{core} is the core velocity, v_∞ is the terminal velocity, $h_{\rm eff}$ is the scale height expressed in terms of R_* and β is the acceleration parameter. When modelling hot stars, typical values of β are $0.4 < \beta < 5.0$, for values that are more appropriate to B supergiants please refer to §3.2. The physical significance of v_{core} and v_0 are not well understood but for B supergiants the values $v_{core} = 0.002$ km/s and $v_0 = 0.1$ km/s are adopted as suggested by D.J. Hillier.

It is also possible to specify a two-part velocity law such that the outer part of the stellar wind is accelerating faster than the inner part. In this case, Equation 2.53 is modified by the addition of another velocity v_{ext} to represent the velocity of this extended acceleration region in the outer wind:

$$v(r) = \frac{v_0 + (v_\infty - v_{ext} - v_0)(1 - R_*/r)^{\beta_1} + v_{ext}(1 - \frac{R_*}{r})^{\beta_2}}{1 + \frac{v_0}{v_{core}} e^{\frac{R_* - r}{h_{\rm eff}}}} \tag{2.54}$$

Finally there is also the option of reading in a hydrostatic structure from a TLUSTY model in order to obtain an improved hydrodynamical structure in the model. The TLUSTY structure is joined to a *pseudo-hydrostatic* photospheric velocity structure with the condition that both $v(r)$ and $\frac{dv}{dr}$ are continuous at the connecting point, which occurs at a velocity of the order of a few km/s. This is the preferred velocity law option when modelling supergiants as it has a large affect on the resulting wind structure, since the density scales with mass loss at the connection point.

2.4.3.4 Clumping

It is possible to simulate the effect of clumping on the stellar spectrum by using this option. CMFGEN assumes a smooth, homogeneous stellar wind but observational evidence

suggests that stellar winds are clumped, unstable and inhomogeneous (see e.g. Dessart & Owocki 2003; Dessart & Owocki 2005; Massa *et al.* 2003; Bouret *et al.* 2003). The method used involves the use of a volume filling factor to represent the density enhancement in the wind due to the presence of clumps. The filling factor is given by the following expression:

$$f = f_\infty + (1 - f_\infty)e^{(-\frac{v}{v_{cl}})} \tag{2.55}$$

where f_∞ is the filling factor specified by the user and v_{cl} is the velocity at which clumping is "switched on" in the wind, which again can be specified by the user. Typically values of $f_\infty = 0.1$ and $v_{cl} = 30$ km/s are used for OB supergiants. When clumping is included in a model, it is necessary to reduce $\dot{M}$ by a factor of $\sqrt{(f_\infty)}$ in order to avoid artificial density enhancement in the wind.

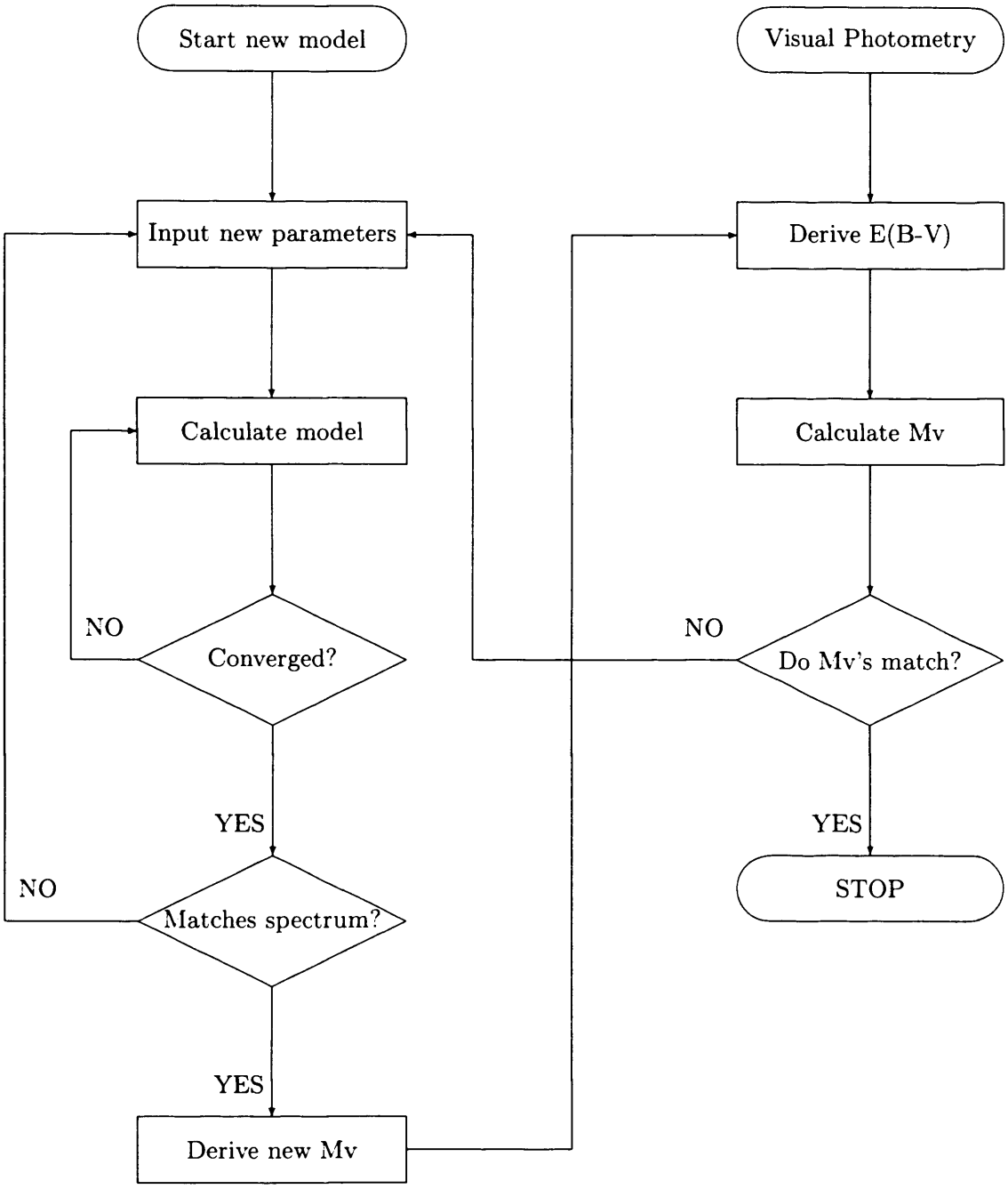

Figure 2.5: summarises our method for modeling B supergiants with CMFGEN

CHAPTER 3

Optical stellar atmosphere modelling

In this chapter, the analysis of B supergiant stellar atmospheres and winds using optical spectroscopy will be described. The analyses rely on the application of the nLTE, line-blanketed stellar atmosphere codes TLUSTY (Hubeny & Lanz, 1995; Lanz, 2003) and CMFGEN (Hillier & Miller, 1998) as discussed in §2. The suitability of B supergiants for this work is shown and a detailed presentation of the method employed for the model analysis of B supergiant spectra is given. The sample of 20 Galactic B supergiants analysed in this chapter is introduced in §3.1 and the derivation of fundamental parameters is presented in §3.2.

3.1 Observational data

Galactic B supergiants are amongst the most luminous stars in our Galaxy, making them ideal candidates for research involving high resolution spectroscopy. This eases the task of deriving fundamental parameters for these objects since clear diagnostics for constraining the temperature, luminosity, mass loss rate and abundances of each star are readily available (see §3.2.1). This section focuses on the main spectral features observed in B supergiants and the details of the sample for which fundamental parameters have been derived.

3.1.1 Features of B supergiant spectra

Like the spectra of other early-type stars, those of B supergiants are dominated by hydrogen and helium lines as well as a number of atomic metal lines: C, N, O, S, Si, Mg,

Ni, P, Ca, Al & Fe. All B supergiants show evidence of stellar wind contamination in their Balmer lines in that their profiles appear to be filled in when compared to a purely photospheric profile, as found by Lennon *et al.* (1992) for a sample of Galactic B supergiants. Over the years growing evidence has suggested that many OB stars, including B supergiants, are helium rich and also undergo a significant amount of CNO processing in their cores during their main-sequence evolution (see e.g., McErLean *et al.* 1999). Such surface enrichments are attributed to the effects of mass loss and rotation, with current stellar evolution models suggesting that massive stars are produced from (initially) very fast rotators that undergo mixing and loss of angular momentum (due to enhanced mass loss) on the main-sequence (Maeder & Meynet 2001; see §3.2.6 for more details).

Figs 3.1 and 3.2 show typical B0–B5 optical spectra from our sample illustrating their main spectral features including those lines used as diagnostics for determining fundamental parameters (see §3.2.1 for more details). A typical O star optical spectrum is characterised by strong H and He I & II lines. These lines are still present in early B stars ($T_{\rm eff} \leq 30$ 000 K), although the He II lines become weaker until they are barely observable in a B1 spectrum. He II 4686 Å is sensitive to mass loss in the wind and is observed in emission in O stars with strong winds, however B supergiants have weaker winds so it is only seen in absorption in early B0-B1 supergiants. These spectra are rich in He I lines that increase in strength up to B2, after which they become weaker. The primary diagnostics used for spectral classification of B stars are the silicon lines, whose behaviour defines the B spectral type subgroups. Si IV 4089 Å decreases in strength until it is no longer detectable by B2.5, at which point Si II 4128-30 Å becomes more prominent and stronger towards later spectral types. Si III 4552 Å increases in strength up to B2, equalling Si IV 4089 Å in strength around B0.5-0.7 and exceeding it by B1, it then decreases such that Si II 4128-30 Å matches its strength at B3 and has exceeded it by B5. At spectral types of B5-B9, the Si II 4128-30 Å become stronger than both Si III 4552 Å and He I 4121, 4144 Å and the Mg II 4481 Å line is also stronger than He I 4471 Å. The He I 4471 Å line is of particular interest because, along with Mg II 4481 Å, it provides a useful secondary diagnostic for spectral classification. As Mg II 4481 Å becomes stronger towards lower $T_{\rm eff}$, He I 4471 Å decreases until both lines are equal in strength around B7 (Lennon *et al.*, 1992). At spectral type B8, Fe II lines being to appear prominent around 4550 Å .

There is also a considerable number of CNO lines present in the spectra, some of which display morphological CNO anomalies that are indicative of the amount of CNO processing that the star has undergone (Walborn, 1976). N II and N III lines are present, with N II reaching a maximum strength at a spectral type of B2 Ia and the N III line at 4097 Å (blended with Hδ) providing a good indicator of nitrogen enrichment/deficiency. Lennon *et al.* (1992) note that the N II 4631 Å is blended with Si IV down to B2.5. B supergiant spectra are also rich in O II lines that increase in strength up to B1 and in some cases are blended e.g. O II 4070 (blended with C III) & 4650 Å (blended with C III). Carbon is also present in the form of C II and C III, the latter only being observed in blends with O II.

With regard to differences between the luminosity classes Ia, Ib, Iab and II (see Fig. 3.3), the first noticeable difference is that the hydrogen Balmer lines are broader for lower luminosities. The ratio of Si III 4552 Å / He I 4387 Å is used as the principal luminosity class diagnostic, but other He I lines, He II 4686 Å and the Si IV lines at 4089 & 4116 Å also display a sensitivity to luminosity.

3.1.2 The Galactic B supergiant sample

Optical and UV spectra have been collected for a sample of 20 Galactic B supergiants, covering the spectral range of B0–B5 and including Ia, Ib, Iab & II luminosity classes as well as a hypergiant. Stars were only included in the sample if both optical and *IUE* data were available for them. Where possible, stars were selected such that there would be 2 different luminosity classes at each spectral sub-type. However this was not possible for B1 & B3 as no B1 Ia, B3 Ib stars were available with both optical & *IUE* spectra. The details of observational data for each star are given in Table 3.1.3. Fifteen of the chosen B supergiants belong to OB associations (Humphreys, 1978), so for these stars, the absolute magnitude given in Table 3.1.3 is based on the distance to the relevant association.

For fifteen of the twenty B supergiants in our sample, the optical spectra were taken from an existing data set (see Lennon *et al.* 1992 for further details). The blue spectra were observed using the 1-m Jacobus Kapteyn Telescope (JKT) at the Observatorio del Roque de los Muchacos, La Palma in October 1990 with the Richardson-Brealey Spectrograph and a R1200B grating. They have a wavelength coverage of 3950 – 4750 Å, a spectral resolution of 0.8 Å and a signal-to-noise ratio $\sim$ 150. The red spectra were obtained with

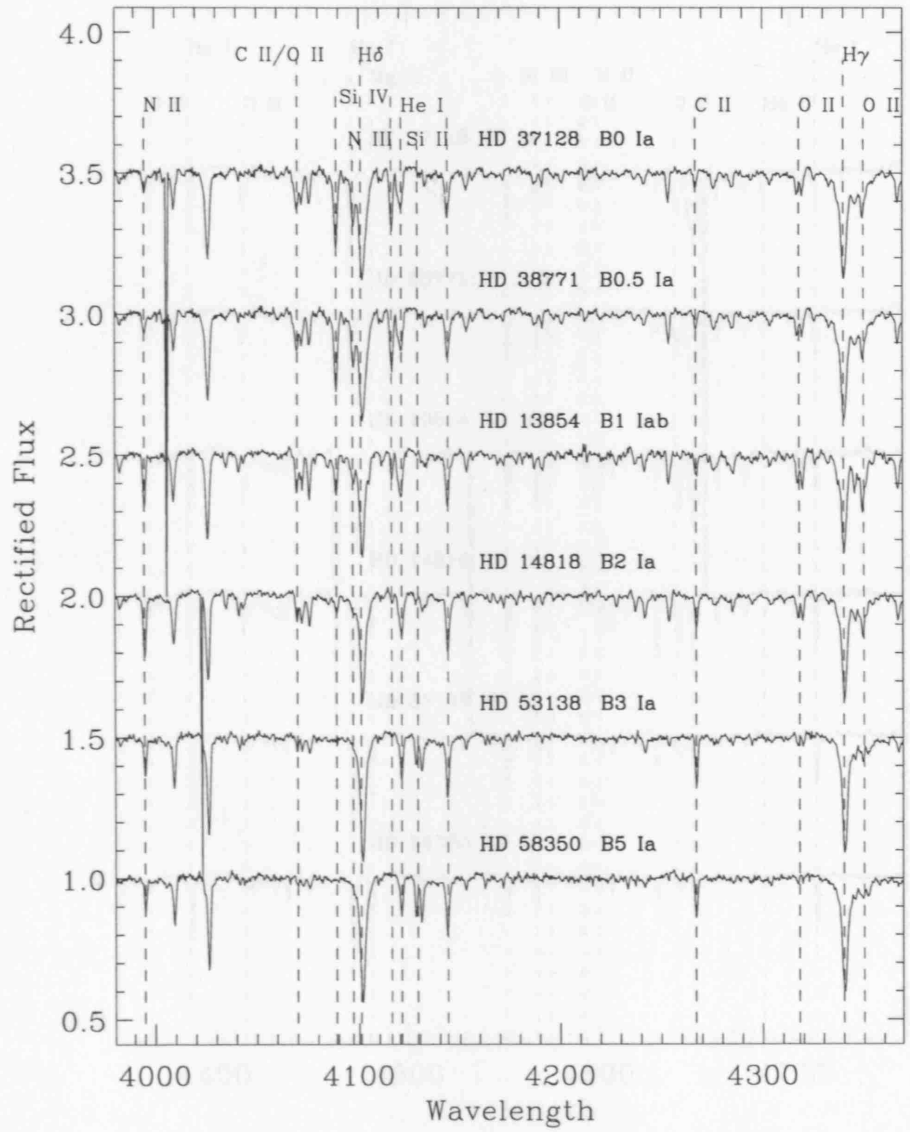

Figure 3.1: Examples of Galactic B supergiant spectra (3990 – 4360 Å) ranging from B0-B5 in spectral type with temperature decreasing from top to bottom. The main spectral features are Hγ λ4340 & Hδ λ4101; He I λ 4121, 4144; Si II $\lambda\lambda$ 4128-30; Si IV λ 4089,4116; N II λ 3995; N III λ 4097; C II λ 4267 and O II $\lambda\lambda$ 4070 (blend), 4317-4319 & 4350 (blend). Note in particular the behaviour of the Si II and IV lines with spectral type.

the 2.5-m Isaac Newton Telescope (INT) using the Intermediate Dispersion Spectrograph (IDS) and cover a wavelength range of 6260 – 6870 Å (Lennon *et al.*, 1992). The spectral

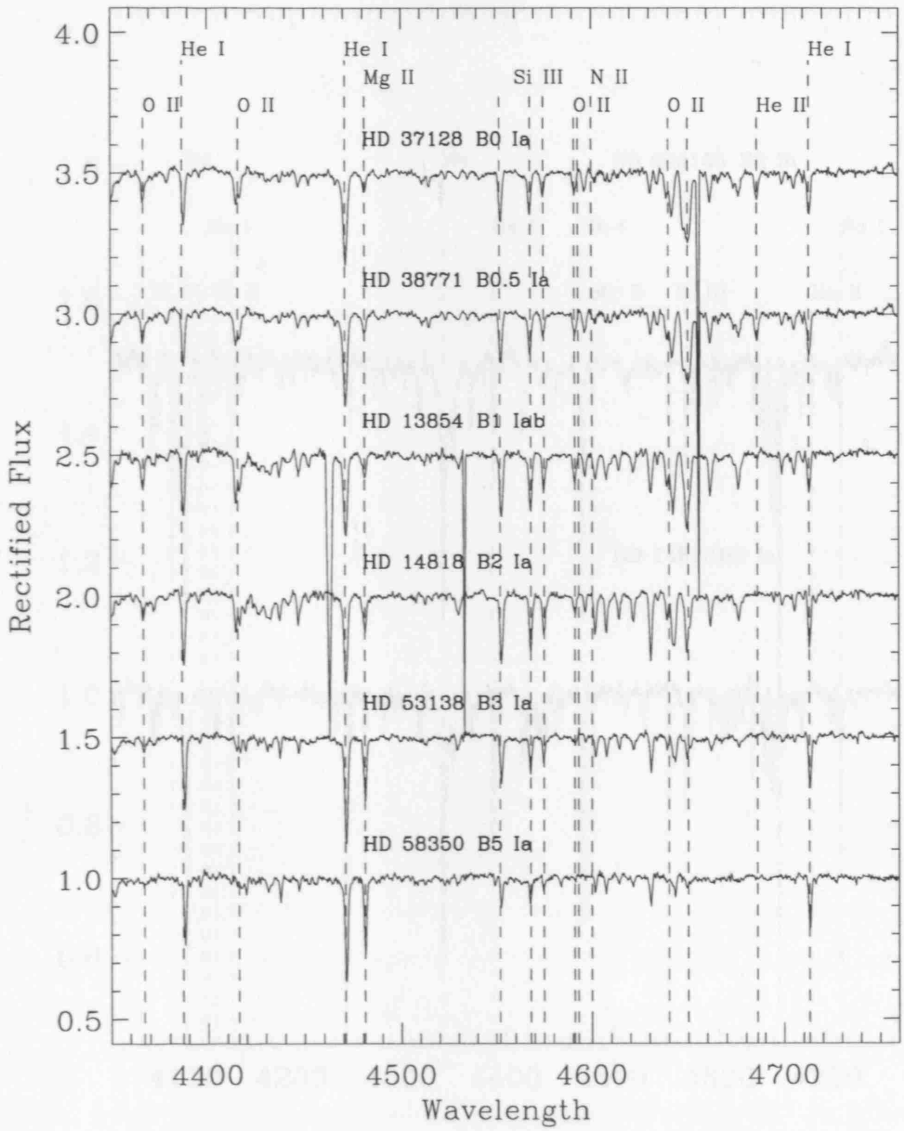

Figure 3.2: Examples of Galactic B supergiant spectra (4360 – 4750 Å) ranging from B0-B5 in spectral type with temperature decreasing from top to bottom. The main spectral features are He I λ 4387, 4471, 4713; He II λ 4686; Mg II $\lambda\lambda$ 4481; Si III $\lambda\lambda$ 4552, 4568, 4575 ; N II λ 4631 and O II $\lambda\lambda$ 4367, 4415-4417, 4591-4596, 4640 (blend) & 4650 (blend). Note in particular the behaviour of the Si III lines and the ratio of He λ 4471 / Mg II λ 4481 with spectral type.

resolution is 0.7 Å and the signal-to-noise ratio is > 100. Spectra for HD 192660, HD 185859, HD 190066 & HD 191243 were taken at the INT in July 2003, again using the

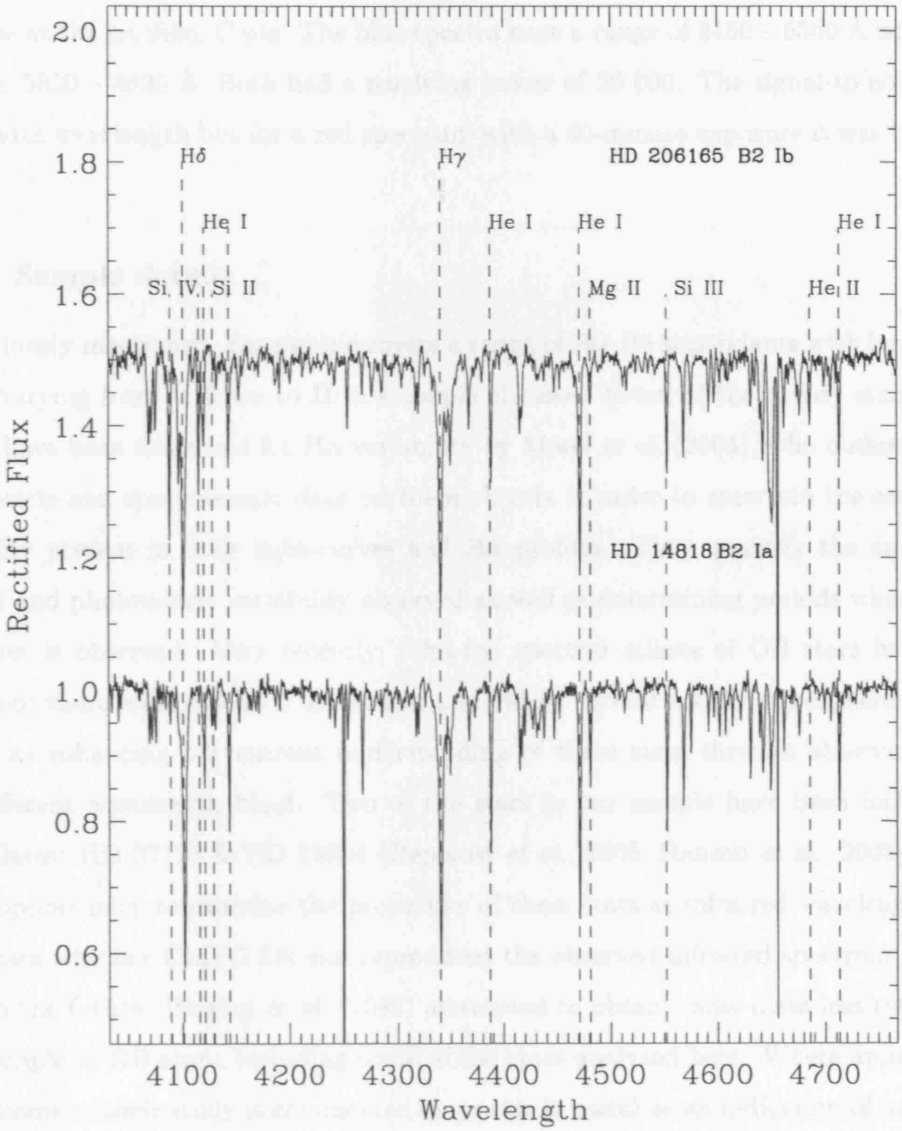

Figure 3.3: shows a comparison of B2 Ia and Ib spectra (4050 – 4750 Å) with luminosity sensitive lines shown. Note that Hδ and Hγ have broader wings in HD 206165, a B2 Ib star, than in HD 14818, a B2 Ia star.

IDS. The R400B grating was used for the blue spectra, giving a central wavelength λ_c of 4300 Å, whereas the R600R grating was used for the red spectra, giving λ_c 6550 Å. The signal-to-noise ratio was > 100 and the spectral resolution was 0.7 Å. Finally high resolution time-averaged blue & red spectra of HD64760 were provided by Dr. R. K. Prinja (see Kaufer & Stahl 2002 for more details). These spectra were taken in 1996

on the HEROS fiber-linked echelle spectrograph, which was mounted on the ESO 50-cm telescope at the La Silla, Chile. The blue spectra have a range of 3450 – 5560 Å whilst the red have 5820 – 8620 Å. Both had a resolving power of 20 000. The signal-to-noise ratio varied with wavelength but for a red spectrum with a 40-minute exposure it was typically > 150.

3.1.3 Sample details

As previously mentioned, our sample covers a range of B0–B5 supergiants with luminosity classes varying from Ia down to II in a couple of cases. Seven of the twenty stars in our sample have been examined for Hα variability by Morel *et al.* (2004), who obtained both photometric and spectroscopic data on these objects in order to ascertain the amount of variability present in their light-curves and Hα profiles. They quantify the amount of spectral and photometric variability observed as well as determining periods where cyclic behaviour is observed. Very recently, infra-red spectral atlases of OB stars have been published; there will provide a useful test and aid to current stellar atmosphere models, as well as enhancing our current understanding of these stars through observing them in a different wavelength band. Two of the stars in our sample have been included in such atlases: HD 37128 & HD 13854 (Repolust *et al.*, 2005; Hanson *et al.*, 2005), giving us the opportunity to examine the properties of these stars at infra-red wavelengths and investigate whether CMFGEN can reproduced the observed infra-red spectrum at some point in the future. Bieging *et al.* (1989) attempted to obtain radio mass loss rates for a large sample of OB stars, including some of the stars analysed here. Where appropriate, the outcome of their study is commented on as this is useful as an indication of how radio quiet the B supergiants are in this sample. This is important since we intend to attempt to derive more accurate observed mass loss rates for B supergiants in the future and need to identify suitable targets for observing in the radio. Each star in our sample will now be discussed in more detail, highlighting any interesting features belonging to the star and commenting on any recent research that has been carried out on each object.

- ϵ **Ori**: There are several intriguing aspects of this star that are worth mentioning. Firstly it has been noted as moderately nitrogen deficient by Walborn (1976). Secondly it is known to undergo significant variations in Hα, with Morel *et al.* (2004) reporting variations of 81.9 %. Further studies by Prinja et al. (2004) have revealed

Table 3.1: Details of observational optical & UV data

HD no.	Alias	Sp. Type	V	B-V	M_V	Association	m-M	Optical	*IUE*
37128	ϵ Ori	B0 Ia	1.70	-0.19	-6.95	Ori OB1b	7.8[1]	L1992	SWP30272
192660	-	B0 Ib	7.38	0.67	-7.0	Cyg 0B8	11.8[3]	INT2003	SWP44625
204172	60 Cyg	B0.2 Ia	5.94	-0.08	-6.2	Cyg OB4	6.2	L1992	SWP48900
38771	κ Ori	B0.5 Ia	2.04	-0.18	-6.51	Ori OB1c	8.0[1]	L1992	SWP30267
185859	-	B0.5 Ia	6.48	+0.44	-6.6	-	13.08	INT2003	SWP47509
213087	26 Cep	B0.5 Ib	5.46	+0.37	-6.2	Cep OB1	12.7	L1992	SWP02735
64760	-	B0.5 Ib	4.24	-0.15	-6.2	-	10.44	RKP	SWP53781
2905	κ Cas	BC0.7Ia	4.16	+0.14	-7.09	Cas OB14	10.2[3]	L1992	SWP54038
13854	V551 Per	B1 Iab(e)	6.47	+0.28	-6.73	Per OB1	11.8[2]	L1992	SWP02737
190066	-	B1 Iab(e)	6.53	+0.18	-6.1	-	12.63	INT2003	SWP18310
190603	V1768 Cyg	B1.5 Ia+	5.64	+0.54	-7.0	-	12.56	L1992	SWP4325
193183	-	B1.5 Ib	7.01	+0.44	-6.24	Cyg OB1	11.3[3]	L1992	SWP52716
14818	V554 Per	B2 Ia	6.25	+0.30	-6.93	Per OB1	11.8[3]	L1992	SWP18658
206165	V337 Cep	B2 Ib	4.74	+.30	-6.44	Cep OB2	13.2	L1992	SWP06336
198478	55 Cyg	B2.5 Ia	4.84	+0.40	-6.43	Cyg OB7	9.6[2]	L1992	SWP38688
42087	3 Gem	B2.5 Ib	5.75	+0.22	-6.26	Gem OB1	10.9[3]	L1992	SWP08645
53138	24 CMa	B3 Ia	3.01	-0.11	-7.1	-	10.11	L1992	SWP30271
58350	η CMa	B5 Ia	2.41	-0.07	-7.0	-	9.41	L1992	SWP30198
164353	67 Oph	B5 II(Ib)	3.97	+0.02	-4.2	Coll 359	6.5	L1992	SWP08560
191243	-	B5 II(Ib)	6.09	+0.16	-6.5	Cyg OB3	11.8[3]	INT2003	SWP07737

Observational data for the sample of 20 Galactic B Supergiants. Spectral types, V magnitudes and values of B-V are taken from Lennon *et al.* (1992) for all stars except HD192660, HD 185859 & HD190066 & HD 64760. The references for the spectral types of these 4 stars are as follows: HD 192660 from Walborn (1971); HD185859 from Lesh (1968); HD 190066 from Hiltner (1956) and HD 64760 from Hoffleit & Jaschek (1982) (from which the V magnitude of HD 64760 was also taken). V magnitudes for the remaining 3 stars were obtained from Fernie (1983). Values of $(B-V)_0$ taken from Fitzgerald (1970). Absolute visual magnitudes, distance moduli and cluster associations have been taken from: 1. Brown *et al.* (1994), 2.Garmany & Stencel (1992) or 3. Humphreys (1978). For stars not associated with a cluster, an absolute visual magnitude scale based on spectral type (Egret, 1978) was used. L1992 refers to archive data obtained from Lennon *et al.* (1992), INT2003 denotes data taken on the 2.5m INT & RKP marks data supplied by R.K. Prinja.

variability in not only Hα but also Hβ, He absorption & metal lines with a 1.9 day period. A modulating S-wave pattern has been discerned in the weaker lines, which cannot be fully explained by current non-radial pulsation models (Townsend, 1997). These results highlight a direct connection between photospheric activity and perturbations in the stellar wind. Recently Hanson *et al.* (2005) obtained a near-infrared (H & K band) spectrum of this star, which shows both the hydrogen Brackett and He I lines to be extremely deep and narrow. Finally this star is the only normal early B supergiant to have a measured thermal radio flux (Blomme et al. 2002), from which a radio mass loss rate of $\log \dot{M} = -5.72$ was derived.

- κ **Ori**: Like ϵ Ori, κ Ori also exhibits spectral variability in Hα. Its Hα profile was studied in detail by Rusconi *et al.* (1980) who described it as a double-peaked absorption profile with a central emission core and broad profile wings, with variations on long (of the order of days)and short (of the order of minutes) time scales. More recently Morel *et al.* (2004) reported that changes in the profile amplitude and morphology of 32.6 %. Walborn (1976) noted it as an example of a morphologically normal B supergiant in terms of the relative strengths of its CNO spectral lines.

- **HD 192660**: Bidelman (1988) noted that this star showed a "faint Hα emission with a slight P Cygni absorption", based on observations taken at the Lick observatory in 1957. Our spectrum of this star shows a very similar Hα profile that is also only weakly in emission. Walborn (1976) & Schild (1985) both noted that HD192660 displays evidence for nitrogen deficiency.

- **HD 204172**: Lennon *et al.* (1992) revise the spectral classification of this star from B0 Ib to B0.2 Ia due to the strength of its Si IV lines and narrowness of its H lines. Comparing its UV resonance lines to those of the B0 Ib star HD 164402 supports the change to a more luminous spectral type (Prinja *et al.*, 2002). This star has been proposed as a runaway OB star candidate by Mdzinarishcvili & Chargeishvili (2005) and it also has a slight nitrogen deficiency (Walborn, 1976).

- **HD 64760**: This star is classified as a rapid rotator, having a $v \sin i$ of 265 km/s. Many interesting studies have been carried out regarding the periodic and sinusoidal modulations of its optical and UV lines (Massa *et al.*, 1995*b*; Fullerton *et al.*, 1997; Kaufer & Stahl, 2002), which have turned HD 64760 into a key object for im-

proving our understanding of the spatial structure and variations of hot star winds. More recently, Kaufer *et al.* (2006) found, for the first time, direct observational evidence for a connection between multi-periodic non-radial pulsations (NRPs) in the photosphere and spatially structured winds. More specifically, they can use the interference of multiple photospheric pulsation modes on hourly timescales with wind modulation periods on time scales of several days. A beat period of 6.8 days seen in the photosphere and base of the wind however does not match with the derived periods of 1.2 and 2.4 days for wind variability, being closer to the longer 5-11 day repetitive timescales observed for discrete absorption components (DACs) in the *IUE* data sets. Evidently the precise nature of the wind-photosphere connection in this star is a complex one. Using hydrodynamical simulations, Cranmer & Owocki (1996) succeeded in confirming the existence of co-rotating interaction regions (CIRs). These are spiral structures in the wind that are produced through the collisions of fast and slow streams rooted in the stellar surface. Hoogerwerf et al. (2001) put this star forward as a potential candidate for a runaway OB star since it is currently located behind the Vel OB2 association. Using Monte-Carlo simulations, they retraced the orbit of this star back to the association, estimating that it left about 6 Myr ago.

- **HD 185859**: This star has not been reported as displaying any significant Hα variability.

- **HD 213087** Bieging *et al.* (1989) attempted to derive a radio mass loss rate for this star, but only achieved an upper limit of $\log \dot{M} \leq -5.63$. Again no significant Hα variability is recorded for this star.

- κ **Cas**: Walborn (1972) classified this star as carbon rich, giving it a spectral type of BC0.7 Ia, when comparing its optical spectrum with that of HD 216411, a B0.7 Ia star. He found that the nitrogen lines in κ Cas were barely detectable, whereas the O II - C III blends were very prominent. Since Walborn also recognised that HD 216411 possesses a well developed nitrogen spectrum, he described κ Cas as carbon-rich, rather than nitrogen-weak, with respect to a morphologically-normal B supergiant . Walborn had previously suggested that all OB stars begin their post-main-sequence evolution with an enhancement of carbon (Walborn, 1971), which then becomes depleted as the star evolves and produces nitrogen as a by-product of

the CNO bi-cycle. Therefore the implication of classifying κ Cas as a BC 0.7 Ia star is that it is less evolved than other stars in the sample. Please consult §3.2.6 for a discussion of the carbon rich status of this star based on the results presented in that section. Bieging *et al.* (1989) attempted to constrain an upper limit of $\log(\dot{M}_{\rm radio}) \leq -5.45$ for this star.

- **HD 13854**: McErLean *et al.* (1999) describe this star as 'highly processed' i.e. displaying a large amount of CNO processing in its spectrum. Its Hα profile is seen mostly in emission, assuming a P Cygni shape. Morel *et al.* (2004) found that not only does the Hα profile of this star vary by 47.3 %, but that these variations have a period of 1.047 days $\pm$0.01. *Hipparcos* light curves also show evidence for periodic behaviour.

- **HD 190066**: has not been previously cited as showing any remarkable features in either Hα or its CNO spectral morphology.

- **HD 190603**: is an early B hypergiant (e.g. Rivinius *et al.* (1997)), meaning that a P Cygni profile shape is observed in at least one of its Balmer lines. In the case of HD 190603, it is the Hβ line that is observed as a P Cygni profile, whereas Hα is seen in emission with a slight asymmetry.

- **HD 193183**: has not been previously cited as showing any remarkable features in either Hα or its CNO spectral morphology.

- **HD 14818**: possesses an Hα profile with a P Cygni profile. Morel *et al.* (2004) report variations of 34.8 % in the Hα profile and, like HD 13854, they find that this star also shows periodic behaviour in its *Hipparcos* light curve.

- **HD 206165**: displays an Hα profile in absorption. Bieging *et al.* (1989) estimated an upper limit of $\log \dot{M} \leq -5.85$ for this star, but again there was no definite detection of non-thermal emission from this star.

- **HD 198478**: has not been previously cited as showing any remarkable features in either Hα or its CNO spectral morphology.

- **HD 42087**: also has its Hα profile in emission but more importantly Morel *et al.* (2004) reported significant Hα variability of 91.2 % (*greater* than the percentage variability that they found for ϵ Ori), for which they find strong evidence of cyclic

behaviour on a periodicity of 25 days ± 1-4 days. Moreover, the Hα variability correlates with variability in the He I 6678 Å line, such that as Hα emission increases, He I 6678 becomes weaker. Morel *et al.* (2004) also find periodic variability in its *Hipparcos* light curve.

- **HD 53138**: Walborn (1976) notes that this star shows a morphologically normal CNO spectrum, despite other authors associating this star with OBN/OBC groups. It undergoes 66.4 % Hα variability (Morel *et al.*, 2004). de Zeeuw *et al.* (1999) questioned the membership of this star to the OB association Collinder 121 on account of its insignificant proper motion.

- **HD 58350**: displays 44.1 % varibility in Hα (Morel *et al.*, 2004).de Zeeuw *et al.* (1999) also revoked the membership of this star to Collinder 121 on account of its small parallax.

- **HD164353**: Lennon *et al.* (1992) advocated the spectral reclassification of this star from B5 Ib to B5 II.

- **HD 191243**: the same spectral type is adopted as for HD 164353 for the same reasons.

3.2 Derivation of fundamental parameters

Fundamental parameters were derived for this sample of stars using the nLTE stellar atmosphere codes TLUSTY (Hubeny & Lanz, 1995; Lanz, 2003) and CMFGEN (Hillier & Miller 1998; see §2.3 and §2.4 for more details). The application of TLUSTY, a plane-parallel photospheric code that does not account for the presence of a stellar wind, to modelling supergiants is valid as long as it is used solely to model purely photospheric lines. An existing grid of TLUSTY models (Dufton *et al.*, 2005); (see §2.3.5) was used in this work to provide a hydrostatic structure that could be input into CMFGEN, since the latter code does not solve for the momentum equation and therefore requires a density/velocity structure. The TLUSTY input provides the subsonic velocity structure and the supersonic velocity structure in the CMFGEN model is described by a β - type law. The two structures are joined to a hydrostatic density structure at depth, such that the velocity and velocity gradient are consistent. All parameters except $\log g$ were derived using CMFGEN and the precise details of the methods employed will be discussed next. The general

method employed was to produce a grid of CMFGEN models of varying temperatures and luminosities and to compare these synthetic spectra to observed spectra in order to constrain these two parameters (§3.2.1). Once satisfactory values had been derived for the temperature and luminosity of a star, the mass loss rate, β velocity law, turbulent velocity ($v_{\rm turb}$) (§3.2.3) and CNO abundances (§3.2.6) could be constrained. These parameters are all sensitive to changes in temperature and luminosity so can only be derived once those values have been fixed. All models were calculated assuming solar abundances for silicon, magnesium, aluminium, phosphorous, sulphur, calcium and iron and adopting a relative number fraction of 5:1 for H:He.

3.2.1 Temperature, Luminosity and log g derivation

In B stars the silicon lines are used as the primary temperature diagnostics, having the advantage that the abundance is well known as silicon is unaffected by nuclear processing. For B0-B2 supergiants the Si IV 4089 Å and Si III 4552 Å lines provide the main temperature diagnostics. Si IV 4089 Å decreases in strength as the temperature decreases until it is barely detectable at a spectral type of B2.5, which corresponds to $T_{\rm eff} \sim 18\,000$ K. At this point the Si II 4128-30 Å doublet is present and replaces Si IV 4089 Å as the main temperature diagnostic for B2.5 - B9 stars, along with Si III 4552 Å. The He I lines at 4144 Å, 4387 Å, 4471 Å & 4713 Å and magnesium line at 4481 Å were used as secondary criteria for both temperature and luminosity, since they are sensitive to changes in both parameters. The principal luminosity criteria for B0-B1 supergiants is the ratio of Si IV 4089 Å to He I 4026 Å, 4121 Å and/or 4144 Å, whereas for stars later than B1 the ratio of Si III 4552 Å to He I 4387 Å is used. In order to assign a temperature to an individual star, the observed spectrum was compared to a grid of models and the temperature of the model that provided the best fit 'by eye' to the appropriate silicon lines was chosen. This temperature would then be confirmed by checking that model also succeeded in fitting the helium lines listed earlier and Mg II. The following method was used to constrain the luminosity. Observed values of M_V, the absolute visual magnitude and V, the magnitude in the V-band at $\sim$ 550-nm were used, together with the estimate of $A(V)$, to obtain an initial estimate of the distance modulus. Optical photometry and ultraviolet spectroscopy were then dereddened with respect to the model spectral energy distribution (which has been divided by the sqaure of the distance to account for the fact that the model assumes the star to be at a distance of 1 kpc) to obtain revised estimates of E(B-V) and M_V. This

M_V derived from the model was then compared to an observed M_V, if the values matched then the model luminosity was correct. If not the value of M_V was translated into a bolometric correction to obtain an estimate of the corrected luminosity for the model, which was then rerun with this value for the luminosity. This iterative process was continued until the observed and model values of M_V were in agreement. Estimates of log g were made from TLUSTY fits to the Hγ lines of the observed spectra. Hγ was chosen as the log g diagnostic since Hα & Hβ suffer from too much wind fill emission; Hδ was used as a secondary diagnostic to check for consistency with values of log g derived from Hγ.

3.2.2 The B supergiant temperature scale

The values of $T_{\rm eff}$, log g, log $(L/L_{\odot})$, E(B-V) and M_V derived for each of the 20 B supergiants in the sample are listed in Table 3.2. These results show that B0-B5 supergiants have a range in $T_{\rm eff}$ of 14 500 – 30 000 K, in log $(L/L_{\odot})$ of 4.30 – 5.73 and that their stellar radii vary from about 20 - 71 $R_{\odot}$. They also exhibit a range of $-6.04 \leq M_V \leq -7.12$ in brightness, confirming their status as some of the brightest stars in our Galaxy. The actual temperature scale for B supergiants derived here is shown in Fig. 3.2.2, plotted against spectral type. Looking at Table 3.2, we can see that the $T_{\rm eff}$ of a B0 Ia/Ib is 28 000 - 30 000 K. A B0.5 Ia/Ib would then be expected to have $T_{\rm eff} \sim$ 26 000 K and a B1 Ia/Ib $T_{\rm eff} \sim$ 20 000 – 21 000 K. In other words a drop of up to 10000 K in temperature is witnessed between B0-B1. At lower spectral types, the $T_{\rm eff}$ scale shows a more gradual decrease in $T_{\rm eff}$, displaying a B2 Ia/Ib of $T_{\rm eff} \sim$ 18 000 K, B3 Ia of $T_{\rm eff} \sim$ 16 500 K and B5 Ia/Ib of $T_{\rm eff}$ of $\sim$ 15 000 K. The Galactic O star $T_{\rm eff}$ scale published by Repolust *et al.* (2004) ranges from an O2 If star with $T_{\rm eff}$ = 42 500 K down to an O9.5 Ia star with $T_{\rm eff}$ = 29 000 K and an O9.5 Ib star with $T_{\rm eff}$ = 32 000 K, meaning that the B supergiant $T_{\rm eff}$ scale presented here carries on smoothly from the Galactic O supergiant $T_{\rm eff}$ scale. Similarly the B supergiant $T_{\rm eff}$ scale ends with B5 Ib stars having $T_{\rm eff} \approx$ 15 000 K and the Galactic A supergiant $T_{\rm eff}$ scale derived by Venn (1995) begins with a $T_{\rm eff}$ of 9950 K. A gap between the B and A supergiant $T_{\rm eff}$ scales is expected since none of the recent B star $T_{\rm eff}$ scales include B6-9 stars. This problem is partly an observational one since not many B6-9 stars are known. The B supergiant temperature scale derived here is compared to other published values (Trundle *et al.*, 2004; Trundle & Lennon, 2005; McErLean *et al.*, 1999; Crowther *et al.*, 2006) in Table 3.3. Where each author has several stars with the same spectral type, the values are averaged and marked with an asterisk

in the table. Note that the results of McErLean *et al.* (1999) were obtained with an unblanketed stellar atmosphere code. If we compare our derived $T_{\rm eff}$ values with those of the unblanketed McErLean *et al.* (1999) $T_{\rm eff}$ scale, the use of a stellar-atmosphere code with a full treatment of line blanketing has the effect of lowering $T_{\rm eff}$ by 1000 - 2000 K for Galactic B supergiants. This is not as drastic as the reduction found for O supergiants, which can be as high as 7000 K for extreme stars (Crowther *et al.*, 2002). If we compare our derived $T_{\rm eff}$'s to those of McErLean *et al.* (1999), with whom we have 10 target stars in common (HD 37128, HD 38771, HD 2905, HD 13854, HD 193183, HD 14818, HD 206165, HD 42087 & HD 53138), we find reasonably good agreement except for B1 Ia/Iabs, where the McErLean *et al.* (1999) results imply that a B1 supergiant is 2500 - 3000 K hotter than our values. The SMC B supergiant temperature scale (Trundle *et al.*, 2004; Trundle & Lennon, 2005) also implies a much hotter B1 supergiant, but it is expected that SMC stars will be hotter than Galactic stars (see e.g. the O star temperature scales of Massey *et al.* (2005) (SMC) and Repolust *et al.* (2004) (Galactic) where the SMC stars are up to 4000 K hotter than the Galactic ones). The sample of B supergiants in this work include B Iab, Ib & II stars compared to the other authors who based their work on B Ia & Iab stars only. The results in this thesis work show there is a difference of $T_{\rm eff} \leq 2500$ K between B Ia and B Iab/Ib/II stars.

An example of a CMFGEN fit to the optical spectrum of the star κ Cas is shown in Fig. 3.5, showing that an excellent model fit to the observed optical spectrum has been achieved, particularly to the temperature diagnostic lines Si III 4552 Å & Si IV 4089 Å. CMFGEN fits to each of the 20 stars in the sample are displayed in Appendix A. However the model overestimates the broadening on the blue side of H δ and underestimates the broadening in the wings of He I 4471 Å and to a smaller extent Si III 4552 Å, 4568 Å and 4575 Å. Values of $T_{\rm eff}$ were derived with an accuracy of $\pm$ 1000 K, though $T_{\rm eff}$ can be constrained to an accuracy of $\pm$ 500 K. However constraining the luminosity from the spectral energy distribution can affect some diagnostic lines in the model (e.g. Si IV 4089) such that a revision of the value of $T_{\rm eff}$ used for the model may be necessary, so $\Delta T_{\rm eff}$ $\pm$ 1000 K is adopted (see Fig. 3.7 for an example). An example of how $T_{\rm eff}$ can be constrained to an accuracy of $\pm$ 500 K is shown in Fig. 3.6 for the star HD 58350, where two CMFGEN models of $T_{\rm eff}$ = 15 000 K and 15 500 K respectively are compared. Additionally Fig. 3.7 demonstrates the effect of varying luminosity on the $T_{\rm eff}$ diagnostic lines. The higher

Table 3.2: Fundamental parameters of Galactic B supergiants

HD no.	Sp. type	$T_{\rm eff}$ (K)	log g	log (L/L$_\odot$)	$R_*(R_\odot)$	E(B-V)	M_V	v_e sin i
37128	B0 Ia	27500	3.13	5.73	32.4	0.08	-6.89	91
192660	B0 Ib	30000	3.25	5.74	23.4	0.80	-6.66	94
204172	B0.2 Ia	28500	3.13	5.48	22.4	0.12	-6.07	87
38771	B0.5Ia	26000	3.00	5.48	27.0	0.07	-6.48	91
185859	B0.5Ia	26000	3.13	5.54	29.1	0.53	-6.54	74
213087	B0.5Ib	27000	3.13	5.69	32.0	1.30	-6.20	88
64760	B0.5Ib	28000	3.38	5.48	23.3	0.15	-6.36	265
2905	BC0.7Ia	23500	2.75	5.48	33.0	0.29	-7.00	91
13854	B1 Iab	20000	2.50	5.54	49.2	0.60	-6.41	97
190066	B1 Iab	21000	2.88	5.54	41.4	0.55	-6.04	82
190603	B1.5 Ia+	19500	2.38	5.41	44.5	0.70	-6.85	79
193183	B1.5 Ib	18500	2.63	5.00	30.8	0.70	-6.43	68
14818	B2 Ia	18000	2.38	5.40	51.4	0.62	-6.70	82
206165	B2 Ib	18000	2.50	5.18	39.8	0.56	-6.64	73
198478	B2.5 Ia	17500	2.25	5.26	46.1	0.40	-7.26	61
42087	B2.5 Ib	18000	2.50	5.11	36.6	0.60	-6.11	71
53138	B3 Ia	16500	2.25	5.30	54.7	0.35	-6.79	58
58350	B5 Ia	15000	2.13	5.18	57.3	0.05	-7.12	50
164353	B5 Ib	15500	2.75	4.30	19.6	0.71	-6.15	44
191243	B5 Ib	14500	2.75	5.30	70.8	0.93	-6.59	38

Atmospheric parameters ($T_{\rm eff}$, log g, log $(L/L_\odot)$, $R_*(R_\odot)$, E(B-V), M_V& v_e sin i) derived for the sample of 20 Galactic B supergiants. Values of v_e sin i are taken from Howarth *et al.* (1997) and are expressed in km/s.

Table 3.3: Comparison of B supergiant $T_{\rm eff}$ scales

Sp type	This thesis	Trundle	McErlean	Crowther
B0 Ia	27.5	27.0*	28.5	27.38*
B0 Ib	30.0	-	-	-
B0.2 Ia	28.5	-	28.5	-
B0.5 Ia	26.0	27.25*	27.5	26.0*
B0.5 Ib	27.0†	-	26.5*	-
B0.7 Ia	23.5	-	24.0	22.88
B1 Ia	-	23.75*	-	22.0
B1 Iab/Ib	20.5*	-	23.25*	21.75*
B1.5 Ia	19.5	21.25*	21.25	18.17
B1.5 Ib	18.5	-	22.25*	-
B2 Ia	18.0	19.0	19.83	18.63*
B2 Ib	18.0	-	20.83*	-
B2.5 Ia	17.5	16.5	18.0	16.5
B2.5 Ib	18.0	-	20.5	-
B3 Ia	16.5	14.0	17.88*	15.75*
B4 Iab	-	-	16.5	-
B5 Ia	15.25*	14.5*	15.38*	-
B5 Ib/II	15.0*	-	15.83*	-

Values of $T_{\rm eff}$ (expressed in terms of 10^3 K) obtained in this thesis work and from Trundle *et al.* (2004); Trundle & Lennon (2005); McErLean *et al.* (1999); Crowther *et al.* (2006). Values marked with an asterisk denote where values from one author have been averaged. † the B0.5 Ib star HD 64760 has been omitted here because it is a rapid rotator.

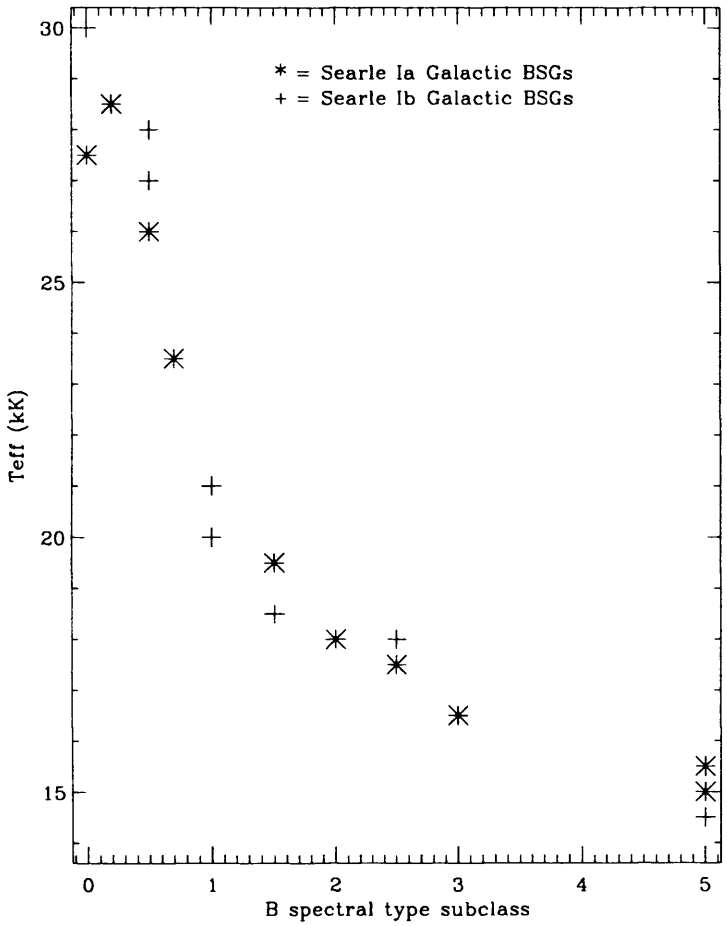

Figure 3.4: The Galactic B supergiant $T_{\rm eff}$ scale.

luminosity model (red line, $L = 3.5 \times 10^5 L/L_\odot$) produces a much stronger Hδ line and increases the Hϵ lines, whilst reducing the strength of the silicon lines. If this luminosity was assumed for this star, $T_{\rm eff}$ would have to be increased to improve the fit to the Si IV & Si III lines, however it is clear that this luminosity is incorrect for this star due to the overestimation of the Hδ line.

An example of a TLUSTY log g fit to the Hγ profile of ϵ Ori is shown in Fig. 3.8. TLUSTY is a purely photospheric code therefore the model Balmer lines are also photospheric, but in B supergiants the observed Balmer lines suffer from wind contamination, where hydrogen photons emitted in the wind at the same wavelengths as Hγ & Hδ 'fill in' the absorption profile. This makes it appear more 'shallow' when compared to a photospheric profile and explains the difference in depth between the two profiles shown in

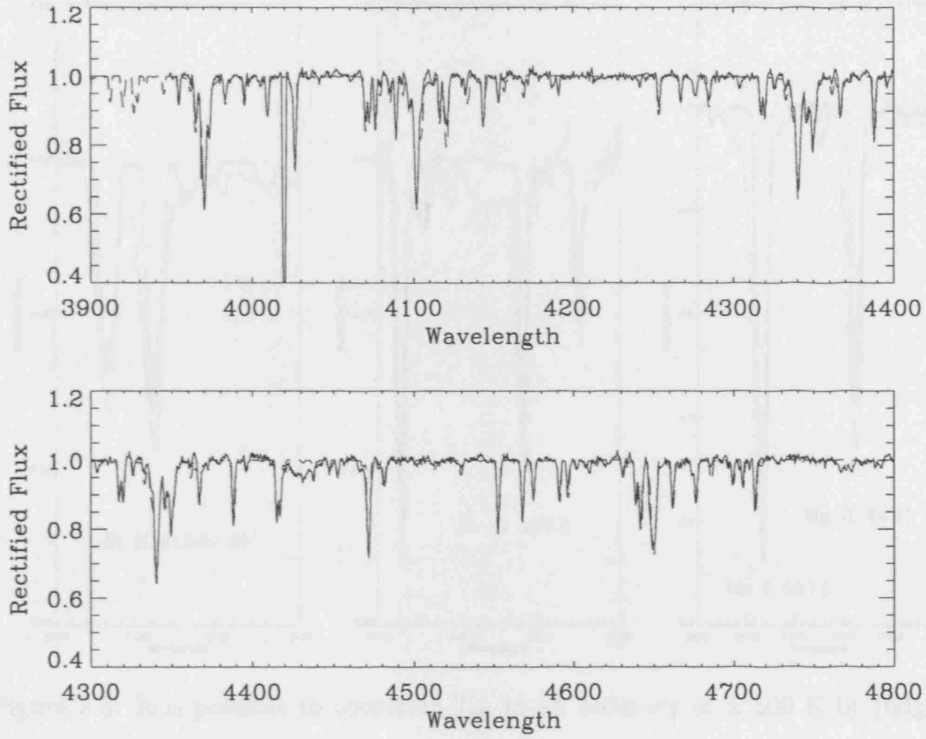

Figure 3.5: Overall CMFGEN fit to the optical spectrum of κ Cas (3950 Å - 4750 Å. The solid black line is the observed spectrum and the red dotted line denotes the CMFGEN model fit.

Fig. 3.8. The error on the log g estimates is 0.13 dex as demonstrated in Fig. 3.8, where three different model profiles are shown, corresponding to log g = 3.00, 3.13 & 3.25 respectively against the observed Hγ line of ϵ Ori. When fitting the Hγ line, priority is given to achieving a good fit to the profile wings, since the observed profile is contaminated by the stellar wind and it is not possible to make a decent fit to the whole observed profile using a purely photospheric Hγ model line. Another difficulty in fitting the Hγ line comes from the O II blend present around 4350 Å, however, Hγ is the best diagnostic line to use for constraining log g as Hα & Hβ suffer from too much wind fill emission. The Hδ line was used as a secondary diagnostic for constraining log g to confirm the value derived from fitting Hγ. The $T_{\rm eff}$ - log g scale derived from this work is shown in Fig. 3.2.2, where higher log g values are found for B Ib stars. The log g values derived for B Ia stars are 0.1 – 0.2 dex higher than those obtained by Kudritzki *et al.* (1999); Crowther *et al.* (2006) for a sample of Galactic B supergiants, whereas the Trundle *et al.* (2004);

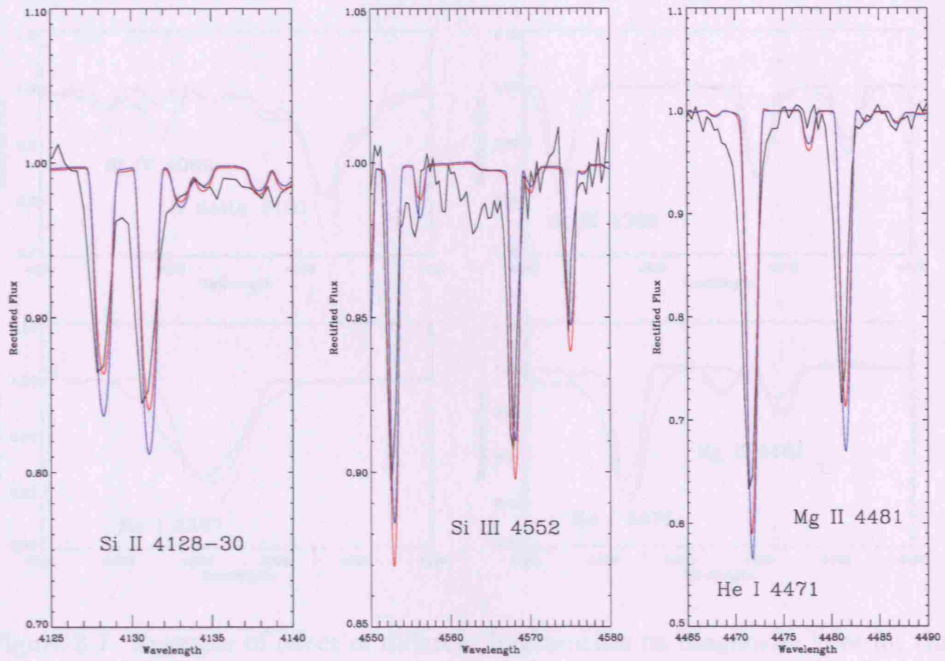

Figure 3.6: It is possible to constrain $T_{\rm eff}$ to an accuracy of $\pm$ 500 K by judging the fits 'by eye'. CMFGEN fits to the star HD 58350 (B5 Ia) are shown above for the $T_{\rm eff}$ diagnostic lines Si II 4128-30, Si III 4552, He I 4471 and Mg II 4481. The blue line represents a model with $T_{\rm eff}$ = 15000 K and the red line a model with $T_{\rm eff}$ = 15500 K; both models have log $(L/L_{\odot})$= 5.18 and log $\dot{M}$ = -6.15.

Trundle & Lennon (2005) values for SMC B supergiants are generally higher than those for Galactic B supergiants.

3.2.2.1 Quality of individual line fits

Overall CMFGEN has succeeded in providing excellent fits to the observed spectrum of each star. The models succeed in reproducing the H, He, Si & Mg lines quite accurately. However, some individual spectral lines are more difficult to model than others. The Si IV 4089 Å line is often underestimated in B0-B2 supergiants, with the effect being most pronounced in B1-B2 supergiants, which might be partly due to a blend with O II. Since the Si IV line is photospheric, the problem can be alleviated by including a TLUSTY hydrostatic structure in the CMFGEN model. It is also noticeable that the model Si IV

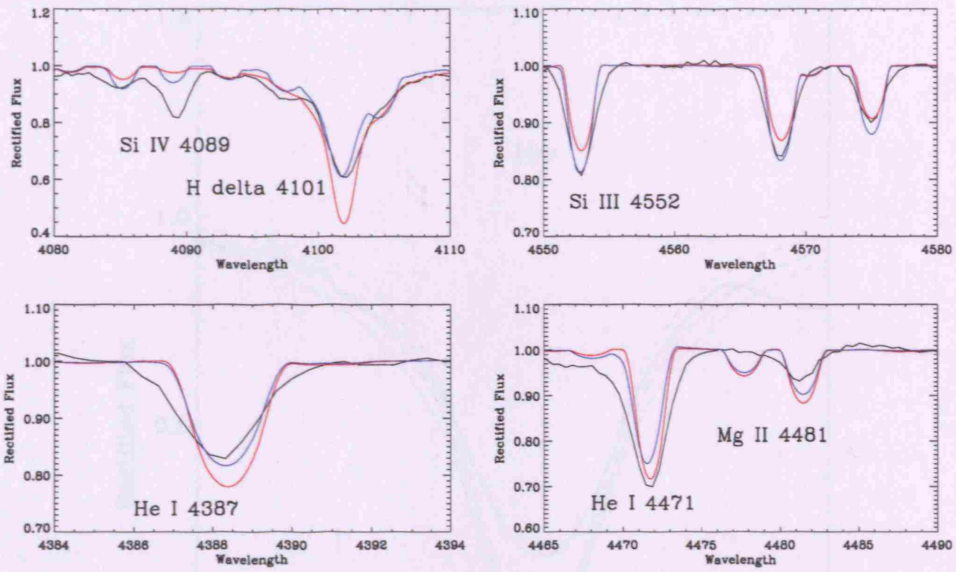

Figure 3.7: Example of effect of different luminosities on diagnostic lines for the B1 Iab star HD 190066. Parameters for both models are $T_{\rm eff}$ = 21 000 K & $\dot{M}$ = 7×10^{-7}, with the blue line indicating a model with $L_* = 3 \times 10^5$ and the red line indicating $L_* = 3.5 \times 10^5$.

line displays a slight sensitivity to mass loss, however this effect is purely produced by the code and is *not* observed. The values of $T_{\rm eff}$ derived for these stars can still be justified since greater weight is given to fitting the Si III, Mg II and He I lines and usually in these cases the model spectrum fits these lines very well. For example, the model fit to the B0.5 Ia star κ Ori underestimates the observed Si IV 4089 line, only reproducing and also to a lesser extent the He I 4471 line. However excellent fits are achieved to the Si III 4552, He I 4144 & 4387 lines, as well as the overall spectrum, using a model with a higher $T_{\rm eff}$ that provided a better fit to the Si IV line would provide a worse fit to the rest of the observed spectrum. More examples of this can be seen for the CMFGEN fits to HD 13854, HD190066, HD 190603 & HD 193183 in the appendix. In the model fits to these stars, the Si IV synthetic profile is very weak compared to the observed one, implying that a model with higher $T_{\rm eff}$ should be used, but conversely the model also underestimates the Si III 4552 & He I 4144, 4387 & 4471 lines, suggesting a lower $T_{\rm eff}$ would be a better fit. In this situation, priority is given to these latter lines i.e. Si III is given priority over Si IV. In the cases of HD 190603 & HD 193183, the ratio of He I/Mg II and the other He I lines are

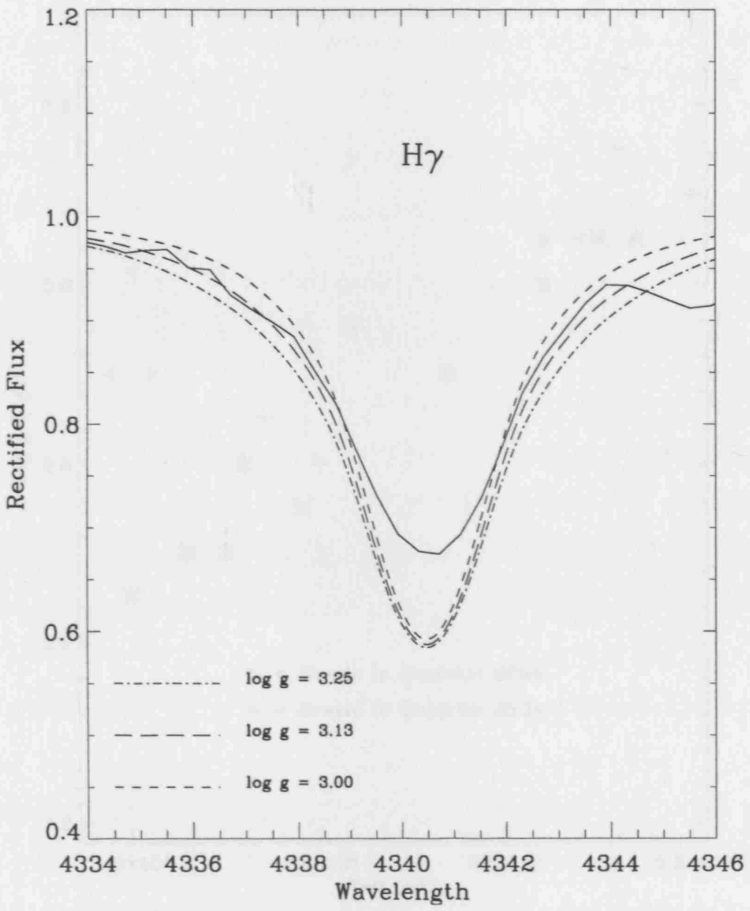

Figure 3.8: Example of different log g fits to Hγ profile of ϵ Ori to demonstrate the margin of error on the estimates of log g derived in this work.

given greater weighting than the Si III/Si IV ratio.

The CMFGEN model fits to $T_{\rm eff}$ and luminosity diagnostic lines are described below for each of the 20 B supergiants in our sample.

- **HD 192660**: An excellent fit is achieved to the observed spectrum of this star, particularly to the He I lines. The Si III and Si IV lines are slightly underestimated but Mg II is fitted well.
- **HD 37128 (ϵ Ori)**: The overall model fit is very good, with good fits to Mg II 4481 Å, He I 4144 Å and 4387 Å but He I 4471 Å is underestimated and the observed

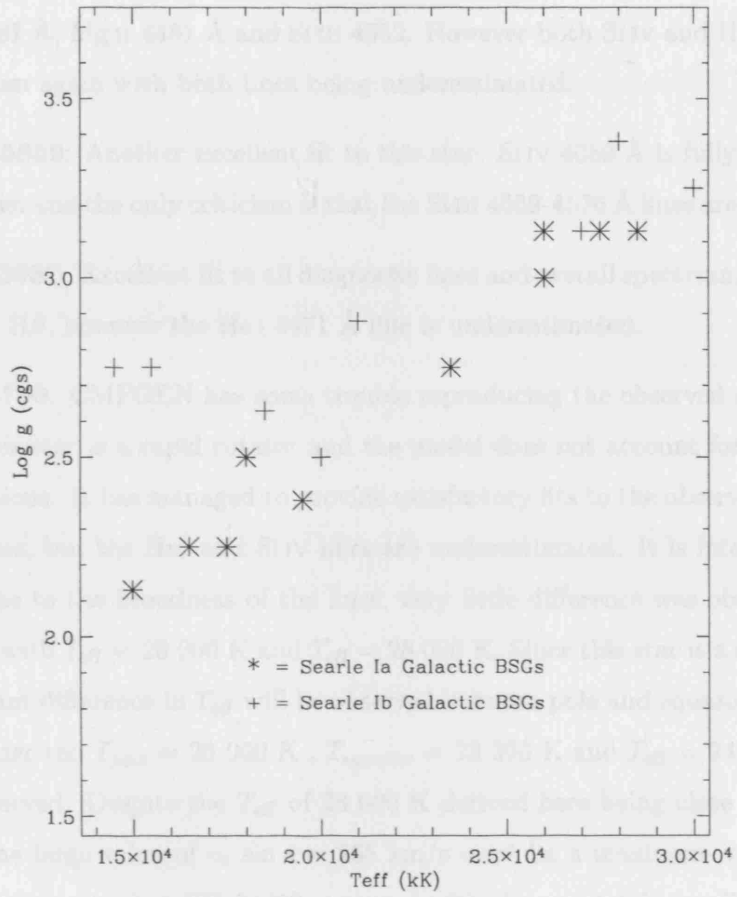

Figure 3.9: The Galactic B supergiant $T_{\rm eff}$ - log g scale.

broadening on the blue wing is not reproduced by the model. Hβ and Hγ are overestimated by the model. CMFGEN does not reproduce the Si IV 4089 Å line well, underestimating it by about 40 % whilst the Si III lines around 4550 - 4580 Å are overestimated. This problem cannot be successfully alleviated by increasing $T_{\rm eff}$ to fit the Si IV line as the line remains severely underestimated regardless of the assumed $T_{\rm eff}$. It is possible that this situation is an example of the sensitivity of the model Si IV line to the assumed value for $\dot{M}$ causing the observed discrepancy.

- **HD 204172**: Similar fit to HD 37128, but He I lines are slightly overestimated except He I 4471 Å, which is again underestimated (but not to the extent that it was in HD 37128). Again Si IV is slightly underestimated (but less severely than for HD 37128) and Si III is largely overestimated.

- **HD 38771 (κ Ori)**: Very good fit to the overall spectrum, especially Hβ, He I 4144 Å & 4387 Å, Mg II 4481 Å and Si III 4552. However both Si IV and He I 4471 Å pose a problem again with both lines being underestimated.

- **HD 185859**: Another excellent fit to this star. Si IV 4089 Å is fully reproduced by the model and the only criticism is that the Si III 4552-4576 Å lines are overestimated.

- **HD 213087**: Excellent fit to all diagnostic lines and overall spectrum, even including Hγ and Hβ, however the He I 4471 Å line is underestimated.

- **HD 64760**: CMFGEN has some trouble reproducing the observed diagnostic lines since this star is a rapid rotator and the model does not account for rotation in its calculations. It has managed to provide satisfactory fits to the observed Hβ, Hγ and Si III lines, but the He I and Si IV lines are underestimated. It is interesting to note that, due to the broadness of the lines, very little difference was observed between models with $T_{\rm eff}$ = 26 000 K and $T_{\rm eff}$ = 28 000 K. Since this star is a rapid rotator, a significant difference in $T_{\rm eff}$ will be observed between pole and equator. Kaufer *et al.* (2006) derived T_{pole} = 29 000 K , $T_{equator}$ = 23 300 K and $T_{\rm eff}$ = 24 600 as seen by the observed. Despite the $T_{\rm eff}$ of 28 000 K derived here being close to the value of T_{pole}, the large value of v_e sin i = 265 km/s must be a maximum value (where sin 90^o =1) suggests that HD 64760 is viewed with the equator in our line of sight.

- **HD 2905 (κ Cas)**: An excellent fit is made to the overall observed spectrum of this star as well as the key diagnostic lines, with the Si III & Si IV lines being only slightly underestimated.

- **HD 13854**: A reasonable fit is obtained to the observed spectrum, however it is difficult to fit all the diagnostic lines satisfactorily. A $T_{\rm eff}$ of 20 000 K fits the H and He I lines better but largely underestimates the Si III and Si IV lines. Conversely, a $T_{\rm eff}$ of 22 000 K provides a much better match to the silicon lines, but grossly overestimates the H and He I lines.

- **HD 190066**: the CMFGEN fit to this star is not quite so good, since Hγ, Hϵ and He I 4144 Å and 4387 Å are largely overestimated whilst Si III and Si IV are quite severely underestimated. This problem is not easily resolved, since increasingly $T_{\rm eff}$ in order to fit Si IV will only reduce the strength of Si III further. However the model does succeed in reproducing the He I 4471 Å line perfectly.

- **HD 190603**: For this star, CMFGEN provides an excellent fit to the He I 4471 Å and Mg II 4481 Å lines, as well as very good fits to He I 4144 Å and 4387 Å. Unfortunately the Si III and Si IV lines are grossly underestimated. Si III lines are better matched with $v_{\rm turb} = 15$ km/s.

- **HD 193183**: A good fit is achieved to the overall spectrum of this star, with reasonable fits to the diagnostic lines. He I 4471 Å is reproduced exactly by the code, but the remaining He I, Hβ, Hγ and Mg II lines are overestimated. Si III and Si IV, on the other hand, are underestimated. It is interesting to note that CMFGEN distinctly produces the Si II doublet at 4128-30 Å before it is observed. In this case, priority is given to the He I lines when fitting the diagnostic lines.

- **HD 14818**: The overall observed spectrum of this star is fitted reasonably well by CMFGEN, but again the He I lines are given more weighting over the silicon lines, which are underestimated by the code. He I 4471 is perfectly reproduced and the other He I lines are only slightly underestimated.

- **HD 206165**: CMFGEN provides a good overall fit to the observed spectrum of HD 206165, particularly Mg II and the He I lines. However the silicon lines are again underestimated, so higher priority is given to fitting the He I lines again for this star.

- **HD 198478**: A very good fit is made to the overall spectrum of this star with the silicon lines and Mg II accurately reproduced by the code. He I 4471 Å is also well reproduced by CMFGEN, but the remaining H and He I lines are overestimated.

- **HD 42087**: Like HD 14818 and HD 206165, the strongest weighting is given to the He I lines when fitting the spectrum of this star. The He I lines were easier to fit whilst the silicon lines posed more of a problem as Si II is overestimated and Si III is slightly underestimated, as is Mg II. However if the $T_{\rm eff}$ is lower enough in order to fit the Si II doublet then the Si III lines will be largely overestimated.

- **HD 53138**: A very good fit has been achieved to the spectrum of this star, with He I 4471 Å, Mg II and the silicon lines reproduced well by the code. However Hβ, Hγ, Hδ and the remaining He I lines are all largely overestimated by CMFGEN.

- **HD 58350**: Good overall fit to the star. The Si III lines are fitted well but all the other lines are overestimated. The spectrum of this star could have been fitted with

a model of either $T_{\rm eff}$ = 15 000 K or 15 500 K, with the higher $T_{\rm eff}$ fitting the Si II doublet better but overestimating the Si III, whilst the reverse is true for $T_{\rm eff}$= 15 000 K which is the derived $T_{\rm eff}$ for this star.

- **HD 164353**: The CMFGEN fit to this star is reasonable, but all the diagnostic lines are somewhat overestimated.

- **HD 191243**: As for HD 164353, all the diagnostic lines are overestimated and the silicon lines imply a lower $T_{\rm eff}$, but it was not possible to run a CMFGEN model at a lower $T_{\rm eff}$ that would converge successfully.

3.2.2.2 Stellar Masses and the Mass Discrepancy

Using our estimates of log g, spectroscopic masses have been derived for each of the 20 B supergiants and imply a range of $8 \leq M_{*} \leq 52$. Estimates of the evolutionary mass, $M_{\rm evol}$, were then obtained using our derived stellar parameters and the stellar evolutionary tracks of Meynet & Maeder (2000). The positions of our 20 Galactic B supergiants on the Hertzsprung-Russell diagram, along with the Crowther *et al.* (2006) Galactic B supergiants, Trundle *et al.* (2004); Trundle & Lennon (2005) SMC B supergiants and Repolust *et al.* (2004) Galactic O stars, are shown in Fig. 3.10. Here, the Meynet & Maeder (2000) stellar evolutionary tracks have been used, which include the effects of rotation and are therefore more appropriate for OB supergiants. A comparison of both masses is shown in Fig. 3.11. For 14 out of the 20 B supergiants, $M_{\rm evol} > M_{\rm spec}$as found by Herrero *et al.* (2002). However, for the 6 other stars, which (excluding the rapid rotator HD 64760) have log $(L/L_{\odot}) \geq 5.54$, $M_{\rm evol} < M_{\rm spec}$. The dependence of the mass discrepancy with luminosity is examined further in Fig. 3.12 and compared to the mass discrepancy for SMC B supergiants investigated by Trundle *et al.* (2004); Trundle & Lennon (2005). Both data sets exhibit a peak in the mass discrepancy at $5.4 \leq \log (L/L_{\odot}) \leq 5.5$ that drops off quite rapidly.

3.2.3 Determination of Stellar Wind Properties

Values for the mass loss rate of each star were constrained by fits to the Hα profile, with each fit aiming to reproduce the overall profile shape and amplitude. Values of v_{∞} are best determined from the UV so values obtained through SEI analysis (see Chapter 5) are

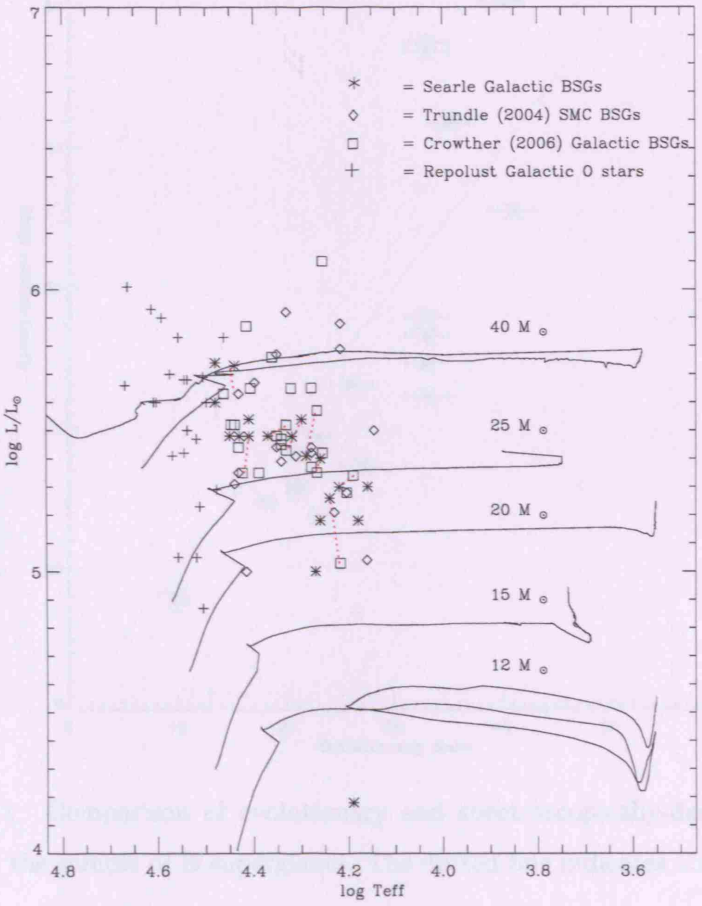

Figure 3.10: Position of the sample of Galactic B supergiants on the Hertzsprung-Russell diagram, along with other Galactic B supergiants (Crowther *et al.*, 2006), SMC B supergiants (Trundle *et al.*, 2004; Trundle & Lennon, 2005) and Galactic O stars (Repolust *et al.*, 2004). Stars common to this work and Crowther *et al.* (2006) are joined by a dotted red line to illustrate the effect of adopting different $T_{\rm eff}$ & $\log L_*$ on the star's position on the HR diagram. Evolutionary tracks are taken from Maeder & Meynet (2001) and imply $15\ M_\odot < M_{\rm evol} \leq 40\ M_\odot$ for the sample of 20 Galactic B supergiants presented in this work.

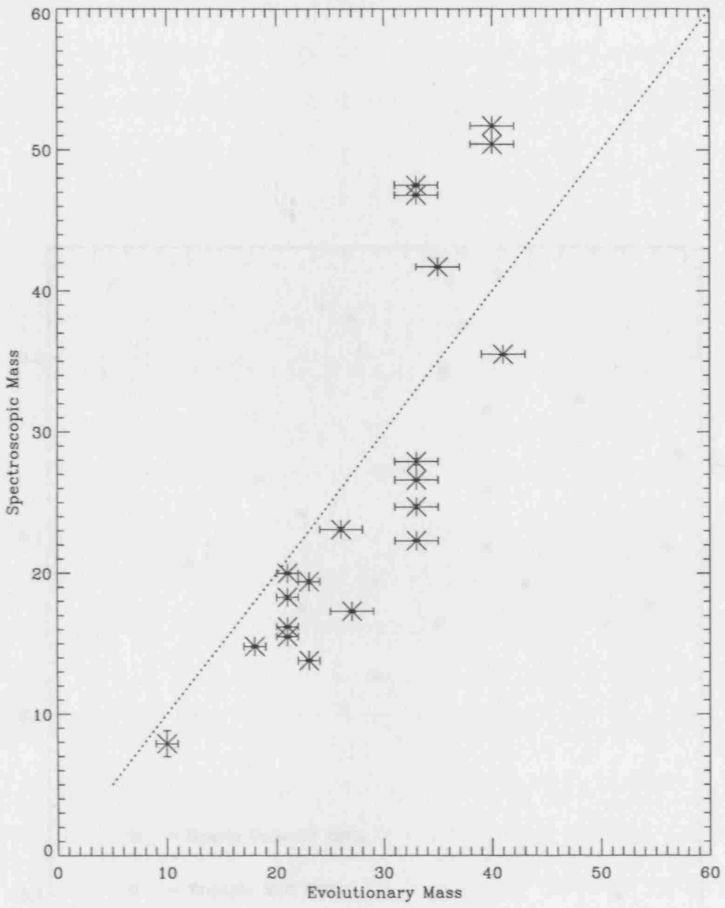

Figure 3.11: Comparison of evolutionary and spectroscopically-derived stellar masses for the sample of B supergiants. The dotted line indicates 1:1 correspondance.

used here. The value of β is also varied in order to improve the shape of the model profile fit with respect to the observed profile, but this has no effect for Hα profiles in absorption, in which case values obtained from SEI analysis were used. Values of the microturbulent velocity, $v_{\rm turb}$, were obtained by fitting the Si III lines at 4552, 4568 & 4575 Å, whilst checking for consistency with adopted temperature and luminosity for a given star. The inclusion of a microturbulent velocity was justified by Howarth *et al.* (1997), when carrying out a study of the rotational properties of OB stars. They found that all the supergiants in their sample (except one) that were earlier than B5 possess $v_e \sin i > 50$ km/s. This result was explained by the presence of a microturbulent and macroturbulent velocity

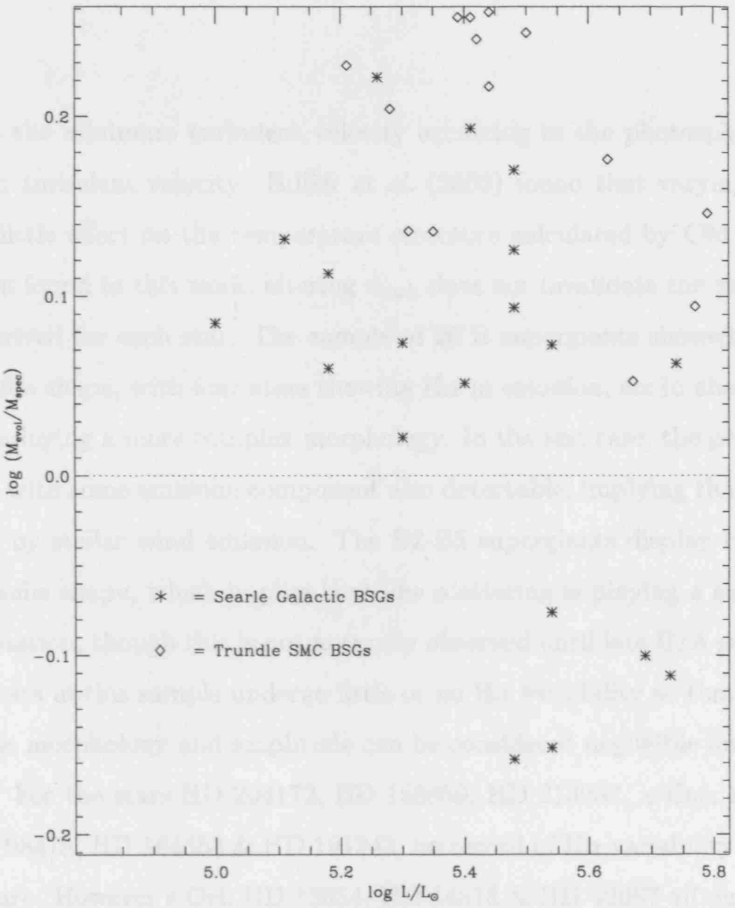

Figure 3.12: Comparison of $\frac{M_{evol}}{M_{spec}}$ with luminosity (B5 Ib/II stars omitted). Values obtained for the 20 Galactic B supergiants (asterisks) are plotted with those derived for SMC B supergiants (diamonds) (Trundle *et al.*, 2004; Trundle & Lennon, 2005). The dotted line indicates 1:1 correspondance.

fields; the latter referring to large-scale velocities superimposed onto the mean velocity flow. In CMFGEN, the effects of these microscopic and macroscopic velocity fields is accounted through the microturbulent velocity, dependent on depth and defined as

$$v_{\rm turb} = v_{\rm min} + \frac{(v_{\rm max} - v_{\rm min})v(r)}{v_\infty} \tag{3.1}$$

where $v_{\rm min}$ is the minimum turbulent velocity occurring in the photosphere and $v_{\rm max}$ is the maximum turbulent velocity. Hillier *et al.* (2003) found that varying the turbulent velocity had little effect on the temperature structure calculated by CMFGEN and the same has been found in this work; altering $v_{\rm turb}$ does not invalidate the values of $T_{\rm eff}$ and luminosity derived for each star. The sample of 20 B supergiants showed some variation in overall profile shape, with four stars showing Hα in emission, six in absorption and the remainder displaying a more complex morphology. In the last case, the profiles are partly in absorption with some emission component also detectable, implying that the profile has been filled in by stellar wind emission. The B2-B5 supergiants display Hα profiles with a P Cygni profile shape, which implies that line scattering is playing a significant role in the line's formation, though this is not normally observed until late B/A supergiants. The majority of stars in this sample undergo little or no Hα variability so that any changes in the line profile morphology and amplitude can be considered negligible for the purpose of this analysis. For the stars HD 204172, HD 185859, HD 213087, κ Cas, HD 190066, HD 193183, HD 198478, HD 164353 & HD 191243, no record of Hα variability has been found in the literature. However ϵ Ori, HD 13854, HD 14818 & HD 42087 all display significant Hα variability according to Morel *et al.* (2004). In view of this problem, for ϵ Ori we have assumed a radio mass loss rate, $\dot{M}_{\rm radio}$, of 1.9×10^{-6} $M_\odot$ yr^{-1}, as measured by Blomme *et al.* (2002), thereby avoiding the inaccuracies involved in deriving $\dot{M}$ from a variable Hα line. Unfortunately this approach is not possible for the other 3 stars since there are no reliable $\dot{M}_{\rm radio}$ values in the literature. The problems associated with deriving $\dot{M}$ from the Hα profiles of these stars are discussed in the next section.

Table 3.4: Stellar wind parameters

HD no.	Sp type	$\dot{M}(10^{-6}M_{\odot}\ \mathrm{yr}^{-1})$	β	v_{∞}	v_{turb}
37128	B0 Ia	1.90	1.1	1600	15
192660	B0 Ib	$2.00 \leq \dot{M} \leq 5.00$	1.3	1850	20
204172	B0.2 Ia	$5.70 \leq \dot{M} \leq 9.00$	1.0	1685	15
38771	B0.5 Ia	$1.20 \leq \dot{M} \leq 1.50$	1.1	1390	15
185859	B0.5 Ia	0.50	1.5	1830	20
213087	B0.5 Ib	$0.70^{+0.4}_{-0.2}$	1.5	1520	20
64760	B0.5 Ib	1.10	1.0	1600	15
2905	BC0.7 Ia	2.50	1.5	850	20
13854	B1 Iab	1.50	1.2	955	10
190066	B1 Iab	0.70	1.5	1275	15
190603	B1.5 Ia+	2.40	1.2	390	15
193183	B1.5 Ib	$0.23 \leq \dot{M} \leq 0.5$	1.5	565	20
14818	B2 Ia	$0.5 \leq \dot{M} \leq 1.00$	1.5	625	15
206165	B2 Ib	$0.1 \leq \dot{M} \leq 0.50$	1.5	640	15
198478	B2.5 Ia	$0.50\ ^{+0.4}_{-0.2}$	1.2	550	20
42087	B2.5 Ib	$0.3 \leq \dot{M} \leq 0.50$	1.2	650	15
53138	B3 Ia	0.45	1.2	500	20
58350	B5 Ia	$0.50 \leq \dot{M} \leq 0.70$	1.0	320	20
164353	B5 Ib	0.06	1.5	450	25
191243	B5 Ib	$0.02 \leq \dot{M} \leq 0.83$	1.0	550	20

Stellar wind parameters ($\dot{M}$, β, v_{∞}, v_{turb}) derived for a sample of 20 Galactic B supergiants. All velocities are expressed in km/s.

3.2.4 Mass loss rates for B supergiants

The mass loss rates obtained for this sample of 20 Galactic B supergiants are listed in Table 3.4 and show that most of these B supergiants have mass loss rates of the order of $-6.0 \leq \log \dot{M} \leq -7.0$. These mass loss rates have been compared to those predicted by the theoretical mass loss prescription of Vink *et al.* (2000), as shown in Fig. 3.14, where the values of $T_{\rm eff}$, $\log L_*$ and M_* derived in the previous section have been input into the relevant mass loss recipes quoted in the paper. When comparing the observationally derived $\dot{M}$ with the Vink *et al.* (2000) $\dot{M}$ predictions, discrepancies of > 20 % are found. This is not entirely surprising, given that observed mass loss rates are over-estimated due to the presence of clumping in the wind and Vink *et al.* (2000) has not accounted for this in his models. A better comparison is found between the mass loss rates presented here and the values obtained by Kudritzki *et al.* (1999), for which there are 8 stars common to both data sets (Fig. 3.15).

CMFGEN fits to the Hα profiles of κ Cas, HD190603, HD 14818, HD 190066, HD 193183 & HD 164353 are given in Fig. 3.13 and the Hα profile fits to all 20 B supergiants are given in Appendix A. In general, reasonable fits are obtained for each star, but several difficulties have been encountered in trying to reproduce the observed Hα profiles. Where Hα has been over- or under-estimated by CMFGEN, $\dot{M}$ has been denoted as a upper/lower limit accordingly, but errors in deriving $\dot{M}$ are no more than a factor of 2. It is clear that all the observed profiles are asymmetric and it is likely that this is caused by the influence of resonant line scattering that is too weak to produce a 'P Cygni'-type profile so merely results in a slightly asymmetric profile. In some stars e.g. HD 213087, it appears to be a redward emission component that partly fills in the profile, to such an extent that in some stars this red component is visible as a separate emission component (e.g. HD 206165) and the Hα profile begins to resemble a P Cygni profile (e.g. HD 14818). In the majority of stars, the peak/trough of the Hα profile has shifted from the line centre as observed in κ Cas. This effect is particularly clear on comparing the Hα profile of κ Cas with that of HD 190603, whose peak is much more central resulting in only a slight asymmetry to the overall profile. It is also of interest to note that CMFGEN predicts a 'bump' in the blueward wing of the Hα profile of HD 190603 that is not present in the observed profile; a similar phenomenon is observed for HD 193183.

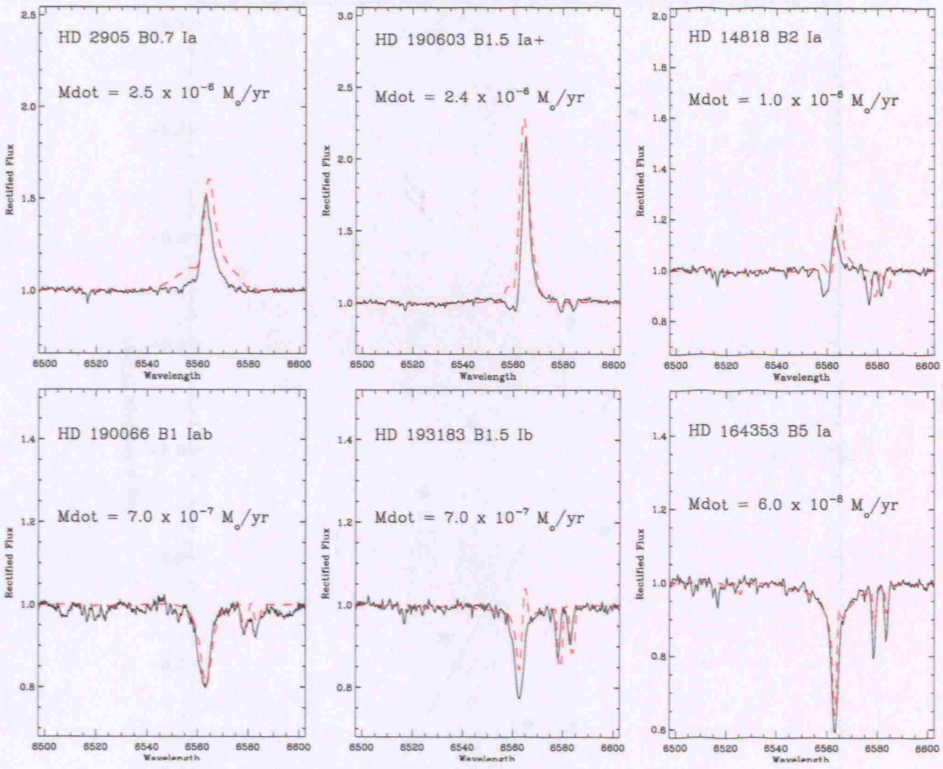

Figure 3.13: Examples of CMFGEN fits to Hα profiles

3.2.4.1 Notes on Hα profiles of individual stars

HD 192660 (B0 Ib) has a strange Hα profile that is weakly in emission (as mentioned in §3.1.3) that CMFGEN is unable to reproduce. Please refer to §3.2.5 for how clumping was used to try and improve the model fit to the Hα profile of HD 192660. HD 13854, HD 14818 & HD 206165 all display Hα lines with a P Cygni profile shape that CMFGEN is unable to fit (the code reproduces the emission profile but completely fails to produce an absorption component in the profile). Although HD 14818 & HD 42087 have been noted as variable, their Hα profiles retain their P Cygni morphology and merely change in strength. The failure of CMFGEN to reproduce the Hα profiles is therefore a more fundamental problem than Hα variability for these two stars. The same problem has previously been encountered by Kudritzki *et al.* (1999); Trundle *et al.* (2004); Trundle & Lennon (2005) when using the stellar atmosphere code FASTWIND. Kudritzki *et al.* (1999) suggested that the absence of line-blanketing in the version of FASTWIND they used could affect

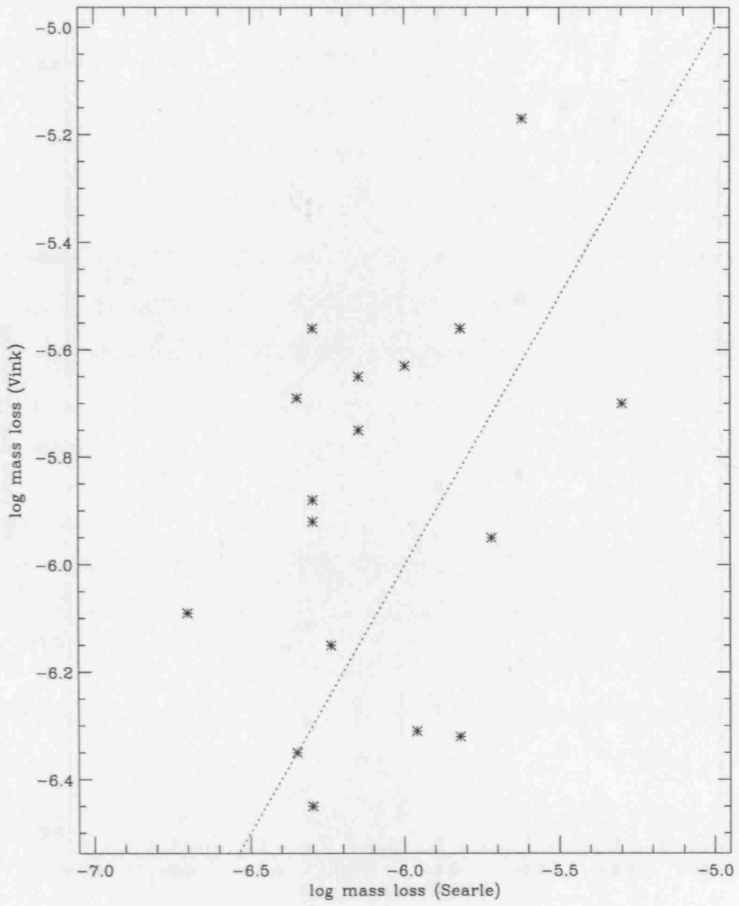

Figure 3.14: Comparison of CMFGEN derived mass loss rates with theoretical mass loss rates predicted by the Vink *et al.* (2000) mass loss prescription. The dotted line indicates 1:1 correspondance.

the stratification of the source function of Hα in the wind, but this was dismissed by Trundle *et al.* (2004) who had used a version of FASTWIND that included an approximate treatment of line blanketing, yet still failed to reproduce an observed Hα profile displaying a P Cygni morphology. However, in a few cases e.g., HD 14818, Crowther *et al.* (2006) had more success in reproducing the Hα profile of this star, adopting $\dot{M} = 5.5 \times 10^{-7}$ $M_{\odot}$ yr^{-1}, whereas I found a model with $\dot{M} = 5.0 \times 10^{-7}$ underestimated the observed profile. This is in part due to a slight difference in fundamental parameters (Crowther *et al.* (2006) obtain $T_{\rm eff} = 18500$ K, log $(L/L_{\odot}) = 5.35$ and $\beta = 2.0$ for this star). This and other examples also highlight some inconsistencies in the code where adopting not

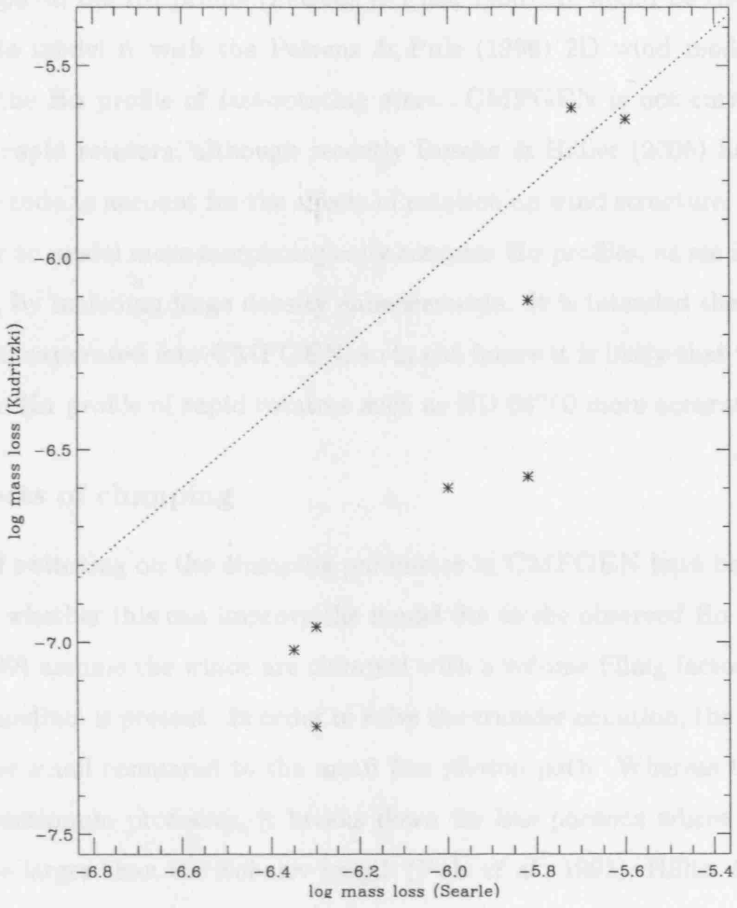

Figure 3.15: Comparison of CMFGEN derived $\dot{M}$ with those of Kudritzki *et al.* (1999) for 8 stars common to both samples

only different stellar parameters but also other parameters governing e.g., the convergence and iteration properties of the code can lead to different solutions. The Hα profiles of HD 198478 & HD 42087 are overestimated by the code, which also produces a slight absorption component that is not actually observed. A model with a lower value of $\dot{M}$ does not resolve the problem since it produces an Hα profile that is completely in absorption. The values of $\dot{M}_{\mathrm{H}\alpha}$ obtained for these stars have been quoted as upper/lower limits as appropriate given the quality of the individual fits to Hα (see Table 3.4).

One star that has a particularly striking Hα profile is the rapid rotator HD 64760, whose profile is mostly in absorption but has both blue and red emission humps in the line profile wings. These humps are produced by the effects of differential rotation of an expanding

stellar envelope on the Hα profile (Petrenz & Puls, 1996). It would be therefore be more appropriate to model it with the Petrenz & Puls (1996) 2D wind model designed for synthesising the Hα profile of fast-rotating stars. CMFGEN is not currently equipped to deal with rapid rotators, although recently Busche & Hillier (2005) have produced a semi-analytic code to account for the effects of rotation on wind structure. Their code has the capability to model more morphologically complex Hα profiles, as see in the spectrum of HD 64760, by including large density enhancements. It is intended that the new code will soon be incorporated into CMFGEN, so in the future it is likely that CMFGEN will reproduce the Hα profile of rapid rotators such as HD 64760 more accurately.

3.2.5 Effects of clumping

The effects of switching on the clumping parameter in CMFGEN have been investigated to determine whether this can improve the model fits to the observed Hα profiles. Hillier & Miller (1999) assume the winds are clumped with a volume filling factor f and that no inter-clump medium is present. In order to solve the transfer equation, the clumps are also assumed to be small compared to the mean free photon path. Whereas this assumption is valid for continuum processes, it breaks down for line photons where the clumps are thought to be larger than the Sobolev length (Puls *et al.*, 1993); Hillier & Miller (1999) supposed that this will not affect results drastically but without testing the validity of the assumption. The volume filling factor, is defined as:

$$f = f_\infty + (1.0 - f_\infty)e^{-\frac{v}{v_{cl}}} \tag{3.2}$$

where f_∞ is the filling factor at v_∞ and v_{cl} is the velocity at which clumping is 'switched on' in the wind. Normally a value of 200 km/s is adopted for v_{cl}. Equation 3.2 provides a distribution of clumping in the wind such that $f \rightarrow 1$ as $v \rightarrow 0$ and $f \rightarrow f_\infty$ as v approaches large values. The density in any clump is described by

$$\rho(r) = \frac{\dot{M}}{4\pi r^2 v(r) f(r)} \tag{3.3}$$

and the average density distribution is simply parameterised by $\bar{\rho} = f\rho$. The inclusion of clumping in a model requires the mass loss rate to be reduced by a factor $\sqrt{f}\dot{M}$ in order to keep the wind consistent with homogeneous models. (It is evident from Equation 3.3 that the addition of the filling factor to this revised equation of mass continuity will increase $\dot{M}$ and therefore the density ρ, so $\dot{M}$ has to be reduced to keep the density constant). The filling factors explored in this work vary between $0.01 \leq f \leq 0.5$, where other authors e.g. Hillier *et al.* (2003); Bouret *et al.* (2005) favour values of $f \sim 0.1$ for OB supergiants. However we find that there are restrictions in the range of f-values we can use, since too high a value can result in a model spectrum that has all its lines in emission. Fig. 3.16 shows the effect of different filling factors ($0.01 \leq f_\infty \leq 0.5$) on the model H$\alpha$ profile for HD 190603. Since $\dot{M}_{\mathrm{H}\alpha}$ is dependent on ρ^2, Hα is quite sensitive to the filling factor. In the case of HD 190603, a better fit is achieved to the redward side of the profile with $f_\infty = 0.1 - 0.5$, but this value grossly underestimates the overall profile strength. A higher value such as $f_\infty \geq 0.5$ is not appropriate since it would produce a model spectrum with all the spectral lines in emission. Conversely reducing f_∞ to 0.01 results in a model that fails to produce an Hα profile in emission. It is noticeable that a lower f_∞ value also produces a narrower Hα profile than observed. The clumped models do not succeed in resolving the failure to model the small blue absorption component seen in the Hα profile. It is also possible to vary a second clumping parameter, v_{cl}. As shown in Fig. 3.16, switching clumping on 'earlier' (i.e., at a lower velocity) produces a much weaker and narrower Hα profile, comparable to a model Hα profile with $f_\infty = 0.05$ and $v_{cl} = 200$ km/s.

The effect of clumping on the Hα profile of HD 192660 was also investigated, since CMFGEN had particular trouble in reproducing the observed Hα profile for this star. The filling factor was varied from 0.1-0.3, using a value of $f > 0.3$ results in a synthetic spectrum with all the spectral lines in emission. However even with the inclusion of clumping with different filling factors, CMFGEN is unable to reproduce the observed Hα profile, with f = 0.3 overestimating the amount of emission and f = 0.1, 0.2 underestimating it, resulting in an absorption profile (see Fig. 3.17 for the clumped fits to the Hα profile). Again it is evident that lower f_∞ values produces narrower Hα profiles. The effect of clumping on the He II 4686 Å has also been examined for the case of HD 192660 (since it is a B0 Ib star, He II is still present, if weak, and furthermore He II is useful as a secondary mass loss diagnostic, given that the Hα profile is difficult to model in this star). It is in-

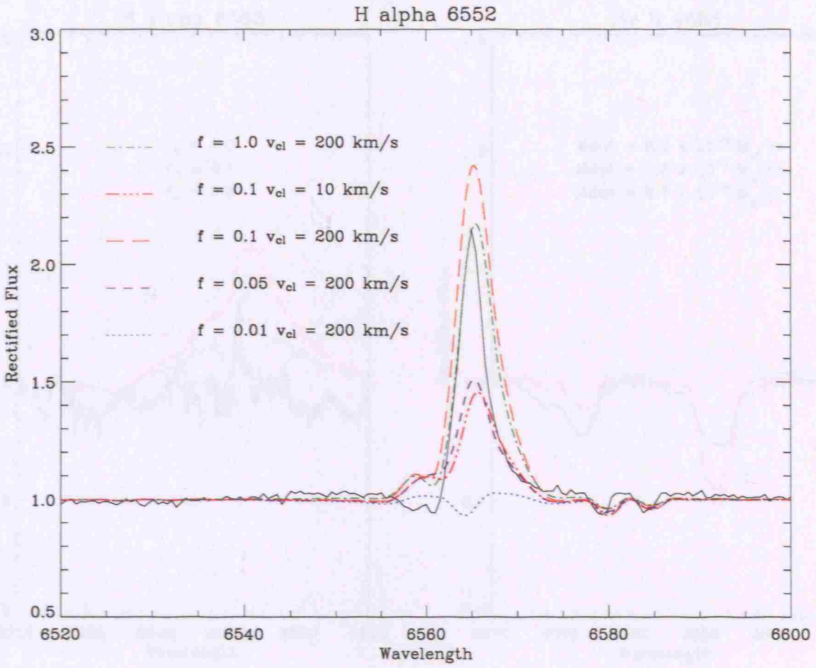

Figure 3.16: CMFGEN Hα profiles computed for the star HD 190603, using different filling factors to simulate varying degrees of clumping. A homogeneous model with no clumping has f = 1.0.

teresting to note that the homogeneous model ($f_\infty = 1.0$) predicts that He II should be in emission when it is observed in absorption; conversely, all three clumped models produce a stronger absorption line than observed.

3.2.6 Derivation of CNO abundances

With improvements in the treatment of metal lines in nLTE stellar atmosphere codes such as CMFGEN or FASTWIND, it is now possible to obtain accurate abundances by fitting (by eye) appropriate diagnostic lines for each element. For nitrogen, we use the N III 4097 Å line for B0 – B2 stars (which is blended with Hδ) and the N II 3995 Å, N II 4447 Å & 4630 Å lines (for all B stars) as primary diagnostics. The main diagnostics for carbon and oxygen are the 4267 Å and 4367 Å lines respectively; however their abundances are confirmed by checking for good fits to O II blends at 4070 Å, 4317 – 4319 Å & 4650 Å, the O II lines at 4590 Å, 4596 Å & 4661 Å and the C II doublet at 6578, 6582 Å. An example of a CMFGEN fit to four of the CNO diagnostic lines of the star κ Cas is shown in Fig.

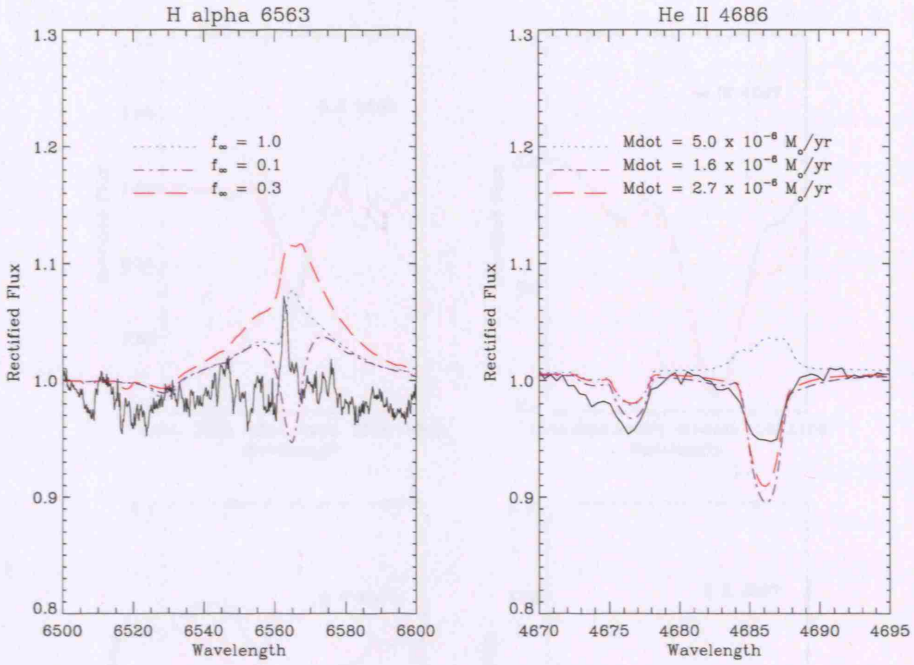

Figure 3.17: Clumped CMFGEN fits to the Hα profile of HD 192660. None of the fits succeed in producing a satisfactory fit to the Hα profile.

3.18. The errors on constraining the CNO abundances using this method were typically $\sim$ 0.1 dex.

3.2.7 Evidence for CNO processing in B supergiants

As previously mentioned, it was Walborn (1976) who first suggested that the nitrogen and carbon anomalies found in OB stars can be explained by their evolutionary status, with OBC stars being the least evolved. It therefore follows that a typical OB supergiant should display some partial CNO processing, in the form of nitrogen enrichment accompanied by CO depletion. Several authors (e.g., Trundle *et al.*, 2004; Trundle & Lennon, 2005; Evans *et al.*, 2004*a*; Venn, 1995) have found N enrichments and CO depletions in OBA stars with respect to solar abundances. All 20 B supergiants in our sample show evidence for partial CNO processing in their spectra. The details of the CNO abundances derived for individual stars are given in Table 3.5. The majority of Galactic B supergiants show a modest nitrogen enrichment, but some stars (HD 37128, HD 192660 and HD 191243) are

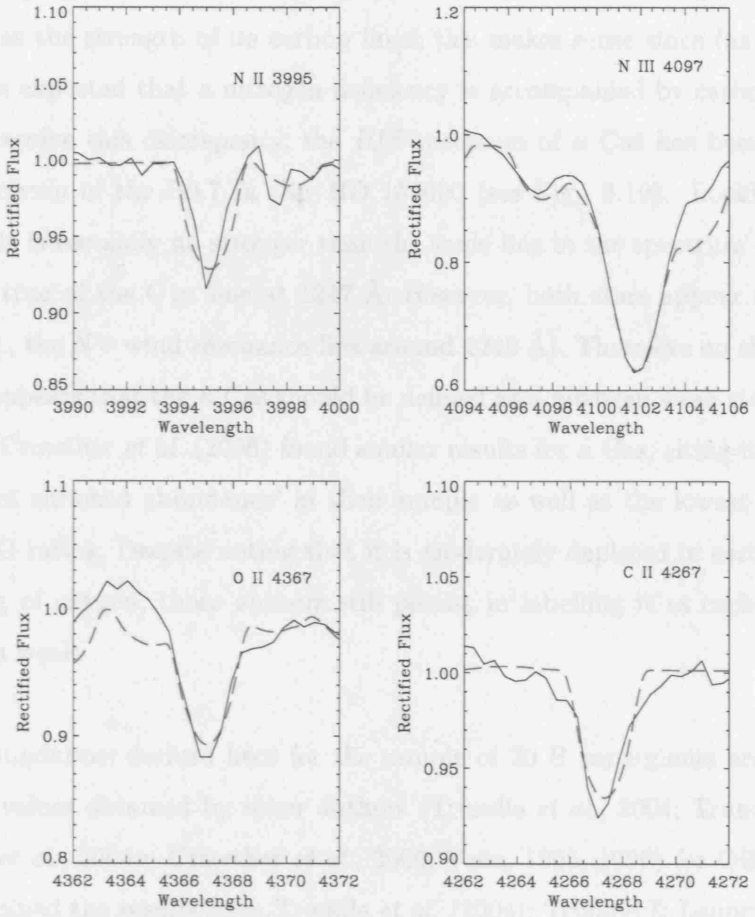

Figure 3.18: CMFGEN fit to the CNO diagnostic lines (N III 4097 Å, N II 3995 Å, C II 4267 Å & O II 4367 Å) of κ Cas

slightly nitrogen deficient. Walborn (1976) observed that Orion belt stars such as HD 37128 (ϵ Ori) are nitrogen deficient due to the weakness of the N III 4097 Å & 4640 Å (blend) spectral lines. The largest nitrogen enhancements are seen for B1 – B2 stars (HD 13854, HD 190603 & HD 14818). It is of interest to note that Walborn (1976) classed HD 13854 as a morphologically normal B supergiant (as well as HD 38771), whereas we have found a modest yet significant N enrichment in this star.

There is still an intriguing contradiction that κ Cas, which has been defined as a carbon-rich star (Walborn, 1976) has very similar CNO abundances to the stars HD 64760, HD 213087 which have not been noted as carbon rich by any other authors. The original cri-

teria for classifying κ Cas as a carbon-rich star were based on the weakness of its nitrogen lines as well as the strength of its carbon lines; this makes sense since (as Walborn 1976 explains) it is expected that a nitrogen deficiency is accompanied by carbon enrichment. In order to resolve this discrepancy, the *IUE* spectrum of κ Cas has been compared to the *IUE* spectrum of the B0.7 Ia star HD 154090 (see Fig. 3.19). Looking at the C II 1324 Å line, it is certainly no stronger than the same line in the spectrum of HD 154090. The same is true of the C III line at 1247 Å. However, both stars appear to be nitrogen weak (see e.g., the N V wind resonance line around 1240 Å). Therefore on the basis of this evidence, it appears that the κ Cas should be defined as a nitrogen weak star, rather than carbon rich. Crowther *et al.* (2006) found similar results for κ Cas, citing it as having the 'least nitrogen enriched abundance' in their sample as well as the lowest values for the N/C and N/O ratios. Despite noting that it is moderately depleted in carbon and shows no processing of oxygen, those authors still persist in labelling it as carbon rich rather than nitrogen weak.

The CNO abundances derived here for the sample of 20 B supergiants are compared in Table 3.6 to values obtained by other authors (Trundle *et al.*, 2004; Trundle & Lennon, 2005; Evans *et al.*, 2004*a*; Crowther *et al.*, 2006; Venn, 1995, 1999) for OBA supergiants . I have combined the results from Trundle *et al.* (2004); Trundle & Lennon (2005) SMC B supergiants to obtain mean CNO abundances based on a sample of 18 stars (but only 13 were used for the mean oxygen abundance since oxygen abundances were not derived for some B2.5-5 stars due to weak, unmeasurable O II lines). The data from Evans *et al.* (2004*a*) were purely based on CNO abundances derived from OB supergiants so that the results for nebular and H II regions included by the authors for comparison were omitted. It is clear from Table 3.6 that more CNO enrichment occurs in stars belonging to the Magellanic Clouds than Galactic stars. This is in accordance with Evans *et al.* (2004*a*), who found that OB supergiants in the LMC display a nitrogen enrichment that is greater than the nitrogen enrichments in Galactic B supergiants. Evans *et al.* (2004*a*) conclude that their sample of Magellanic Cloud stars show significant nitrogen enrichment due to efficient rotational mixing. Fig. 3.20 shows the dependence of nitrogen enhancement with stellar rotation; it is clear from the data there is an increasing spread in nitrogen enrichment, rather than a clear increase in the mean values, with higher v_e sin i. The CNO abundances show no clear trend with effective temperature.

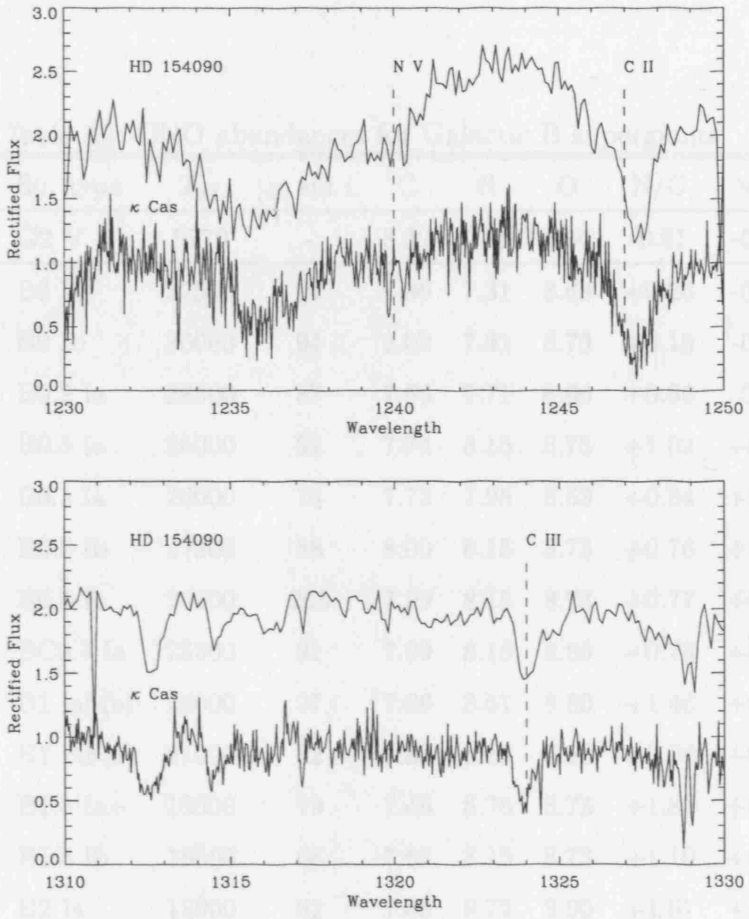

Figure 3.19: Comparison of the relative strengths of the N and C lines in κ Cas and HD 154090

3.2.8 The Wind-Luminosity–Momentum Relation

The concept of a Wind-Luminosity–Momentum Relation (hereafter WLR) was first proposed by Kudritzki *et al.* (1995), using the prediction from the theory of radiatively driven winds that there is a strong dependence of the total mechanical momentum flow $\dot{M}v_\infty$ of the stellar wind on stellar luminosity (e.g., Castor *et al.*, 1975), which can be described as

$$\dot{M}v_\infty \propto R_*^{-\frac{1}{2}} L^{\frac{1}{\alpha_{eff}}} \tag{3.4}$$

The importance of the WLR lies in its potential as an extra-galactic distance indicator

Table 3.5: CNO abundances for Galactic B supergiants

HD no.	Sp. type	$T_{\rm eff}$	$v_e \sin i$	C	N	O	N/C	N/O
SUN	G2 V	5770	-	8.39	7.78	8.66	-0.61	-0.88
37128	B0 Ia	27500	91	7.66	7.31	8.68	+0.26	-0.49
192660	B0 Ib	30000	94	8.02	7.51	8.73	+0.10	-0.40
204172	B0.2 Ia	28500	87	7.66	7.71	8.66	+0.66	-0.07
38771	B0.5 Ia	26000	91	7.74	8.15	8.73	+1.02	+0.30
185859	B0.5 Ia	26000	74	7.72	7.95	8.53	+0.84	+0.30
213087	B0.5 Ib	27000	88	8.00	8.15	8.73	+0.76	+0.30
64760	B0.5 Ib	28000	265	7.99	8.15	8.73	+0.77	+0.30
2905	BC0.7 Ia	23500	91	7.99	8.16	8.80	+0.78	+0.24
13854	B1 Iab(e)	20000	97	7.66	8.51	8.80	+1.46	+0.59
190066	B1 Iab(e)	21000	82	7.88	8.15	8.53	+0.88	+0.50
190603	B1.5 Ia+	19500	79	7.48	8.76	8.73	+1.89	+0.91
193183	B1.5 Ib	18500	68	7.66	8.15	8.73	+1.10	+0.30
14818	B2 Ia	18000	82	7.66	8.72	8.90	+1.67	+0.70
206165	B2 Ib	18000	73	7.96	8.15	8.43	+0.80	+0.60
198478	B2.5 Ia	17500	61	7.86	8.29	8.45	+1.04	+0.72
42087	B2.5 Ib	18000	71	7.76	8.11	8.80	+0.96	+0.19
53138	B3 Ia	16500	58	7.78	8.32	8.60	+1.15	+0.60
58350	B5 Ia	15000	50	7.78	8.29	8.75	+1.12	+0.42
164353	B5 Ib/II	15500	44	7.78	7.89	8.53	+0.72	+0.24
191243	B5 Ib/II	14500	38	7.70	7.65	-	+0.56	-

Derived CNO abundances for the sample of Galactic B supergiants (expressed as $\log\left(\frac{N_x}{N_H}\right)+12$). The amount of nitrogen enrichment relative to carbon and oxygen respectively is given in the last two columns, calculated as $\log\left(\frac{N_x}{N_H}\right)_* - \log\left(\frac{N_x}{N_H}\right)_\odot$ - $\log\left(\frac{N_y}{N_H}\right)_* - \log\left(\frac{N_y}{N_H}\right)_\odot$.

Table 3.6: Comparison of mean CNO abundances for OBA supergiants.

Author	Stellar group	C	N	0	N/C	N/0
This work	Gal BSGs	7.79	8.12	8.68	+0.57	+0.26
Crowther(2006)	Gal BSGs	7.87	8.33	8.47	+0.68	+0.59
Trundle(2004-5)	SMC BSGs	7.27	7.71	8.13	+1.38	1.04
Evans(2004)	LMC OBSG	7.49	8.55	8.02	+1.28	+1.26
Evans(2004)	SMC OBSG	7.30	7.94	8.01	+0.86	+0.66
Venn(1995)	Gal ASGs	8.14	8.05	-	+0.13	-
Venn(1999)	SMC ASGs	-	7.33	8.14	-	-0.08

Mean CNO abundances, N/C & N/O enhancements obtained in this work are compared with those of Magellanic Cloud B supergiants (Trundle *et al.*, 2004; Trundle & Lennon, 2005; Evans *et al.*, 2004*a*) and Galactic and SMC A supergiants (Venn, 1995, 1999). CNO abundances, N/C & N/O defined as stated for Table 3.5

provided that it is reliably calibrated. Once the mass loss rate, terminal velocity and stellar luminosity have been determined from stellar spectra, a properly calibrated WLR can be used to determine the distance to the star's host galaxy. The WLR can also be used to estimate stellar wind energy and momentum input using the proportionality of the ratio $\frac{v_\infty}{v_{esc}}$ as well as mass loss rates, which is useful for stellar evolutionary tracks. The proportionality shown in Equation 3.4 was first confirmed observationally by Puls *et al.* (1996) for a sample of Galactic and Magellanic Cloud O stars with $5.5 \leq \log L_* \leq 6.5$. For $\log L_* < 5.5$, a linear fit was not possible, demonstrating the dependence of the WLR on spectral type. Kudritzki *et al.* (1999) then showed that a linear fit to the WLR was also possible for galactic BA supergiants. Since then many authors (Repolust *et al.*, 2004; Markova *et al.*, 2004; Massey *et al.*, 2004; Massey *et al.*, 2005; Trundle *et al.*, 2004; Trundle & Lennon, 2005) have published values for wind momenta when deriving fundamental parameters for sets of OBA stars using

$$D_{mom} = \dot{M} v_\infty R_*^{0.5} \tag{3.5}$$

where R_* is in solar radii, $\dot{M}$ in g/s and v_∞ in cm/s to give D_{mom} in units of cgs. Assuming a WLR with the form

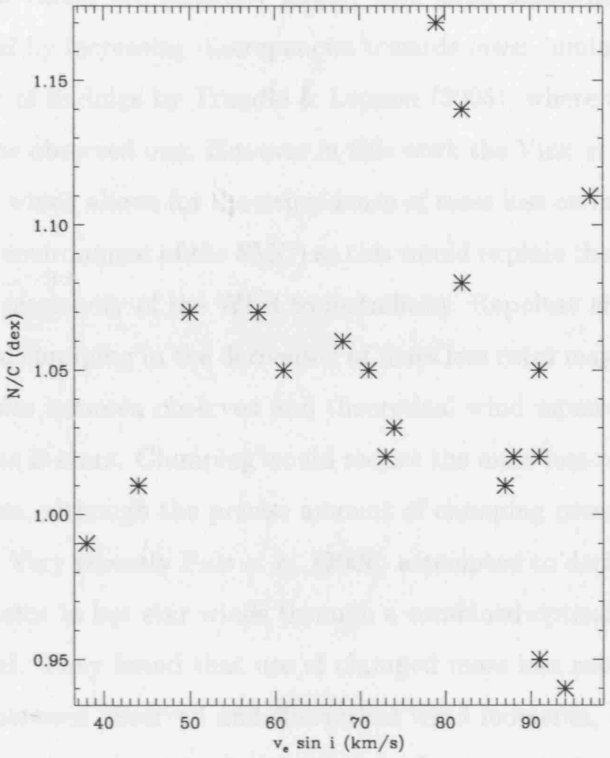

Figure 3.20: Dependence of N/C abundances on v_e sin i for the sample of 20 Galactic B supergiants.

$$logD_{mom} = logD_0 + x \log (L/L_\odot) \tag{3.6}$$

a linear regression can be used to constrain the coefficients x and $logD_0$. The reciprocal of x can be thought of as the *effective exponent* α_{eff} (see Equation 3.4). Applying a linear regression to our data gives $logD_0 = 20.3$ and $x = 1.51$. Looking at Fig. 3.21, it can be seen that the hotter spectral types i.e. O stars have a steeper WLR than cooler B spectral types. This is to be expected if, as proposed by Vink *et al.* (1999), Fe II & Fe III lines are responsible for driving the subsonic part of the wind, corresponding to lower ionisation stages. Fig. 3.21 also illustrates the effect of metallicity on the WLR, with the more metal poor environment of the Magellanic Cloud hosting stars with lower values of D_{mom}. This effect is particularly noticeable between Galactic and SMC B supergiants. Our values of D_{mom} are compared to those predicted by the theoretical WLR prescription of Vink *et al.* (2000), using the parameters derived for our sample of stars in this chapter. It is found

that the theoretical values are generally larger, with good agreement found for early B supergiants followed by increasing discrepancies towards lower luminosities. Interestingly this is the opposite of findings by Trundle & Lennon (2005), where the theoretical WLR was smaller than the observed one. However in this work the Vink *et al.* (2001) WLR prescription was used, which allows for the dependence of mass loss on metallicity (crucial for the low metallicity environment of the SMC) so this would explain the difference, as well as demonstrating the sensitivity of the WLR to metallicity. Repolust *et al.* (2004) suggested that the inclusion of clumping in the derivation of mass loss rates may help to alleviate the existing discrepancies between observed and theoretical wind momenta, which also exist for O stars as well as B stars. Clumping would reduce the mass loss rate and consequently lower wind momenta, although the precise amount of clumping present in OB star winds remains uncertain. Very recently Puls *et al.* (2006) attempted to derive better constraints on the clumping factor in hot star winds through a combined optical, infra-red and radio analysis of the wind. They found that use of clumped mass loss rates did produce much better agreement between observed and theoretical wind momenta, since for O stars the observed wind momenta were originally higher than the theoretical ones, but the inclusion of clumping reduced the value of $\dot{M}$ and consequently D_{mom}. Unfortunately, for the case of Galactic B supergiants it is the theoretical D_{mom} values that are higher, so the use of lower, clumped $\dot{M}$ would not resolve the discrepancy. This may indicate a fundamental difference between the structure and inhomogeneity of O and B star winds. At present, it is not possible to obtain a reliable calibration of the WLR, until the problems associated with its dependence on luminosity and metallicity, as well as the effect of clumping on observed mass loss rates, are resolved.

3.3 Chapter 3 summary

In this chapter the sample of 20 Galactic B supergiants has been introduced with a revised B supergiant $T_{\rm eff}$ scale (derived using a stellar atmosphere code that includes the effects of line blanketing) giving a range of $14.5kK \leq T_{\rm eff} \leq 30kK$ for these stars. This scale shows a drop of up to 10kK from B0 Ia/b to B1 Iab and a difference of up to 2000 K between Ia and Ib stars. Very good agreement is generally found between our $T_{\rm eff}$ scale and other unblanketed or Magellanic Cloud B supergiant $T_{\rm eff}$ scales, except around B1 where other

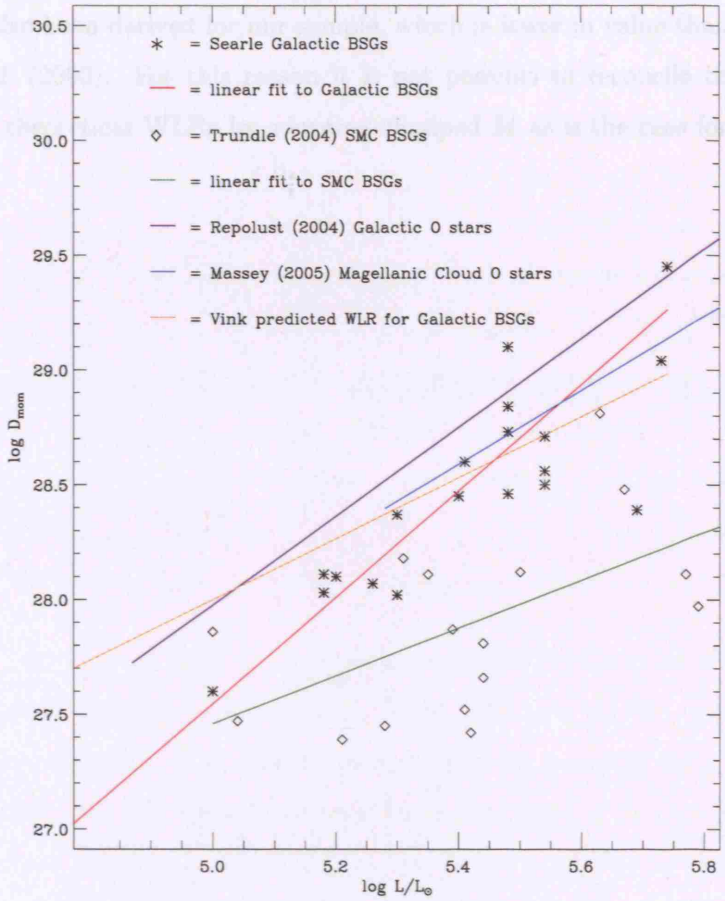

Figure 3.21: The Wind-Luminosity Momentum Relation for OBA stars. Note the dependence of the WLR on spectral type and metallicity. The theoretical WLR predicted by Vink *et al.* (2000) is calculated for our sample of Galactic B supergiants and is represented by the orange line.

scales tend to be 2000 – 3000 K hotter. The 20 Galactic B supergiants also displayed a range of $2.1 \leq \log g \leq 3.4$ in surface gravity. Mass loss rates derived from Hα proved B supergiant winds to be generally weaker than those of O supergiants (as expected since they are lower-luminosity objects) with $\dot{M}$ ranging from $-7.22 \leq \log \dot{M} \leq -5.30$. These values are in very good agreement with those of Kudritzki *et al.* (1999) and those predicted by Vink *et al.* (2000). The inclusion of clumping can have a significant effect on the model Hα profiles, but has not proved to be a solution in fitting Hα profiles with complex morphologies. All 20 B supergiants also shown signs of CNO processing, with the largest nitrogen

enrichments being seen for B1-B2 supergiants. Finally a Wind-Momentum–Luminosity relation has also been derived for our sample, which is lower in value than that predicted by Vink *et al.* (2000). For this reason it is not possible to reconcile this difference in observed and theoretical WLRs by adopting clumped $\dot{M}$ as is the case for O stars.

CHAPTER 4

Extending stellar atmosphere models to the UV

This chapter describes the work undertaken in using CMFGEN to model the ultraviolet (UV) spectrum of Galactic B supergiants. Although many studies choose to focus on deriving stellar parameters from optical spectra only, the potential for a unique UV $T_{\rm eff}$ scale is discussed. All OB supergiants emit large quantities of flux at UV wavelengths, so it is important to discern if UV spectra imply the same $T_{\rm eff}$ as that implied from analysing optical spectra for any given star. Additionally if a CMFGEN model can successfully reproduce the observed optical spectrum of an OB supergiant, reproducing the observed UV spectrum of the star provides a significant test of the reliability of the stellar atmosphere model. Suitable methods and diagnostic lines for deriving $T_{\rm eff}$ from the UV are discussed in the opening sections. Details of the comparison between optical and UV modelling with CMFGEN are then presented and finally the effects of the inclusion of clumping on the P Cygni profiles in the models are investigated.

4.1 Deriving $T_{\rm eff}$ from UV spectra

The IUE spectra of B supergiants display a range of elements at various ionisation stages. The most prominent spectral features are the wind resonance lines: N V $\lambda\lambda$ 1238.82, 1242.80; C IV $\lambda\lambda$ 1548.20, 1550.77; Si IV $\lambda\lambda$ 1393.76, 1402.77; Si III $\lambda\lambda$ 1206.50; C II $\lambda\lambda$ 1334.53, 1335.71 & Al III $\lambda\lambda$ 1854.72, 1862.79, which are sensitive to changes in $T_{\rm eff}$, luminosity, mass loss and elemental abundance. These lines do not make ideal $T_{\rm eff}$ diagnostics

since they are not solely dependent on $T_{\rm eff}$; in particular individual carbon and nitrogen abundances need to be derived for each star as these elements are affected by nuclear processing. The situation is complicated by the fact that C IV and often Si IV are saturated so varying these parameters no longer results in any discernible change to the line profile. The dependence of Si IV on luminosity is clearly demonstrated by the fact that it is more saturated in B Ia stars than B Ibs. It is also possible to constrain the velocity law (i.e. v_∞ & β) from the C IV profile when it is saturated, else Si IV can be used. However it would be of greater use to find purely photospheric lines (rather than wind resonance lines) to use as $T_{\rm eff}$ diagnostics, for which abundances are well known and knowledge of the velocity law and mass loss rate are not required. Potentially the dependence of the line strength of these photospheric lines on $T_{\rm eff}$ could be investigated, with a view to constructing an empirical UV $T_{\rm eff}$ scale if a strong dependence is found. It would then be possible to obtain a value of $T_{\rm eff}$ for a star *solely* from the UV by measuring the line strength of a photospheric line and using an empirical UV $T_{\rm eff}$ calibration to translate the line strength into a temperature. This is a much quicker and more efficient method for determining $T_{\rm eff}$ from the UV spectrum of a star in comparison with the more complex approach of using a code such as CMFGEN to model the star's UV spectrum. We examine therefore whether an empirical UV $T_{\rm eff}$ scale can be derived for the sample of 20 Galactic B supergiants. Individual values of $T_{\rm eff}$ (from CMFGEN) were derived for each star in §3.2.2, so line strength measurements of UV photospheric lines made for each of the 20 B supergiants can then be assigned the same value of $T_{\rm eff}$. These data can then be used to obtain a more general expression for the dependence of a particular UV photospheric line on $T_{\rm eff}$, from which a calibration for an empirical UV $T_{\rm eff}$ scale could be obtained.

Massa (1989) investigated the potential of photospheric silicon lines as indicators of $T_{\rm eff}$ in detail, finding several potentially useful lines that were sensitive to $T_{\rm eff}$ and luminosity. The study focused on Si II and Si III lines in B0.5 - B5 stars (over a range of luminosity classes), since Si II is too weak in early B stars and Si III suffers from too many blends at spectral types later than B5. Silicon lines are the ideal candidates for such a study because their abundance is unaffected by nuclear processing. Five silicon lines were selected for equivalent width measurements [W_λ]: Si II λ 1265, Si III λ 1294, Si III λ 1299, Si II λ 1309 and Si III λ 1417. The dependence of W_λ for each silicon line on spectral type, on the other silicon lines under consideration and the Balmer jump index [c_1] and Hβ index was

examined (Massa, 1989). The latter two parameters are useful to probe the sensitivity of W_λ[Si II] and W_λ[Si III] to stellar parameters since $[c_1]$ is sensitive to changes in $T_{\rm eff}$ (especially near the main sequence) but independent of surface gravity effects, whereas the reverse is true of Hβ. However, this independence between $T_{\rm eff}$ and gravity effects is lost at higher luminosities, with $[c_1]$ becoming sensitive to changes in both $T_{\rm eff}$ and log g. It is found that the lines Si II λ 1309 and Si III λ 1294 display very similar behaviour to Si II λ 1265 and Si III λ 1299 respectively. To summarise, Massa (1989) cite the line ratio of Si II λ1265/Si III λ1299 for determining $T_{\rm eff}$ from UV spectra, whereas the ratio Si III λ1417/Si III λ1299 is a useful luminosity diagnostic.

For our investigation, we decided to concentrate on the ratio of Si II λ1265/Si III λ1299. Measurements of W_λ for both lines were made for each star from the sample of 20 Galactic B supergiants presented in Chapter 3, in order to see if the trends found by Massa (1989) could be reproduced. Since we have already obtained *individual* $T_{\rm eff}$ for each of the 20 B supergiants using nLTE, fully line-blanketed code, the values of W_λ [Si II λ1265] and W_λ [Si III λ1299] measured for each star can be attributed to an individual $T_{\rm eff}$, producing an accurate UV $T_{\rm eff}$ scale. If these silicon lines provide a clear trend with $T_{\rm eff}$, a prescription describing the dependence of W_λ [Si II λ1265]/ [Si III λ1299] on $T_{\rm eff}$ can be constructed using a least squares fit routine. The purpose of this empirical equation is to make it possible to derive a value of $T_{\rm eff}$ purely from UV (IUE) spectra, simply by measuring the value of W_λ for Si II λ1265 and Si III λ1299 and using the derived relation to find the corresponding $T_{\rm eff}$. This would remove the need to obtain optical spectra from which to derive stellar parameters when carrying out a study that only involves UV spectra and would be of great use for this purpose.

However several problems were encountered when we tried to undertake this investigation. First of all, it is difficult to determine precisely where the continuum lies in UV spectra due to the effects of line blanketing. The IUE spectra had been carefully rectified, but it is necessary to be consistent in deciding where to make the measurement of W_λ i.e. where the wings of the line profile meet the continuum. Fig. 4.1 gives an example of where W_λ measurements would be made for Si III λ1299 and Si II λ1309 in the *IUE* spectrum of HD 14818, assuming the continuum lies at a flux level of 1.0. Given the difficulty in determining precisely where the continuum lies, the best approach is to assume it lies

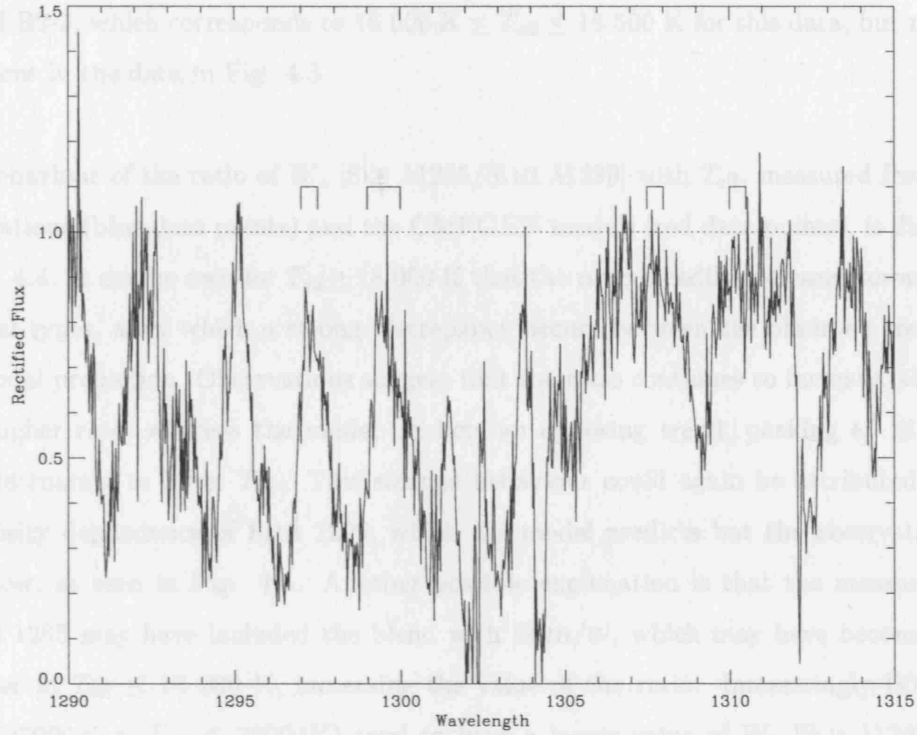

Figure 4.1: Example of measuring W_λ of Si III λ1299 & Si II λ1309 from the *IUE* spectrum of HD 14818 (B2 Ia). Square brackets denote region where W_λ measurement would be made. Continuum is assumed to lie at flux level of 1.0, as marked by the dotted line.

at a given flux and consistently make W_λ measurements from this point. Si II λ1265 is very weak for B0 supergiants and suffers from some blending with Fe III/IV, whereas Si III λ1299 is a triplet line with 3 very strong components again complicated by blends with Fe III/IV. The trend of Si II λ1265 with $T_{\rm eff}$ is shown in Fig. 4.2, which increases towards later spectral types. The data cannot be fitted linearly since the values of W_λ for $T_{\rm eff}$ $\leq$ 20 000 K imply a much steeper gradient than the data above 20 000 K. Additionally the data are quite scattered, particularly around 18 000 K where Δ W_λ = 400, with no consistent difference in the behaviour between B Ia & B Ib stars. This makes it difficult to fit a curve to the data whose equation can be used for an empirical $T_{\rm eff}$ scale, since the scattered nature of the data will introduce errors $\geq$ 2000 K in $T_{\rm eff}$. No clear trend was found for W_λ Si III λ1299 in Fig. 4.3, where the data is even more scattered, partly due to

the luminosity dependence of this line. Massa (1989) found that W_λ Si III λ1299 peaked around B2-3, which corresponds to 18 000 K $\leq T_{\rm eff} \leq$ 16 500 K for this data, but no peak is evident in the data in Fig. 4.3.

The behaviour of the ratio of W_λ [Si II λ1265/Si III λ1299] with $T_{\rm eff}$, measured from both observations (blue data points) and the CMFGEN models (red data points), is displayed in Fig. 4.4. It can be seen for $T_{\rm eff} \geq$ 18 000 K that the ratio steadily increases toward later spectral types, after which a strong discrepancy occurs between the observed trend and the model prediction. Observations suggest that the ratio continues to increase, although at a higher rate, whereas the model predicts an opposing trend, peaking at 18 000 K then decreasing to lower $T_{\rm eff}$. This strange behaviour could again be attributed to the luminosity dependence of Si III 1299, which the model predicts but the observations do not show, as seen in Fig. 4.3. Another possible explanation is that the measurements of Si II 1265 may have included the blend with Fe III/IV, which may have become much stronger at $T_{\rm eff} \leq$ 18 000 K, increasing the value of the ratio. Interestingly B0–0.5 Ib stars ($27000K \leq T_{\rm eff} \leq 30000K$) tend to have a larger value of W_λ [Si II λ1265]/Si III λ1299] than B0-0.5 Ia stars, but this is probably due to inaccuracies in measuring the Si II λ1265 line at high $T_{\rm eff}$ where it is quite weak. Due to the somewhat complex nature of these silicon lines and their behaviour with $T_{\rm eff}$, it is difficult to construct a reliable UV empirical $T_{\rm eff}$ calibration from the data. More data points would be required, especially above $T_{\rm eff}$ = 20 000 K in order to achieve a high quality fit to the data and obtain an equation for determining $T_{\rm eff}$ for a given value of W_λ.

4.1.1 Testing the UV predictions of CMFGEN

The next step of our investigation was to examine if the 'best fit' CMFGEN models used in Chapter 3 would also provide a good fit to the UV silicon lines, thus confirming that $T_{\rm eff}$ diagnostics at both optical and UV wavelengths implied the same value of $T_{\rm eff}$ for each star. Unfortunately this was not the case, since CMFGEN was unable to accurately reproduce any of the five previously mentioned Si II & Si III diagnostic lines. This explains the discrepancy encountered between empirical and model measurements of W_λ [Si II λ1265]/Si III λ1299], as illustrated in Fig. 4.4. An example of a CMFGEN comparison to these lines is given in Fig. 4.5 for the B2 Ia star HD 14818 and the corresponding final CMFGEN

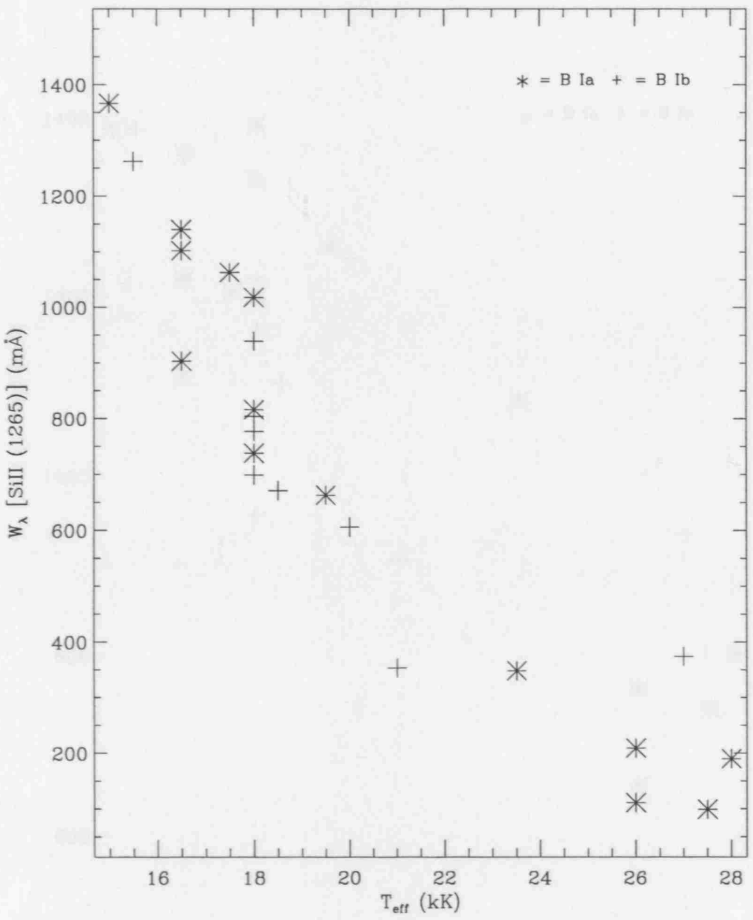

Figure 4.2: Dependence of W_λ (Si II λ1265) on $T_{\rm eff}$. W_λ is measured in m Å, B Ia stars are denoted by an asterick whereas B Ib stars are marked with a plus sign.

model with $T_{\rm eff}$ = 18 000 K, L = 2.5 $\times 10^5$ $L/L_\odot$ and $\dot{M} = 1.1 \times 10^{-6}$ $M_\odot$ yr^{-1}. Two other models with $T_{\rm eff}$ = 17 500 K, L = 2.4 $\times 10^5$ $L/L_\odot$, $\dot{M} = 1.2 \times 10^{-6}$ $M_\odot$ yr^{-1} and $T_{\rm eff}$ = 18 500 K, L = 2.5 $\times 10^5$ $L/L_\odot$, $\dot{M} = 1.8 \times 10^{-6}$ $M_\odot$ yr^{-1} respectively are also shown to demonstrate the effects of changing $T_{\rm eff}$ on these lines. A direct comparison of the observed and model Si II λ1265 line profiles is difficult since the continuum is raised about this line, but it is apparent that the model produces an asymmetric profile (whereas the observed profile is symmetric) shifted by about 1 Å blue-ward relative to the observed line profile centre. The model profile is also much broader than the observed profile and varying $T_{\rm eff}$ by $\pm$ 500 K has no significant effect on this line. In the case of Si II λ1309, the model line profile is more narrow and shallow than the observed one. Changes in $T_{\rm eff}$ are

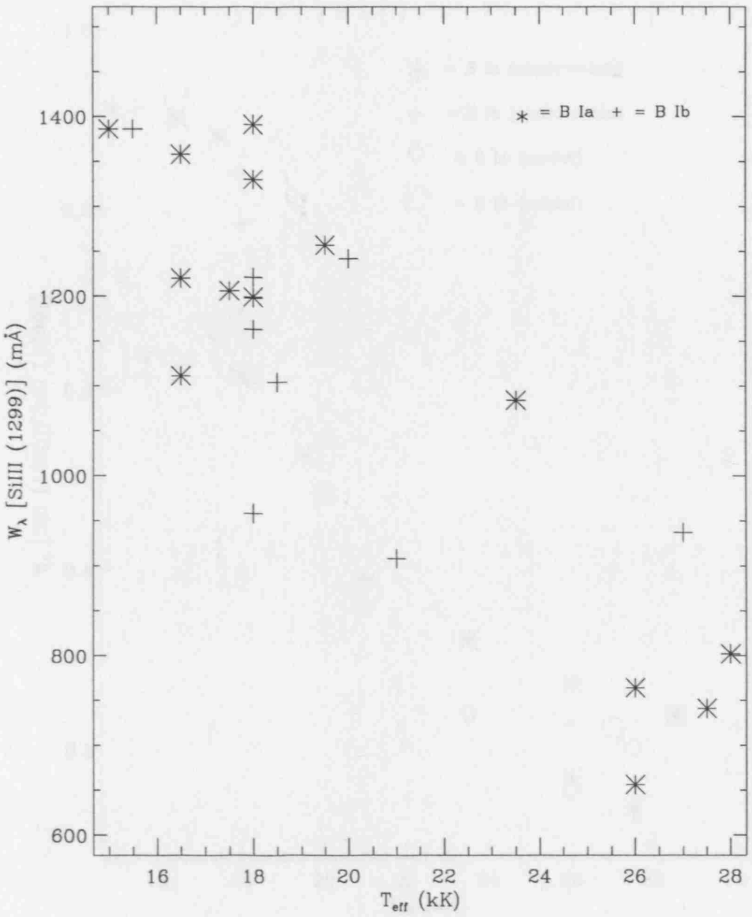

Figure 4.3: Dependence of W_λ (Si III λ1299) on $T_{\rm eff}$. W_λ is measured in mÅ, B Ia stars are denoted by an asterick whereas B Ib stars are marked with a plus sign.

more apparent on this line, though still make no significant improvement to the overall line fit. For Si III λ1294 & λ1299, the model line profiles are again asymmetric, unlike the observed profiles and the blue wings of these lines are overestimated whilst the absorption troughs are underestimated. The model profile of Si III λ1417 is both asymmetric and wider than observed, again with a slight overestimation of the blue wing accompanied by a small underestimation of the absorption trough (but these effects are not as drastic as those seen for Si III λ1294 & λ1299). In fact, all three observed Si III lines appear to show some evidence of broadening due to the stellar wind despite being photospheric, which is also evident in the model profiles in the form of asymmetry. Additionally change in $T_{\rm eff}$ appears to have no affect on these lines; however the higher value of $\dot{M}$ for the $T_{\rm eff}$

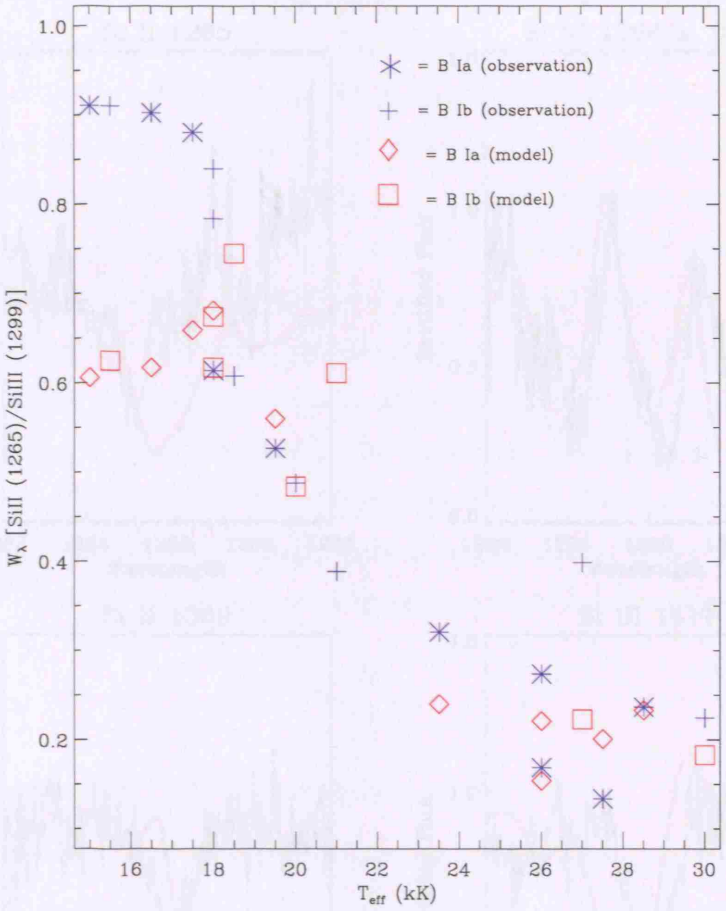

Figure 4.4: Dependence of the ratio W_λ (Si II λ1265/Si III λ1299) on $T_{\rm eff}$. Observational W_λ are marked in blue whilst values of W_λ measured from CMFGEN models are shown in red.

= 18 500 K model (blue line) produces a deeper absorption trough for the profile. To conclude, varying $T_{\rm eff}$ and even $\dot{M}$ has a small affect on these lines, but will not succeed in reproducing the observed lines accurately, with the correct broadness and symmetry

4.2 The optical/UV discrepancy in wind lines

In the previous section, the potential for finding diagnostic lines from which to derive $T_{\rm eff}$ was investigated and it was examined whether the CMFGEN models derived from the optical could also fit UV $T_{\rm eff}$ sensitive lines. A large number of UV lines are also strongly

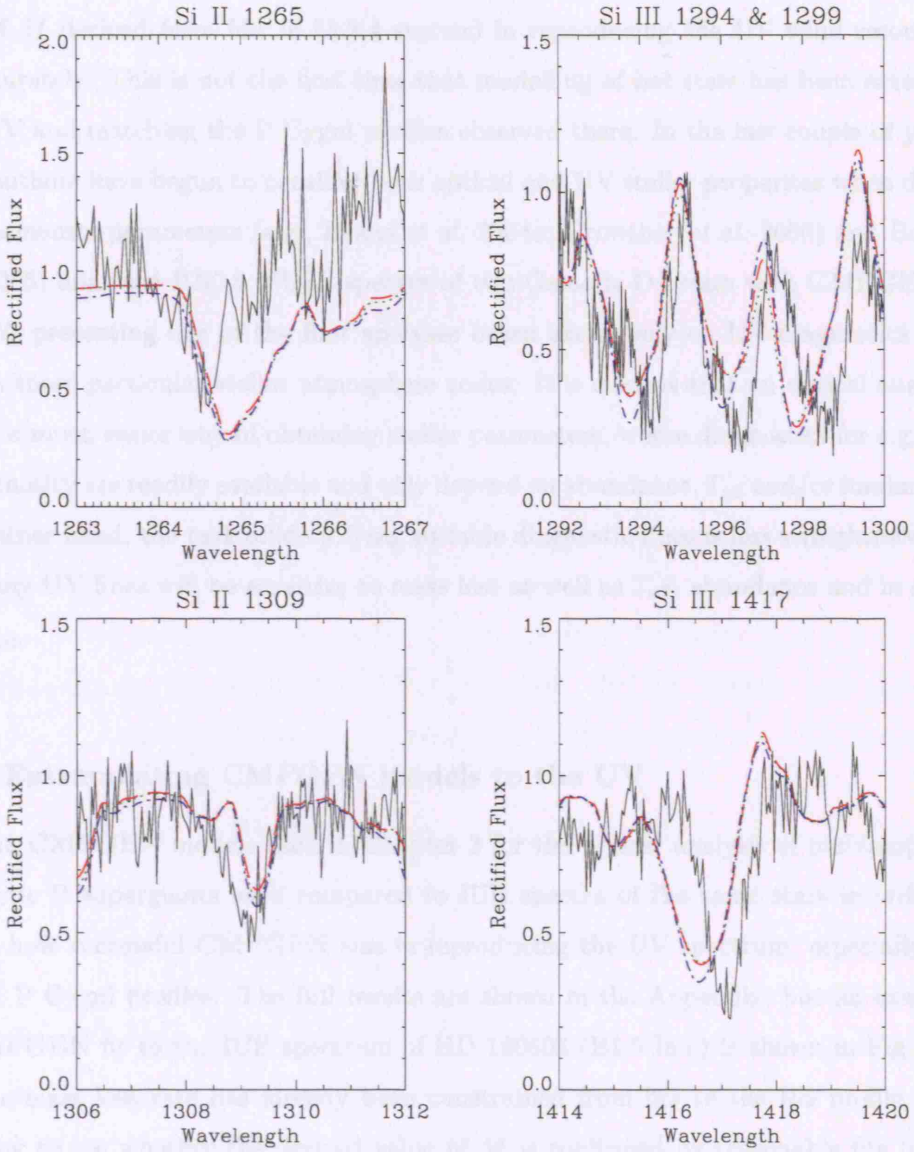

Figure 4.5: CMFGEN model fit to the *IUE* spectrum of HD 14818 (B2 Ia), focusing on the UV silicon $T_{\rm eff}$ diagnostics: Si II λ1265 & λ1309, Si III λ1294, λ1299 & λ1417. The 'best fit' model derived from the optical has $T_{\rm eff}$ = 18 000 K, L = 2.5 $\times 10^5$ $L/L_\odot$ and $\dot{M} = 1.1 \times 10^{-6}$ $M_\odot$ yr^{-1} (dashed red line). Others models have $T_{\rm eff}$ = 17 500 K, L = 2.4 $\times 10^5$ $L/L_\odot$, $\dot{M} = 1.2 \times 10^{-6}$ $M_\odot$ yr^{-1} (dotted green line) and $T_{\rm eff}$ = 18 500 K, L = 2.5 $\times 10^5$ $L/L_\odot$, $\dot{M} = 1.8 \times 10^{-6}$ $M_\odot$ yr^{-1} (dot-dashed blue line).

affected by mass loss from the wind, so it is also of interest to investigate whether the values of $\dot{M}$ derived from Hα in §3.2.4 succeed in reproducing the UV wind resonance lines accurately. This is not the first time that modelling of hot stars has been extended to the UV and matching the P Cygni profiles observed there. In the last couple of years, several authors have begun to consider both optical and UV stellar properites when deriving fundamental parameters (e.g., Evans *et al.* 2004*a*; Crowther *et al.* 2006) and Bouret *et al.* (2005) analysed IUE & FUSE spectra of two Galactic O4 stars with CMFGEN & TLUSTY, presenting one of the first analyses based exclusively on UV diagnostics that also uses these particular stellar atmosphere codes. It is evident that an optical analysis provides a much easier way of obtaining stellar parameters, where diagnostics for e.g. $T_{\rm eff}$ and luminosity are readily available and only depend on abundance, $T_{\rm eff}$ and/or luminosity. On the other hand, the task of identifying suitable diagnostic lines is less straightforward, since many UV lines will be sensitive to mass loss as well as $T_{\rm eff}$, abundance and in some cases $v_{\rm turb}$.

4.2.1 Extrapolating CMFGEN models to the UV

The same CMFGEN models used in Chapter 3 for the optical analysis of our sample of 20 Galactic B supergiants were compared to IUE spectra of the same stars in order to examine how successful CMFGEN was in reproducing the UV spectrum, especially the observed P Cygni profiles. The full results are shown in the Appendix, but an example of a CMFGEN fit to the IUE spectrum of HD 190603 (B1.5 Ia+) is shown in Fig. 4.6. Since the mass loss rate has already been constrained from fits to the Hα profile, it is interesting to see whether the derived value of $\dot{M}$ is confirmed by reasonable fits to the UV P Cygni profiles. It has been shown in Chapter 3 that the values of $\dot{M}_{\rm H\alpha}$ derived using CMFGEN are in very good agreement with those predicted by Vink *et al.* (2000) and those obtained by Kudritzki *et al.* (1999), so it is reasonable to believe that these values of $\dot{M}$ may produce a model UV spectrum that at least reasonably matches the observed wind diagnostics. Looking at the case of HD 190603 shown in Fig. 4.6, the fit to the observed Hα profile is good. However, it is clear that CMFGEN does not reproduce any of the observed P Cygni profiles accurately, implying that a different value of $\dot{M}$ would be appropriate for the UV. The model fails to produce sufficient high velocity absorption in the UV wind resonance lines, to the extent that the predicted C IV $\lambda\lambda$ 1548.2, 1550.8

line is only present as a photospheric line with no evidence of wind contamination. N V is not seen as a P Cygni profile in this star, but the model does not even produce a distinct, weak photospheric line at 1238 Å. However, better fits are achieved at lower ionisation: C II $\lambda\lambda$ 1335.66, 1335.71; Si IV $\lambda\lambda$ 1393.8, 1402.8 & Al III $\lambda\lambda$ 1854.7, 1862.8. The observed C II $\lambda\lambda$ 1335.66, 1335.71 line is saturated but the model produces an unsaturated line, which suggests that a model with a higher value of $\dot{M}$ is required. Adopting a higher value for $\dot{M}$ though would worsen the effect of the model overestimating the red wings of the Si IV $\lambda\lambda$ 1393.8, 1402.8 doublet. It would have a more positive effect on the Al III $\lambda\lambda$ 1854.7, 1862.8 line, since the observed blueward doublet is beginning to saturate but the model blueward doublet is clearly unsaturated, again supporting a higher mass loss rate. The CMFGEN fit to Hα would worsen if a higher value of $\dot{M}$ was adopted, illustrating the discrepancy between the mass loss rates implied from the optical and UV. It is also noticeable when comparing the observed and model Si IV P Cygni profiles that the model doublet components are narrower than observed. Like C IV, this is due to the model predicting to little absorption at high velocities. For HD 190603, these problems arise in spite of the fact that the value adopted for $\dot{M}$ provides a good fit to the Hα profile.

An example of a better CMFGEN fit to the UV wind resonance lines is given in Fig. 4.7 for the B2 Ia star HD 14818. The observed Hα profile displays a P Cygni profile, which has not been successfully reproduced by the model (as discussed in §3.2.4). Despite this, very good fits have been obtained to Si IV and Al III in comparison to those obtained for HD 190603, though again a lack of high velocity absorption causes the model to under-estimate the broadness of the absorption trough for Si IV. However, the same failure occurs in reproducing the P Cygni profile of C IV line, whilst N V shows no evidence of wind contamination. The fit to C II is reasonable, although the model predicts too much redward emission and as a result does not match the redward side of the absorption trough. Conversely an example of a worse fit than either of the previous cases is shown in Fig. 4.8 for HD 53138 (B3 Ia). Its observed Hα profile is in absorption but shows a small amount of red-ward emission and is reasonably well matched by CMFGEN. On the other hand, the UV P Cygni profiles are in general poorly matched by the model, with none of the five wind line profiles being well reproduced. The same problems seen for HD 190603 & HD 14818 in matching N V, C IV and Si IV are also seen here. The red-ward emission in C II is grossly over-estimated and the model produces an asymmetric Al III

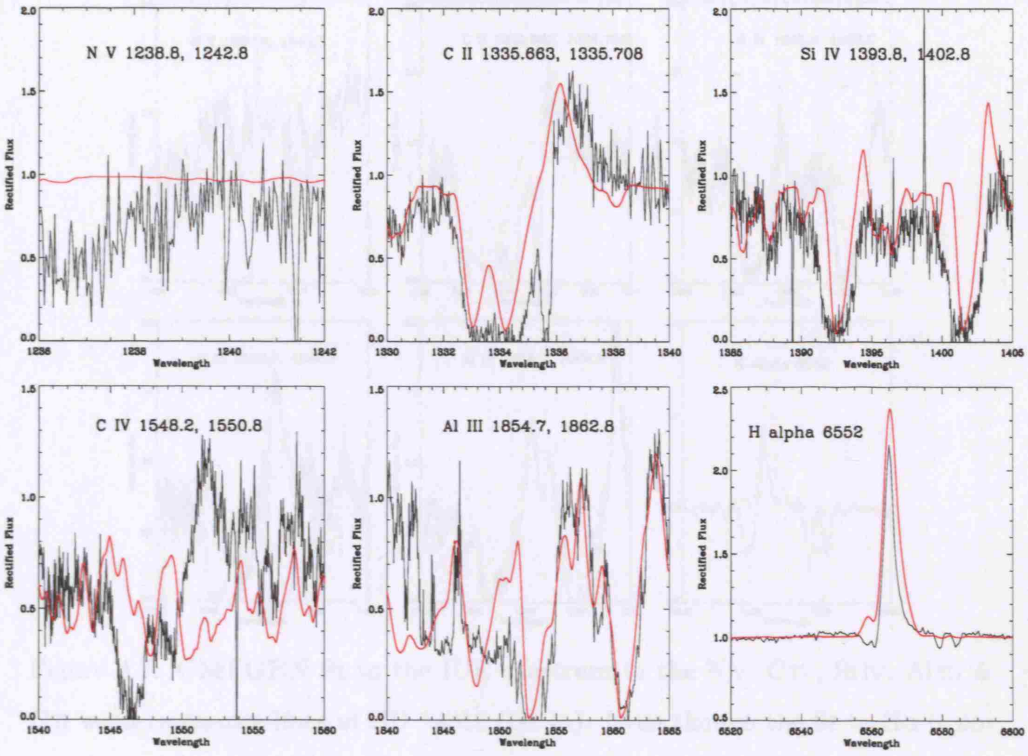

Figure 4.6: CMFGEN fit to the IUE spectrum to the N V, C IV, Si IV, Al III & C II wind resonance lines of HD 190603 (B1.5 Ia+). Note that a good fit to Hα does not guarantee the same mass loss rate will provide a good fit to the UV P Cygni profiles. Model parameters are $T_{\rm eff}$ = 19 500 K, log $(L/L_{\odot})$ = 5.41 & $\dot{M}$ = 2.4 $\times 10^{-6}$ $M_{\odot}$.

profile that is not observed. In both cases the model predicts saturated lines when the observed profiles are not saturated (though C II is beginning to saturate a little). The high velocity absorption in Al III is over-estimated to the extent that it predicts saturation to occur at a higher velocity than observed. It is therefore clear from Fig. 4.6, Fig. 4.7 & Fig. 4.8 that a discrepancy exists between the value of $\dot{M}$ required to fit the Hα and UV wind resonance lines (hereafter referred to as the *optical/UV discrepancy*).

As mentioned in Chapter 3, values of v_{∞} were obtained from SEI modelling of C IV $\lambda\lambda$ 1548.2, 1550.8 (the wind resonance line that is the most sensitive to the velocity law) and the adopted values are shown in Table 3.4 of Chapter 3. It was not possible to independently confirm these values through CMFGEN modelling, since the code cannot

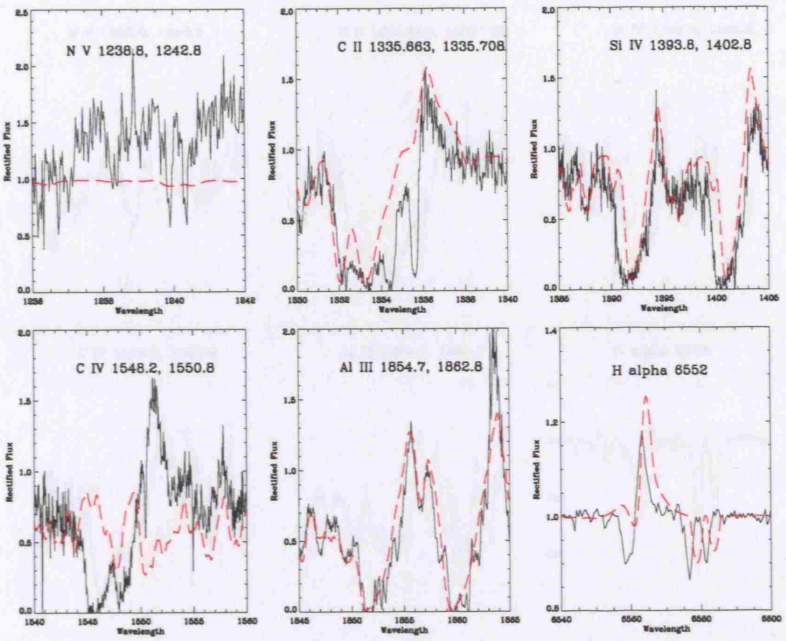

Figure 4.7: CMFGEN fit to the IUE spectrum to the N V, C IV, Si IV, Al III & C II wind resonance lines of HD 14818 (B2 Ia). Even though the fit to Hα is not perfect, a reasonable fit is made to the UV P Cygni profiles, particularly Si IV & Al III. Model parameters are $T_{\rm eff}$ = 18 000 K, log $(L/L_{\odot})$ = 5.40 & $\dot{M}$ = 1.0 $\times 10^{-6}$ $M_{\odot}$.

reproduce the C IV profile. This was also a problem for β, since the values presented in Table 3.4 were tailored to suit Hα and may not be appropriate for the wind resonance lines, where the wind may be accelerating at a faster speed. Seven of the 20 B supergiants show agreement between values of β derived from CMFGEN and SEI modelling, whereas for a further six stars the discrepancy between Hα and SEI derived β values is $\leq$ 20%. The remaining stars displaying large discrepancies between Hα and UV-derived values of β all have Hα profiles in absorption or evidence of a P Cygni profile, making it harder to determine β accurately from the Hα profile. The exception to this is the hypergiant star HD 190603, whose β value appears to double from β = 1.2 (from Hα) in the inner wind to β = 3.0 (from C IV) in the outer part of the wind, suggesting a velocity law that slows down in the outer wind, which seems unlikely. The assumption of a smoothly accelerating velocity law is not entirely valid in an inhomogeneous and turbulent stellar wind (but works well for the purpose of these models) so it is possible that such a velocity law is

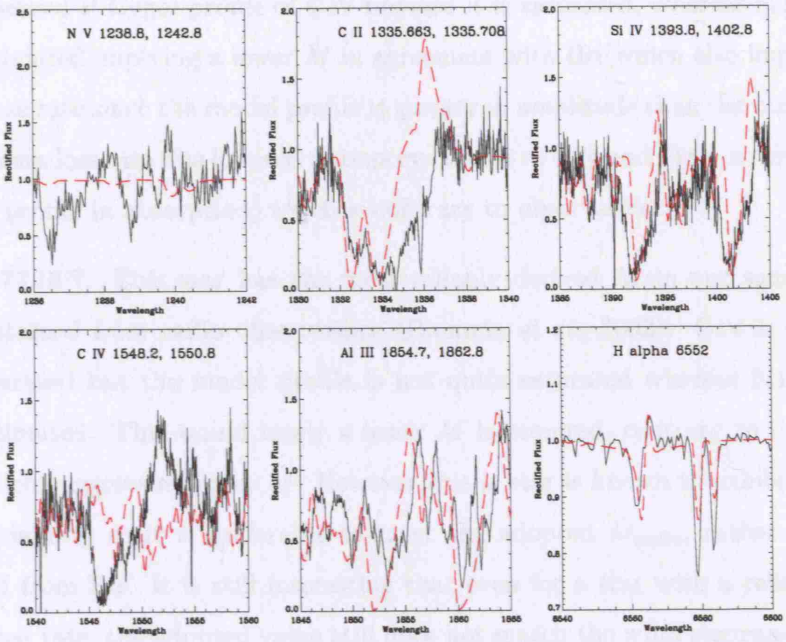

Figure 4.8: CMFGEN fit to the IUE spectrum to the N V, C IV, Si IV, Al III & C II wind resonance lines of HD 53138 (B3 Ia). Although a good fit has been made to Hα with the adopted mass loss rate, CMFGEN does not reproduce the observed UV P Cygni profiles well. Model parameters are $T_{\rm eff}$ = 16 500 K, log $(L/L_{\odot})$ = 5.30 & $\dot{M}$ = 4.5 $\times 10^{-7}$ $M_{\odot}$.

inappropriate for this particular star.

4.2.2 Quality of individual line fits

The details and problems encountered with the CMFGEN model fits to the IUE spectra of the individual 20 Galactic B supergiants are summarised below. Stars which display Hα in emission (indicating a strong stellar wind) are denoted by ^{e} and those in absorption denoted by ^{a}, whereas 'P Cygni'-shaped Hα profiles are marked by ^{p} and Hα profiles that are known to show significant variation (as noted by Morel *et al.* 2004) are labelled ^{v}.

- **HD192660**^{e}: The observed Hα profile of this star was difficult to model (see §3.2.4 & 3.2.5) so the adopted value of $\dot{M}_{\rm H\alpha} = 5.0 \times 10^{-6}$ $M_{\odot}$ yr^{-1}is an upper limit. It is not therefore expected that the $\dot{M}$ of this model will give a good fit to the UV wind resonance lines and this certainly appears to be the case. Only C IV & Si IV are present as wind resonance lines in this star. CMFGEN is only able to match

the observed P Cygni profile of C IV because it is saturated, whereas Si IV is largely overestimated implying a lower $\dot{M}$ in agreement with Hα(which also implies a lower mass loss rate since the model profile is greater in amplitude than the observed one). If the mass loss rate was lowered to improve the fit to C IV and Si IV, it would produce an Hα profile in absorption, which is contrary to observation.

- **HD 37128**^{ev}: This star has the most reliably derived $\dot{M}$ in our sample since it was obtained from radio observations (Blomme *et al.*, 2002). C IV is observed to be saturated but the model profile is not quite saturated whereas Si IV is largely overestimated. This would imply a lower $\dot{M}$ is required, contrary to the model fit Hα which suggests a higher $\dot{M}$. However this is star is known to exhibit significant Hα variability so it is preferable to trust the adopted $\dot{M}_{\rm radio}$, rather than an $\dot{M}$ implied from Hα. It is still interesting that even for a star with a reliably-derived mass loss rate, the adopted value still does not match the wind resonance lines very well.

- **HD 204172**^{a}: The fits to this star in the UV are exactly the same quality as those seen in the previous two stars for C IV & Si IV, although the observed Si IV P Cygni profile is much weaker.

- **HD 38771**^{a}: Again the models fits seen here are similar to the previous stars, with the only difference being that the fit to the blue-ward side of the C IV profile is significantly worse.

- **HD 185859**^{a}: A very good fit was made to the observed Hα profile of this star in §3.2.4. This is generally reflected in the UV, though the model produces a Si IV whose red-ward emission and blue-ward absorption is much stronger than observed. The observed C IV profile is however is well matched by the model, and even Al III is quite accurately reproduced, though no stellar wind contamination is present in these lines.

- **HD 213087**^{a}: The adopted $\dot{M}_{\rm H\alpha}$ for this star was a lower limit, yet in the UV Si IV is again grossly over-estimated, suggesting a lower $\dot{M}$ still. C IV is saturated therefore the model can reproduce the profile well.

- **HD 64760**^{a}: The quality of the model fit to its UV spectrum is the same as for HD 213087; the saturated C IV profile is well matched but Si IV is much stronger than

observed.

- **HD 2905**^{e}: For this star (B0.7 Ia) there is clear change in the ionisation balance, since C IV is no longer saturated but Si IV is saturated and both C II and Al III show evidence of broadening from the stellar wind in their line profiles. The model only manages to produce a photospheric profile for C IV instead of a P Cygni profile. The model Si IV profile is still overestimated and asymmetric (but not as much as before) compared to the observed profile, whereas Al III is grossly overestimated and very asymmetric compared to its observed profile. The fit to Hα was also good for this star if only a little too high as it slightly overestimated the profile amplitude, but yet again the UV implies a lower $\dot{M}$.

- **HD 13854**^{pv}: The Hα profile of this star is a P Cygni profile so it was difficult to constrain an accurate value of $\dot{M}_{\mathrm{H}\alpha}$ (see §3.2.4) as CMFGEN could not fully reproduce the observed Hα profile. In the UV the model Al III is much stronger and more asymmetric than the observed profile, suggesting a lower $\dot{M}$ but Si IV is matched very well by the model compared to previous attempts. C IV is observed to be almost saturated yet the model only shows a photospheric profile.

- **HD 190066**^{a}: This star's observed Al III profile is quite weak and severely underestimated by the model profile. C IV is observed to be saturated but again the model profile is weak and photospheric. The reverse is true of Si IV for which the model produces a saturated P Cygni profile whereas the observed profile is clearly unsaturated.

- **HD 190603**^{e}: Already discussed see beginning of section.

- **HD 193183**^{a}: The $\dot{M}$ derived from Hα was an upper limit (see Table 3.4), indicating a lower $\dot{M}$ is preferable. This view is supported by the model fits to the UV P Cygni profiles. CMFGEN overestimates the Al III profile, producing a saturated profile with huge asymmetry when the observed profile is unsaturated. The observed Si IV profile is not well reproduced by the model either, with the model profile having too narrow an absorption trough whilst the red-ward part of both doublet components is in emission, a feature which is not present in the observation. C IV is approaching saturation, yet the model only produces a photospheric profile. However the situation is somewhat reversed for C II, which shows no evidence for wind contamination

observationally, but the model produces a highly asymmetric profile with a slightly broadened red-ward doublet.

- **HD 14818**^{pv}: Already discussed see beginning of section.

- **HD 206165**^{a}: CMFGEN does not manage to reproduce any of the P Cygni profiles of this star accurately. C IV is virtually saturated, but the model only produces a photospheric profile. C II is also quite strong yet the model completely overestimates the red-ward side of the profile. It also retains the individual doublet profiles; clearly the model has not generated enough optical depth in this line. The reverse is true for Al III, where the model produces too much absorption, resulting in a saturated profile which is not observed. The usual problems with Si IV are encountered, namely the red sides of both model doublets are too strong and the absorption troughs are too narrow.

- **HD 198478**^{e}: The differences between model and observed C II and C IV are the same as for HD 206165. A better model fit is found for Al III, although again the model profile is saturated when the observed profile is not quite yet saturated. The red side of the Si IV doublet is matched better than usual for this star but the model still fails to reproduce the full width of the absorption trough.

- **HD 42087**^{av}: In this star CMFGEN is more successful in producing sufficient high-velocity absorption to match the blue-ward side of the Si IV doublet, but at the expense of having too little absorption at lower velocities, resulting in an overestimation of the amount of emission on the red-ward side. As usual, the model C IV profile is photospheric when a clear P Cygni profile is observed for this line. C II also shows evidence for wind contamination but CMFGEN gives a very poor fit to this line, grossly over-estimating the red-ward side of the profile. Like HD 206165, it is not saturating this line enough, but produces a saturated Al III profile whilst the observed line is not fully saturated.

- **HD 53138**^{av}: Already discussed see beginning of section.

- **HD 58350**^{pv}: Again C II is badly reproduced by the model for this star for same reasons given for HD 53138, 42087 & 206165. C IV is seen to be quite weak here, but the model profile is even weaker still. The model fit to the Si IV profile is much better

than usual, with only a slight over-estimation of the red-ward side of each doublet being apparent. Al III is overestimated by the model, which produces a saturated profile rather than an unsaturated one as observed.

- **HD 164353**[a]: This star possesses the lowest mass loss rate in the sample ($\dot{M}$ = 6×10^{-8} $M_{\odot}$ yr^{-1}) so also has the weakest wind. This is clearly reflected in the weakness of its P Cygni profies. C IV is weakest observed so far in the sample of 20 B supergiants yet still shows evidence of high velocity absorption in the stellar wind that is not reproduced by the model. The observed Si IV is also quite weak, and the model profile is narrow and asymmetric, over-estimating both the absorption and emission parts of the doublet. The model C II and Al III display the same gross estimation seen for previous stars, producing saturated profiles when the observed profiles are unsaturated.

- **HD 191243**[a]: The model fit to the P Cygni profiles of this star is very similar to those for HD 164353. The only difference is that the model overestimates Si IV even more in terms of both the absorption and emission of each doublet.

In general, CMFGEN only succeeds in matching the C IV line when it is saturated in early B supergiants, at which point it is no longer sensitive to $T_{\rm eff}$ and $\dot{M}$ so a reliable fit cannot be obtained as altering these parameters will have no affect on the model line profile. Otherwise, CMFGEN manages to reproduce most of the observed P Cygni profile for C II, Al III and Si IV, but fails to produce enough high velocity absorption to reproduce the full extent of the observed absorption trough. As a result, the model often under-estimates the blueward absorption as well as over-estimating the redward emission, especially in the case of Si IV. This can sometimes lead to the model giving an asymmetry to the P Cygni profile that is certainly not observed in the spectrum. Additionally, CMFGEN never succeeds in producing the N V P Cygni profile when present in B0 – B1 supergiants and even when a weak, photospheric profile is observed, the model fails to produce a discernible spectral line at the correct wavelength for N V. In the hotter B supergiants, the model grossly underestimates the photospheric Al III & C II lines. However when the same resonance lines are seen as P Cygni profiles, the model has a tendency to reproduce them as saturated when they are observed to be unsaturated. These problems in matching the UV P Cygni profiles have also been encountered by Evans *et al.* (2004*a*) and Crowther *et al.* (2006).

4.2.3 Modelling the UV exclusively

The CMFGEN models examined in the last section demonstrate a clear discrepancy between $\dot{M}_{\mathrm{H}\alpha}$ and the value of $\dot{M}$ implied by the P Cygni profiles of the wind resonance lines. It is hardly surprising that they are unsuccessful in reproducing the observed UV wind diagnostics accurately. In this section, the possibility of modelling a star solely from its UV spectra will be investigated (ignoring any prior knowledge of values of parameters from the optical) to see if the UV can be reproduced more accurately if the fit to the optical spectrum of the same star is ignored.

Looking back to the problems mentioned in the previous section, one potential difficulty is immediately apparent. CMFGEN is unable to reproduce the C IV line accurately, which makes it hard to constrain v_∞ & β from this line. Suitable UV T_{eff} diagnostics also need to be found besides the photospheric Si II and Si III lines discussed in §4.1. Si IV could be a good candidate but it is also very sensitive to luminosity and mass loss; moreover it is often saturated, reducing its sensitivity to both parameters, and CMFGEN rarely reproduces it accurately. Other potential T_{eff} diagnostics are Al III and C II which also show some sensitivity to mass loss. Another possible T_{eff} diagnostic is the photospheric Si II 1526.7, 1533.4 Å line, but CMFGEN does not model these lines well either, often completely failing to reproduce the blue-ward part of the doublet. An additional constraint in determining T_{eff} in the UV can be found from the Fe III - Fe IV blanketed continuum around 1250 - 1900 Å, which depends solely on T_{eff}.

However in practice, it is difficult to disentangle the effects of T_{eff} and $\dot{M}$ on Si IV, Al III and C II, plus they are often too saturated to be sensitive enough to these parameters. When Si IV is not observed to be saturated, CMFGEN still predicts a saturated profile that is virtually insensitive to T_{eff} & $\dot{M}$, making it difficult to use as a T_{eff} & $\dot{M}$ diagnostic. For B0-B1 supergiants, the model often produces a saturated C IV P Cygni profile and over-estimates the Si IV P Cygni profile. It would therefore seem logical that adopting a model with a lower mass loss rate would provide a better fit to the observed C IV and Si IV lines. Looking at Fig. 4.9, it can be seen that this is not the case, since lowering the value of $\dot{M}$ from 5.0×10^{-6} to 2.6×10^{-6} has no affect on the wind resonance lines (implying that they are still optically thick), despite producing model Hα profiles in emission and

absorption respectively. Note that the broad feature seen in the model between 1242 - 1247 Å is *not* N V but C III, which interestingly enough *does* show some sensitivity to mass loss. It could still be argued that a larger decrease in mass loss is required to fit these lines. However Fig. 4.10 disproves this idea as yet again no difference is seen between P Cygni profiles for models with $\dot{M} = 6 \times 10^{-8}$ $M_{\odot}$ yr^{-1} (red dashed line) and $= 1.8 \times 10^{-7}$ $M_{\odot}$ yr^{-1} (blue dotted line) respectively. This is in spite of the fact that this difference in mass loss again results in model Hα profiles in emission and absorption, as well as having a significant difference on the amplitude of Ly α (1216 Å). HD 164353 presents an interesting case study for how CMFGEN deals with the ionisation in the stellar wind, as it is a B5 Ib/II star that possesses a very weak wind with $\dot{M} = 6 \times 10^{-8}$ $M_{\odot}$ yr^{-1} and can be thought of as a star with negligible mass loss and stellar wind contamination. This is confirmed by looking at the observed C II and Al III resonance lines (Fig. 4.10), which show some asymmetric broadening. However the model predicts strongly saturated profiles for both lines despite the low mass loss rate adopted for the model, again suggesting that the predicted ionisation structure is at fault. It appears that CMFGEN predicts ionisation fractions for C II and Al III that are too high, resulting in a large optical depth that produces too many absorbers at too high a velocity. The observed profiles on the other hand show us that absorption is only occurring around the rest velocity of the line. The model over-estimation of C II and Al III may therefore only be resolvable by lowering the ionisation fraction of these two elements.

In addition to the wind resonance lines, the UV excited lines can potentially be used to provide additional constraints on the mass loss adopted for the model. An example is the Si IV 1122, 1128 Å line in the FUV, whose upper energy level is coincident with the lower energy level of Si IV 1400 Å. This means that if the model over-populates the lower level of Si IV 1400 Å, the upper level of Si IV 1122, 1128 Å will also be over-populated, pushing the line into emission when it is observed to be in absorption. If this predicted line is seen to be in emission in a model when the observed line is in absorption, this is a direct indication that the adopted mass loss rate of the model is too high. However, this relies on either *FUSE* or *Copernicus* data being available for a given star. Fig. 4.11 shows an example of this line in absorption can be seen for the B1.5 Ia+ star HD 190603, where the model reproduces the line well, confirming the adopted mass loss rate. There are no examples of Si IV 1128 Å being in emission in the models used for the sample of

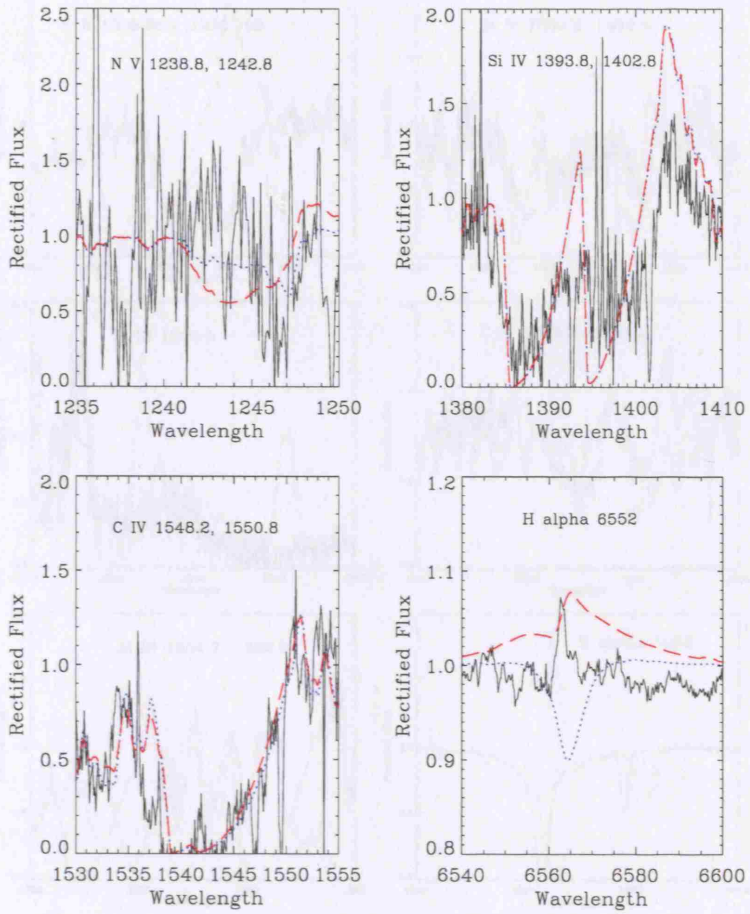

Figure 4.9: Comparison of UV wind resonance lines of HD 192660 for models with $\dot{M} = 5.0 \times 10^{-6}\ M_{\odot}$ (red dashed line) and $2.6 \times 10^{-6}\ M_{\odot}$ (blue dotted line) for HD 192660 (B0 Ib).

20 Galactic B supergiants, so this would suggest that the adopted mass loss rates are not grossly over-estimated.

It is possible to provide alternative perspectives on the UV behaviour by comparing the ionisation stages present in any given star, rather than trying to reproduce individual line profiles. Fig. 4.12 shows the predicted ionisation structure against w at four different $T_{\rm eff}$; 27 500 K, 23 500 K, 18 000 K and 15 000 K for the six ions (N V, C IV, Si IV, Si III, Al III & C II). CMFGEN predicts that Si IV will be dominant as expected for $T_{\rm eff} = 27\ 500$ K, but shows very low levels of N V and C IV. This is hardly surprising since it explains

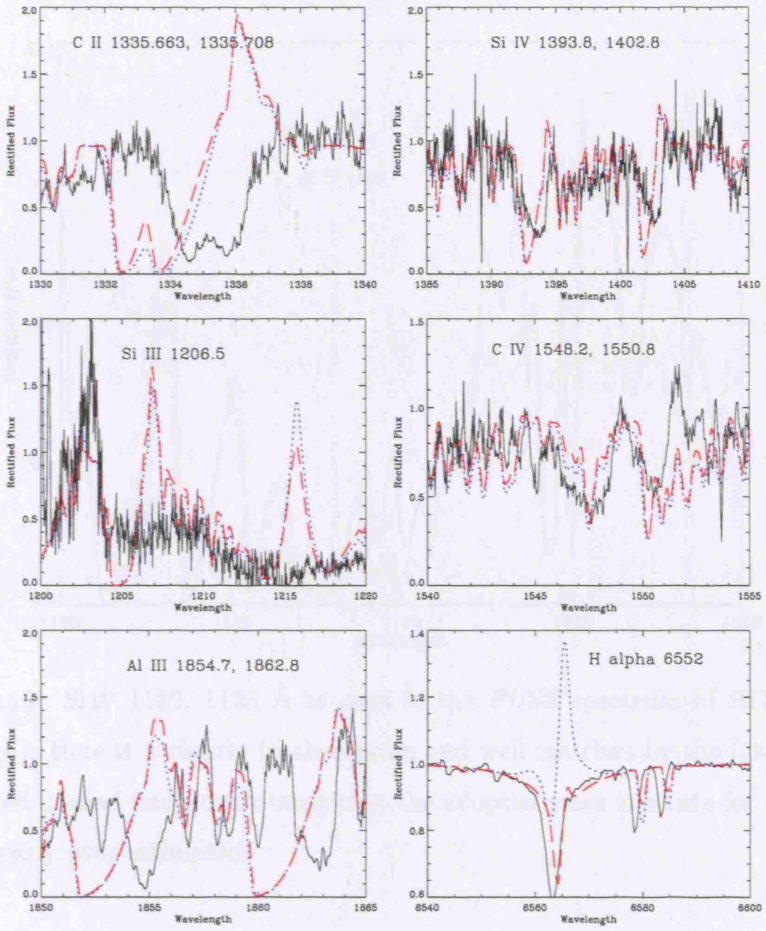

Figure 4.10: Comparison of UV wind resonance lines of HD 164353 for models with $\dot{M} = 6 \times 10^{-8}\ M_{\odot}\ \mathrm{yr}^{-1}$ (red dashes line) and $= 1.8 \times 10^{-7}\ M_{\odot}\ \mathrm{yr}^{-1}$ (blue dotted line) respectively

the complete absence of a N V P Cygni profile (when present observationally), as well as the difficulties in generating a P Cygni profile for C IV when it is unsaturated. It is also interesting to note that the levels of ionisation drop off rapidly in the model as w increases, which is direct evidence of the model failing to generate enough high-velocity absorption to sustain the same level of ionisation further out in the wind. This is the reason for the 'narrowness' of the model C IV and Si IV P Cygni profiles compared to the broad absorption troughs of the observed P Cygni profiles. If the model cannot sustain enough ionisation in the inner and outer parts of the wind, then it will be unable to fully reproduce the blue-ward part of the profile. CMFGEN predicts Si IV to be dominant down to T_{eff}

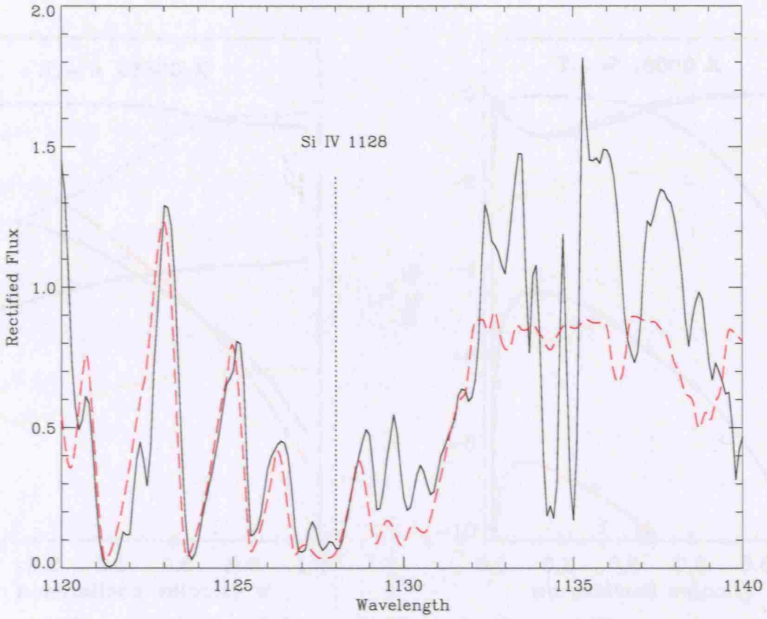

Figure 4.11: Si IV 1122, 1128 Å as seen in the *FUSE* spectrum of HD 190603 (B1.5 Ia+). Here it is clearly in absorption and well matched by the CMFGEN model (red dashed line), confirming that the adopted mass loss rate for this star is not grossly over-estimated.

= 18 000 K, at which point Si III and Al III take over as the dominant ions in the wind. At this $T_{\rm eff}$, C II has also increased in strength, becoming a dominant ion at $T_{\rm eff} = 15\,000$ K.

4.3 Inclusion of clumping in models

In order to try and improve the CMFGEN fits to the UV, the effect of including clumping in the CMFGEN models was investigated. For details of the inclusion of clumping in CMFGEN models, please refer to §2.4.3.4 & §3.2.5. To summarise, clumping is parameterised by a 'filling factor' approximation such that the filling factor decreases exponentially as the radius increases

$$f = f_\infty + (1 - f_\infty)e^{-\frac{v}{v_{cl}}} \tag{4.1}$$

where f_∞ is the filling factor at v_∞ and v_{cl} is the velocity at which clumping is 'switched

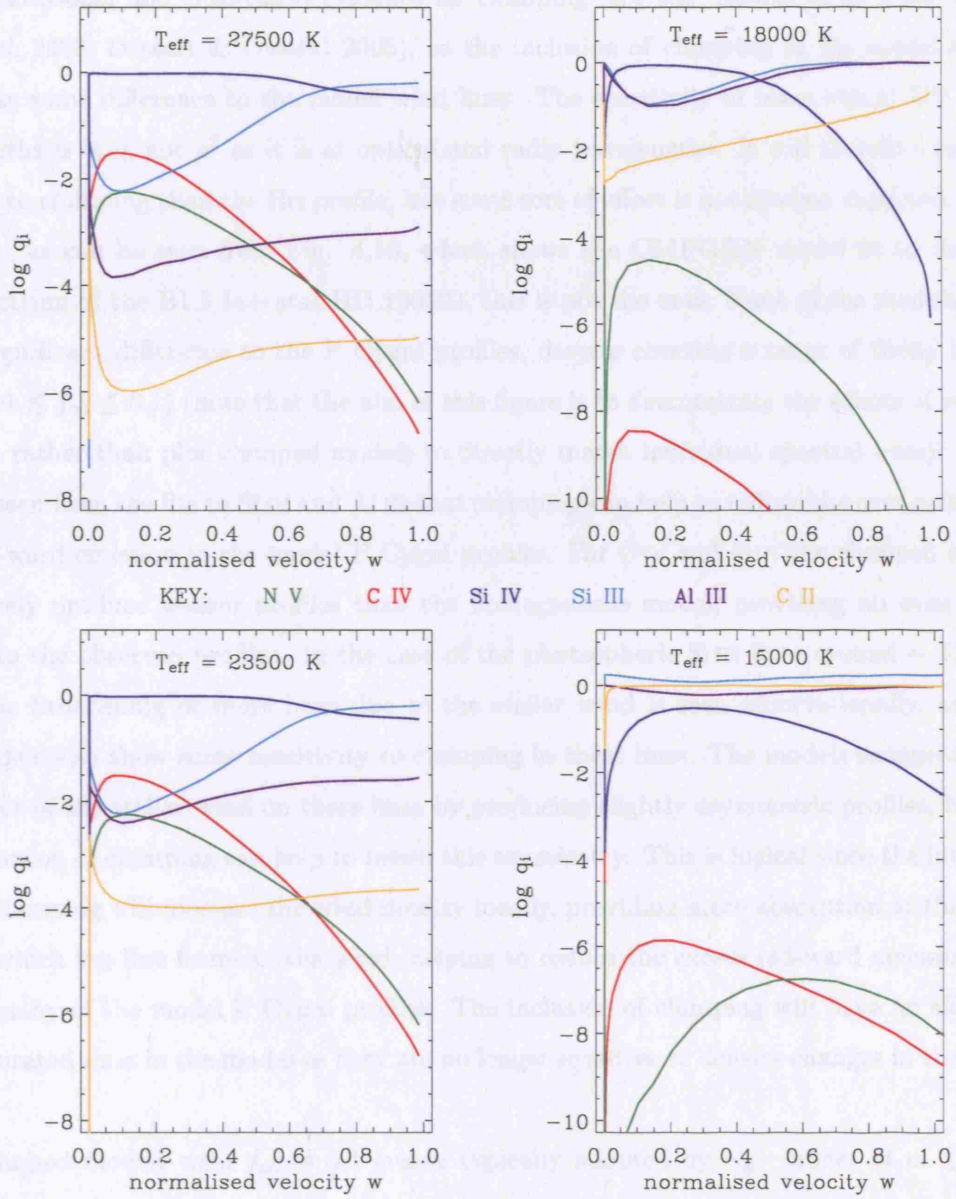

Figure 4.12: CMFGEN predicted ionisation structure at different $T_{\rm eff}$, plotted against normalised veocity w. The ions are colour-coded as follows: N V = green, C IV = red, Si IV = dark blue, Si III = light blue, Al III = purple and C II = yellow. Si IV is predicted to be dominant for B0-B2 supergiants ($30000K \leq T_{\rm eff} \leq 18000K$, after which Si III, Al III and C II take over as the dominant ions in the wind for $T_{\rm eff} \leq$ 18 000 K.

on' in the wind. As the P Cygni profiles are formed in the wind, where there is strong observational and theoretical evidence for clumping (see e.g. Bouret *et al.* 2003; Massa *et al.* 2003; Dessart & Owocki 2005), so the inclusion of clumping in the model should make some difference to the model wind lines. The sensitivity of mass loss at UV wavelengths is $\propto \rho$, not ρ^2 as it is at optical and radio wavelengths. It will therefore respond less to clumping than the Hα profile, but some sort of effect is nonetheless expected. However, as can be seen from Fig. 4.13, which shows the CMFGEN model fit to the IUE spectrum of the B1.5 Ia+ star HD 190603, this is not the case. None of the models make a significant difference to the P Cygni profiles, despite covering a range of filling factors ($0.01 \leq f_\infty \leq 0.1$) (note that the aim of this figure is to demonstrate the effects of varying f_∞, rather than plot clumped models to directly match individual spectral lines). It can be seen from the fits to Si IV and Al III that clumping can help to reduce the over-estimated red-ward emission in the model P Cygni profiles. For C IV and C II, the clumped models merely produce weaker profiles than the homogeneous model, providing an even worse fit to the observed profiles. In the case of the photospheric Si III lines around $\sim$ 1300 Å, some broadening of these lines due to the stellar wind is seen observationally, and the models also show some sensitivity to clumping in these lines. The models exaggerate the effect of the stellar wind on these lines by producing slightly asymmetric profiles, but the inclusion of clumping can help to lessen this asymmetry. This is logical since the inclusion of clumping will increase the wind density locally, providing more absorption at the point at which the line forms in the wind, helping to reduce the excess red-ward emission seen in many of the model P Cygni profiles. The inclusion of clumping will have no affect on saturated lines in the model as they are no longer sensitive to density changes in the wind.

Clumped models with $f_\infty = 0.1$ (value typically adopted by e.g. Hillier *et al.* (2003)) were run for 9 of the stars in our sample, but none of these models make a significant improvement on the homogeneous models and fail to make a better fit to the observed UV spectrum. In general, the inclusion of clumping is not needed to improve the line fits, contrary to the findings of Bouret *et al.* (2003). In their paper, Bouret *et al.* (2003) found that a good fit to the P V P Cygni profile in the O4 If+ supergiant HD 190429A could not be achieved without using a clumped model with $f_\infty = 0.04$. They also find that the inclusion of clumping significantly improves the model fits to O V 1371 Å & N IV 1718 Å. The failure of clumped models to match the observed P Cygni profiles of B supergiants is

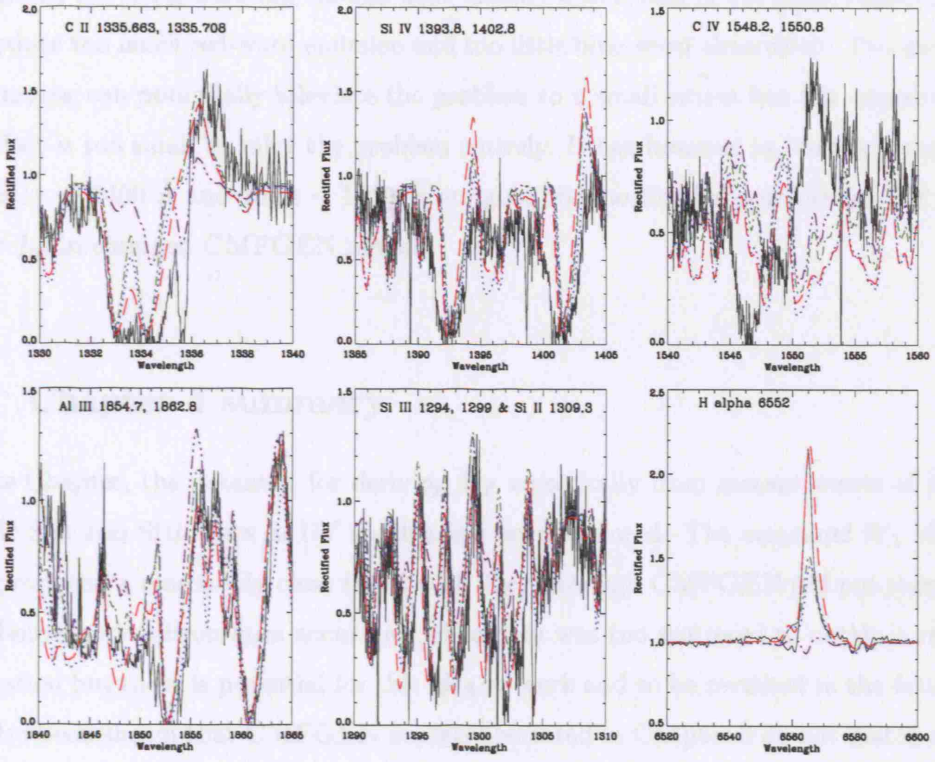

Figure 4.13: Effect of varying the filling factor on the P Cygni profiles of HD 190603 when including clumping in the models. The clumped models have f_∞ = 1.0 (red), 0.1 (blue), 0.05 (green) and 0.01 (purple). A value of v_{cl} = 200 km/s was assumed for all models. N.B. A filling factor of f = 1.0 indicates a homogeneous model with no clumping.

a problem since there is ample observational and theoretical evidence for the presence of clumping in stellar winds (see discussion in §3.2.5), so technically clumped models should be used for modelling all 20 B supergiants. However, the treatment of clumping in CMFGEN is done through a crude 'filling factor' approach which is most probably highly unphysical, so it is not very surprising that a clumped model fails to provide a satisfactory fit to the observed wind resonance lines. It is still strange that other authors e.g. (Bouret *et al.* (2003) claim that clumped models succeed to make a significant improvement in O supergiants, yet this is not true of B supergiants. Given the evidence presented in this chapter, the root of the problem in fitting the UV wind resonance lines appear to lie in the ionisation structure rather than the adopted $T_{\rm eff}$ & $\dot{M}$ of any given model. It is clear that

the models are not generating enough high-velocity absorption in the wind, causing them to produce too much red-ward emission and too little blue-ward absorption. The inclusion of clumping can potentially alleviate the problem to a small extent but the magnitude of the effect is too small to solve the problem entirely. It can however at least be concluded that Si IV $\sim$ 1400 Å and Al III $\sim$ 1860 Å are good diagnostics for constraining the filling factor f_∞ in clumped CMFGEN models.

4.4 Chapter 4 summary

In this Chapter, the potential for deriving $T_{\rm eff}$ empirically from measurements of photospheric Si II and Si III lines in UV spectra has been explored. The measured W_λ of these lines produced a reasonably clear trend with $T_{\rm eff}$, although CMFGEN did not reproduce the photospheric silicon lines accurately. The data was too scattered to obtain a reliable calibration but there is potential for this idea to work and to be revisited in the future. It has also been shown that CMFGEN models presented in Chapter 3 do not match all the UV wind diagnostics well. The N V P Cygni profile is never produced by the model and C IV is only matched well when it is saturated; else the model does not predict enough P Cygni emission to match the observed P Cygni profile. Additionally the model often over-estimates Si IV, Al III and C II, again the only decent matches that the model provides to these lines are when the observed P Cygni profiles are saturated. It becomes clear when the ionisation structure of the CMFGEN models is analysed that they do not produce enough high-velocity absorption in the wind, causing the model to produce P Cygni profiles whose blue-ward parts are weaker and narrower than observed. This problem is not alleviated by the inclusion of clumping or X-rays in the model and implies that the model lacks the fundamental physics needed to generate accurate profiles of the stellar wind diagnostics. The occurrance of this *optical-UV discrepancy* challenges our understanding of the physics of hot star winds and needs further investigation.

CHAPTER 5

SEI modelling of UV wind resonance lines

This chapter describes research carried out to obtain empirical ionisation fractions from UV P Cygni profiles in the winds of Galactic B supergiants. §5.1 highlights the importance of UV wind resonance lines for obtaining information concerning the stellar winds and §5.1.1 introduces the SEI method and its use in obtaining ionisation fractions from wind resonance lines. Empirical trends of ionisation fractions obtained for the sample of 20 B supergiants as functions of $T_{\rm eff}$, radius and velocity are discussed in §5.2, and are compared to the ionisation structures predicted by CMFGEN. Finally, the implications of these results, including why they support the argument for a reduction in the observed mass loss rates for OB stars, are discussed.

5.1 Analysing UV wind resonance lines

UV P Cygni profiles provide strong signatures of the presence of stellar winds in OB star spectra and encode a wealth of information on their properties. They are produced by resonance scattering, when an absorbed photon is re-emitted essentially immediately by spontaneous emission. For UV resonance lines, these transitions are (by definition) connected to the ground level. The formation of UV resonance lines is controlled primarily by the optical depth of a particular line,

$$\tau_S(r) = \frac{\bar{\chi}(r) R_* \lambda}{v_\infty dv/dr} \tag{5.1}$$

in the Sobolev approximation, where $\bar{\chi(r)}$ is the frequency-integrated line opacity given by

$$\bar{\chi(r)} = \frac{\pi e^2}{m_e c} f n_l(r), \tag{5.2}$$

e is the electron charge, m_e the electron mass, f the oscillator strength and n_l the occupation number of the lower level of the transition. Note that the radius r is given here in stellar radii, and the velocity v in terms of v_∞. The nature of optical depth of spectral lines that form in an expanding atmosphere or outflowing stellar wind is completely different to that of lines formed in a hydrostatic photosphere. In stellar winds, optical depth is a *local* quantity and this is why it is useful to invoke the *Sobolev* approximation. The photon/atom interaction region is confined to the *Sobolev* length $L_{sob} = v_{th}/dv/dr$, already discussed in detail in §2.2.1. If we rewrite n_l in terms of local density $\rho(r) = \dot{M}/4\pi R_*^2 r^2 v_\infty v$ then the optical depth becomes

$$\tau_S(r) = \frac{k(r)}{r^2 v dv/dr} \tag{5.3}$$

where the line strength $k(r)$ is defined as

$$k(r) = E(r)X(r)\frac{\dot{M}}{R_* v_\infty^2}\frac{(\pi e^2)/(m_e c)}{4\pi m_H}\frac{A_k}{1+4Y_{He}} f\lambda \tag{5.4}$$

and E is the excitation factor of the lower level, X the ionisation fraction, A_k the elemental abundance with respect to hydrogen and Y_{He} the helium abundance. Provided that the occupancy of the ground state of the atom is consistent with the density stratification in the wind, then the local density scales with the quantity $\dot{M}/\ R_* v_\infty^2$, otherwise known as Q_{res}. Once the velocity law has been constrained, values of $\dot{M}$ can in principle be determined through fitting the observed P Cygni profiles with a model. However, it is clear from Equation 5.4 that $\dot{M}$ cannot be determined independently of the ionisation fraction, excitation factor (either as $f(r)$ or a mean value) and elemental abundance; it is

ensnared in the product $E(r)X(r)A_k\dot{M}/R_*$. For the sample of 20 Galactic B supergiants presented in Chapter 3, reliable values of A_k, $\dot{M}$ & R_* are available (see Tables 3.2, 3.4 & 3.5), which only leaves $X(r)$ and $E(r)$ to be determined. Values of $E(r)$ can be estimated from atomic data, leaving $X(r)$ as the only remaining unknown quantity. One of the aims of the work covered in this chapter is to examine the distribution of the ions present in B supergiant winds as a function of radius, with a view to constraining $X(r)$. Once the empirical values of $X(r)$ are obtained, these can be used to improve on model estimates of ionisation structure, enabling the future determination of $\dot{M}$ from UV wind resonance lines.

Another potential problem in deriving $\dot{M}$ from UV wind resonance lines is that some of the lines become saturated, meaning in practice $\tau_S \geq 3$ throughout the wind for the line in question. This is usually a problem for the N V, C IV and Si IV resonance lines in early B supergiants, whereas at lower $T_{\rm eff}$ it sometimes occurs in Al III and C II. Assuming a constant ionisation fraction and excitation factor throughout the wind, the line optical depth is governed by mass loss and the steepness of the velocity law

$$\tau_S \propto \frac{1}{r^2 v dv/dr} \propto \frac{1}{v(r)^{\frac{1}{\beta}-2}} \tag{5.5}$$

The absorption trough that results from such a line shows (almost) 'zero intensity', so that the overall profile shape is determined by the emission part of the profile, i.e., the source function in the optically thick case. This in turn depends solely on the velocity gradient (at large optical depths), since the occupancy of energy levels no longer has an effect on the profile shape once the line is saturated. For this reason, strongly saturated P Cygni profiles should in principle be ideal candidates for measuring v_∞ (from the position of the blue absorption edge) and β (from the shape of the emission peak). On the other hand, due to the insensitivity of a saturated line to the occupancy of the energy levels of the ion, it is only possible to derive lower limits for the product $E(r)X(r)A_k\dot{M}/R_*$. Unsaturated P Cygni profiles ($\tau_S \leq 1$) are therefore normally used as diagnostics for determining $E(r)X(r)A_k\dot{M}/R_*$, since both the absorption and emission parts of the profile are sensitive to the line opacity. It can be obtained by applying line fits to the unsaturated P Cygni profiles using a model that samples the line optical depth as a function of

velocity. This principle is the basis of the SEI method, as used by Lamers *et al.* (1987) and is discussed in further detail in the next section (5.1.1).

Using the SEI method, it has been possible to analyse the N V $\lambda\lambda$ 1238.82, 1242.80; C IV $\lambda\lambda$ 1548.20, 1550.77; Si IV $\lambda\lambda$ 1393.76, 1402.77; Si III $\lambda\lambda$ 1206.50; C II $\lambda\lambda$ 1334.53, 1335.71 & Al III $\lambda\lambda$ 1854.72, 1862.79 wind-formed resonance lines in our sample to examine the behaviour of these ions in the stellar winds of B supergiants. These will hereafter be referred to as N^{4+} , C^{3+} , Si^{3+} , Si^{2+} , C^{+} & Al^{2+}. The line properties are summarised in Table 5.1. In the $T_{\rm eff}$ range of B supergiants (14 500 K $\leq T_{\rm eff} \leq$ 30 000 K), N^{4+} has the highest ionisation potential out of the six chosen ions. It is only seen in B supergiants hotter than 18 000 K and is referred to as a 'super-ion' in the wind. 'Super-ions' are only expected to be abundant in the hottest stars, since at higher temperatures photoionisation from the ground state cannot ionise the next lowest ion, as the probability of ionising the next lowest ionisation state is reduced because bound-free absorption of He II largely suppresses the stellar continuum flux blue-ward of 228 Å. This means that an additional source of ionisation is required in order to produce the N^{4+} resonance line in its observed abundance. In the case of O stars, it was suggested that super-ion abundances were modified via *Auger ionisation* , following the prediction by Cassinelli & Olson 1979 that hot star winds must emit X-rays in order to explain the presence and strength of super-ions. X-rays have since been observed in OB star winds (Chlebowski *et al.*, 1989; Berghoefer *et al.*, 1996), their origin and production is known to originate from shocks in an unstable flow (Owocki *et al.*, 1988). C^{3+} has the next highest ionisation potential and is detected in all luminous B stars, though it is usually saturated in early B Ias. Si^{3+} is another strong abundant ion, present over the entire range in $T_{\rm eff}$ of B supergiants. It is predicted to be the dominant ion in early B supergiant winds according to CMFGEN, and this will be discussed further in §5.2. Si^{2+} is also detected over most of the B supergiant $T_{\rm eff}$ range and, together with Si^{3+}, these ions could prove to be useful wind diagnostics since they are present over a wide range of $T_{\rm eff}$, less likely to be saturated than C^{3+} and are unaffected by nuclear processing. Al^{2+} is only observed in cooler B supergiants with $T_{\rm eff} \leq$ 23 000 K but could potentially be very useful, since it is unaffected by nuclear burning and has a low abundance, meaning that it is highly unlikely to be saturated. Lastly, C^{+} is also only detected in cooler B supergiants, shows a strong dependence on stellar luminosity and is rapidly destroyed at $T_{\rm eff} \geq$ 18 000 K.

Ion	A_E	λ_{blue}	λ_{red}	χ	Δv	$\psi(Si\,iv)$
C II	8.39	1335.663	1335.708	11.26 - 24.38	10	2.20
C IV	8.39	1548.203	1550.777	47.89 - 64.48	499	3.90
Al II	6.37	1670.787	-	5.98 - 18.82	-	0.36
Al III	6.37	1854.716	1862.790	33.49 - 45.13	-	0.12
N V	7.78	1238.821	1238.821	77.45 - 97.86	965	0.64
Si III	7.51	1206.50	-	16.34 - 33.49	-	2.80
Si IV	7.51	1393.755	1402.750	33.49 - 45.13	1936	1.00

Table 5.1: Properties of UV resonance lines observed in *IUE* spectra. Elemental solar abundances (A_E) are taken from the solar photosphere (Asplund *et al.*, 2005) and are expressed as $log\frac{N}{N_H} + 12$. λ_{blue} & λ_{red} are the rest wavelengths (in Å) of the blue and red doublet components respectively (Morton, 1991, 2003). χ gives the lower and upper ionisation potentials for each resonance line (Moore, 1970) and Δv is the separation between doublet component in km/s. ψ is the relative strength of the resonance line compared to Si IV $\lambda\lambda 1393.76, 1402.77$.

In addition to deriving empirical ionisation fractions and examining their behaviour with $T_{\rm eff}$ and velocity, it is also possible to compare these empirical values to model predictions. The CMFGEN models presented in Chapter 3 predict the ionisation structure of the stellar wind at a given $T_{\rm eff}$, and the predicted trends of ionisation fraction with $T_{\rm eff}$ and velocity are compared to empirical trends in §5.2.3. Another strongly debated issue concerning the ionisation state of B supergiant winds is the *bi-stability jump*. Based on an idea put forward by Pauldrach & Puls (1990*a*) (in connection with a study of the Luminous Blue Variable star P Cygni), it asserts that the stellar wind can exist in one of two stable states depending on the ions acting as the dominant drivers of the wind. The switch between these states should occur near spectral type B1 ($T_{\rm eff} \sim$ 21 000 K) and is known as the *bi-stability jump*. Observationally this jump was noted by Lamers *et al.* (1995), who found that the average value of the ratio of $\frac{v_\infty}{v_{\rm esc}}$ doubled between 3.9 $\leq$ log $T_{\rm eff} \leq$ 4.25 and 4.3 $\leq$ log $T_{\rm eff} \leq$ 4.7. It is also predicted to occur around $T_{\rm eff} \sim$ 25 000 K by the theoretical models of Vink *et al.* (2000). The precise $T_{\rm eff}$ at which the jump may

occur is prone to shift as it is sensitive to local temperature and density conditions. This phenomenon will be discussed further in §5.11. It is difficult to determine whether the *bi-stability jump* really exists based on a data set of 20 B supergiants, only two of which have $T_{\rm eff}$ near 21 000 K. A additional data set of 86 Galactic B Ia–II stars has been assembled for which *IUE* spectra have been obtained but no optical spectra are available. These stars have measured values of v_∞ but individual stellar parameters have not been derived for these stars. In order to assign values of $T_{\rm eff}$, log $(L/L_\odot)$, R_*, $M_*$and $v_{\rm esc}$ to these stars, parameterisations of these properties vs. spectral type were derived from linear fits to the results presented in Table 3.2 for the initial sample of 20 Galactic B supergiants. The values of $T_{\rm eff}$, log $(L/L_\odot)$, R_*, M_* and $v_{\rm esc}$ adopted for each type are shown in Table 5.4 of §5.11, along with the individual values of v_∞ for the initial sample of 20 B supergiants and the additional data set of 86 B Ia–II stars.

5.1.1 The SEI line synthesis code

The *Sobolev with exact integration* (SEI) method was first employed by Lamers *et al.* (1987), based on a concept introduced by Hamann (1981). For a resonance line that forms in the monotonic flow of the stellar wind, the source function can be evaluated with the Sobolev approximation, resulting in an exact formal integral which provides an accurate description of the observed line profile. A modified version produced by Haser (1995) included a radially dependent macroturbulent velocity, which is important since neglecting the presence of chaotic motions in the wind can lead to significant errors in the derived ionisation fractions (Lamers *et al.*, 1987). More recently, Massa *et al.* (2003) adapted the SEI method to analyse a sample of LMC O stars, using a set of 21 independent velocity bins whose amplitudes were adjusted in order to fit the optical depth of each ion P Cygni profile. In general, the method assumes a homogeneous, spherically-symmetric wind described by a smoothly accelerating velocity law and takes full account of blending between components of closely-spaced doublets. Values of $T_{\rm eff}$, R_* and log $(L/L_\odot)$ for each star are input into the code (taken from Table 3.2) whilst the derived CN abundances presented in Table 3.5 are assumed together with solar abundances (Asplund *et al.*, 2005) for silicon and aluminium. The velocity law is determined by fitting a saturated C IV P Cygni profile to constrain v_∞ & β; for cooler stars where C IV is unsaturated a saturated Si IV or Al III line can be used. Once the velocity law has been determined, the model is then used to reproduce the overall observed P Cygni profile for each ion analysed. Each model fit

yields measurements of the run of optical depth as a function of velocity for each ion that is analysed. This information can then be converted into the product of the mass loss rate and the ionisation fraction $\dot{M}q_i(v)$, using the input values for R_* and abundance. The quantity $\dot{M}q_i$ can be subsequently converted into values of $q_i(v)$ (the velocity-dependent ionisation fraction) *if* reliable estimates of the mass loss rate obtained either from radio measurements or Hα can be found for each star.

As discussed previously in §3.2.4, current observational mass loss rates for B supergiants are highly uncertain. This is primarily due to the lack of knowledge of the amount and extent to which B supergiant winds are clumped. Despite this, $\dot{M}_{\rm radio}$ provides the most reliable method of obtaining $\dot{M}$ since its determination depends on measuring an excess of continuum flux rather than fitting a variable line profile. However, the majority of B supergiants are too weak to be detected (Bieging *et al.*, 1989). Constraining $\dot{M}$ from model fits to the observed Hα profile thus remains the only practical method of determining mass loss for B supergiants. However it is difficult to obtain reliable values of $\dot{M}$ for several reasons. In a number of stars, the Hα profile undergoes significant variations, yet the models assume a steady-state, stationary wind that does not account for this variability. The model would need to be updated with an accurate knowledge of the wind density distribution in order to obtain a more precise value of $\dot{M}$. In addition, further variations are evident in the underlying photospheric component of the Hα line, which again are not accounted for by the model, introducing further error into the determination of Hα. This would also require a photospheric model to compensate for these variable photospheric features in order to improve the accuracy of the derived value of $\dot{M}$. For these reasons it would be preferable to derive mass loss rates from UV P Cygni profiles but, as stated previously, this is currently not possible due to a lack of a detailed knowledge of the ionisation structure of OB supergiant winds. In view of the dilemma in 'disentangling' $\dot{M}$ from q_i, the best approach is to assume the best available estimates of $\dot{M}$ in order to obtain estimates of q_i. In this analysis we use the mass loss rates derived in §3.2.4 from CMFGEN model fits to the Hα profile.

The specific details of the version of the SEI method used in this work are as follows. In order to analyse each ion, the following parameters are required as input:

- *Terminal velocity*: — needed to calculate the normalised velocity, defined as $w \equiv \frac{v(r)}{v_\infty}$

.

- *Velocity Law*: — a standard β - law of the form

$$w(x) = w_0 + (1 - w_0)\Big(1 - \frac{1}{x}\Big)^\beta \tag{5.6}$$

is used for an expanding wind (Lamers *et al.*, 1987); $x = \frac{r}{R_*}$ where R_* is the stellar radius and $w_0 = 0.01$ is adopted. β is a free parameter constrained by fitting the profile of a saturated wind line such as C^{3+}. The velocity law is governed by β and the shape of the velocity law subsequently affects the density distribution as described by the equation of mass continuity,

$$\dot{M} = 4\pi R_*^2 v_\infty x^2 w(x)\rho(x) \tag{5.7}$$

hence β also controls the overall profile shape; a small β value (e.g. 0.5) will produce a synthetic profile with a shallower and broader red emission peak than will a larger value (e.g. 2), since a low-β wind accelerates faster, causing low-velocity, red-shifted material to be occulted by the stellar disk.

- *Turbulent velocity*: — In order to allow for the effect of the macroscopic velocity field (due to e.g., shocks in the wind) on the line profile, a turbulent velocity field is incorporated into the code. It is described by a Gaussian distribution with a 1 σ dispersion parameter w_D and smooths out the distribution of $\tau(w)$ in the wind, which has the effect of extending saturated parts of P Cygni profiles by several times w_D.

- *Input photospheric spectrum*: — No accurate templates of purely photospheric FUV/UV flux distributions for OB stars exist, so high-resolution *IUE* spectra of B dwarf and giant stars are used as photospheric standards, adopting one standard per spectral type. The B stars chosen display little or no evidence of a stellar wind in their spectra and are also low $v_e sini$ objects. The photospheric standards were rotationally

broadened through convolution with a rotational profile so that they matched the rotational broadening of the B supergiant spectra. In general, agreement between observed photospheric absorption lines and those produced by SEI is good.

- *Optical depth in the wind*: — In the SEI method, the optical depth is assumed to be described by the *radial Sobolev optical depth*, $\tau_{\rm rad}$. This is a free parameter (once the velocity law and input photospheric spectrum have been constrained) which is modelled in a set of 21 independent velocity bins whose values are adjusted to fit the observed P Cygni profile. This avoids the problem of assuming a functional form for the optical depth distribution and any consequential biases. However, the model fitting technique depends upon the condition that only material with $w \leq w_i + w_D$ contributes to the formation of the line profile at w_i, assuming the stellar wind is a monotonically expanding, spherically symmetric outflow (this problem is discussed further in e.g. Lamers *et al.* 1999*b*). Using this technique, it is possible to determine the value of $\tau_{\rm rad}$ that fits the observed profile at $w \approx 1$ and then progress inwards to fit the rest of the absorption trough. For each optical depth bin i at velocity w_i, the value of $\tau_{\rm rad}(w_i)$ is adjusted until a satisfactory fit to the observed P Cygni profile at w_i is achieved. Derived values of $\tau_{\rm rad}(w_i)$ should be reliable provided that the assumption of spherical symmetry and the velocity law used are both valid for each individual star.

- *Ion fractions*: — These are the quantities required in order to investigate the ionisation structure of the stellar wind and are more physically meaningful than $\tau_{\rm rad}$. The ionisation fraction q_i is related to $\tau_{\rm rad}$ by the following equation

$$q_i(w) = \frac{m_e c}{\pi e^2} \frac{4\pi\mu m_{\rm H}}{f\lambda_0 A_E} \frac{R_* v_\infty^2}{\dot{M}} x^2 w \frac{dw}{dx} \tau_{\rm rad}(w) \tag{5.8}$$

where $q_i(w)$ is the fraction of the element E in ionisation state i at velocity w; μ is the mean molecular weight of the plasma; A_E is the abundance by number of element E relative to hydrogen ; m_e is the mass of an electron; e is the charge on an electron; c is the speed of light; f is the oscillator strength and λ_0 the rest wavelength of the line being analysed.

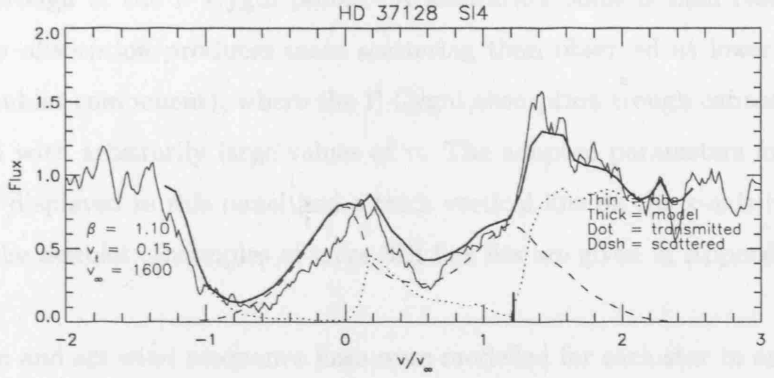

Figure 5.1: Example of SEI model fit to the Si IV $\sim \lambda\lambda$1393.76, 1402.77 line of the B0 Ia star ϵ Ori (HD 37128)

All these parameters must be input to the SEI code before attempting to fit a wind line, otherwise they are treated as free parameters.

5.1.2 Obtaining values of q_i from SEI

First the parameters of the velocity were derived from a saturated wind line, usually C IV $\lambda\lambda$1548.20, 1550.77 since it is usually highly saturated and strongly sensitive to the velocity field (Kudritzki & Puls, 2000). The dispersion parameter w_D was allowed to vary for each line to obtain an estimate of the turbulent velocity. The wind resonance lines were then modelled by applying a least squares fitting algorithm to the 21 bins of optical depth (producing a histogram representation of the optical depth as in Fig. 5.1) until a good fit to the observed P Cygni profile was achieved. If difficulties were encountered in fitting the P Cygni profile by varying τ, the photospheric parameters could be altered again in an attempt to improve the situation.

An example of an SEI fit to the Si IV $\sim \lambda\lambda$ 1393.76, 1402.77 line of the B0 Ia star ϵ Ori (HD 37128) is shown in Fig. 5.1. It shows the SEI model fit (*thick solid line*) to the observed P Cygni profile (*thin solid line*), along with the separate transmitted (*dotted line*) and scattered (*dashed line*) components of the model profile. Separating the transmitted and scattered components of the model profile provides useful insight into the line fitting procedure. An increase in τ at high velocity in order to decrease the transmitted flux will consequently increase the forward-scattered component at lower velocities in the

absorption trough of the P Cygni profile. A saturation point is then reached once the high-velocity absorption produces more scattering than observed at lower velocities (in the same doublet component), where the P Cygni absorption trough cannot be deepened further even with arbitrarily large values of τ. The adopted parameters for the velocity law are also displayed in this panel and a thick vertical line on the x-axis marks the rest velocity of the doublet. Examples of more SEI line fits are given in Appendix B.

Between two and six wind resonance lines were modelled for each star in our sample. An additional *IUE* data set of 86 B Ia – II stars was assembled for the analysis presented in Prinja *et al.* (2005), again for which two – six P Cygni profiles were modelled. This means that in total, given that, on average, four P Cygni profiles are present in each star, about 424 wind resonance lines have been analysed for 106 stars. This is a *very* comprehensive data set that allows us to investigate the trends in ionisation structure over a wide range of $T_{\rm eff}$ and luminosity. Obviously those lines that appear to be purely photospheric would not yield reliable values of $\dot{M}q_i$, so are omitted from the analysis. Using the stellar parameters presented in §3.2, $\dot{M}q_i$ was calculated from the values of $\tau_{\rm rad}$ obtained from the SEI modelling. Two different values for $\dot{M}q_i$ are given: $\dot{M}q_i^{0.5}$, (the value of $\dot{M}q_i$ at $w = 0.5$) and $< \dot{M}q_i >$ (the value of $\dot{M}q_i$ averaged over $0.2 \leq w \leq 0.9$). The values of $\dot{M}$ derived in §3.2.4 were then used to obtain estimates for $q_i^{0.5}$ and $< q_i >$. These final values of $q_i^{0.5}$ and $< q_i >$ are listed in Table 5.3.

5.2 Results of empirical q_i for Galactic B supergiants

The wind parameters adopted for the SEI line profile fits are given in Table 5.2 and imply a range of $0.5 \leq \beta \leq 3.0$ — larger than the range of $1.0 \leq \beta \leq 1.5$ derived from the optical stellar wind analysis in §3.2.3. This result is not entirely surprising since it is unlikely that a consistent velocity law with one β value is realistic, hence the option to use a 2-part β velocity law in codes such as CMFGEN, since the inner and outer parts of the wind are likely to be accelerating at different rates. In the majority of cases, the values of $\log q_i^{0.5}$ and $\log < q_i >$ agree to within $\pm$ 0.1 – 0.2 $\log q_i$, but there are a significant number of cases where the discrepancies are larger, up to a value of $\sim$ 1 in $\log q_i$. However it is of greater importance to note that *both* values of $\log q_i$ are found to be very small (never exceeding 4% regardless of how the mean q_i value is calculated), with none of the mean q_i

approaching unity. This result is particularly surprising given that $q_i Al^{2+}$, $q_i Si^{2+}$ & $q_i Si^{3+}$ should all peak within the given spectral type range. In the following sections, the trends of q_i with $T_{\rm eff}$ and normalised velocity w will be investigated in more detail.

5.2.1 Trends of q_i with $T_{\rm eff}$

Fig. 5.2 shows the trends of $\dot{M}q_i$ with $T_{\rm eff}$, whereas Fig. 5.3 gives the trends of the mean q_i with $T_{\rm eff}$. There is a strong link between the $T_{\rm eff}$ range over which a particular ion appears and the energy needed to create and destroy it. Results of $\dot{M}q_i$ determined from saturations or non-detections have been excluded. $< \dot{M}q_i(N^{4+}) >$ shows a plateau over 21 000 K $\leq T_{\rm eff} \leq$ 29 000 K then rapidly drops off at lower $T_{\rm eff}$, disappearing completely around 18 000 K. For $< q_i(N^{4+}) >$ there is a gradual increase (rather than a plateau) from $T_{\rm eff}$ = 18 000 – 29 000 K and the 'drop-off' between 18 000 – 20 000 K is not observed. The high $< q_i(N^{4+}) >$ value at $T_{\rm eff}$ = 28 500 K comes from the B0.2 Ia star HD 204172, which is slightly nitrogen weak and has a N^{4+} profile similar to both ϵ and κ Ori, making it difficult to explain why this star has a value of $< q_i(N^{4+}) >$ that is an order of magnitude higher than other stars of a similar $T_{\rm eff}$. $< \dot{M}q_i(C^{3+}) >$ also shows a similar pattern to $< \dot{M}q_i(N^{4+}) >$, displaying a plateau over a slightly larger range in $T_{\rm eff}$ of 20 000 K - 29 000 K then rapidly decreasing two orders of magnitude towards $T_{\rm eff}$ = 15 000 K. However the trend for $< q_i(C^{3+}) >$ is quite different, showing peaks at $T_{\rm eff}$ = 18 000 K and 28 000 K. It is probable that the peak at 18 000 K is not real since it only really depends on one data point (with log $q_i \sim 1.5$; if this data point is ignored then $< q_i(C^{3+}) >$ would appear to increase slightly from 24 000 K to 18 000 K before dropping off). Both $< \dot{M}q_i(Si^{3+}) >$ and $< q_i(Si^{3+}) >$ show a more interesting trend. The highest value of $< q_i(Si^{3+}) >$ is seen around $T_{\rm eff}$ = 28 000 K, after which $< q_i(Si^{3+}) >$ rapidly drops about an order of magnitude until $T_{\rm eff}$ = 28 000 K, gradually increases up to $T_{\rm eff}$ = 18 000 K then experiences another rapid drop towards lower $T_{\rm eff}$. $< \dot{M}q_i(Si^{2+}) >$ does not demonstrate a clear trend, with values undulating and showing peaks at $T_{\rm eff}$ = 28 000 K and $T_{\rm eff}$ = 22 000 K. For $< q_i(Si^{2+}) >$ a clearer trend does emerge, with values decreasing quite rapidly from 29 000 K to 23 500 K, then gradually increasing to 15 000 K. $< q_i(Al^{2+}) >$ is present in 8 of the 20 stars analysed, but shows a clear peak at $T_{\rm eff}$ = 20 000 K, which is harder to discern in $< \dot{M}q_i(Al^{2+}) >$ where a peak appears around 20 000 K. Finally $< q_i(C^{+}) >$ is only detected in 4 stars with $T_{\rm eff} \sim$ 18 000 K so it is not possible to draw any accurate conclusions about the variation of $< q_i(C^{+}) >$ with $T_{\rm eff}$ from this data. In general the B

Table 5.2: SEI velocity law parameters

HD No	Sp. Type	v_∞	β	$v_{\rm turb}$	$\dot{M}_{\rm H\alpha}(10^{-6}M_\odot)$	Notes on Hα
37128	B0 Ia	1600	1.10	0.16	1.90	var
192660	B0 Ib	1850	1.30	0.12	$\leq$5.00	P Cyg
204172	B0.2 Ia	1940	0.90	0.11	$\geq$0.57	abs
38771	B0.5 Ia	1390	1.10	0.15	1.1	var
185859	B0.5 Ia	1440	0.75	0.12	0.50	abs
213087	B0.5 Ib	1485	0.50	0.10	$\geq$0.45	abs
64760	B0.5 Ib	1600	1.00	0.10	1.10	rot
2905	B0.7 Ia	850	1.60	0.17	2.50	em
13854	B1 Iab(e)	955	1.00	0.13	1.50	P Cyg
190066	B1 Iab(e)	1285	0.90	0.12	0.70	abs
190603	B1.5 Ia+	390	3.00	0.17	$\leq$2.40	em
193183	B1.5 Ib	720	1.20	0.12	$\leq$1.00	abs
14818	B2 Ia	625	2.06	0.12	$\leq$1.00	P Cyg, var
206165	B2 Ib	675	2.00	0.11	$\leq$0.50	P Cyg
198478	B2.5 Ia	550	1.00	0.23	$\leq$0.50	em
42087	B2.5 Ib	650	1.16	0.14	$\leq$0.50	P Cyg, var
53138	B3 Ia	500	1.00	0.15	0.45	P Cyg, var
58350	B5 Ia	200	1.00	0.23	$\leq$0.50	abs, var
164353	B5 Ib/II	450	1.00	0.08	0.06	abs
191243	B5 Ib/II	550	1.00	0.23	$\geq$0.83	abs

Velocity law parameters derived from SEI modeling of UV wind lines. Note that the values of $v_{\rm turb}$ are averages of the $v_{\rm turb}$ values derived from each wind resonance line. Values of $\dot{M}_{\rm H\alpha}$ are taken from Table 3.4. Abbreviations for the notes are as follows: var = variable, abs = absorption, em = emission, rot = rapid rotator and P Cyg = some degree of a 'P Cygni' type profile morphology.

Table 5.3: Empirical q_i for the sample of 20 Galactic B supergiants

HD	Sp. Type	$< q_i N^{4+} >$	$q_i^{0.5} N^{4+}$	$< q_i C^{3+} >$	$q_i^{0.5} C^{3+}$	$< q_i Si^{3+} >$	$q_i^{0.5} Si^{3+}$	$< q_i Si^{2+} >$	$q_i^{0.5} Si^{2+}$	$< q_i Al^{2+} >$	$q_i^{0.5} Al^{2+}$	$< q_i C^{+} >$	$q_i^{0.5} C^{+}$
37128	B0 Ia	-2.82	-2.80	-2.71	-2.67	-2.44	-2.41	-3.25	-3.55	-	-	-	-
192660	B0 Ib	-	-	-2.31	-2.39	-2.99	-2.96	-	-	-	-	-	-
204172	B0.2 Ia	-1.42	-1.43	-1.69	-1.51	-1.60	-1.53	-2.31	-2.48	-	-	-	-
38771	B0.5 Ia	-2.70	-2.56	-2.05	-2.06	-2.77	-2.64	-3.66	-3.87	-	-	-	-
185859	B0.5 Ia	-2.30	-2.14	-1.83	-1.63	-2.38	-2.20	-	-	-	-	-	-
213087	B0.5 Ib	-2.39	-2.30	-1.68	-1.55	-1.99	-2.04	-2.74	-2.94	-	-	-	-
64760	B0.5 Ib	-2.72	-2.58	-3.18	-2.98	-2.74	-2.61	-3.67	-3.59	-2.87	-2.63	-	-
2905	B0.7 Ia	-	-	-2.52	-2.76	-2.82	-3.10	-3.55	-3.78	-2.37	-2.50	-	-
13854	B1 Iab(e)	-3.14	-3.81	-2.06	-2.07	-2.26	-2.22	-3.20	-3.08	-	-	-	-
190066	B1 Iab (e)	-3.12	-3.09	-2.55	-2.60	-2.97	-2.87	-3.25	-3.07	-2.75	-2.49	-	-
190603	B1.5 Ia+	-5.16	-6.51	-2.48	-3.39	-3.16	-4.14	-4.09	-4.62	-2.30	-3.96	-	-
193183	B1.5 Ib	-2.90	-3.20	-1.63	-1.61	-2.37	-2.27	-	-	-	-	-	-
14818	B2 Ia	-3.97	-4.70	-2.18	-3.30	-2.27	-2.89	-3.42	-3.57	-1.45	-1.81	-1.70	-2.55
206165	B2 Ib	-3.17	-4.19	-1.90	-2.78	-2.42	-2.97	-3.01	-3.57	-1.93	-1.89	-2.54	-3.00
198478	B2.5 Ia	-	-	-2.48	-2.69	-2.47	-2.66	-	-	-1.91	-1.60	-2.12	-2.24
42087	B2.5 Ib	-	-	-2.25	-2.29	-2.56	-2.44	-2.10	-1.82	-2.77	-2.63		
53138	B3 Ia	-	-	-2.33	-2.20	-2.50	-2.50	-2.72	-2.70	-2.07	-1.71	-2.21	-1.96
58350	B5 Ia	-	-	-3.85	-3.24	-4.12	-4.20	-	-	-3.31	-2.70	-	-
164353	B5 Ib/II	-	-	-2.60	-2.25	-3.12	-2.87	-3.01	-2.64	-	-	-	-
191243	B5 Ib/II	-	-	-3.86	-3.85	-3.12	-2.87	-	-	-	-		

Empirical q_i for the sample of 20 Galactic B supergiants. $< q_i >$ is derived from the value of $< \dot{M} q_i >$ integrated over $0.2 \leq w \leq 0.9$, whereas $q_i^{0.5}$ is derived from the value of $\dot{M} q_i^{0.5}$ evaluated at $w = 0.5$.

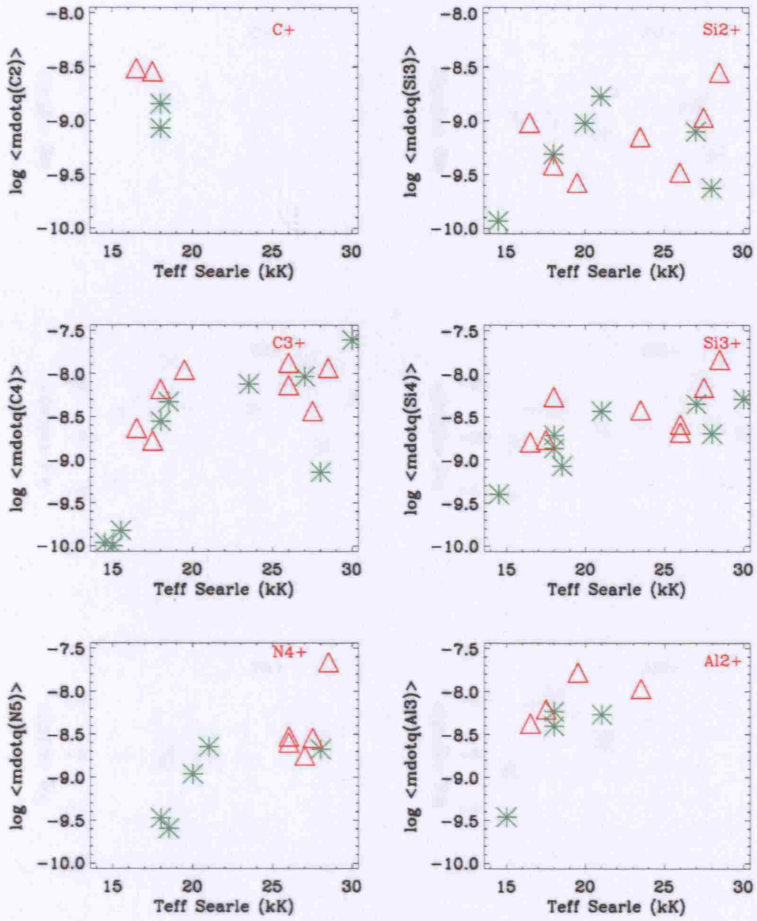

Figure 5.2: Trend of $< \dot{M} q_i >$ with $T_{\rm eff}$. The B Ia supergiants are represented by triangles and the B Ibs by an *.

Ias tend to have higher mean q_i than the B Ibs for similar $T_{\rm eff}$, though this is not the case for $< q_i(\mathrm{Si}^{2+}) >$ at lower $T_{\rm eff}$ (15 000 – 23 500 K).

These results support those of Prinja *et al.* (2005), where a preliminary analysis of 106 B0–B5 stars was undertaken to derive mean values of q_i. For this analysis the $T_{\rm eff}$ scale of Humphreys & McElroy (1984) was used (as opposed to values of $T_{\rm eff}$ derived for each star) as values of $\dot{M}$ were obtained using the Vink *et al.* (2000) mass loss prescription. Hence the advantage of analysis undertaken in this thesis work is that individual stellar $T_{\rm eff}$ and $\dot{M}$ values are used, avoiding the problem of dealing with 'spectral bins' when comparing $< q_i >$ with $T_{\rm eff}$ and the discrepancy associated with $\dot{M}$ calculated using the Vink *et al.*

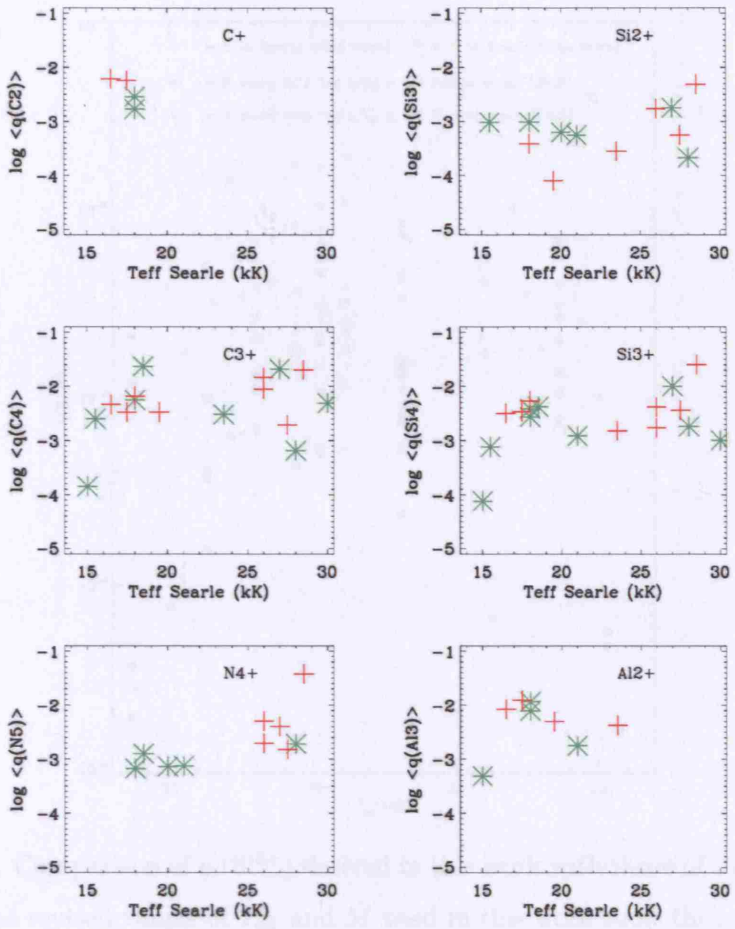

Figure 5.3: Trend of $< q_i >$ with $T_{\rm eff}$. The B Ia supergiants are represented by + and the B Ibs by an *.

(2000) mass loss prescription and those derived from Hα. Prinja *et al.* (2005) found similar trends between mean q_i and $T_{\rm eff}$ for their 106 stars, since the use of a revised $T_{\rm eff}$ scale lowering $T_{\rm eff}$ values by 1000 – 2000 K does not drastically change the range in $T_{\rm eff}$ over which Al^{2+}, $Si^{3+}$and Si^{2+} peak. This is proved by Fig.s 5.4 & 5.5, where a comparison of the two data sets has been made. However, there are some distinct differences, which are partly due to the difference in sample sizes. For example, $< q_i Si^{3+} >$ still shows a peak around $T_{\rm eff}$ = 20 000 K but the stronger peak detected at 28 000 K is not present in the Prinja *et al.* (2005) data. The peak in $< q_i Al^{2+} >$ around 18 000 – 20 000 K is clearly shown in both data sets. Since Prinja *et al.* (2005) analysed a much larger sample of stars, they were able to distinguish a trend for $< q_i C^{+} >$, where it increases from 15 000 K, peaks at 18 000 K and then suddenly disappears. This effect does not depend on stellar luminosity,

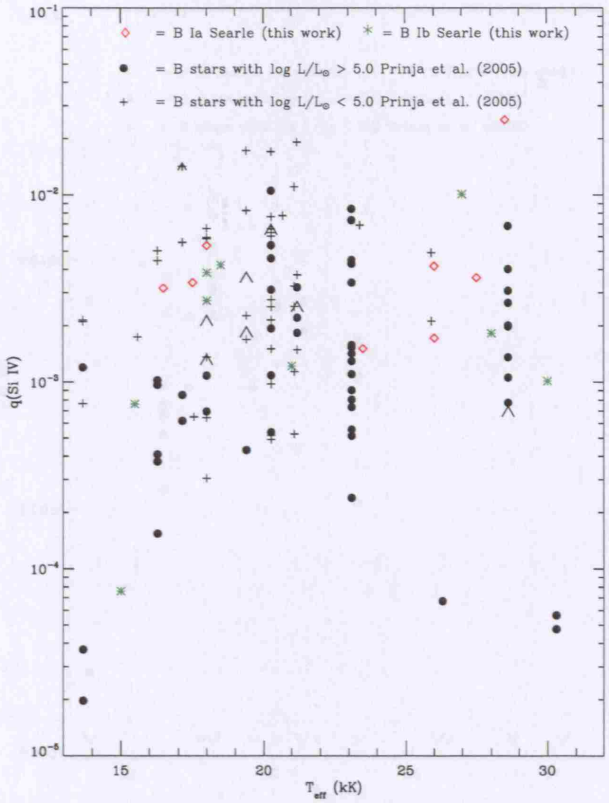

Figure 5.4: Comparison of $q_i(\mathrm{Si}^{3+})$ derived in this work with those of Prinja *et al.* (2005). The revised values of T_{eff} and $\dot{M}$ used in this work show that the Prinja *et al.* (2005) results are still valid, though the peak in $q_i(\mathrm{Si}^{3+})$ observed at $T_{\mathrm{eff}} \sim$ 20 000 K appears around 18 000 K in the smaller sample with revised T_{eff}.

but could be explained by the proximity of the ionisation potentials of C^+ at 24.38 eV and He I at 24.48 eV (Prinja *et al.*, 2005). The stellar radiation field in the He^+ continuum (228 Å$\leq \lambda \leq$ 506 Å) can be drastically increased by up to a factor of 30 (Kurucz, 1991) through the ionisation of He to He^+ in the stellar photosphere. Such a huge increase in the stellar radiation field could result in converting all the C^+ present in the wind into C^{2+}. Prinja *et al.* (2005) also noticed that N^{4+} appears in the wind around 18 000 K, which could also be related to this increase in the stellar radiation field in the He^+ continuum. It is certainly possible for this radiation to produce N^{3+} and if this occurs in significant quantities, ionisation of excited levels in N^{3+} can lead to the production of N^{4+} in the wind.

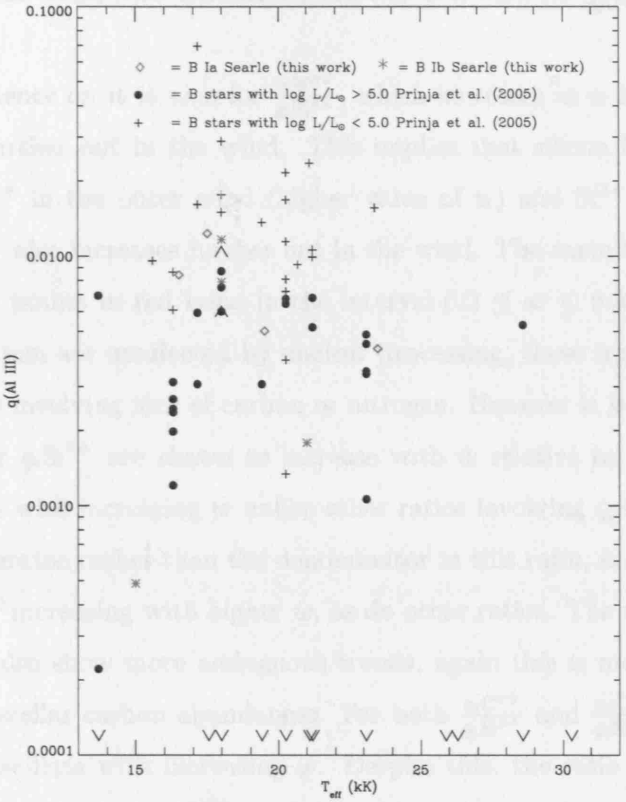

Figure 5.5: Comparison of $q_i(\mathrm{Al}^{2+})$ derived in this work with those of Prinja *et al.* (2005). The revised values of $T_{\rm eff}$ and $\dot{M}$ used in this work show that the Prinja *et al.* (2005) results are still valid.

5.2.2 Trends of q_i with w

It is also of interest to examine the behaviour of q_i with velocity in order to work out whether ionisation increases or decreases further out in the wind. Relative q_i have been plotted against w for $0.2 \leq w \leq 0.9$, which roughly corresponds to $1.2 \leq \frac{r}{R_*} \leq 10$. Fig. 5.6 shows the relative ionisation q_i of $\frac{q_i\mathrm{Si}^{2+}}{q_i\mathrm{Si}^{3+}}$, $\frac{q_i\mathrm{Si}^{2+}}{q_i\mathrm{Al}^{2+}}$, $\frac{q_i\mathrm{Si}^{3+}}{q_i\mathrm{Al}^{2+}}$, $\frac{q_i\mathrm{N}^{4+}}{q_i\mathrm{C}^{3+}}$, $\frac{q_i\mathrm{N}^{4+}}{q_i\mathrm{Si}^{3+}}$, $\frac{q_i\mathrm{N}^{4+}}{q_i\mathrm{Si}^{2+}}$, $\frac{q_i\mathrm{N}^{4+}}{q_i\mathrm{Al}^{2+}}$, $\frac{q_i\mathrm{C}^{3+}}{q_i\mathrm{Si}^{3+}}$, $\frac{q_i\mathrm{C}^{3+}}{q_i\mathrm{Si}^{2+}}$ and $\frac{q_i\mathrm{Al}^{2+}}{q_i\mathrm{C}^{+}}$ against w. The data are colour-coded such that red points represent data from a star with 26 000 K $\leq T_{\rm eff} \leq$ 28 000 K; green represents stars with 18 000 K $\leq T_{\rm eff} \leq$ 26 000 K and blue represents stars with 14 500 K $\leq T_{\rm eff} \leq$ 18 000 K. Note that only values of q_i derived from *unsaturated* line profiles are included in the data. Trends of the relative ionisation stages of nitrogen and carbon will be less clear since many of the stars in our sample show varying degrees of CNO processing (see §3.2.6); this may well

explain why no clear trend with normalised velocity w is seen for $\frac{q_i N^{4+}}{q_i C^{3+}}$.

A stronger dependence on w is seen for $\frac{q_i N^{4+}}{q_i Si^{3+}}$, which increases as w increases and $\frac{q_i N^{4+}}{q_i Si^{2+}}$, which decreases further out in the wind. This implies that silicon is more likely to be in the form of Si^{3+} in the outer wind (higher value of w) and Si^{2+} in the inner wind. The ratio of $\frac{q_i N^{4+}}{q_i Al^{2+}}$ also increases further out in the wind. The same is true of $\frac{q_i Si^{2+}}{q_i Al^{2+}}$ and $\frac{q_i Si^{3+}}{q_i Al^{2+}}$, if the data points in red lying in the interval $0.2 \leq w \leq 0.3$ are ignored. Since silicon and aluminium are unaffected by nuclear processing, these trends should be more reliable than those involving ions of carbon or nitrogen. However it is still a little strange that *both* $q_i Si^{2+}$ & $q_i Si^{3+}$ are shown to increase with w relative to $q_i Al^{2+}$. For $\frac{q_i Al^{2+}}{q_i C^{3+}}$, the ratio decreases with increasing w unlike other ratios involving $q_i Al^{2+}$. However since $q_i Al^{2+}$ is the numerator rather than the denominator in this ratio, it still provides strong evidence for $q_i Al^{2+}$increasing with higher w, as do other ratios. The remaining ion ratios involving carbon also show more ambiguous trends, again this is most probably due to different intrinsic stellar carbon abundances. For both $\frac{q_i C^{3+}}{q_i Si^{3+}}$ and $\frac{q_i C^{3+}}{q_i Si^{2+}}$, the data is seen to converge and oscillate with increasing w. Despite this, the ratio of $\frac{q_i C^{3+}}{q_i Si^{3+}}$ suggests a decrease as w increases whereas $\frac{q_i C^{3+}}{q_i Si^{2+}}$ implies an increase to-wards higher w. This directly contradicts the earlier conclusion drawn from the ratios of $\frac{q_i N^{4+}}{q_i Si^{3+}}$ and $\frac{q_i N^{4+}}{q_i Si^{2+}}$, which hinted that $q_i Si^{3+}$ was present in large quantities further out in the wind. This dilemma should be settled by examining the ratio of $\frac{q_i Si^{3+}}{q_i Si^{2+}}$. In the trends for the hotter stars in the range 18 000 K $\leq T_{\rm eff} \leq$ 28 000 K (red & green data) where Si^{3+} is dominant, the ratio decreases further out in the wind, suggesting that there is less Si^{3+} present in the wind at this distance. The reverse appears to be true of Si^{2+}, since the trend for the cooler stars ($T_{\rm eff} \leq$ 18 000 K) implies that more Si^{2+} is found further out in the wind; however, this evidence is only based on the behaviour of the ions in a single star so cannot be assumed as typical. It is also clear from this plot that the trends of q_i with w are not smooth, providing more evidence for the clumped and highly structured nature of these stellar winds. A larger data set is required to discern clearer trends of the relative ionisation fractions with normalised velocity. It would then be possible to test the finding of Prinja *et al.* (2005), that ionisation fractions tended to *higher* ionisation stages further out in the wind; there is certainly evidence here to support that statement. Interestingly these findings are in contradiction with those of O stars, which show that ionisation *decreases* with increased distance from the star (Massa *et al.*, 2003).

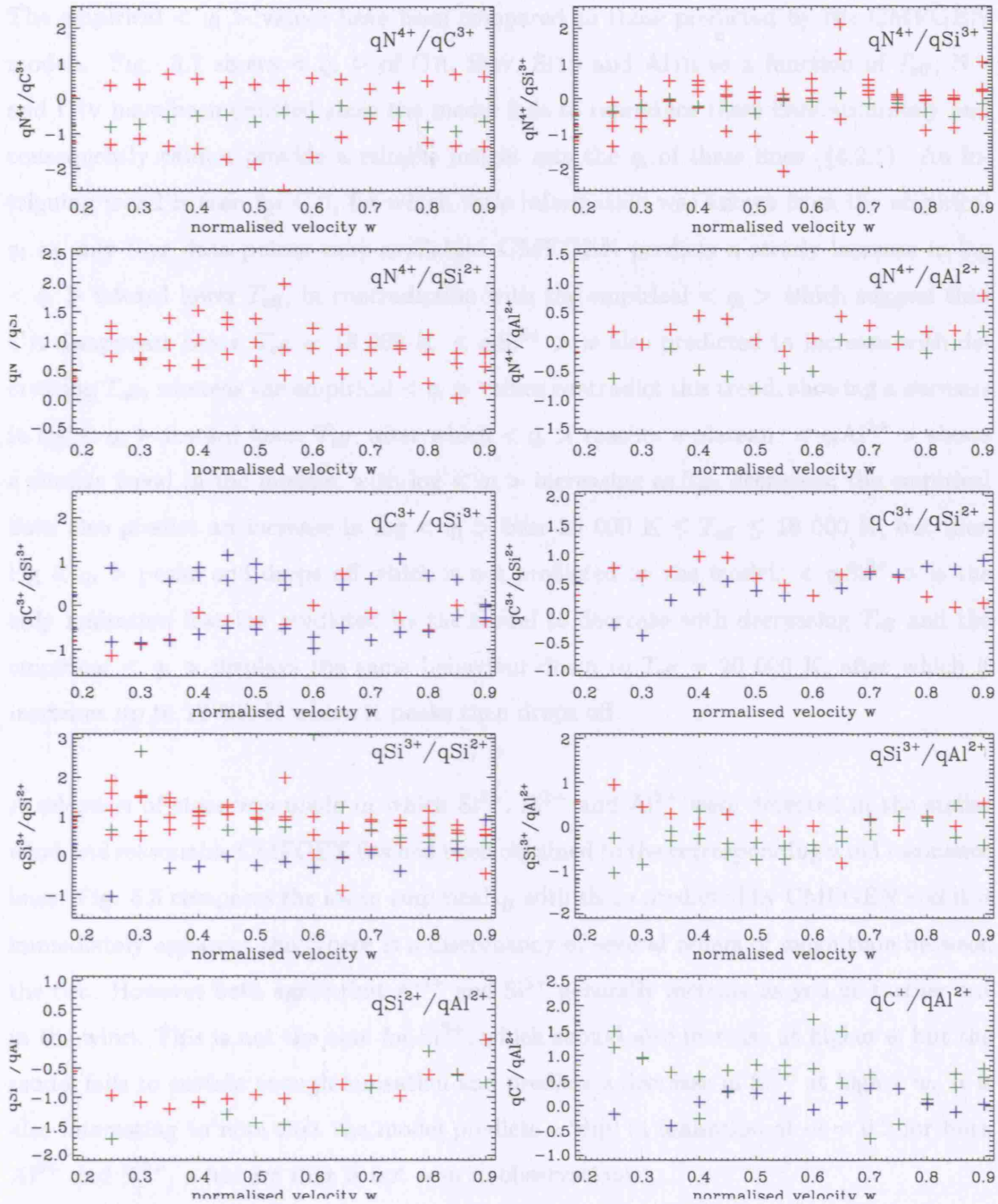

Figure 5.6: Relative q_i vs. normalised velocity w. The data is colour-coded according to the adopted temperature of the star from which the relative ionisation fraction was taken; red denotes 26 000 K $\leq T_{\rm eff} \leq$ 30 000 K, green 18 000 K $\leq T_{\rm eff} \leq$ 26 000 K and blue $T_{\rm eff} \leq$ 18 000 K.

5.2.3 Comparison of model and empirical q_i

The empirical $< q_i >$ values have been compared to those predicted by the CMFGEN models. Fig. 5.7 shows $< q_i >$ of C II, Si IV, Si III and Al III as a function of $T_{\rm eff}$; N V and C IV have been omitted since the model fails to reproduce these lines accurately and consequently cannot provide a reliable insight into the q_i of these lines (§4.2.1). An intriguing trend is seen for C II, for which little information was known from the empirical q_i as only four data points were available. CMFGEN predicts a steady increase in log $< q_i >$ toward lower $T_{\rm eff}$, in contradiction with the empirical $< q_i >$ which suggest that C II disappears below $T_{\rm eff}$ = 18 000 K. $< q_i {\rm Si}^{2+} >$ is also predicted to increase with decreasing $T_{\rm eff}$, whereas the empirical $< q_i >$ values contradict this trend, showing a *decrease* in log $< q_i >$ toward lower $T_{\rm eff}$, after which $< q_i >$ reaches a plateau. $< q_i {\rm Al}^{2+} >$ shows a similar trend in the models, with log $< q_i >$ increasing as $T_{\rm eff}$ decreases; the empirical data also predict an increase in log $< q_i >$ over 25 000 K $\leq T_{\rm eff} \leq$ 18 000 K, but then log $< q_i >$ peaks and drops off which is not predicted by the model. $< q_i {\rm Si}^{3+} >$ is the only ionisation fraction predicted by the model to decrease with decreasing $T_{\rm eff}$ and the empirical $< q_i >$ displays the same behaviour down to $T_{\rm eff}$ = 20 000 K, after which it increases up to 18 000 K where it peaks then drops off.

A selection of stars was made in which Si^{3+}, Si^{2+} and Al^{2+} were detected in the stellar wind *and* reasonable CMFGEN fits had been obtained to the corresponding wind resonance lines. Fig. 5.8 compares the mean empirical q_i with those predicted by CMFGEN and it is immediately apparent that there is a discrepancy of several orders of magnitude between the two. However both agree that Al^{2+} and Si^{2+} generally increase as you go further out in the wind. This is not the case for Si^{3+}, which should also increase at higher w but the model fails to sustain enough ionisation and predicts a decrease in Si^{3+} at higher w. It is also interesting to note that the model predicts a 'dip' in ionisation at $w = 0.2$ for both Al^{2+} and Si^{2+}, a feature that is not seen in observations.

5.3 Potential sources of error in our results

As highlighted by Fullerton *et al.* (2006), estimates of $\dot{M} q_i$ and q_i for various ions are likely to be affected by uncertainties in the values of $\dot{M}$ derived from Hα, abundance of each ion and the variability of the P Cygni profiles of the ions analysed. Each parameter will now

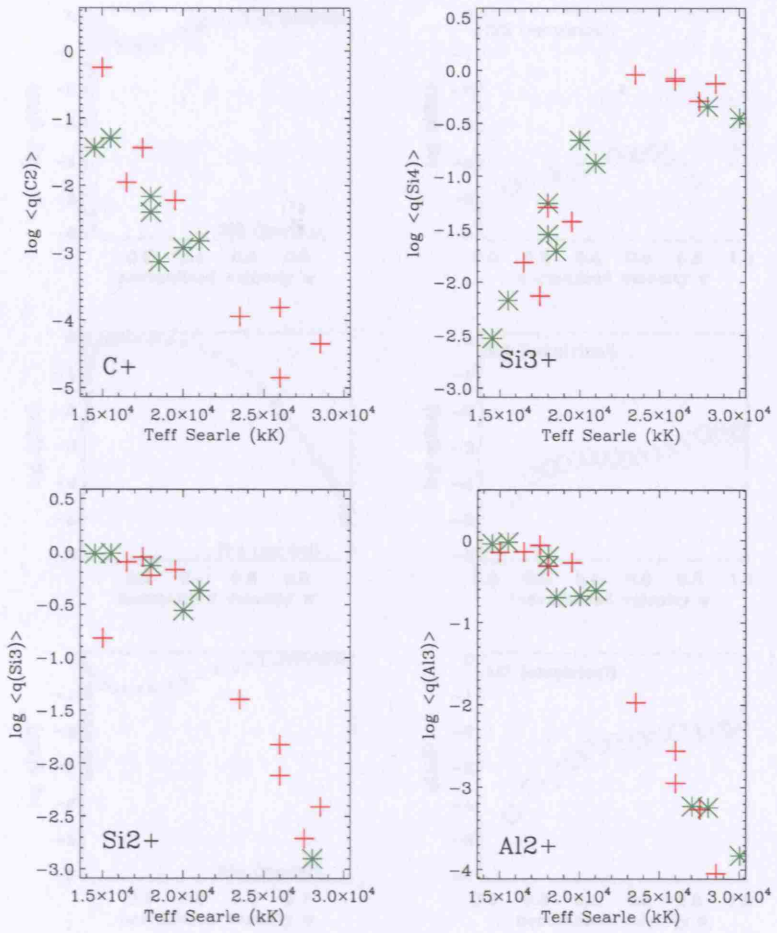

Figure 5.7: Trends of mean CMFGEN q_i of C^{+}, Si^{2+}, Si^{3+} and Al^{2+} with $T_{\rm eff}$. B Ia stars are marked in red with a plus sign whereas B Ibs are denoted in green with an asterisk.

be examined for any systematic bias which could have affected the data.

5.3.1 Errors in $\dot{M}_{\rm H\alpha}$

The most significant problem encountered in determining $\dot{M}$ is that CMFGEN is unable to reproduce Hα when it assumed a P Cygni-shaped profile, which led to an overestimation of $\dot{M}$ (these $\dot{M}$ are therefore denoted as upper limits). Even for some Hα in emission, the mass loss rate is slightly overestimated (see e.g., κ Cas and HD 190603 in Fig. 3.13). The reliability of each individually derived $\dot{M}$ is different. For example, two of the stars in our sample, ϵ and κ Ori (HD 37128 and HD 38771 respectively) are known to display

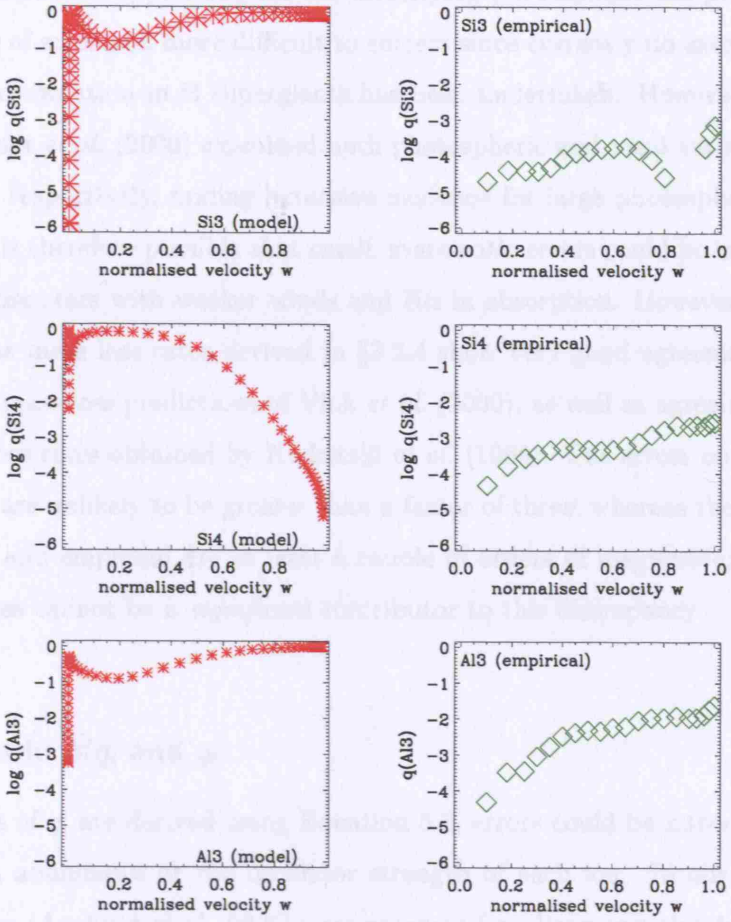

Figure 5.8: Comparison of model and empirical q_i for HD 190603

significant variability in Hα. In addition to this, CMFGEN encounters several problems in reproducing some of the observed Hα profiles, as discussed in detail in §3.2.4, therefore some derived values of $\dot{M}$ have been denoted as upper/lower limits where the model Hα profile has over/under- estimated the observed profile.

The mass loss rate is also sensitive to the stellar parameters, particularly $T_{\rm eff}$ and luminosity. As Fullerton *et al.* (2006) remarked, $\dot{M}_{\rm H\alpha}$ is affected by changes in $T_{\rm eff}$ as its determination depends on the wind density distribution and the excitation equilibrium of H. Given that newly derived parameters have been used in this work, this is unlikely to be a large source or error.

The issue of compensating precisely for the underlying photospheric Hα profile is a more probable source of error and more difficult to correct since currently no extensive study of photospheric Hα variation in B supergiants has been undertaken. However Prinja *et al.* (2004) and Kaufer *et al.* (2006) examined both photospheric and wind variability of ϵ Ori and HD 64760, respectively, finding extensive evidence for large photospheric variations in each star. It is therefore possible that small, systematic errors could be introduced into our data for those stars with weaker winds and Hα in absorption. However, it should be recalled that the mass loss rates derived in §3.2.4 show very good agreement (to within 20 %) with the mass loss predictions of Vink *et al.* (2000), as well as agreeing with observational mass loss rates obtained by Kudritzki *et al.* (1999). The errors on the mass loss rates used here are unlikely to be greater than a factor of three, whereas the discrepancies between model and empirical are at least a couple of orders of magnitude; therefore the error in mass loss cannot be a *significant* contributor to this discrepancy.

5.3.2 Errors in $\dot{M}q_i$ and q_i

Since the values of q_i are derived using Equation 5.8, errors could be introduced through uncertainties in abundance or the oscillator strength of each ion. In our SEI analysis, solar abundances (Asplund *et al.*, 2005) were assumed for silicon and aluminium, which is not expected to introduce any important errors into our analysis, particularly since these elements are unaffected by nuclear processing. For carbon, nitrogen and oxygen, the CNO abundances derived in §3.2.6 are adopted and should be reliable. Since these abundances were obtained for individual stars, it is highly improbable that they could contribute to a systematic error. Similarly it can be safely assumed that the oscillator strengths of the transitions are also reliable.

Another potential flaw is that the expectation of some ions to reach unity in the B star spectral range may be mistaken. The CMFGEN models certainly support the view that Si^{3+} is dominant for early B0–B2 supergiants, after which Si^{2+} and Al^{2+} become dominant for B2–B5 supergiants, as discussed in §5.2.3. Here it was also pointed out that the models contradict the observations in predicting C^{+} to still be dominant around $T_{\rm eff}$= 15 000 K, since it is seen to disappear at this temperature. It is somewhat harder to justify the expectation of $< q_i N^{4+} >$ and $< q_i C^{3+} >$ approaching unity since the models are not

capable of reproducing the P Cygni profiles (see §4.2.1) so cannot provide us with a reliable estimation of their ionisation state. The fact remains that *all* the values of q_i are *consistently* at least two orders of magnitude lower than expected and none of the potential sources of error discussed above could have produced a systematic error that could be responsible for the small q_i values obtained for all ions.

5.4 Implications for Mass Loss Rates

In the previous section it was shown that no plausible source of important, systematic error in obtaining $\dot{M}q_i$ could be found, so the estimates will be treated as reliable. In that case, the cause of the discrepancy between empirical and predicted values of q_i must lie with the derivation of $\dot{M}$; however, it has already been shown that the magnitude of error in constraining $\dot{M}$ from Hα is apparently not large enough to resolve the discrepancy between model and empirical values of q_i.

In order to resolve the issue of unexpectedly low empirical q_i values, it is therefore necessary to review the assumptions of the standard model, particularly that stellar winds are smooth and homogeneous. If clumping were incorporated into these estimates of $\dot{M}$ (see §3.2.5), the values of $\dot{M}$ would be lowered and therefore the values of q_i obtained from $\dot{M}q_i$ would be higher. Looking again at Fig. 5.8, the empirical q_i values from Si^{3+}, Si^{2+} and Al^{2+} need to increase by 2–4 orders of magnitude, which requires the corresponding mass loss rates to be 2.4×10^{-8} – 2.4×10^{-10} $M_\odot$ yr^{-1}. These lower $\dot{M}$ values in turn suggest that values of $10^{-6} \leq f_\infty \leq 10^{-3}$ need to be used when the clumping option is switched on in CMFGEN. It is uncertain if such small filling factors are realistic, since the current treatment of clumping in CMFGEN is quite crude and has yet to be justified as appropriate for inhomogeneous line driven winds. However, given the many caveats and problems associated with obtaining observed mass loss rates in the optical and radio wavelength regions, such a drastic reduction is not implausible.

This problem is not unique to B supergiants, but it also an important issue for O stars. Previous work to examine the UV wind resonance lines of O stars has been carried out by, e.g., Lamers *et al.* (1999*a*), who investigated the dependence of the ionisation fractions on temperature and density. It is noticeable that the values they obtained for the ioni-

sation fractions are 2 to 4 orders of magnitude below unity. More recently Massa *et al.* (2003) used *FUSE* spectra to determine values of q_i for a sample of LMC O stars, again employing the SEI method on the resonance lines of C III, N III, S IV, P V, S VI and O VI. They found that none of the derived ionisation fractions approach unity, even for ions that are expected to be dominant in O star winds, such as P V. Another interesting result is that the wind ionisation appears to shift towards lower ionisation stages further out in the wind (with the exception of O VI and S VI), which contradicts the scenario predicted by the nebular approximation, as well as current indications found for B supergiants (both in this work and by Prinja *et al.* 2005). Differing dominant production mechanisms are also implied for O VI and S VI according to these results.

Following on from this work, Fullerton *et al.* (2006) carried out a study of the behaviour of P^{4+} in the winds of 40 Galactic O stars. P^{4+} is predicted to be dominant in mid-O star winds according to both morphological O star spectral trends and detailed FASTWIND modelling of O stars. Additionally, P^{4+} is a good candidate to use to examine the low q_i problem further since it has a low cosmic abundance, and therefore rarely saturates, as well as being unaffected by nuclear processing in the star. Given that P^{4+} is dominant for mid-O stars, $q_i(P^{4+})$ is expected to approach unity over some corresponding range in $T_{\rm eff}$ so $< \dot{M} q_i(P^{4+}(w)) >$ should agree with $\dot{M}_{\rm H\alpha}$ and/or $\dot{M}_{\rm radio}$ for the same range. However, this is not the case, Fullerton *et al.* (2006) found that the values of $< \dot{M} q_i(P^{4+}(w))$ are consistently smaller than the values of $\dot{M}(\rho^2)$ (see Fig. 5.9) and the magnitude of this discrepancy shows no dependence on whether $\dot{M}(\rho^2)$ is taken from $\dot{M}_{\rm H\alpha}$ or $\dot{M}_{\rm radio}$. However there is a trend with spectral type. The smallest deviation is found for O4 – O7.5 stars, whilst O2 – O3.5 & O8 – O9.7 stars show an even larger discrepancy. The largest deviation from a 1:1 correlation line is found for a group of 5 mid-O dwarfs and giants, who have $\dot{M}(\rho^2)$ based on $\dot{M}_{\rm H\alpha}$ and upper limits for $\dot{M} q_i(P^{4+})$, meaning that the blue (stronger) component of the P^{4+} doublet has $\tau_{\rm rad}(w) \leq 0.05$. Adopting the appropriate values of $\dot{M}_{\rm H\alpha}$ or $\dot{M}_{\rm radio}$ for each star, this translates as the value of $q_i(P^{4+})$ never exceeding ~ 0.11 for supergiants, ~ 0.06 for giants and ~ 0.04 for dwarf stars. Understanding the clumped and inhomogeneous nature of OB star winds is crucial to resolving the issue of low q_i values, but requires knowledge of the distribution of material in the wind. As noted by Massa *et al.* (2003), the *porosity* of the wind could be the prime cause of the problem. If a sufficient amount of dense material present in a smooth wind is redistributed such that

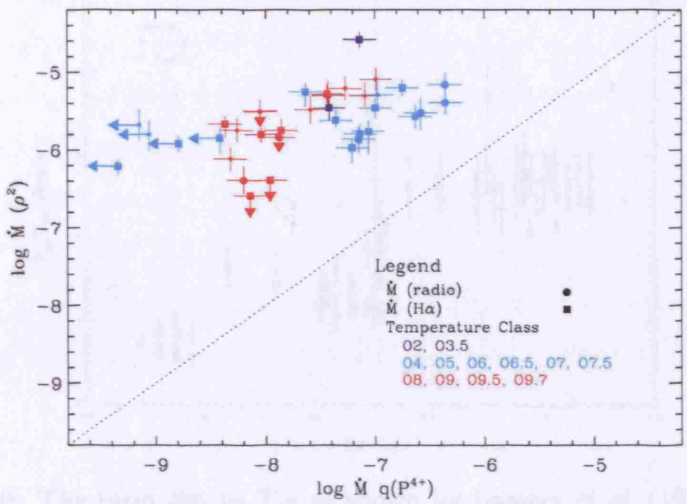

Figure 5.9: Comparison of $\dot{M}(\rho^2)$ with $\dot{M}q_i(\mathrm{P}^{4+})$for a sample of 40 Galactic O stars. Values of $\dot{M}q_i(\mathrm{P}^{4+})$ are consistently lower than $\dot{M}(\rho^2)$, with the size of the discrepancy depending on luminosity class. The dotted line indicates a 1–1 correlation between $\dot{M}(\rho^2)$ and $\dot{M}q_i(\mathrm{P}^{4+})$.

the wind consists of optically-thick clumps dispersed by transparent voids, then unlike the case of a smooth wind, the material present in the wind would only cover a fraction of the solid angle surrounded by the star, meaning that less radiation will be scattered into the line of sight. This will result in an unsaturated absorption trough *despite* the presence of optically-thick clumps since they do not cover the entire surface of the star at any velocity, allowing unattenuated flux to escape. It then follows that fitting a P Cygni profile formed in a clumped wind with a smooth, homogeneous wind model will lead to an under-estimation of τ_{rad}, resulting in low values of q_i.

The first strong implication of this is that the standard model for hot star winds needs to be revised. It would, however, have large consequences for stellar evolutionary and star-formation calculations, since the predictions of these theoretical models depend heavily on the mass loss from massive stars and subsequent injection of material into the ISM. In the case of stellar evolution, mass loss from a star constantly alters the stellar mass, so that a change of several orders of magnitude in mass loss will, for example, affect whether a massive star ends its life as a neutron star or black hole. This in turn affects the expected

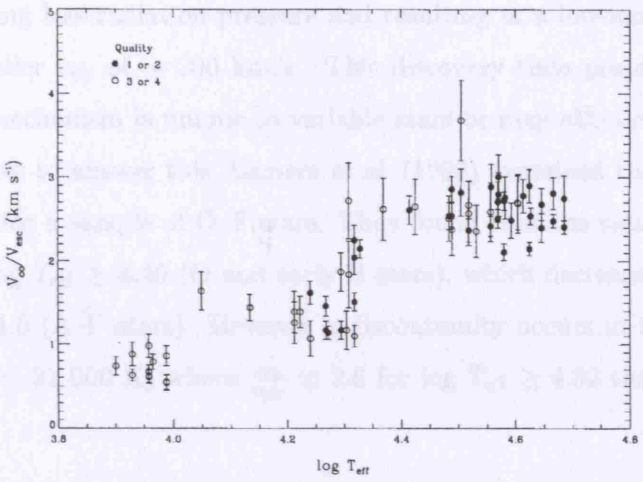

Figure 5.10: The ratio $\frac{v_\infty}{v_{\rm esc}}$ vs $T_{\rm eff}$ as shown by Lamers *et al.* (1995). Note the discontinuity around log $T_{\rm eff}$ = 4.3 ($T_{\rm eff}$ = 21 000 K) corresponding to the bi-stability jump.

number of black holes and neutron stars in any given galaxy, which will have consequences for its galactic evolution. A reduction in mass loss rates would also have a significant impact on the chemical and dynamical evolution of the ISM. Models of star-forming regions will also be affected, since they are reliant on the ionising UV flux supplied by hot, massive stars. A reduction in the observed mass loss rates of these stars will decrease the amount of UV flux emitted into these regions. The formation of 'superbubbles' in clusters as a result of the presence of hot, massive stars winds would also be affected by a reduction in mass loss, altering the dynamical evolution of the ISM.

5.5 Bi-stability jump

The concept of a *bi-stable* stellar wind was first proposed by Pauldrach & Puls (1990*b*) whilst undertaking a theoretical study of the stellar wind of the Luminous Blue Variable P Cygni (B1.5 Ia+, $T_{\rm eff}$ = 19 300 K). Their models showed two solutions for a radiatively-driven wind, where the optical depth in the Lyman continuum is close to unity and the wind can be bi-stable. The first solution corresponds to a highly-ionised, low-density wind where large amounts of radiation pressure produce a 'high' v_∞ of $\sim$ 600 km/s. However a small drop in $T_{\rm eff}$ ($\leq$ 1000 K) forces the wind to recombine to a lower ionisation state,

therefore producing less radiation pressure and resulting in a low-ionisation high-density wind with a smaller v_∞ of $\sim$ 200 km/s. This discovery then prompts the question of whether such a mechanism is unique to variable stars or may also occur in normal B supergiants. In order to answer this, Lamers *et al.* (1995) examined the dependence of the ratio $\frac{v_\infty}{v_{\rm esc}}$ on $T_{\rm eff}$ for a sample of O–F stars. They found that the ratio $\frac{v_\infty}{v_{\rm esc}}$ has a value of 2.58 ± 0.20 for $\log T_{\rm eff} \geq 4.40$ (O and early B stars), which decreases to 0.72 ± 0.15 for $\log T_{\rm eff} = 3.9 - 4.0$ (A–F stars). However a discontinuity occurs in the ratio around $\log T_{\rm eff} \backsimeq 4.32$ ($T_{\rm eff} \sim 21\,000$ K) where $\frac{v_\infty}{v_{\rm esc}} \backsimeq 2.6$ for $\log T_{\rm eff} \geq 4.32$ then drops by a factor

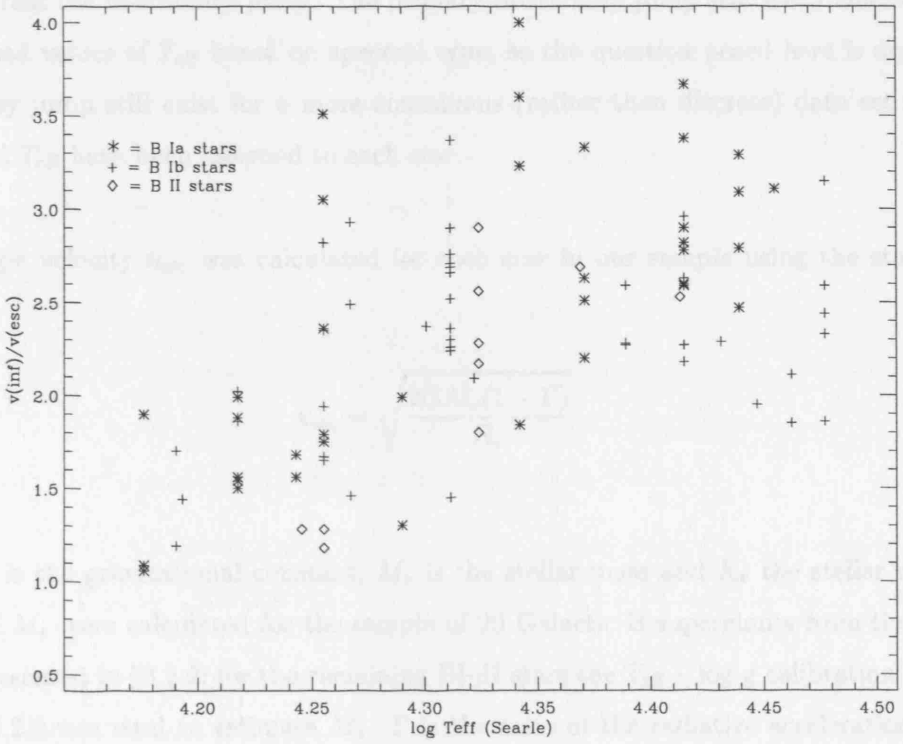

Figure 5.11: Plotting $\frac{v_\infty}{v_{\rm esc}}$ vs. $T_{\rm eff}$ for the sample of B0–B5 stars implies that the bi-stability jump for B supergiants is more of a gradual increase in $\frac{v_\infty}{v_{\rm esc}}$ with increasing $T_{\rm eff}$. B Ia stars are denoted by an asterisk, B Ib by + and B II by a diamond symbol.

of two for log $T_{\rm eff} \leq 4.32$ such that $\frac{v_\infty}{v_{\rm esc}} \backsimeq 1.3$. They named this observed discontinuity the *bi-stability jump*. It is possible that this data set suggests a second jump around log $T_{\rm eff} \backsimeq 4.05$ ($T_{\rm eff} \sim 10\ 000$ K), but Lamers *et al.* (1995) are sceptical since the evidence is only based on one data point and data is sparse in the region $4.0 \leq log T_{\rm eff} \leq 4.2$. A few years later the bi-stability jump was examined in more detail by Prinja & Massa (1998), who found that the 'jump' became more of a gradual decrease in $\frac{v_\infty}{v_{\rm esc}}$ with decreasing $T_{\rm eff}$ once more data points were included around log $T_{\rm eff} \backsimeq 4.32$. This effect was investigated theoretically by Vink *et al.* (1999), whose models predicted a jump in $\frac{v_\infty}{v_{\rm esc}}$ to occur around $T_{\rm eff} \sim 25\ 000$ K, caused by the recombination of Fe IV to Fe III. Since Fe III is a more efficient line driver in the stellar wind than Fe IV, an increase in $\dot{M}$ by a factor of 5 also occurs across the bi-stability jump. The primary bi-stability jump study of Lamers *et al.* (1995) used values of $T_{\rm eff}$ based on spectral type, so the question posed here is does the bi-stability jump still exist for a more continuous (rather than discrete) data set where individual $T_{\rm eff}$ have been assigned to each star.

The escape velocity $v_{\rm esc}$ was calculated for each star in our sample using the standard equation

$$v_{\rm esc} = \sqrt{\frac{2GM_*(1-\Gamma)}{R_*}} \tag{5.9}$$

where G is the gravitational constant, M_* is the stellar mass and R_* the stellar radius. Values of M_* were calculated for the sample of 20 Galactic B supergiants from the log g values presented in §3.2.2; for the remaining BI–II stars the $T_{\rm eff}$ – log g calibration shown in Fig. 3.2.2 was used to estimate M_*. Γ is the ratio of the radiative acceleration from electron scattering to the stellar gravity i.e.,

$$\Gamma = \frac{\sigma_e L_*}{4\pi G M_* c} \tag{5.10}$$

where σ_e is the electron scattering opacity defined as $\frac{n_e \sigma_T}{\rho}$ (n_e is the electron density, σ_T is the Thomson scattering cross-section and ρ is the gas density). A value of 0.3 $cm^{-2}g$ was assumed for σ_e, which is consistent with values adopted by Evans *et al.* (2004*b*) and

Lamers *et al.* (1995).

Unfortunately this question of whether the bi-stability jump really exists or not is not easily answered by our small data set, since we only have 2 data points around the crucial $T_{\rm eff}$ of 21 000 K. The 86 stars from the IUE data set (for which accurate values of v_∞ have been derived) were therefore also included. Temperatures were assigned to these stars using the $T_{\rm eff}$ – spectral type scale presented in Table 3.3; for the 'missing' spectral type of B0.2 Ib, an interpolated $T_{\rm eff}$ of 29 000 K was adopted, and we also assumed B0.5 Iab $\sim$ B0.5 Ib = 27 000 K. For B0.7 Ib stars, $T_{\rm eff}$ = 24 500 K was adopted on the basis that for early B supergiants there is a difference of about 1000 K between Ia and Ib stars and the only B0.7 Ia star in our sample has $T_{\rm eff}$ = 23 500 K. This difference is not present at later spectral types so a B4 Ib star was assumed to have $T_{\rm eff}$ = 15 600 K (Humphreys & McElroy, 1984), same as B4 Ia since Humphreys & McElroy (1984) do not distinguish between the Ia and Ib luminosity classes in their $T_{\rm eff}$ – spectral type scale. There are also a number of giant stars in the IUE sample, for which temperatures were again taken from Humphreys & McElroy (1984).

Table 5.4: Data used to calculate the ratio of $\frac{v_\infty}{v_{\rm esc}}$. The first 20 stars listed in the table are those analysed in Chapter 3 and the remaining stars belong to the IUE data set.

HD no	Sp Type	$v_{\rm esc}$	v_∞	$\frac{v_\infty}{v_{\rm esc}}$	log g	$T_{\rm eff}$	log $(L/L_\odot)$	M_*	R_*	Γ
37128	BO Ia	648.6	1600	2.47	3.13	27.5	5.73	50	32.4	0.251
204172	B0.2 Ia	541.2	1685	3.11	3.13	28.5	5.48	25	22.4	0.279
192660	B0 Ib	587.7	1850	3.15	3.25	30.0	5.74	35	23.4	0.366
38771	B0.5 Ia	492.9	1390	2.82	3.00	26.0	5.48	25	27.0	0.279
185859	B0.5 Ia	631.3	1830	2.90	3.13	26.0	5.54	40	29.1	0.204
213087	B0.5 Ib	663.1	1520	2.29	3.13	27.0	5.69	50	32.0	0.227
64760	B0.5 Ib	819.9	1600	1.95	3.38	28.0	5.48	50	23.3	0.140
2905	B0.7 Ia	420.4	1105	2.63	2.75	23.5	5.48	23	33.0	0.304
13854	B1 Iab	402.2	955	2.37	2.50	20.0	5.54	30	49.2	0.272
190066	B1 Iab	608.9	1275	2.09	2.88	21.0	5.54	50	41.1	0.163

continued on next page

cont. from previous page

HD no	Sp Type	v_{esc}	v_∞	$\frac{v_\infty}{v_{esc}}$	log g	T_{eff}	log $(L/L_\odot)$	M_*	R_*	Γ
190603	B1.5 Ia	299.3	390	1.30	2.38	19.5	5.41	17	44.5	0.356
193183	B1.5 Ib	387.1	565	1.46	2.63	18.5	5.00	15	30.8	0.155
14818	B2 Ia	348.9	625	1.79	2.38	18.0	5.40	23	51.4	0.253
206165	B2 Ib	388.6	640	1.65	2.50	18.0	5.18	20	39.8	0.175
198478	B2.5 Ia	353.4	550	1.56	2.25	17.5	5.26	20	46.1	0.210
42087	B2.5 Ib	334.9	650	1.94	2.50	18.0	5.20	15	36.6	0.248
53138	B3 Ia	319.6	500	1.56	2.25	16.5	5.30	20	54.7	0.233
58350	B5 Ia	293.0	320	1.09	2.13	15.0	5.18	17	57.3	0.205
164353	B5 Ib	377.0	450	1.19	2.75	15.5	4.18	8	19.6	0.044
191243	B5 Ib	131.1	550	4.19	2.75	14.5	5.30	8	70.8	0.582
91452	B0 Ia	501.4	1650	3.29	2.99	27.5	5.62	29	28.6	0.328
91969	B0 Ia	501.4	1400	2.79	2.99	27.5	5.62	29	28.6	0.328
122879	B0 Ia	501.4	1550	3.09	2.99	27.5	5.62	29	28.6	0.328
152667	B0 Ia	501.4	850	1.70	2.99	27.5	5.62	29	28.6	0.328
104705	B0 Ib	644.5	1500	2.33	3.22	30.0	5.68	40	25.8	0.274
167402	B0 Ib	644.5	1575	2.44	3.22	30.0	5.68	40	25.8	0.274
164402	B0 Ib	644.5	1670	2.59	3.22	30.0	5.68	40	25.8	0.274
164637	B0 Ib	644.5	1200	1.86	3.22	30.0	5.68	40	25.8	0.274
113012	B0.2 Ib	621.1	1150	1.85	3.17	29.0	5.65	39	26.9	0.270
224151	B0.2 Ib	621.1	1310	2.11	3.17	29.0	5.65	39	26.9	0.270
219188	B0.5 II	549.0	1390	2.53	3.00	25.9	5.58	34	30.7	0.256
167756	B0.5 Ia	467.8	1715	3.67	2.90	26.0	5.58	27	30.6	0.324
150898	B0.5 Ia	467.8	1580	3.38	2.90	26.0	5.58	27	30.6	0.324
115842	B0.5 Ia	467.8	1215	2.60	2.90	26.0	5.58	27	30.6	0.324
152234	B0.5 Ia	467.8	1300	2.78	2.90	26.0	5.58	27	30.6	0.324
152236	B0.5 Ia+	467.8	470	1.00	2.90	26.0	5.58	27	30.6	0.324
103779	B0.5 Iab	551.3	1450	2.63	3.00	26.0	5.58	34	30.6	0.257
77581	B0.5 Iae	467.8	680	1.45	2.90	26.0	5.58	27	30.6	0.324
99857	B0.5 Ib	551.3	1630	2.96	3.00	26.0	5.58	34	30.6	0.257

continued on next page

cont. from previous page

HD no	Sp Type	v_{esc}	v_∞	$\frac{v_\infty}{v_{esc}}$	log g	T_{eff}	log $(L/L_\odot)$	M_*	R_*	Γ
100276	B0.5 Ib	551.3	1200	2.18	3.00	26.0	5.58	34	30.6	0.257
165516	B0.5 Ib	551.3	1250	2.27	3.00	26.0	5.58	34	30.6	0.257
187459	B0.5 Ib	551.3	1250	2.27	3.00	26.0	5.58	34	30.6	0.257
109399	B0.7 II	491.1	1320	2.69	2.84	23.4	5.50	30	34.7	0.245
152235	B0.7 Ia	412.8	1035	2.51	2.74	23.5	5.51	23	34.5	0.317
91943	B0.7 Ia	412.8	1375	3.33	2.74	23.5	5.51	23	34.5	0.317
154090	B0.7 Ia	412.8	910	2.20	2.74	23.5	5.51	23	34.5	0.317
69882	B0.7 Ib	516.5	1340	2.59	2.91	24.5	5.54	32	32.9	0.250
109867	B0.7 Ib	516.5	1175	2.27	2.91	24.5	5.54	32	32.9	0.250
155985	B0.7 Ib	516.5	1180	2.28	2.91	24.5	5.54	32	32.9	0.250
148422	B1 Ia	380.4	1520	4.00	2.63	22.0	5.46	21	37.4	0.312
163522	B1 Ia	380.4	1230	3.23	2.63	22.0	5.46	21	37.4	0.312
150168	B1 Ia	380.4	1370	3.60	2.63	22.0	5.46	21	37.4	0.312
148688	B1 Ia	380.4	700	1.84	2.63	22.0	5.46	21	37.4	0.312
91316	B1 Iab	424.4	1130	2.66	2.64	20.5	5.41	26	40.7	0.230
94493	B1 Ib	424.4	1430	3.37	2.64	20.5	5.41	26	40.7	0.230
157246	B1 Ib	424.4	615	1.45	2.64	20.5	5.41	26	40.7	0.230
14052	B1 Ib	424.4	1230	2.90	2.64	20.5	5.41	26	40.7	0.230
40111	B1 Ib	424.4	1150	2.71	2.64	20.5	5.41	26	40.7	0.230
47240	B1 Ib	424.4	950	2.24	2.64	20.5	5.41	26	40.7	0.230
52382	B1 Ib	424.4	960	2.26	2.64	20.5	5.41	26	40.7	0.230
119608	B1 Ib	424.4	975	2.30	2.64	20.5	5.41	26	40.7	0.230
191877	B1 Ib	424.4	1140	2.69	2.64	20.5	5.41	26	40.7	0.230
214080	B1 Ib	424.4	975	2.30	2.64	20.5	5.41	26	40.7	0.230
24398	B1 Ib	424.4	1170	2.76	2.64	20.5	5.41	26	40.7	0.230
93827	B1 Ibn	424.4	1000	2.36	2.64	20.5	5.41	26	40.7	0.230
58510	B1 Ib	424.4	950	2.24	2.64	20.5	5.41	26	40.7	0.230
173502	B1 II	438.2	950	2.17	2.68	21.1	5.43	27	39.3	0.233
205139	B1 II	438.2	1000	2.28	2.68	21.1	5.43	27	39.3	0.233

continued on next page

cont. from previous page

HD no	Sp Type	$v_{\rm esc}$	v_∞	$\frac{v_\infty}{v_{\rm esc}}$	log g	$T_{\rm eff}$	log $(L/L_\odot)$	M_*	R_*	Γ
215733	B1 II	438.2	1120	2.56	2.68	21.1	5.43	27	39.3	0.233
223987	B1 II	438.2	790	1.80	2.68	21.1	5.43	27	39.3	0.233
573506	B1 II	438.2	1270	2.90	2.68	21.1	5.43	27	39.3	0.233
106343	B1.5 Ia	401.6	800	1.99	2.56	19.5	5.38	24	43.2	0.225
97522	B1.5 Ib	378.8	1110	2.93	2.48	18.5	5.34	23	46.0	0.220
111934	B1.5 Ib	378.8	945	2.49	2.48	18.5	5.34	23	46.0	0.220
13841	B2 Ib	367.4	1035	2.82	2.44	18.0	5.32	22	47.5	0.217
52087	B2 II	367.4	435	1.18	2.44	18.0	5.32	22	47.5	0.217
141318	B2 II	367.4	470	1.28	2.44	18.0	5.32	22	47.5	0.217
99953	B2 Ia	296.5	530	1.79	2.30	18.0	5.32	16	47.5	0.298
41117	B2 Ia	296.5	530	1.79	2.30	18.0	5.32	16	47.5	0.298
14143	B2 Ia	296.5	530	1.79	2.30	18.0	5.32	16	47.5	0.298
148379	B2 Ia	296.5	520	1.75	2.30	18.0	5.32	16	47.5	0.298
165024	B2 Ia	296.5	1040	3.51	2.30	18.0	5.32	16	47.5	0.298
31327	B2 Ia	296.5	905	3.05	2.30	18.0	5.32	16	47.5	0.298
111990	B2 Ia	296.5	700	2.36	2.30	18.0	5.32	16	47.5	0.298
13866	B2 Ib	367.4	865	2.35	2.44	18.0	5.32	22	47.5	0.217
92964	B2.5 Ia	286.3	480	1.68	2.25	17.5	5.30	15	49.1	0.296
116084	B2.5 Ib	367.4	615	1.67	2.44	18.0	5.32	22	47.5	0.217
72648	B2.5 Ib	358.4	460	1.28	2.40	17.6	5.31	21	48.9	0.215
75149	B3 Ia	266.1	410	1.54	2.16	16.5	5.26	14	52.7	0.293
225094	B3 Ia	266.1	500	1.88	2.16	16.5	5.26	14	52.7	0.293
14134	B3 Ia	266.1	500	1.88	2.16	16.5	5.26	14	52.7	0.293
111973	B3 Ia	266.1	530	1.99	2.16	16.5	5.26	14	52.7	0.293
43384	B3 Iab	333.5	620	1.86	2.30	16.5	5.26	20	52.7	0.208
157038	B3 Iap	266.1	400	1.50	2.16	16.5	5.26	14	52.7	0.293
51309	B3 Ib	333.5	675	2.02	2.30	16.5	5.26	20	52.7	0.208
36371	B4 Ib	313.3	450	1.44	2.22	15.6	5.22	19	56.3	0.203
79186	B5 Ia	236.3	450	1.90	2.00	15.0	5.19	12	59.0	0.286

continued on next page

cont. from previous page

HD no	Sp Type	$v_{\rm esc}$	v_∞	$\frac{v_\infty}{v_{\rm esc}}$	log g	$T_{\rm eff}$	log $(L/L_\odot)$	M_*	R_*	Γ
100943	B5 Ia	236.3	250	1.06	2.00	15.0	5.19	12	59.0	0.286
86440	B5 Ib	311.1	530	1.70	2.21	15.5	5.22	18	56.8	0.203
96248	BC1.5Iab	516.5	690	1.34	2.91	24.5	5.54	32	32.9	0.250
163181	BN0.5 Ia	467.8	1210	2.59	2.90	26.0	5.58	27	30.6	0.324
93840	BN1 Ib	424.4	1070	2.52	2.64	20.5	5.41	26	40.7	0.230

Fig. 5.11 displays the bi-stability jump determined here and strongly supports the findings of Prinja & Massa (1998). For $4.41 \leq log T_{\rm eff} \leq 4.50$ a range of $1.7 \leq \frac{v_\infty}{v_{\rm esc}} \leq 3.1$ is observed, which then increases to a maximum value of $\frac{v_\infty}{v_{\rm esc}} = 3.6$ at log $T_{\rm eff} = 4.40$, and drops to $1.2 \leq \frac{v_\infty}{v_{\rm esc}} \leq 2.8$ around log $T_{\rm eff} \backsimeq 4.32$. This is the point at which the bi-stability jump is supposed to occur. At log $T_{\rm eff} \backsimeq 4.25$, a smaller drop occurs to $1.2 \leq \frac{v_\infty}{v_{\rm esc}} \leq 2.4$ (ignoring the B II stars), then at lower $T_{\rm eff}$ (log $T_{\rm eff} \leq 4.25$) the range in $\frac{v_\infty}{v_{\rm esc}} \sim 0.7$–$1.7$. As noted by Prinja & Massa (1998), a large scatter in $\frac{v_\infty}{v_{\rm esc}}$ is seen at any given $T_{\rm eff}$, but it is not clear why this should be the case. If this scatter is real, then it is possible that an additional physical mechanism in the wind is responsible. Despite this, it is evident from this dataset that $\frac{v_\infty}{v_{\rm esc}}$ *gradually* decreases for log $T_{\rm eff} \leq 4.32$, rather than 'jumping' to lower values.

In order to investigate the cause of this scatter in $\frac{v_\infty}{v_{\rm esc}}$ at any given $T_{\rm eff}$, relative q_i values were plotted against v_∞ to examine whether there was any separation in the ionisation fractions between stars with high and low terminal velocities. This would be direct evidence of a *bi-modal* wind in which the winds of stars with a higher terminal velocity would be in a higher ionisation state than those at a lower terminal velocity. Looking at Fig. 5.12, no clear separation of relative ionisation fractions with v_∞ can be seen, generally there is however some indication of a gradual decrease in ionisation towards lower terminal velocities, but the data is still quite scattered. Another way to probe whether the winds of B supergiants could be bi-stable is to plot the dependence of the quantity Q with v_∞, where $Q = \frac{\dot{M} v_\infty}{R_*^{3/2}}$, in order to determine whether there is a clear separation between stars with winds that are thin, fast and highly ionised and those that are denser and less ionised at slower terminal velocities. Fig. 5.13 shows that the data is very scattered with no discernible trend, disproving the possibility of a bi-stable wind and proving that the

mechanism responsible for this scatter must be intrinsic to the star. It then becomes clear that this unknown mechanism is obviously absent from the Vink *et al.* (2000) theoretical models, producing the bi-stability jump when a more gradual decrease in $\frac{v_\infty}{v_{\rm esc}}$ toward lower $T_{\rm eff}$ is observed.

If this turns out to be true in general (which seems to be the case), this poses a problem for the theoretical models of Vink *et al.* (1999), which still predict the occurrence of a bi-stability jump around $T_{\rm eff} = 25\ 000$ K. The exact point in $T_{\rm eff}$ at which the jump occurs is not quite so crucial since the ionisation equilibrium is sensitive to both $T_{\rm eff}$ and density. For example smaller values of $\frac{v_\infty}{v_{\rm esc}}$ would lead to the jump occurring at higher $T_{\rm eff}$.

The question still remains as to the precise cause of this phenomenon of bi-stable winds in B supergiants. Even though it seems that a jump is not observed but only predicted by theory, a marked decrease in $\frac{v_\infty}{v_{\rm esc}}$ is evidently seen as $T_{\rm eff}$ decreases. Both Prinja & Massa (1998) and Lamers *et al.* (1995) investigated the strength of the C^{3+} and C^{+} P Cygni profiles with v_∞ and found that the ionisation shifts to lower ions as v_∞ decreases. This proves that a strong correlation exists between v_∞ in the vicinity of the bi-stable wind region and the amount of ionisation in the wind.

5.6 Chapter 5 summary

In this chapter the SEI method has been introduced as an effective way of analysing P Cygni resonance lines in hot star stellar winds. This method is used to determine q_i values and show that the empirical values in the wind are *at least* an order of magnitude lower than predictions. These findings support similar results found by, e.g., Massa *et al.* (2003) for O star winds. It appears that these low q_i values can be attributed to clumping in the wind, which will lead to an overestimation of observed mass loss rates (as they assume a smooth, homogeneous wind) and consequently too-small values of q_i. This work therefore re-emphasises the importance of including clumping in stellar wind models, and the necessity of a reduction in observed mass loss rates. This issue affects both O and B stars and demands a revision of our understanding of the nature of hot star winds.

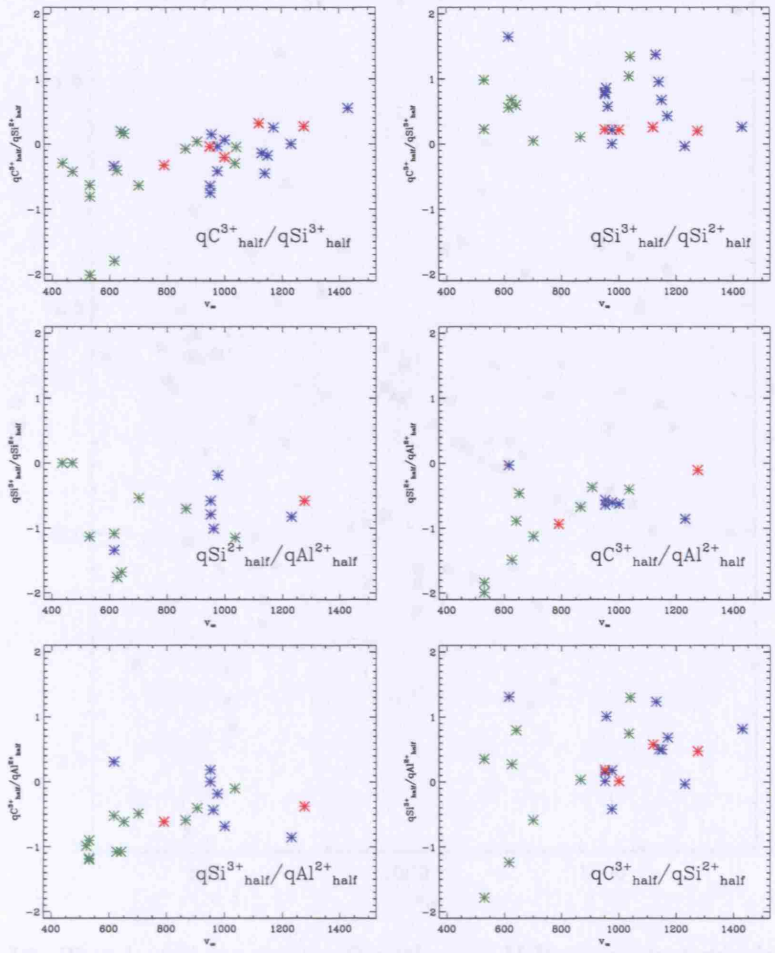

Figure 5.12: Trends of relative $q_i^{0.5}$ with v_∞. The data is colour-coded according to the adopted temperature of the star from which the relative ionisation fraction was taken; red denotes 26 000 K $\leq T_{\rm eff} \leq$ 30 000 K, green 18 000 K $\leq T_{\rm eff} \leq$ 26 000 K and blue $T_{\rm eff} \leq$ 18 000 K.

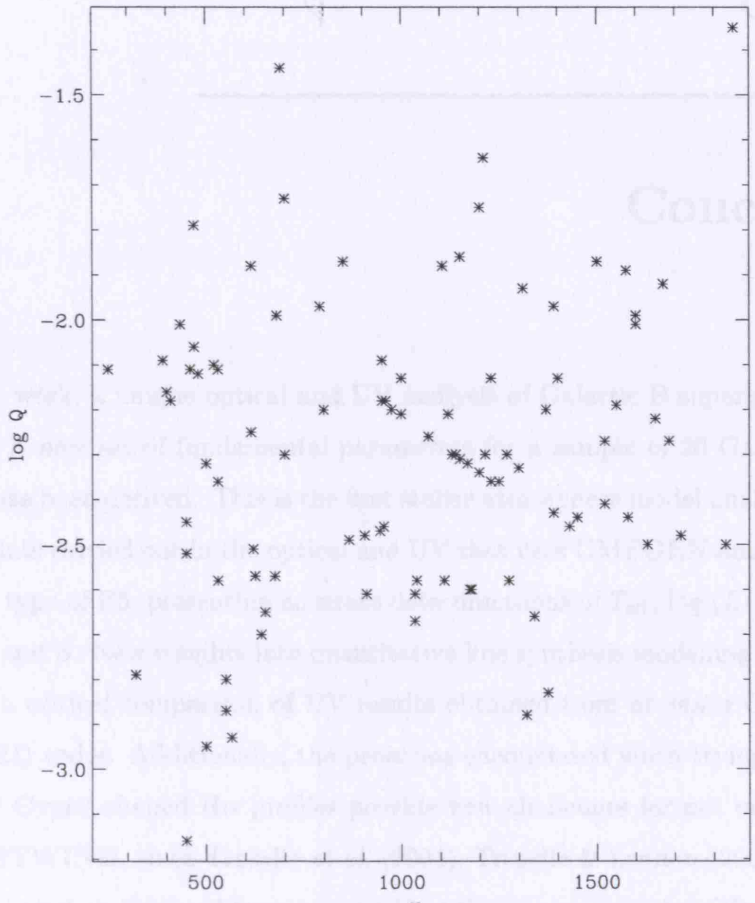

Figure 5.13: Trend of the quantity Q with v_∞. If B supergiant winds were bi-stable, the data would fall into two groups representing stars with a thin, high velocity, high ionisation wind and those with more dense, slow, low ionisation wind. Evidently this is not the case looking at the scatter of the data, so B supergiant winds do not exhibit a clear bi-stable state.

CHAPTER 6

Conclusions

In this thesis work, a unique optical and UV analysis of Galactic B supergiants has been undertaken. A new set of fundamental parameters for a sample of 20 Galactic B0 – B5 supergiants has been derived. This is the first stellar atmosphere model analysis of B Ia, Ib & II supergiants carried out in the optical and UV that uses CMFGEN and extends down to a spectral type of B5, presenting accurate determinations of $T_{\rm eff}$, log $(L/L_{\odot})$, R_{*}, log g, M_{*}, M_{V}, $\dot{M}$ and β. New insights into quantitative line synthesis modelling have also been provided by a critical comparison of UV results obtained from *ab initio* CMFGEN and empirical (SEI) codes. Additionally, the problems encountered when trying to accurately reproduce 'P Cygni'-shaped Hα profiles provide new challenges for not only CMFGEN but also FASTWIND, since Trundle *et al.* (2004); Trundle & Lennon (2005) & Repolust *et al.* (2004) found similar problems in modelling these more complex OB supergiant Hα profiles. It is possible to fit the red-ward part of the emission profile but not the blue absorption trough and even the Puls *et al.* (2006) code (written specifically to model Hα profiles) cannot resolve this problem. This implies that all three codes do not predict the correct temperature structure, as suggested by Trundle & Lennon (2005), and consequently the resulting ionisation structure prevents an accurate reproduction of a 'P Cygni' type Hα profile, as well as the UV P Cygni profiles, as demonstrated in Chapter 4. Despite these difficulties in fitting Hα, the mass loss rates derived by these authors and in this thesis work are still reliable and in good agreement with those predicted by the mass loss prescriptions of Vink *et al.* (2000, 2001). Markova *et al.* (2005) studied the effect of Hα variability on derived mass loss rates for O stars and found no significant difference

for O supergiants; some discrepancy was found however for several O V stars. The other important and interesting main part of this thesis work is the investigation of the ionisation structure of B supergiants. From the CMFGEN models described in Chapters 3 & 4, the predicted ionisation structure over a range of temperatures is available to compare with the empirical ionisation structure obtained by SEI modelling of UV wind resonance lines. This has allowed an entirely original analysis of the ionisation structure of B supergiant winds to be undertaken, as well as providing tests on the validity of the ionisation structure predicted by CMFGEN.

6.1 Implications of these thesis results

A revised temperature scale for Galactic B0 – B5 supergiants has been presented in this thesis that allows for temperature differences between the luminosity classes Ia, Iab, Ib & II. A difference of up to 2 500 K is noted between luminosity classes. The derivation of this $T_{\rm eff}$ scale was based on modelling individual stars and used a nLTE, fully line-blanketed stellar atmosphere code (CMFGEN), meaning that this new $T_{\rm eff}$ scale is much more reliable than those of e.g. Humphreys & McElroy (1984), which did not differentiate between luminosity classes. In comparison to the McErLean *et al.* (1999) Galactic B supergiant $T_{\rm eff}$ scale, which used an unblanketed stellar atmosphere code, the inclusion of line blanketing has lowered $T_{\rm eff}$ by 1000 – 2000 K. An investigation of the ionisation structure using both CMFGEN and an empirical line synthesis code (SEI) has provided intriguing insight into the successes and failures of CMFGEN in the UV. It has also supported previous evidence from (e.g., Prinja & Massa, 1998) that the bi-stability jump is more of a gradual decrease in $\frac{v_\infty}{v_{\rm esc}}$ as a function of $T_{\rm eff}$. Most importantly it supports the argument for a reduction in observed mass loss rates by *at least* an order of magnitude through the comparison of empirically-derived q_i values and those predicted by CMFGEN.

6.1.1 Implications for hot, massive star evolution

Out of the 20 Galactic B supergiants analysed, 18 showed some clear degree of CNO processing in their spectra. The largest nitrogen enrichments are seen for B1-2 supergiants, with the greatest nitrogen enhancement occurring in the B1.5 Ia+ star HD 190603 (log $\frac{N}{C} = +1.89$). Even this value is not indicative of the amount of processing seen in a blue (OB) supergiant that has gone through a red supergiant phase. For example, Fransson

et al. (1989) derived a value of $\frac{N}{C} = 7.8 \pm 4$ for the progenitor of SN1987A, which they deduced had passed through a red supergiant phase before becoming a blue supergiant again and exploding as a supernova. However this observed $\frac{N}{C}$ abundance is quite uncertain so does not provide us with a reliable comparison of $\frac{N}{C}$ enrichment after the red supergiant phase. Another comparison can be found for the blue supergiant Sher 25, as analysed by Smartt *et al.* (2002), where a value of $\frac{N}{C} = 26.3$ was obtained. However, this abundance estimate is also unreliable as it suffers from uncertainties in the absolute carbon abundance. More reliable estimates can be found from Lamers *et al.* (2001),who used the stellar evolutionary tracks of Meynet *et al.* (1994) to investigate whether LBVs passed through a red supergiant phase by quantifying how much CNO processing would occur and comparing it to the observed N/C and N/O abundances in the nebula surrounding the LBV. Interestingly, Lamers *et al.* (2001) conclude that LBVs do not pass through a red supergiant phase and any CNO enrichment occurring during the main-sequence is caused by rotationally-induced mixing. The amount of predicted CNO processing due to rotationally-induced mixing in a star at the end of the main-sequence phase was also calculated. For a 20 $M_{\odot}$star, $0 \leq log\frac{N}{C} \leq 1.3$ and $-0.23 \leq log\frac{N}{O} \leq 0.65$, whereas for a 40 $M_{\odot}$star, $0.2 \leq log\frac{N}{C} \leq 1.45$ and $-0.1 \leq log\frac{N}{O} \leq 1.0$; in both cases these values range over a mixing timescale that is 1–5 times the main-sequence lifetime. The trends of the predicted surface abundances at end of the main-sequence phase for stars with rotationally-induced mixing are shown in Fig. 6.1. Based on these estimates, none of the 20 Galactic B supergiants display evidence of going through a red supergiant phase. These derived CNO abundances also provide a useful constraint for the amount of CNO processing predicted by stellar evolution models (Meynet & Maeder, 2000). It has also been shown that a mass discrepancy exists for Galactic B supergiants, where spectroscopically-derived stellar masses are generally smaller than those estimated from stellar evolutionary tracks, which supports the findings of Trundle & Lennon (2005), where $M_{\rm evol} \geq M_{\rm spec}$ by 0.1 - 0.3 dex.

It is the reduction of mass loss rates that will have the most significant effect on the post-main-sequence evolution of B supergiants and hot, massive stars in general. Meynet *et al.* (1994) explored the effects of enhanced mass loss on massive star evolution by doubling the mass loss rate adopted during the star's evolution. Changing the mass loss rate of the star in this way affects the number of WR stars produced by the evolutionary tracks, with

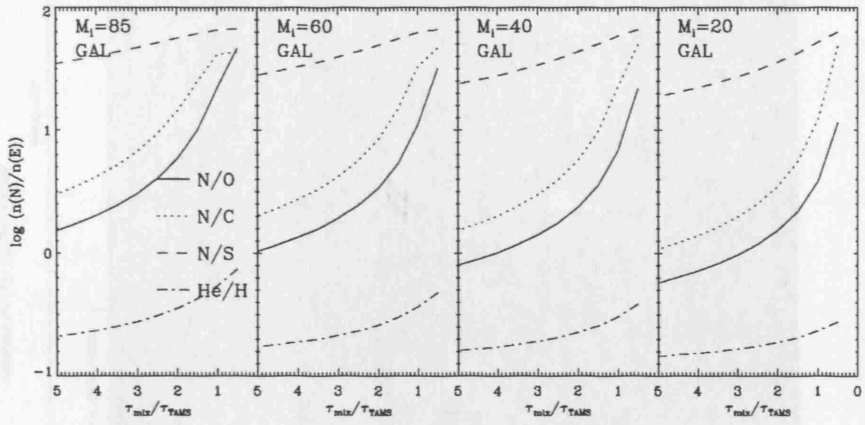

Figure 6.1: Predicted surface N/C & N/O abundances at end of main-sequence phase for stars with rotationally-induced mixing (Lamers *et al.*, 2001)

the resulting number being closer to the observed value. Without adopting larger mass loss rates, it is harder for the evolutionary models to 'make' O stars evolve into WR stars; this is a problematic consequence of the lowering the observed mass loss rates. Another consequence is that smaller mass loss rates also produce a more massive stellar core at the end of nuclear burning, affecting the final end state of the star and consequently producing more black holes than neutrons stars. According to the estimates of Fryer *et al.* (1999), who calculated the required mass of the helium core needed to produce a black hole, the minimum helium core mass needed to form a black hole by fallback is 8 $M_{\odot}$, whereas 15 $M_{\odot}$ is required for a black hole to form directly after the supernova explosion. These helium core masses correspond to a star with an initial mass, $M_{\rm init} \leq 25\ M_{\odot}$ producing a black hole by fallback and a star with $M_{\rm init} \sim 40\ M_{\odot}$ that does not lose mass resulting in a direct black hole. It is interesting to compare these estimates with those of Heger *et al.* (2003), who calculated the evolutionary paths of massive stars in the range $9 \leq M_{*}\ (M_{\odot}) \leq 300$ (neglecting the effects of rotation). These models are based on the assumption that stars with $M_{*} \leq 9\ M_{\odot}$ form white dwarfs at the end of their lives as the final stellar core is not large enough to undergo core collapse. In Fig. 6.2, where it can be seen for solar metallicity that a star with $M_{\rm init} \geq 25\ M_{\odot}$ is predicted to form a black hole, but $M_{\rm init} \geq 40\ M_{\odot}$ is required to form a black hole directly after the supernova explosion. The mass of the stellar core prior to the supernova explosion also affects the amount of

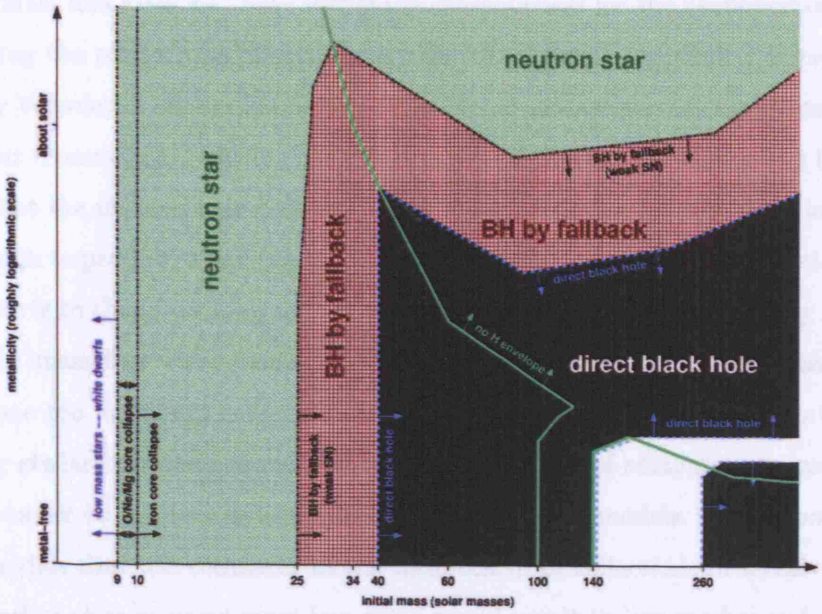

Figure 6.2: Massive star remnants as a function of metallicity (Fig. 1, Heger *et al.* (2003))

energy generated in the explosion. From Fig. 6.2, it is clear that metallicity plays a crucial role in enhancing mass loss and therefore altering the final stages of massive star evolution. Stars with increased metallicity will experience greater mass loss, resulting in smaller helium cores for a given value of $M_{\rm init}$. Even greater mass loss occurs if the star completely loses its hydrogen envelope; this is marked as the region to the right of the green line in Fig. 6.2. The remnant of the collapsed star therefore also depends strongly on metallicity as the size of the helium core before the star collapses is determined by mass loss. In a low metallicity star, a pair-instability supernova can occur where core-collapse can be so strong that no remnant is left behind after the explosion (e.g., Heger & Woosley, 2002); this corresponds to the white region in the bottom-right-hand corner of Fig. 6.2. It is more likely however that, in the low metallicity case, the helium core prior to core-collapse is so large that a black hole forms directly after the supernova explosion. The dependence of the final stages of hot, massive star evolution on mass loss and metallicity emphasise the importance of fully understanding the role of these parameters in the theory of stellar winds.

Smaller mass loss rates also have intriguing consequences for the likelihood of hot, massive stars being the progenitors of gamma-ray bursts. Current gamma-ray burst models proposed by Woosley & Heger (2006) show that higher mass loss rates lead to more transport of angular momentum, reducing the rotation rate of the star throughout its lifetime to the extent that the neutron star produced after the supernova explosion is no longer rotating fast enough to produce a gamma-ray burst. One way to explain the production of gamma-ray bursts is to therefore suggest that they can only occur in low-metallicity environments where the mass loss will be smaller. *Alternatively*, if the mass loss rates assumed in the models are too large and consequently the angular momentum loss is also too large, the resulting stellar rotation rate will be too slow. The use of smaller mass loss rates would make it easier to produce gamma-ray bursts from these models. Stellar population synthesis models that use estimates of the feedback from collections of massive stars would also be affected as reduced mass loss rates would result in less mechanical, chemical and radiative feedback to the ISM. These would have large consequences for galactic chemical evolution, star formation and starburst galaxies.

6.1.2 The role of clumping

In order to improve the accuracy of deriving mass loss rates for hot, massive stars, it is essential to obtain a more precise knowledge of the amount, properties and distribution of clumping in their stellar winds. The existence of clumping calls for a revision of the standard model of stellar winds, which assumes a smooth, homogeneous wind. Studies of line profile variations reveal clues as to where in the wind large and small scale structure is located and provide a useful tool for probing wind structure. Analysis of variations in photospheric lines suggest that inhomogeneities in the wind *may* arise from photospheric disturbances, though an actual causal connection has not been widely demonstrated from such observations. Examples of such studies are as follows. Markova *et al.* (2005) investigated Hα variability in a sample of 15 O4 – O9.7 supergiants. Evidence for significant variability is found, controlled mostly by processes in the wind. 1-D model simulations are applied to determine how the observed Hα variations relate to structure in the stellar wind and photosphere. For intermediate wind densities, a model consisting of coherent or broken clumps that are uniformly distributed across the wind succeeds in reproducing the observations. However, a discordance was found between the model predictions and observations for stars with high or low wind densities and Markova *et al.* (2005) suggest

that the presence of large, coherent structures, partially contained in a volume near the star, could be responsible. Puls *et al.* (2006) built on this work to carry out an examination of the radial extent of the clumping factor based on a combination of simultaneous Hα, infra-red and radio observations. They derived values of $\dot{M}_{\rm radio}$ that are in very good agreement with theoretical predictions and compare them to values of $\dot{M}_{\rm H\alpha}$. In general it is found that $\frac{\dot{M}_{\rm H\alpha}}{\dot{M}_{\rm radio}} = 0.49 \pm 0.1$ for stars displaying Hα in emission, which supports the findings of Fullerton *et al.* (2006). Clumping factors are then constrained by attempting to fit the Hα profile (formed at a distance of r $\leq R_*$ from the star) and radio/infra-red fluxes, investigating what *relative* size of clumping factor is implied at each wavelength, corresponding to different regions of the stellar wind. Absolute clumping factors cannot be derived due to the ρ^2 dependence of Hα and radio/infrared diagnostics. Interestingly they discovered that for dense winds the inner wind where Hα forms is more strongly clumped than the outer wind, which corresponds to the radio/infra-red region. Conversely, for thin winds, similar amounts of clumping are found in both the inner and outer wind. Puls *et al.* (2006) conclude that the implications of their results depend on the *exact* amount of clumping present in the outer wind, which cannot be easily determined since it cannot be measured directly. Extending the data to include observations at mm and far-infra-red wavelengths would help to investigate the amount of clumping in the intermediate region of the wind.

No surveys as complete as those of Markova *et al.* (2005) and Puls *et al.* (2006) exist yet for B supergiants, but several studies aimed at one particular wavelength region are able to give insight into small-scale and large-scale structure in the wind. Prinja *et al.* (2002) presents an excellent review of the various characteristic structures observed in the UV spectra of B0 – B3 supergiants. Studies of photospheric and wind variability in ϵ Ori (Prinja *et al.*, 2004) and HD 64760 Kaufer *et al.* (2006) provide essential constraints on the limitations of non-radial pulsation models (e.g., Townsend, 1997).

Such studies also provide a useful test for theoretical simulations that investigate the consequences of instabilities and inhomogeneities in the stellar wind, in an attempt to find the mechanisms responsible for their existence and propagation in the wind. Runacres & Owocki (2002) investigated small-scale, stochastic structure in the wind, produced by instabilities in the line driving of the inner wind. The propagation of such structures

(namely clumps and shocks) in the wind were described by a radially-stratified clumping factor. They found that the distribution of the structure as it evolves is controlled by two opposing effects. The dense clumps, separated by rarefied gas, expand into these gaps due to pressure; consequently supersonic collisions between these dense clumps then compete to resist this expansion. Once the structure has passed beyond 20 - 30 R_*, it is hardly influenced by the line-driving force, suggesting that evolution of clumps in the outer wind can be treated as a pure gas-dynamical problem in future simulations. These simulations are important as they demonstrate that structure originating at the base of the wind can propagate out to $\sim$ 100 R_* without being destroyed and will therefore affect observational diagnostics at these radii, namely infra-red and radio emission. Runacres & Owocki (2005) then proceeded to investigate the behaviour of structure in the outer wind extending to huge distances ($\sim$ 1000 R_*). Observational evidence does suggest that structure exists further than 100 R_*. One example is the O4f star ζ Pup, for which it is thought that half of its observed thermal radio flux originates beyond 100 R_*, which is also a strong contributor to its X-ray flux, according to Hillier *et al.* (2003). It is therefore vital to our understanding of this star (and similar ones) to examine what mechanisms are needed for structure to exist this far out in the stellar wind. Using a pure-hydrodynamical, 1-D model, Runacres & Owocki (2005) found that the wind can remain clumped out to 1300 R_*, with weak shocks still present. Intriguingly, both Runacres & Owocki (2002, 2005) found that the clumping factor value oscillated over a range of $200 \leq R_* \leq 1300$, representing the region where clumping distribution is controlled by the competing effects of pressure expansion and supersonic-shock compression. Though these models provide excellent insight into the possible structure of massive star winds, further observations are required to confirm how realistic the predicted density distribution really is.

Alternatively, Dessart & Owocki (2003, 2005) use hydrodynamical simulations that incorporate the 2D-effects of the radiation field in order to investigate the lateral extent of clumping in the wind. Combining the findings of both theoretical models results in the following conclusions regarding stellar wind structure. Firstly, the formation and interaction of clumps leads to shocks in the wind, producing X-ray emission and enhancing the extreme UV (EUV) flux (Feldmeier *et al.*, 1997). Authors such as Pauldrach *et al.* (2001) have shown that this can have a huge effect on the ionisation/excitation balance in the wind, for example the presence of super-ions in the wind. Secondly, the inclusion

of clumping alters the smooth structure of a wind model by introducing depth-dependent density enhancements. The dependence of $\dot{M}_{\mathrm{H}\alpha}$ and $\dot{M}_{\mathrm{radio}}$ on ρ^2 means that these parameters are highly sensitive to the amount and distribution of clumping in the wind. The ionisation balance is affected to a lesser extent due to the ρ^2 dependence of the radiative recombination rates, as discussed by (e.g., Bouret *et al.*, 2005).

Further confirmation of the importance of clumping is evident in the application of *ab initio* models to analyse OB supergiants. Bouret *et al.* (2005) found the inclusion of clumping in CMFGEN necessary in order to fit the P V P Cygni profile. This has not been confirmed in this thesis work, as seen in §4.3, where clumping had no significant effect in improving the model fits to the observed UV wind lines. However, it is worth recalling that B supergiant winds are weaker and less dense than those of O supergiants, so whilst clumping *should* be included as we know it exists in the wind, it is not *entirely* surprising that the effect is greater for O supergiants, compared to B supergiants. The current 'filling-factor' approximation used in these models needs to be replaced by a more realistic parameterisation that accounts for the radial stratification of the clumping factor. The time-dependent simulations run by Runacres & Owocki (2002) provide some valuable insight into an alternative method, by defining the clumping factor as

$$f_{cl} = \frac{< \rho^2 >}{< \rho >^2} \geq 1 \tag{6.1}$$

where the angular brackets signify quantities that are averaged over time. The simulations show that for instabilities starting in the wind (i.e., not generated by photospheric disturbances), the wind model becomes significantly clumped at a wind velocity of a few hundred km/s, where $f_{cl} \sim 4$. It then reaches a maximum of $f_{cl} \sim 15$–20 before decaying back to a value of around 4. The idea of using a temporally-averaged clumping factor, rather than one based on a 'filling-factor' approximation, might lead to an improvement in parameterising clumping for the purpose of models such as CMFGEN.

6.2 Future work

The results of this thesis work have highlighted the importance of acquiring accurate mass loss rates and obtaining a more precise knowledge of the clumpy, structured nature of OB supergiant winds. This supports the conclusions of previous work that suggested the presence of clumping in stellar winds results in an over-estimation of observed mass loss rates e.g. Prinja *et al.* (2005); Fullerton *et al.* (2006); Repolust *et al.* (2004); Puls *et al.* (2006). This issue now becomes a question of how to derive accurate mass loss rates that account for the presence of clumping and its effect on mass loss diagnostics. Until our knowledge of the nature and distribution of clumping in the wind is more precise, it cannot be accounted for in any wind model; even then it would be a challenge to find a method by which to parameterise it such that would be computationally efficient enough to operate within another code. It is also vital to understand the respective influences of large-scale structure and small-scale structure in hot, massive stars winds, in order to compensate for their effect on mass loss from the wind when deriving mass loss rates. For these reasons, it would be easiest to constrain mass loss rates from the UV, which is less sensitive to clumping than the optical/IR, but this option is not viable until our knowledge of the ionisation structure of the wind improves and this too is affected by the presence of clumping to some extent. The next preferred method is to obtain radio mass loss rates, as done by Puls *et al.* (2006), compare them to values of $\dot{M}_{\mathrm{H}\alpha}$ and use a simple clumping parameterisation to estimate clumping factors to infer how much clumping is present at optical and radio wavelengths. At present, this method cannot be easily applied to a large sample of B supergiants, since the majority of them do not emit strongly at radio or infra-red wavelengths, resulting in non-detections of the excess flux using current technologies. However a small sample of 6 B supergiants have been selected in an attempt to detect radio/infra-red fluxes using the Australia Telescope Compact Array (ATCA), a radio telescope consisting of 6 22-m antennae and based in New South Wales, Australia. Simultaneous optical observations are also planned for the same 6 B supergiants so that comparisons can be made between $\dot{M}_{\mathrm{H}\alpha}$ & $\dot{M}_{\mathrm{radio}}$. A more viable approach for solving this problem can be found in the form of the current, substantial upgrades for the UK MERLIN radio facility, aimed at providing a uniquely-powerful, high-resolution radio astronomy facility from 2008 onwards. The main improvement in this upgrade is the incorporation of fibre-optic network that can increase the bandwidth up to 4 GHz. Along

with other enhancements, this means that e-MERLIN will be up to 30 times more sensitive than at present, enabling it to permit the detection of 6-cm and 20-cm radio flux for a significantly greater number of OB stars including supergiants, giants and main-sequence stars. e-MERLIN therefore presents the invaluable and exciting possibility of not only understanding wind clumping in hot, massive stars but also obtaining more reliable mass loss rate estimates.

The only other alternative for obtaining reliable mass loss rates for B supergiants is using the Hα profile again, but a more accurate method is required to allow for the complex morphologies of Hα profiles in B1-B5 supergiants. The Hα code presented by Puls *et al.* (1996) provides a fast and reliable method of constraining $\dot{M}_{\mathrm{H}\alpha}$, successfully reproducing the majority of complex Hα lines involving some variant of a P Cygni-type profile. At present this code can only be applied to O stars because the departure coefficients incorporated into the code are only appropriate for O stars. Using the departure coefficients of a stellar atmosphere code like CMFGEN or FASTWIND, these can be integrated into the Puls *et al.* (1996) Hα code to extend its suitability to B supergiants. It would then be possible to carry out a large-scale survey of optical mass loss rates for B supergiants, and by employing a simple clumping parameterisation like the one used by Puls *et al.* (1996) in order to estimate the amount of clumping present in the Hα profile so that the mass loss rate could be adjusted accordingly to compensate for this.

In order to determine the precise nature and distribution of clumping in the wind, we require observations taken simultaneously at different wavelengths. This would allow us to investigate the amount of clumping present in different parts of the wind and how far from the star the wind remains structured. Additional, temporal observations at the same wavelength would give information on the evolution of clumps in a particular region of the wind. All this information would provide useful constrains and tests for theoretical wind simulations (e.g., Runacres & Owocki, 2002, 2005). A multi-wavelength campaign of this nature would be difficult to orchestrate, since it relies on obtaining simultaneous observations on a wide range of different instruments, which is unlikely to be possible. Optical observations are the most straight-forward to obtain, given the large choice of 1–2m ground-based telescopes that would be suitable. Obtaining UV spectra simultaneously with other observations would be difficult given that only the *FUSE* satellite is still operational (though

its services are restricted), therefore it may be necessary to use archive IUE/FUSE/EUVE data. X-ray observations could be obtained from CHANDRA, but the success of this approach depends on how strongly each target star emits at soft X-ray energies; this method would be more appropriate for O supergiants such as ζ Pup which are already known to be observable at these wavelengths. The Very Large Array (VLA) and e-MERLIN are both excellent instruments from which to obtain radio observations at cm wavelengths, which could be complemented by IRAS data at μm wavelengths. Finally, mm and sub-mm data could be obtained using the Submillimetre Common User Bolometer Array (SCUBA) on the James Clerk Maxwell Telescope (JCMT). The most valuable instruments for this type of study are unquestionably VLTI/AMBER and VLTI/MIDI; the combination of the Very Large Telescope Interferometer (VLTI) and a group of beam-combiner instruments AMBER, a near-infra-red interferometer with three 8.3-m unit telescopes (UTs) or MIDI, a mid-infra-red interferometer with two UTs. These instruments are capable of *simultaneous* spatial and spectral observations, such that indications of small and large scale structure in spectral variability could be related to the spatial density distribution of material in the wind. The only problem is whether the large-scale structure present in the stellar wind can be spatially-resolved, given the resolution of these instruments. Such studies are ideally suited to LBVs for example, since they display such extended structures that there is a good chance that they can be resolved. Observational, multi-wavelength campaigns of this nature are a vital step in revising the current theory of massive stars stellar winds to incorporate the effects of clumping and to help us constrain reliable mass loss rate estimates.

APPENDIX A

CMFGEN fits to the observed spectra of 20 Galactic B supergiants

Here the CMFGEN model fits to each of the 20 B supergiants presented in this work are shown. B Ia and B Ib/Iab/II supergiants are presented separately and the fits to the overall optical spectra are given in Figs. A.1, A.2, A.3, A.4, A.5 & A.6 over 3 consecutive wavelength ranges: 4050 – 4250 Å, 4250 – 4450 Å and 4450 – 4560 Å. The optimum CMFGEN model fits to the observed Hα profile are then shown in Fig. A.7 for B Ias and Fig. A.8 for B Ib/Iab/IIs. Lastly, the fits to the overall UV spectra are shown in Figs. A.9, A.10, A.11, A.12, A.13 & A.14. Again, B Ia and B Ib/Iab/II supergiants presented separately and shown over 3 consecutive wavelength ranges: 1230 – 1480 Å, 1480 – 1680 Å and 1680 – 1880 Å.

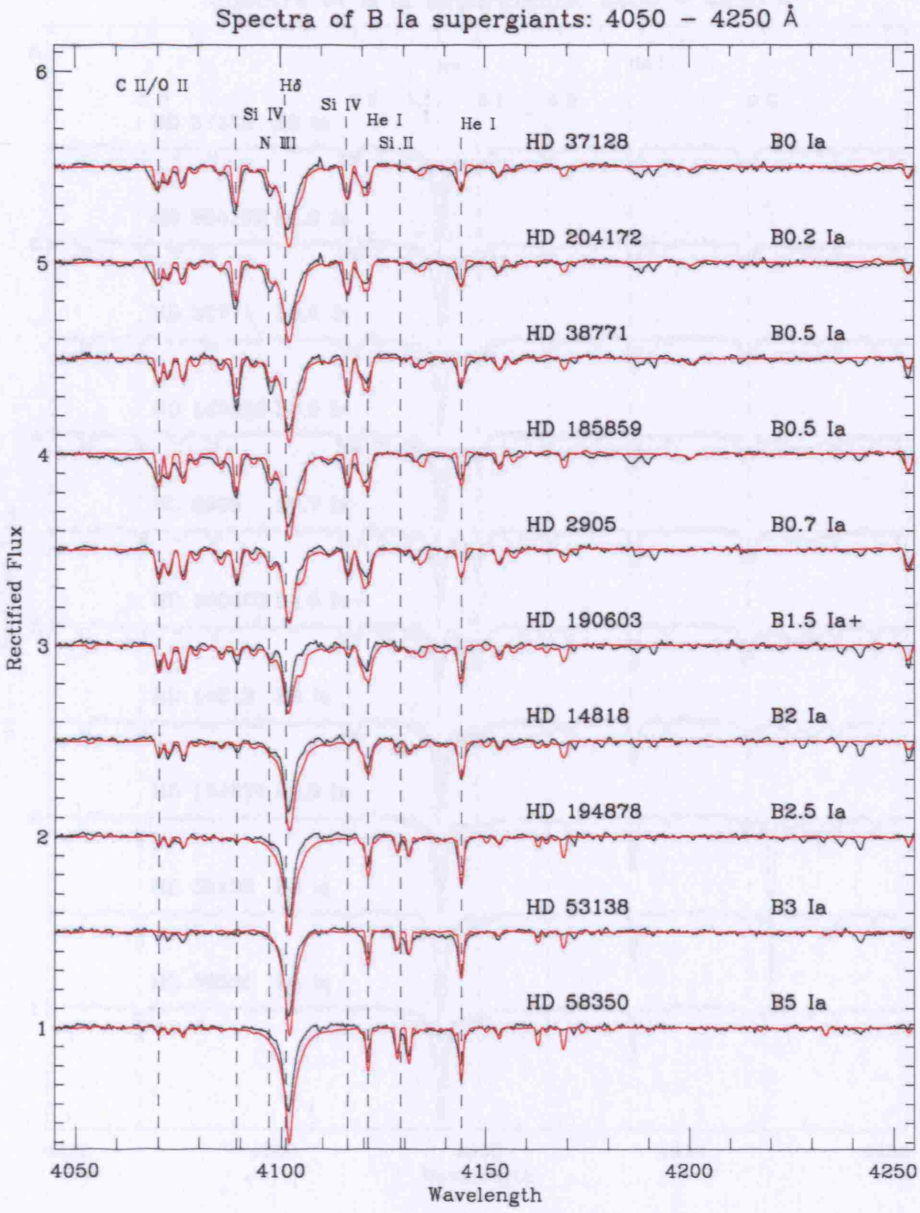

Figure A.1: CMFGEN model fits to the optical spectra of 10 B Ia supergiants, with the $T_{\rm eff}$, luminosity and CNO diagnostic lines marked as shown. Optical spectrum is in black, CMFGEN model fit is shown in red.

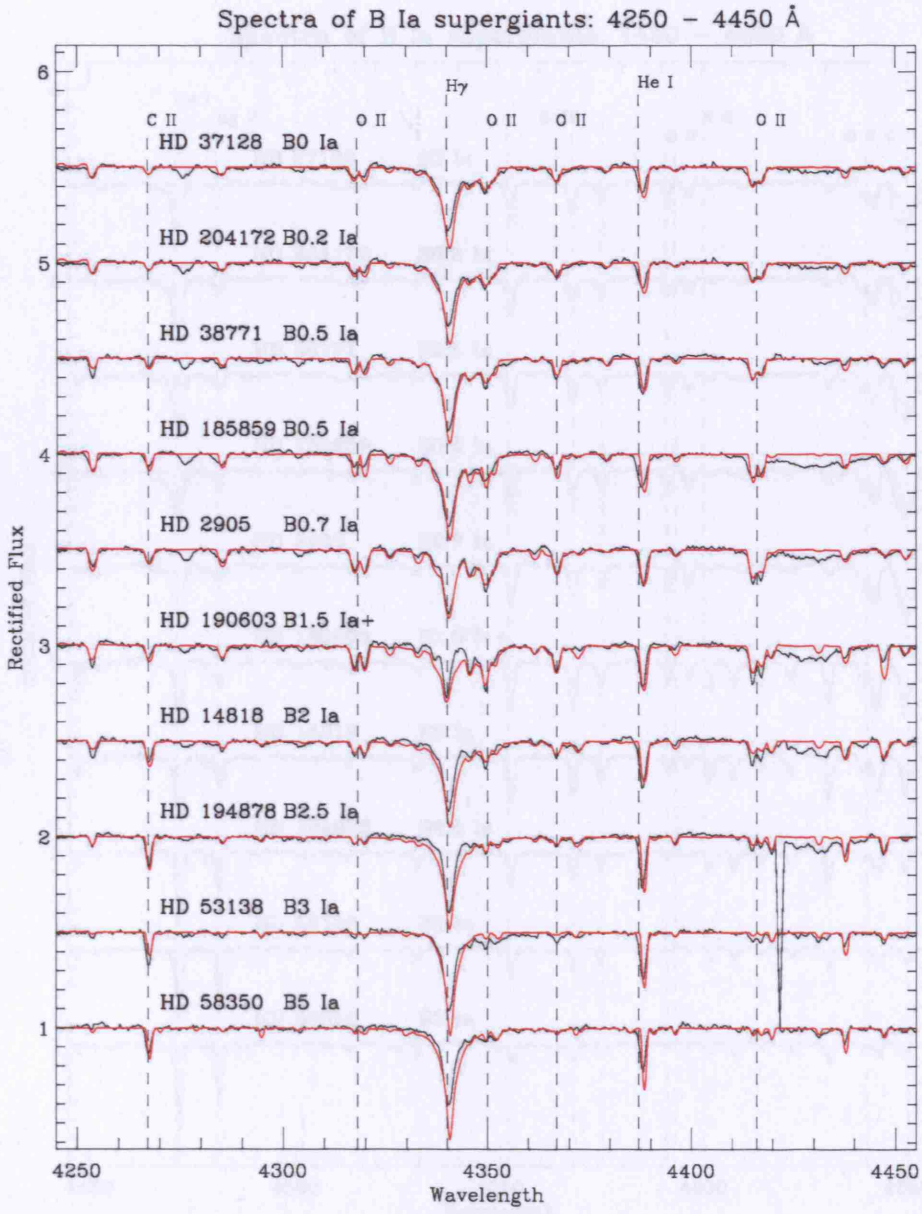

Figure A.2: CMFGEN model fits to the optical spectra of 10 B Ia supergiants, with the $T_{\rm eff}$, luminosity and CNO diagnostic lines marked as shown. Optical spectrum is in black, CMFGEN model fit is shown in red.

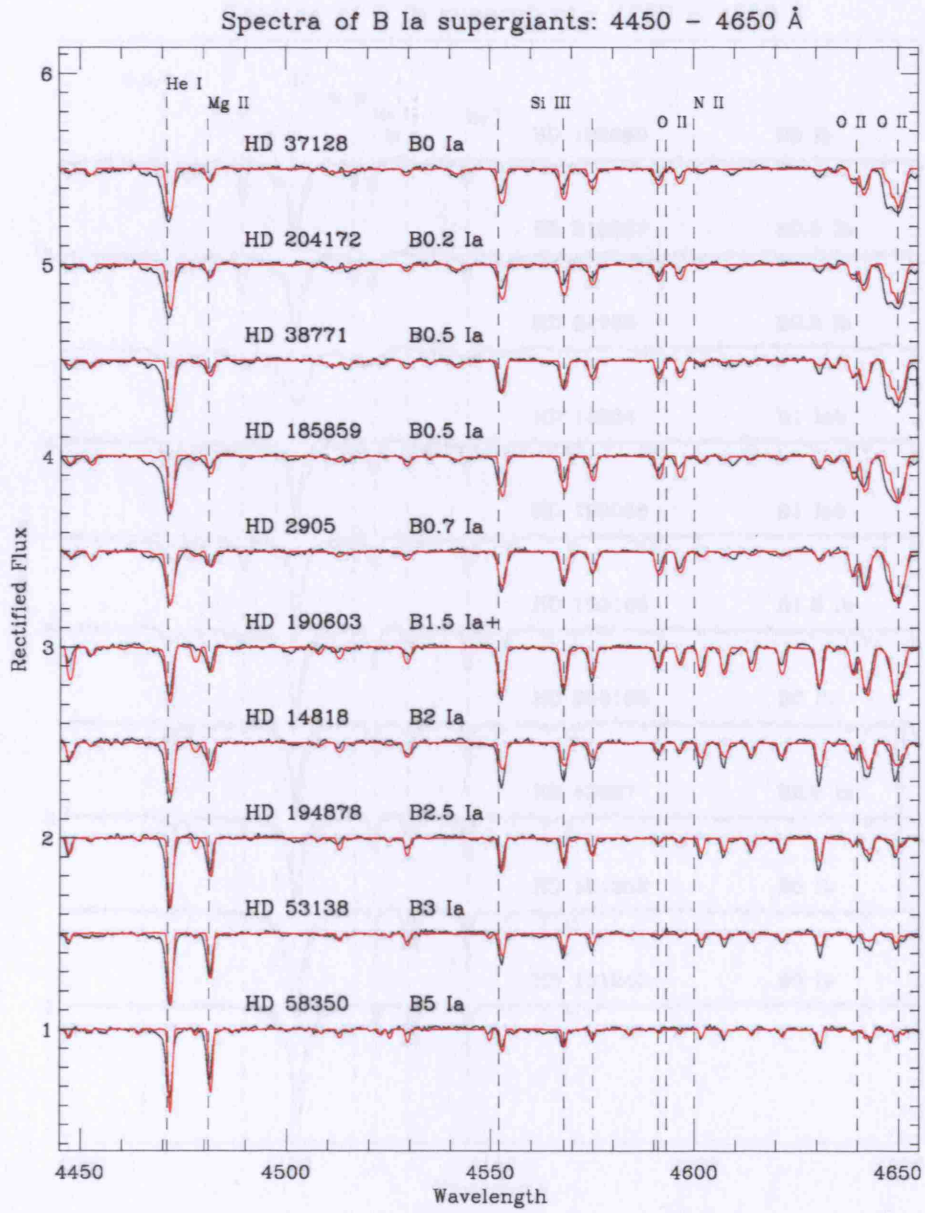

Figure A.3: CMFGEN model fits to the optical spectra of 10 B Ia supergiants, with the $T_{\rm eff}$, luminosity and CNO diagnostic lines marked as shown. Optical spectrum is in black, CMFGEN model fit is shown in red.

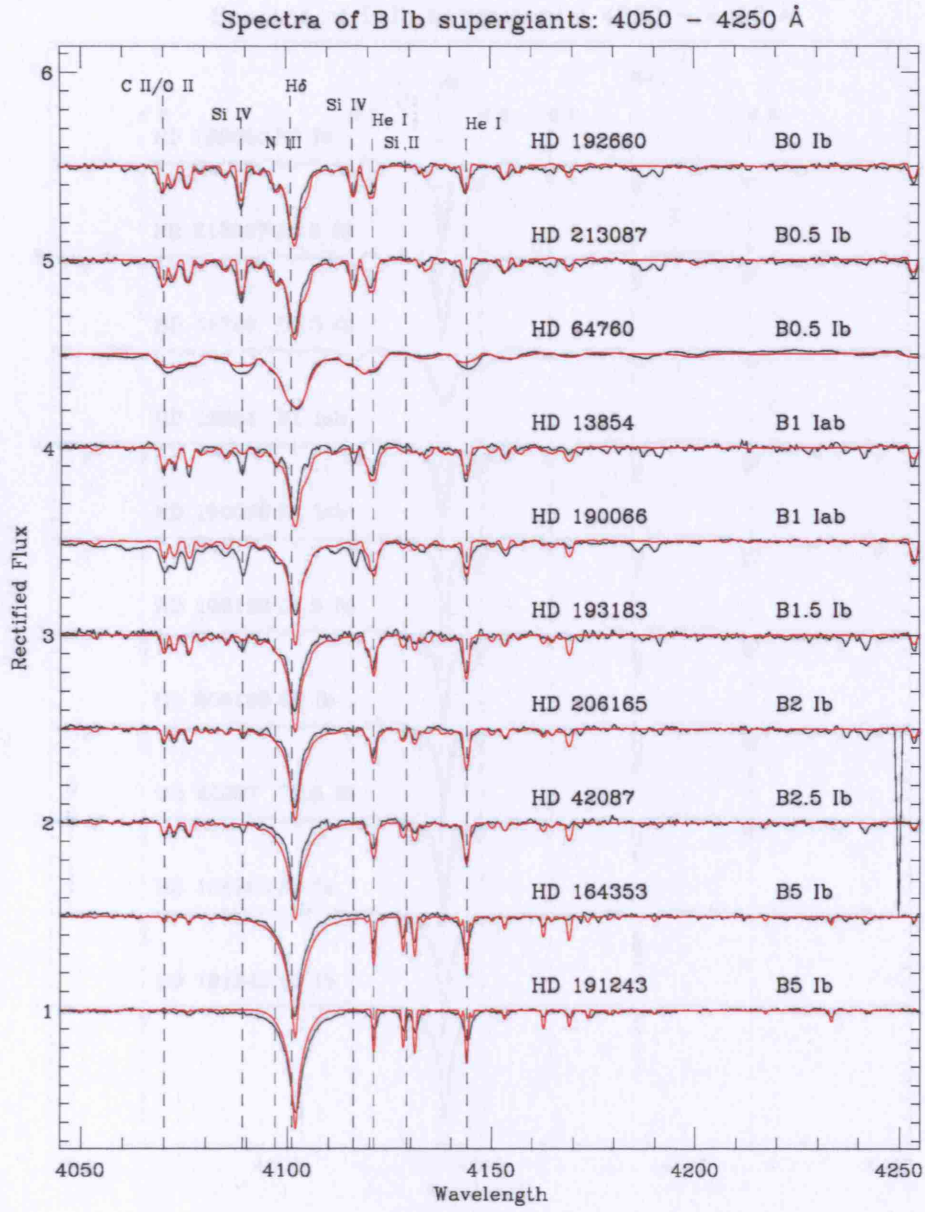

Figure A.4: CMFGEN model fits to the optical spectra of 10 B Ib supergiants, with the $T_{\rm eff}$, luminosity and CNO diagnostic lines marked as shown. Optical spectrum is in black, CMFGEN model fit is shown in red.

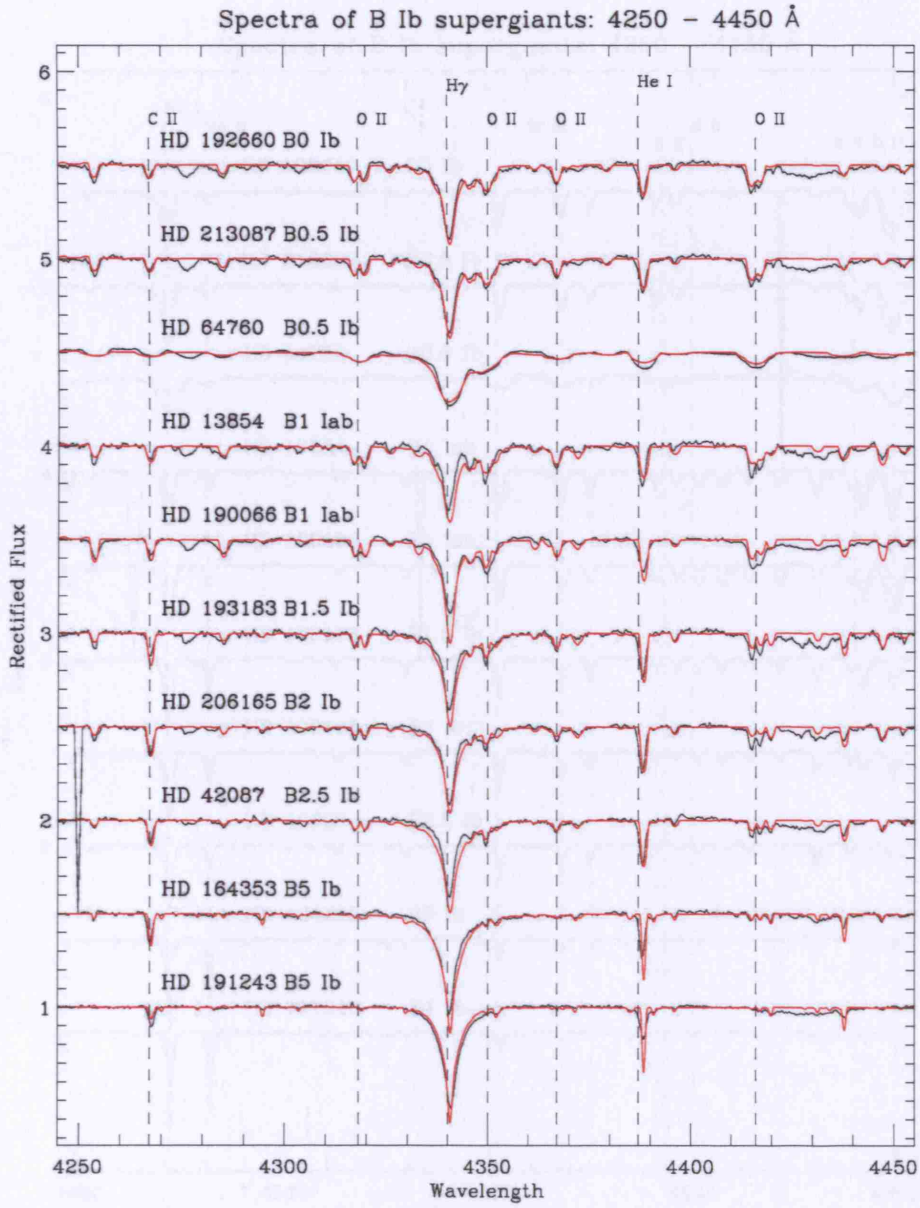

Figure A.5: CMFGEN model fits to the optical spectra of 10 B Ib supergiants, with the $T_{\rm eff}$, luminosity and CNO diagnostic lines marked as shown. Optical spectrum is in black, CMFGEN model fit is shown in red.

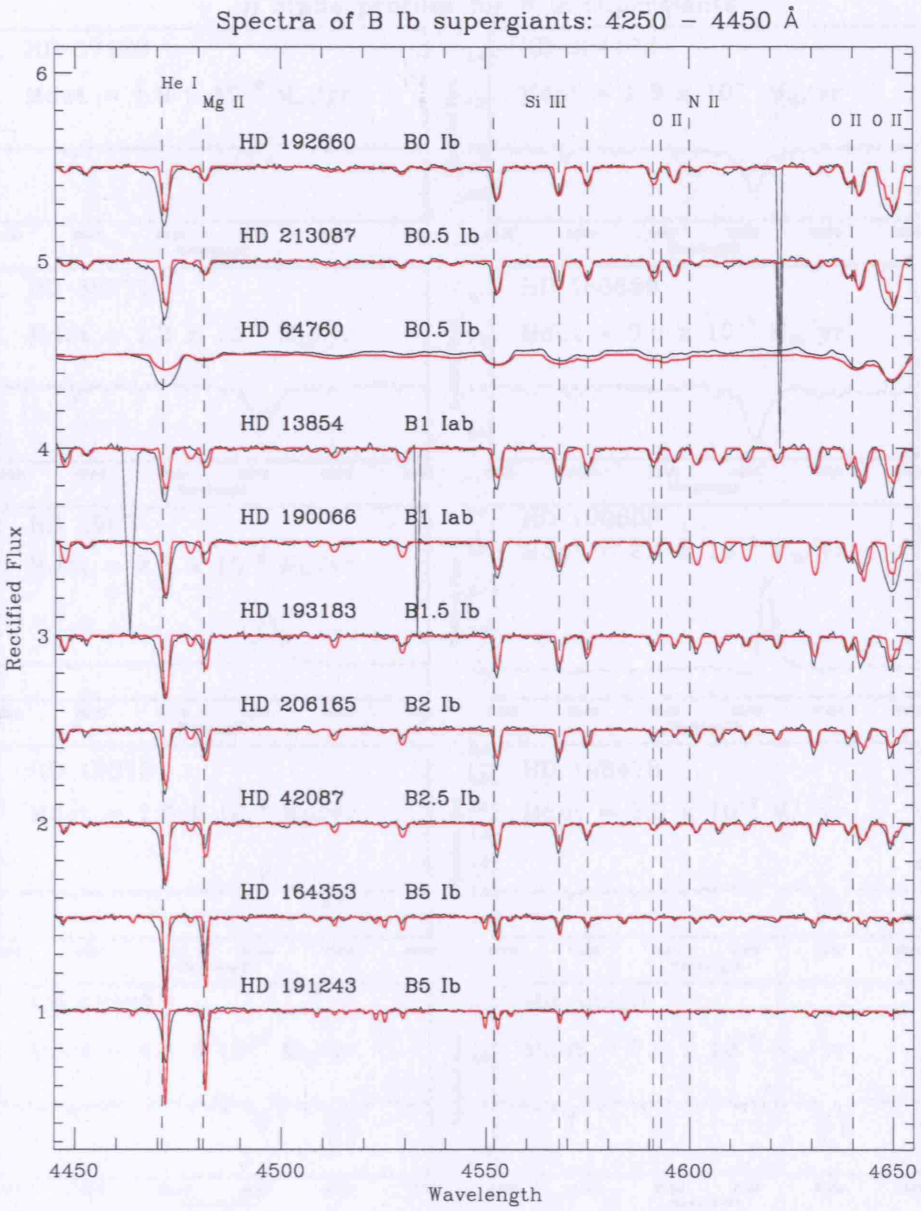

Figure A.6: CMFGEN model fits to the optical spectra of 10 B Ib supergiants, with the $T_{\rm eff}$, luminosity and CNO diagnostic lines marked as shown. Optical spectrum is in black, CMFGEN model fit is shown in red.

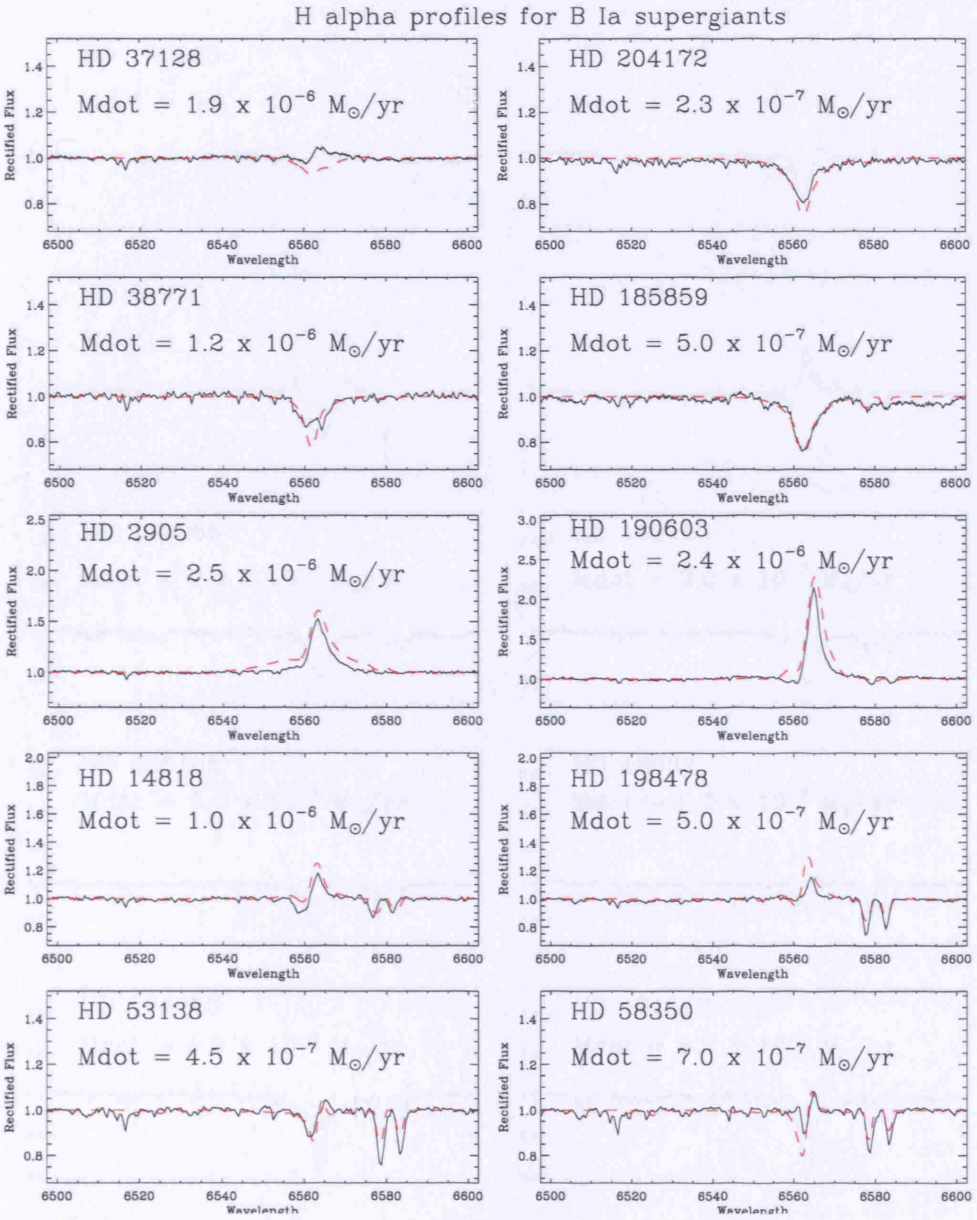

Figure A.7: CMFGEN model fits to the Hα profiles of 10 B Ia supergiants. Optical spectrum is in black, CMFGEN model fit is shown in red. The value of $\dot{M}$ assumed for each star is given below the HD no.

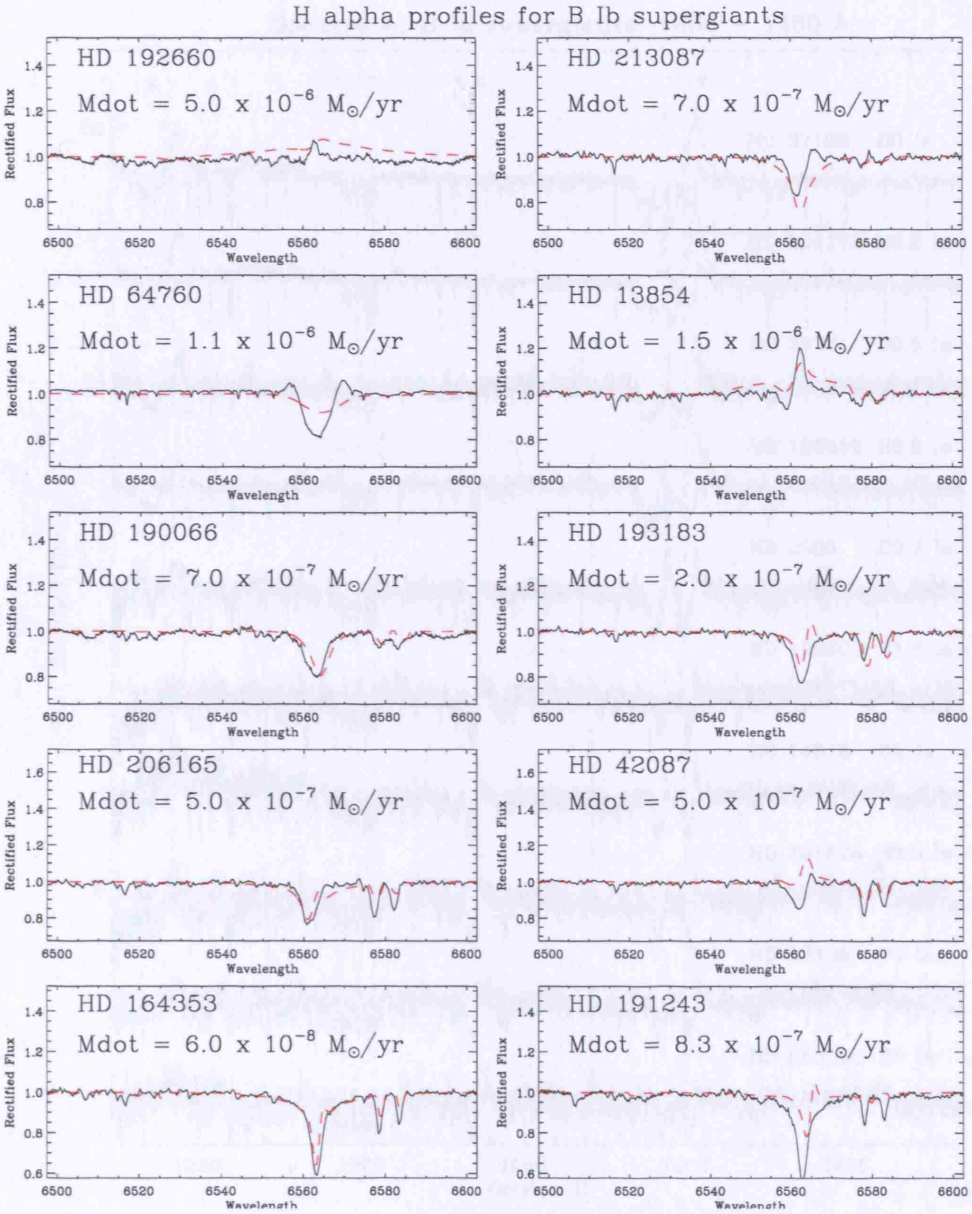

Figure A.8: CMFGEN model fits to the Hα profiles of 10 B Ib supergiants. Optical spectrum is in black, CMFGEN model fit is shown in red. The value of $\dot{M}$ assumed for each star is given below the HD no.

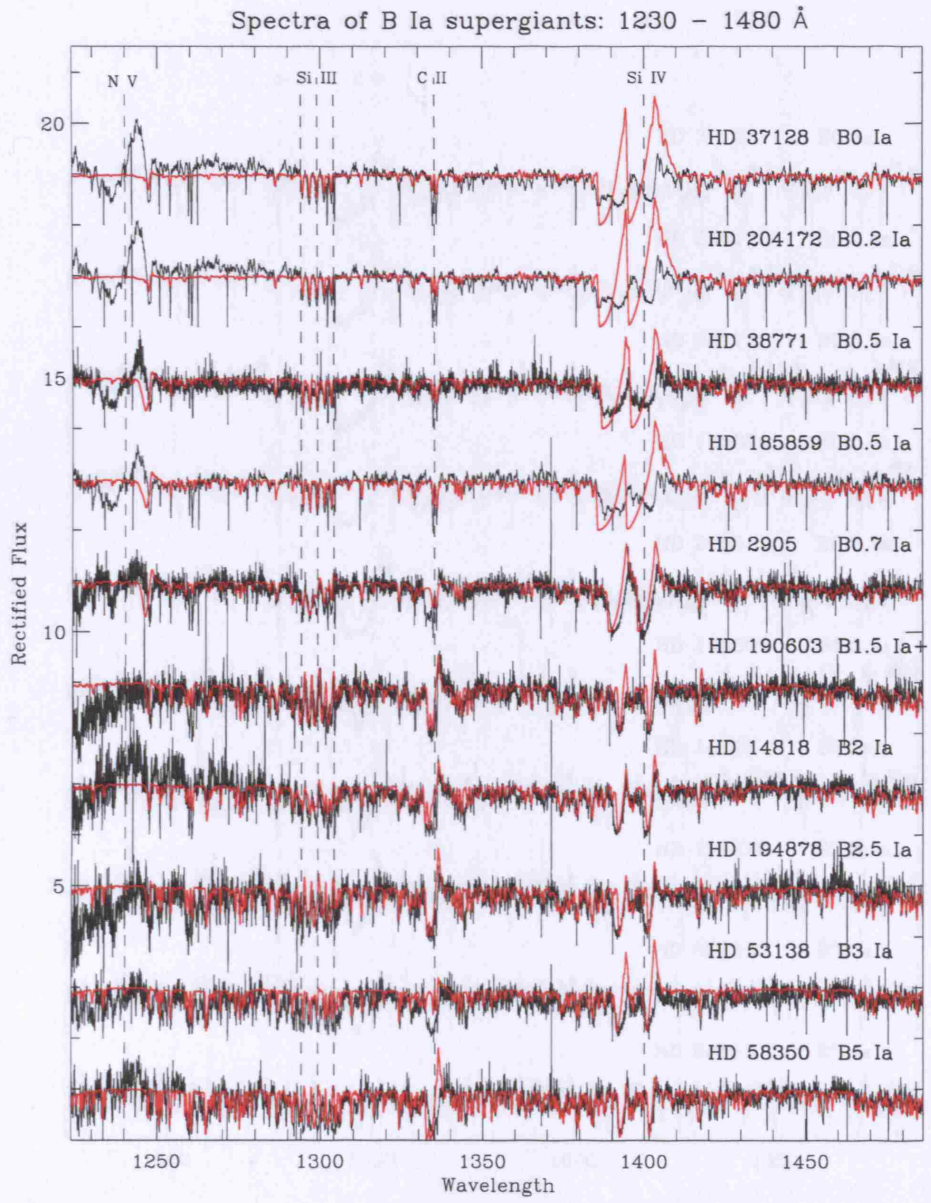

Figure A.9: CMFGEN model fits to the UV spectra of 10 B Ia supergiants, with diagnostic lines marked as shown. UV spectrum is in black, CMFGEN model fit is shown in red.

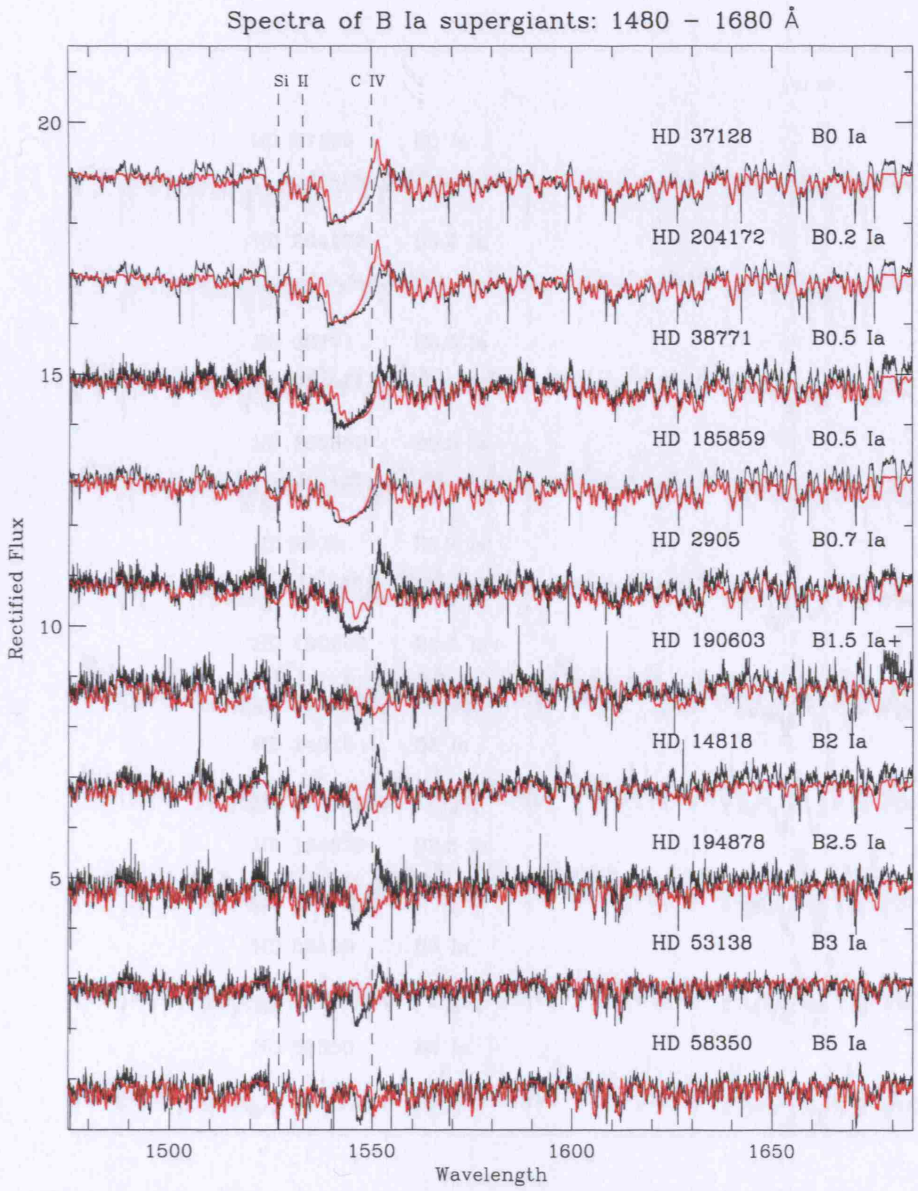

Figure A.10: CMFGEN model fits to the UV spectra of 10 B Ia supergiants, with diagnostic lines marked as shown. UV spectrum is in black, CMFGEN model fit is shown in red.

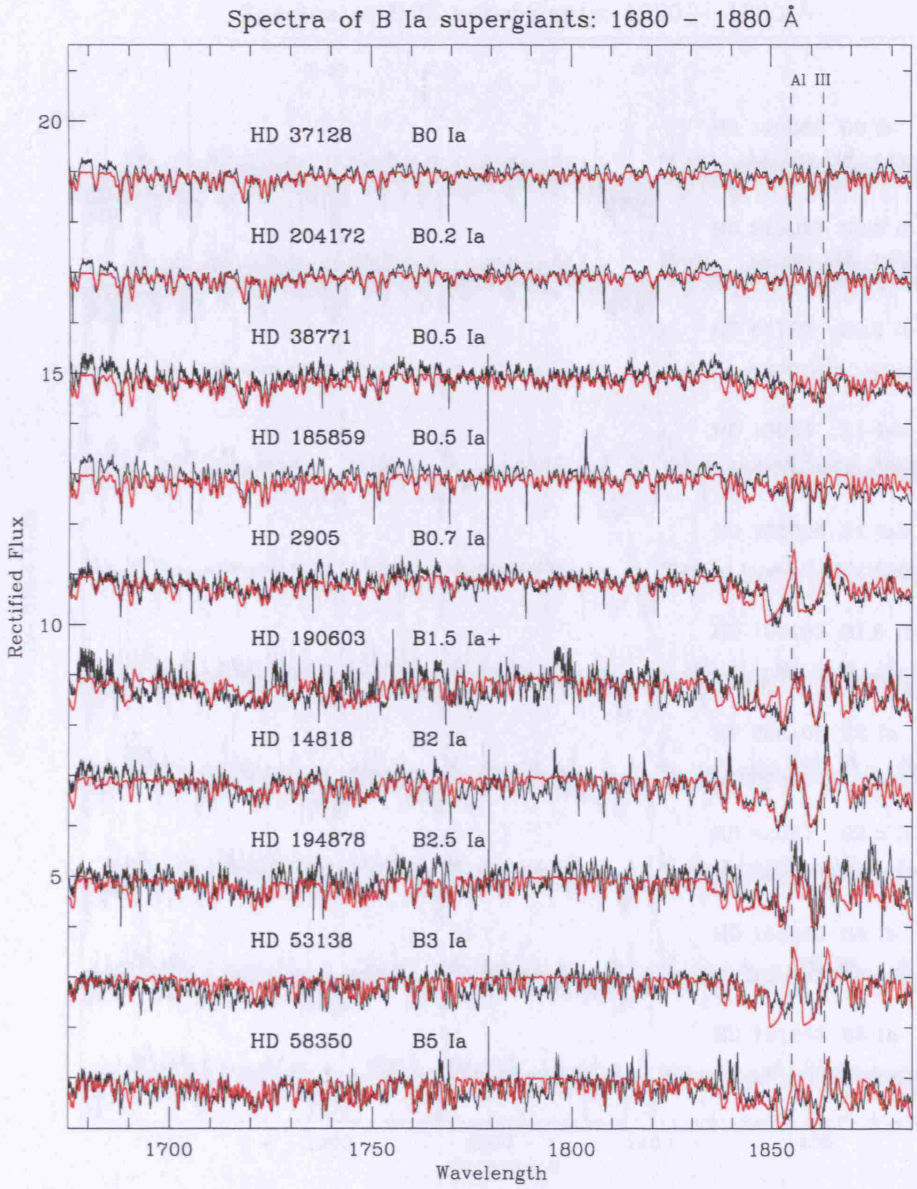

Figure A.11: CMFGEN model fits to the UV spectra of 10 B Ia supergiants, with diagnostic lines marked as shown. UV spectrum is in black, CMFGEN model fit is shown in red.

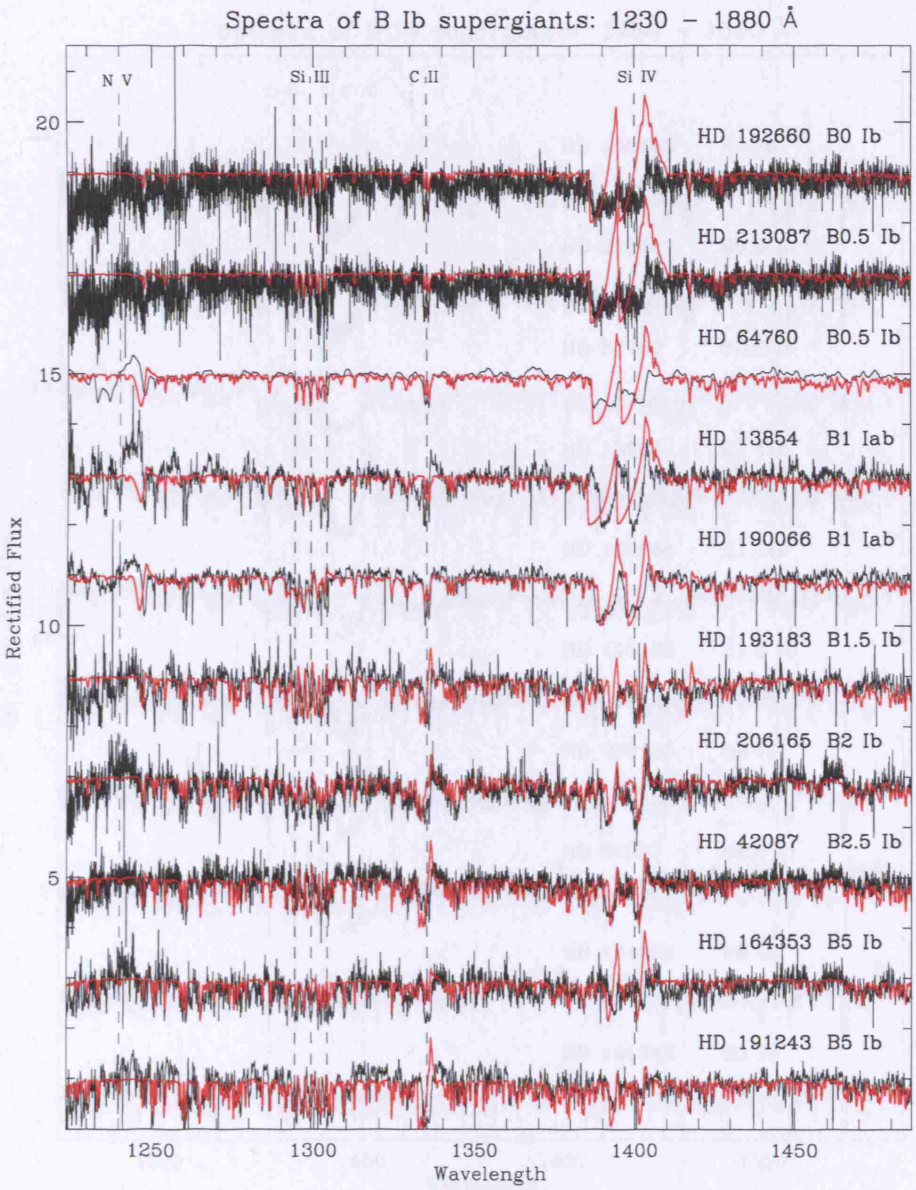

Figure A.12: CMFGEN model fits to the UV spectra of 10 B Ib supergiants, with diagnostic lines marked as shown. UV spectrum is in black, CMFGEN model fit is shown in red.

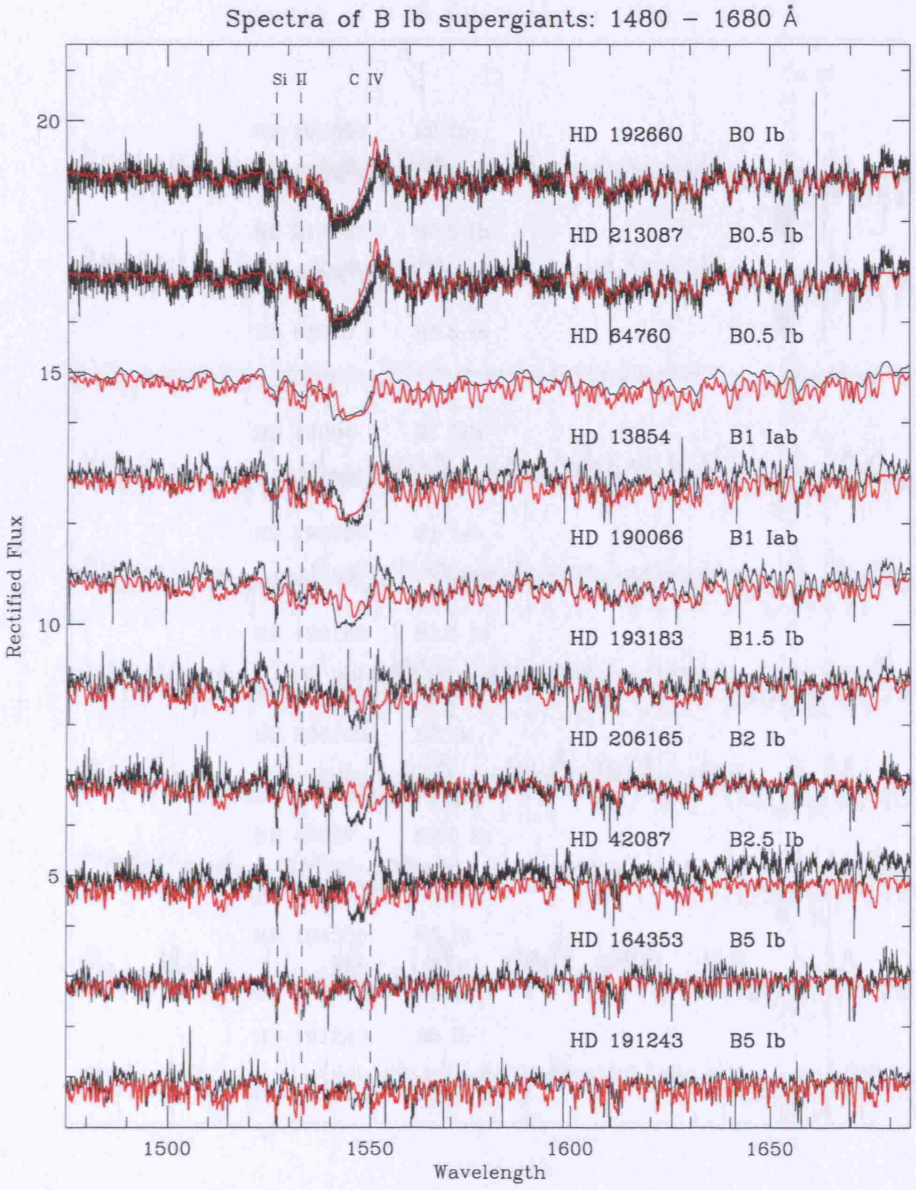

Figure A.13: CMFGEN model fits to the UV spectra of 10 B Ib supergiants, with diagnostic lines marked as shown. UV spectrum is in black, CMFGEN model fit is shown in red.

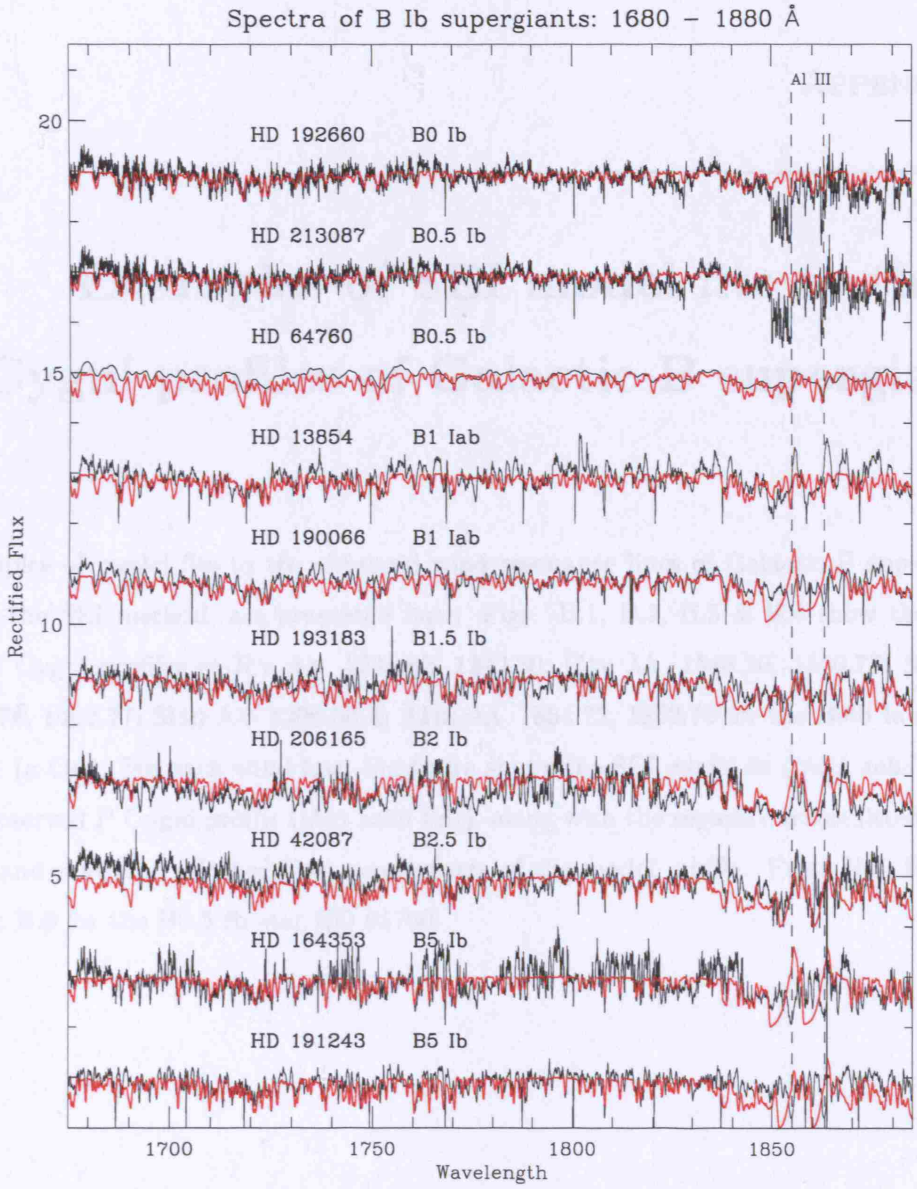

Figure A.14: CMFGEN model fits to the UV spectra of 10 B Ib supergiants, with diagnostic lines marked as shown. UV spectrum is in black, CMFGEN model fit is shown in red.

APPENDIX B

Examples of SEI model fits to the P Cygni profiles of Galactic B supergiants

Examples of model fits to the observed wind resonance lines of Galactic B supergiants, using the SEI method, are presented here. Figs. B.1, B.2, B.3 & B.4 show the fits to the P Cygni profiles of N V $\lambda\lambda$ 1238.82, 1242.80; C IV $\lambda\lambda$ 1548.20, 1550.77; Si IV $\lambda\lambda$ 1393.76, 1402.77; Si III $\lambda\lambda$ 1206.50 & Al III $\lambda\lambda$ 1854.72, 1862.79 for the B0.5 Ia star HD 38771 (κ Ori). For each wind line, the figure shows the SEI model fit (*thick solid line*) to the observed P Cygni profile (*thin solid line*), along with the separate transmitted (*dotted line*) and scattered (*dashed line*) components of the model profile. Figs. B.5, B.6, B.7, B.8 & B.9 for the B0.5 Ib star HD 64760.

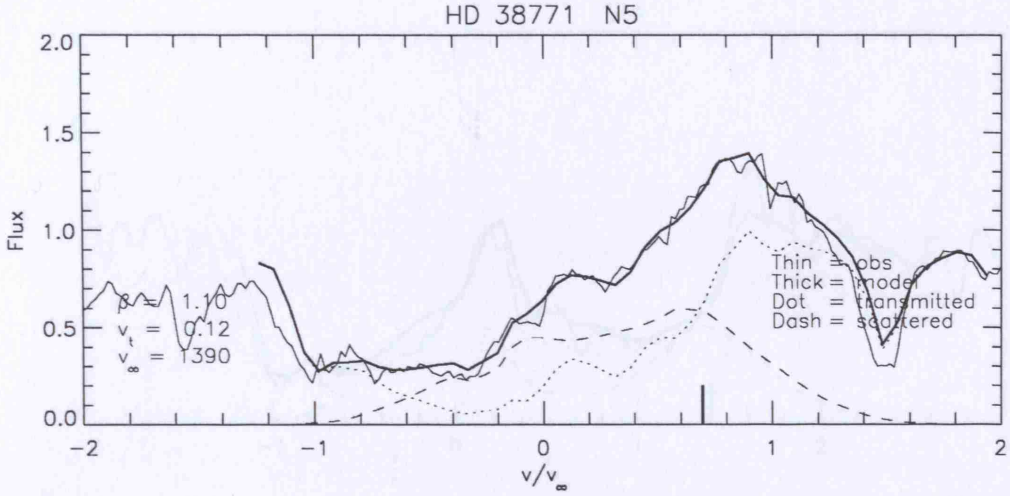

Figure B.1: SEI model fit to N V for HD 38771 (B0.5 Ia)

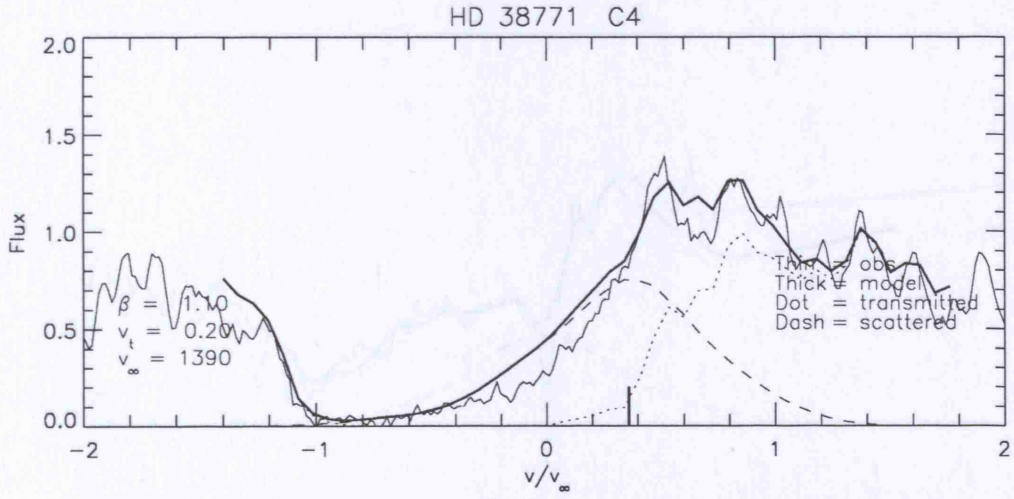

Figure B.2: SEI model fit to C IV for HD 38771 (B0.5 Ia)

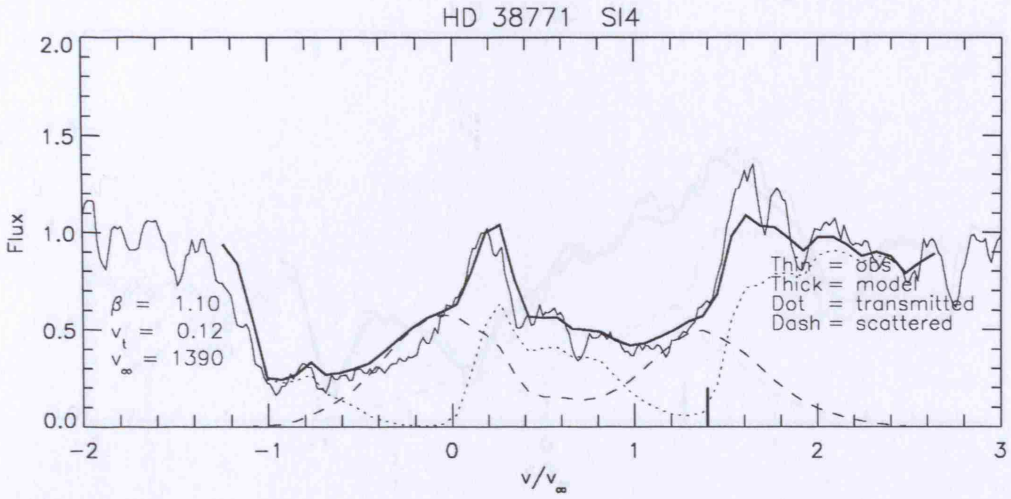

Figure B.3: SEI model fit to Si IV for HD 38771 (B0.5 Ia)

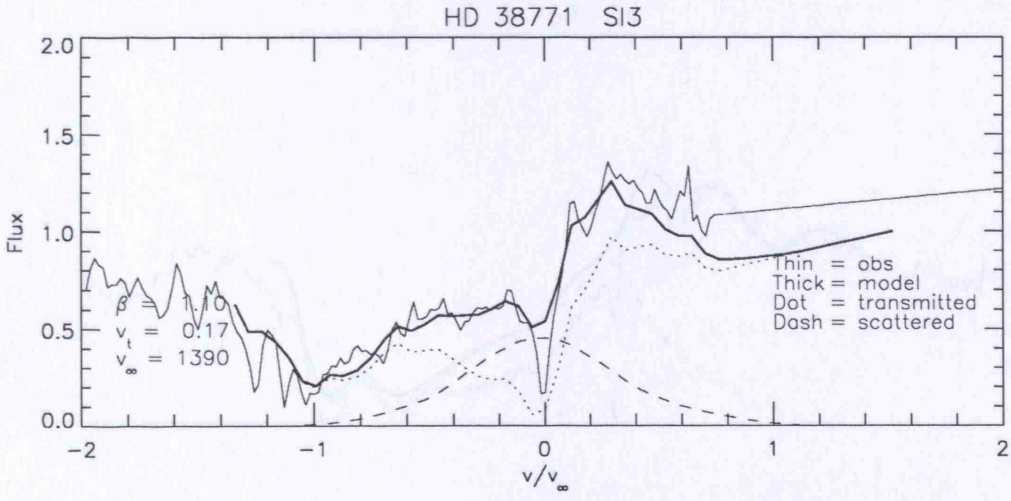

Figure B.4: SEI model fit to Si III for HD 38771 (B0.5 Ia)

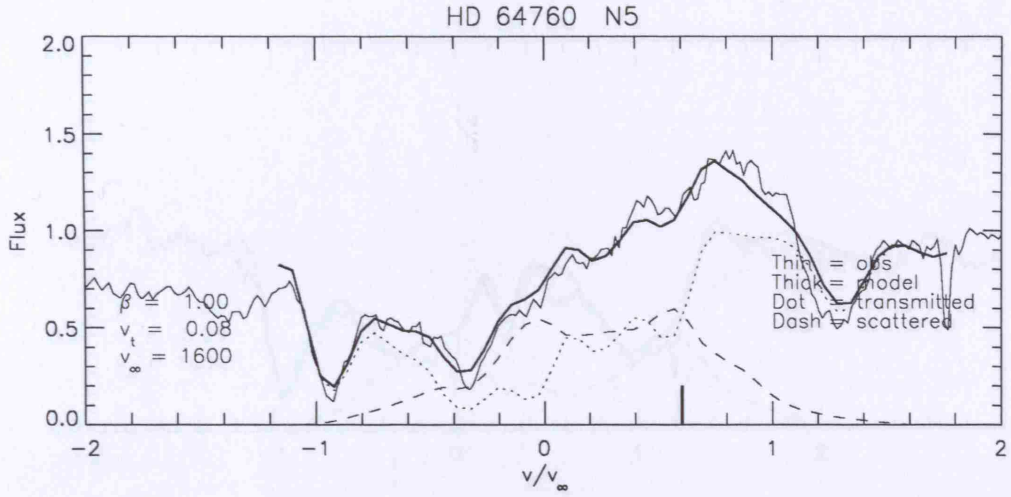

Figure B.5: SEI model fit to N V for HD 64760 (B0.5 Ib)

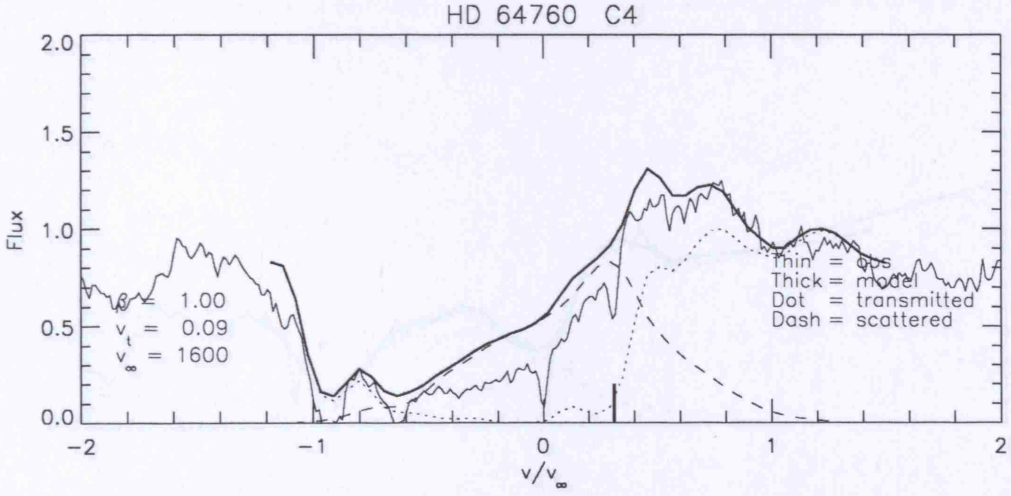

Figure B.6: SEI model fit to C IV for HD 64760 (B0.5 Ib)

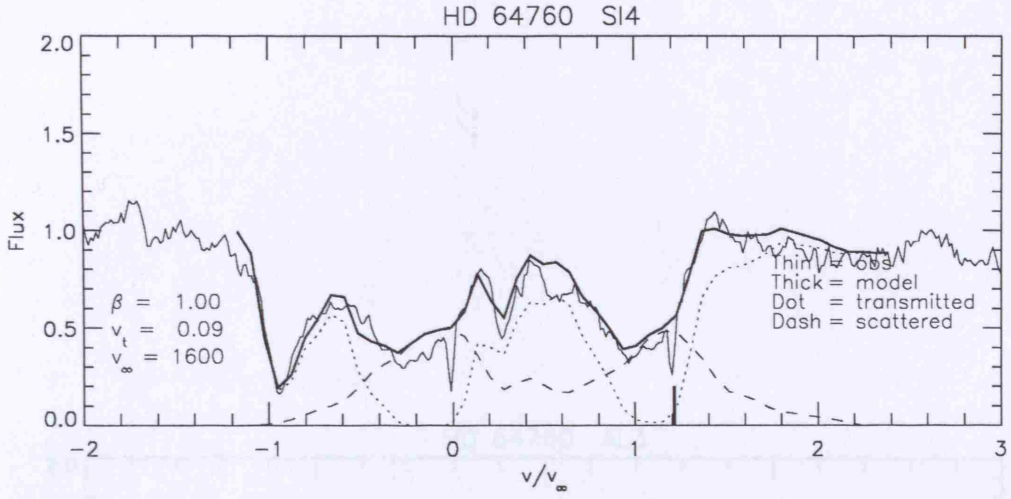

Figure B.7: SEI model fit to Si IV for HD 64760 (B0.5 Ib)

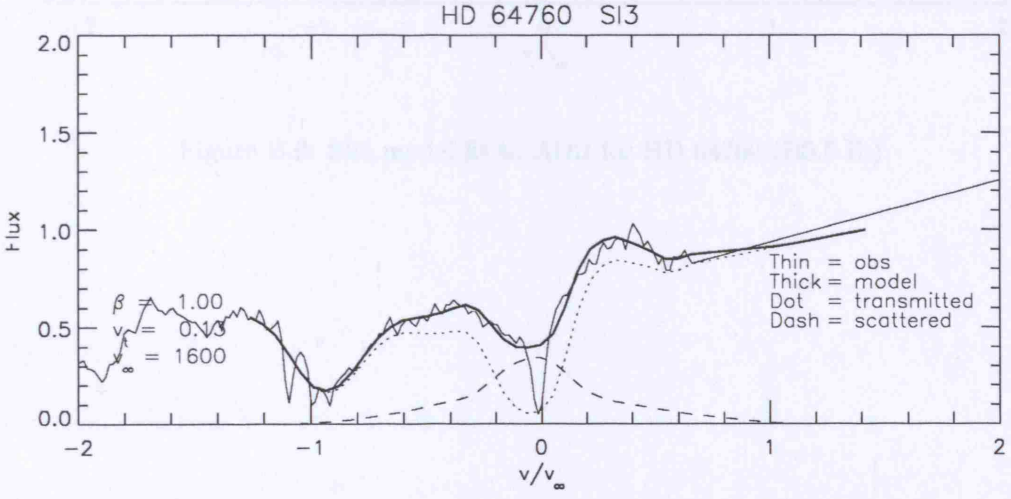

Figure B.8: SEI model fit to Si III for HD 64760 (B0.5 Ib)

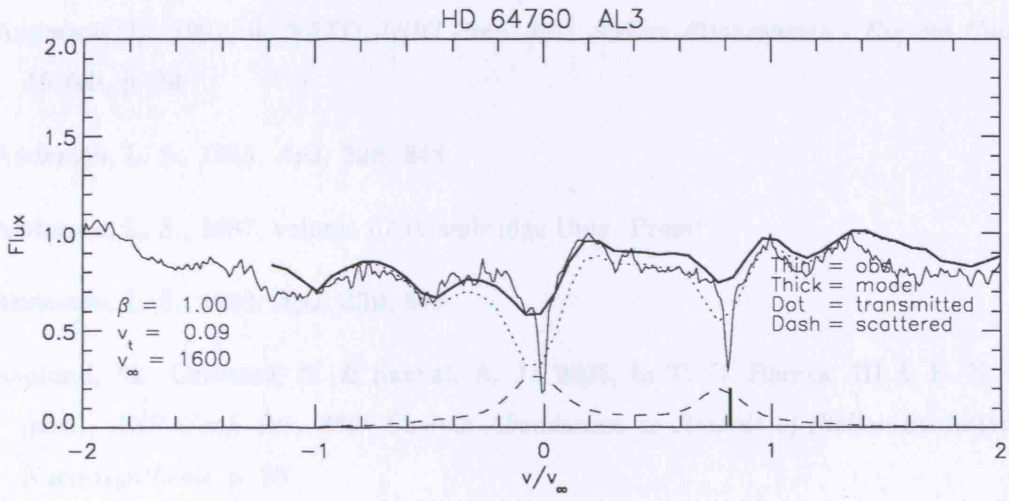

Figure B.9: SEI model fit to Al III for HD 64760 (B0.5 Ib)

Bibliography

Abbott, D. C., 1977, *Ph.D. Thesis*

Abbott, D. C., 1982, *ApJ*, **259**, 282

Anderson, L., 1991, in *NATO ASIC Proc. 341: Stellar Atmospheres - Beyond Classical Models*, p. 29

Anderson, L. S., 1985, *ApJ*, **298**, 848

Anderson, L. S., 1987, volume 67 (Cambridge Univ. Press)

Anderson, L. S., 1989, *ApJ*, **339**, 588

Asplund, M., Grevesse, N. & Sauval, A. J., 2005, in T. G. Barnes, III & F. N. Bash (eds.), *ASP Conf. Ser. 336: Cosmic Abundances as Records of Stellar Evolution and Nucleosynthesis*, p. 25

Auer, L. H. & Mihalas, D., 1969, *ApJ*, **158**, 641

Barlow, M. J. & Cohen, M., 1977, *ApJ*, **213**, 737

Beals, C. S., 1951, *MNRAS*, **111**, 202

Berghoefer, T. W., Schmitt, J. H. M. M. & Cassinelli, J. P., 1996, *A&AS*, **118**, 481

Bianchi, L. Garcia, M., 2002, *ApJ*, **581**, 610

Bidelman, W. P., 1988, *PASP*, **100**, 1084

Bieging, J. H., Abbott, D. C. & Churchwell, E. B., 1989, *ApJ*, **340**, 518

Blomme, R., Prinja, R. K., Runacres, M. C. & Colley, S., 2002, *A&A*, **382**, 921

Blomme, R., van de Steene, G. C., Prinja, R. K., Runacres, M. C. & Clark, J. S., 2003, *A&A*, **408**, 715

Bouret, J.-C., Lanz, T. & Hillier, D. J., 2005, *A&A*, **438**, 301

Bouret, J.-C., Lanz, T., Hillier, D. J., Heap, S. R., Hubeny, I., Lennon, D. J., Smith, L. J. & Evans, C. J., 2003, *ApJ*, **595**, 1182

Bromm, V., Kudritzki, R. P. & Loeb, A., 2001, *ApJ*, **552**, 464

Brown, A. G. A., de Geus, E. J. & de Zeeuw, P. T., 1994, *A&A*, **289**, 101

Busche, J. R. & Hillier, D. J., 2005, *AJ*, **129**, 454

Cannon, C. J., 1973*a*, *J. Quant. Rad. Spectrosc. Radiat. Transfer*, **13**, 627

Cannon, C. J., 1973*b*, *ApJ*, **185**, 621

Cassinelli, J. P., Miller, N. A., Waldron, W. L., MacFarlane, J. J. & Cohen, D. H., 2001, *ApJL*, **554**, L55

Cassinelli, J. P. & Olson, G. L., 1979, *ApJ*, **229**, 304

Castor, J. I., Abbott, D. C. & Klein, R. I., 1975, *ApJ*, **195**, 157

Chlebowski, T., Harnden, F. R. & Sciortino, S., 1989, *ApJ*, **341**, 427

Cranmer, S. R. & Owocki, S. P., 1996, *ApJ*, **462**, 469

Crowther, P. A., Hillier, D. J., Evans, C. J., Fullerton, A. W., De Marco, O. & Willis, A. J., 2002, *ApJ*, **579**, 774

Crowther, P. A., Lennon, D. J. & Walborn, N. R., 2006, *A&A*, **446**, 279

Cunha, K. & Lambert, D. L., 1992, *ApJ*, **399**, 586

Cunha, K. & Lambert, D. L., 1994, *ApJ*, **426**, 170

de Koter, A., Heap, S. R. & Hubeny, I., 1997, *ApJ*, **447**, 792

de Zeeuw, P. T., Hoogerwerf, R., de Bruijne, J. H. J., Brown, A. G. A. & Blaauw, A., 1999, *AJ*, **117**, 354

Dessart, L. & Owocki, S., 2003, *ApJ*, **406**, L1

Dessart, L. & Owocki, S., 2005, *ApJ*, **437**, 657

Dessart, L. & Owocki, S. P., 2005, *A&A*, **437**, 657

Dufton, P. L., Ryans, R. S. I., Trundle, C., Lennon, D. J., Hubeny, I., Lanz, T. & Allende Prieto, C., 2005, *A&A*, **434**, 1125

Egret, D., 1978, *A&A*, **66**, 275

Evans, C. J., Crowther, P. A., Fullerton, A. W. & Hillier, D. J., 2004*a*, *ApJ*, **610**, 1021

Evans, C. J., Lennon, D. J., Trundle, C., Heap, S. R. & Lindler, D. J., 2004*b*, *ApJ*, **607**, 451

Feldmeier, A., Puls, J. & Pauldrach, A. W. A., 1997, *A&A*, **322**, 878

Fernie, J. D., 1983, *ApJS*, **52**, 7

Fitzgerald, M. P., 1970, *A&A*, **4**, 234

Fransson, C., Cassatella, A., Gilmozzi, R., Kirshner, R. P., Panagia, N., Sonneborn, G. & Wamsteker, W., 1989, *ApJ*, **336**, 429

Fryer, C. L., Woosley, S. E. & Hartmann, D. H., 1999, *ApJ*, **526**, 152

Fullerton, A. W., Massa, D. L. & Prinja, R. K., 2006, *ApJ*, **637**, 1025

Fullerton, A. W., Massa, D. L., Prinja, R. K., Owocki, S. P. & Cranmer, S. R., 1997, *A&A*, **327**, 699

Garmany, C. D. & Stencel, R. E., 1992, *A&AS*, **94**, 211

Gies, D. R. & Lambert, D. L., 1992, *ApJ*, **387**, 673

Hamann, W.-R., 1981, *A&A*, **93**, 353

Hanson, M. M. & Conti, P. S., 1994, *ApJL*, **423**, L139+

Hanson, M. M., Conti, P. S. & Rieke, M. J., 1996, *ApJS*, **107**, 281

Hanson, M. M., Kudritzki, R.-P., Kenworthy, M. A., Puls, J. & Tokunaga, A. T., 2005, *ApJS*, **161**, 154

Haser, S. M., 1995, *Ph.D. Thesis*

Heger, A., Fryer, C. L., Woosley, S. E., Langer, N. & Hartmann, D. H., 2003, *ApJ*, **591**, 288

Heger, A. & Woosley, S. E., 2002, *ApJ*, **567**, 532

Hendry, M. A., Smartt, S. J., Maund, J. R., Pastorello, A., Zampieri, L., Benetti, S., Turatto, M., Cappellaro, E., Meikle, W. P. S., Kotak, R., Irwin, M. J., Jonker, P. G., Vermaas, L., Peletier, R. F., van Woerden, H., Exter, K. M., Pollacco, D. L., Leon, S., Verley, S., Benn, C. R. & Pignata, G., 2005, *MNRAS*, **359**, 906

Herrero, A., Kudritzki, R. P., Vilchez, J. M., Kunze, D., Butler, K. & Haser, S., 1992, *A&A*, **261**, 209

Herrero, A., Puls, J. & Najarro, F., 2002, *A&A*, **396**, 949

Hillier, D. J., 1990, *A&A*, **231**, 116

Hillier, D. J., Lanz, T., Heap, S. R., Hubeny, I., Smith, L. J., Evans, C. J., Lennon, D. J. & Bouret, J. C., 2003, *ApJ*, **588**, 1039

Hillier, D. J. & Miller, D. L., 1998, *ApJ*, **496**, 407

Hillier, D. J. & Miller, D. L., 1999, *ApJ*, **519**, 354

Hiltner, W. A., 1956, *ApJS*, **2**, 389

Hoffleit, D. & Jaschek, C., 1982, *The Bright Star Catalogue* (The Bright Star Catalogue, New Haven: Yale University Observatory (4th edition), 1982)

Howarth, I. D., Siebert, K. W., Hussain, G. A. J. & Prinja, R. K., 1997, *MNRAS*, **284**, 265

Hubeny, I. Hummer, D. G. & Lanz, T., 1994, *A&A*, **282**, 151

Hubeny, I., 1988, *Comput. Phys. Comm.*, **52**, 103

Hubeny, I. & Lanz, T., 1995, *ApJ*, **439**, 875

Hubeny, I. & Lanz, T., 2003, *TLUSTY - A User's Guide (Version 200)*

Hummer, D. G. & Mihalas, D., 1988, *ApJ*, **150**, L57

Hummer, D. G., Berrington, K. A., Eissner, W., Pradhan, A. K., Saraph, H. E. & Tully, J. A., 1993, *A&A*, **279**, 298

Humphreys, R. M., 1978, *ApJS*, **38**, 309

Humphreys, R. M. & McElroy, D. B., 1984, *ApJ*, **284**, 565

Kaufer, A., Stahl, O., Prinja, R. K. & Witherick, D., 2006, *A&A*, **447**, 325

Kaufer, A., Stahl, O., Wolf, B., Fullerton, A. W., Gaeng, T., Gummersbach, C. A., Jankovics, I., Kovacs, J., Mandel, H., Peitz, J., Rivinius, T. & Szeifert, T., 1997, *A&A*, **320**, 273

Kaufer, A., Stahl, O., Wolf, B., Gaeng, T., Gummersbach, C. A., Kovacs, J., Mandel, H. & Szeifert, T., 1996, *A&A*, **305**, 887

Kaufer, A. Prinja, R. K. & Stahl, O., 2002, *A&A*, **382**, 1032

Kudritzki, R.-P., Lennon, D. J. & Puls, J., 1995, in J. R. Walsh & I. J. Danziger (eds.), *Science with the VLT*, p. 246

Kudritzki, R.-P. & Puls, J., 2000, *ARA*, **38**, 613

Kudritzki, R. P., Puls, J., Lennon, D. J., Venn, K. A., Reetz, J., Najarro, N., McCarthy, J. K. & Herrero, A., 1999, *A&A*, **350**, 970

Kurucz, R., 1994, *Atomic Data for Fe and Ni. Kurucz CD-ROM No. 22. Cambridge, Mass.: Smithsonian Astrophysical Observatory, 1994.*, **22**

Kurucz, R. L., 1979, *ApJS*, **40**, 1

Kurucz, R. L., 1990, *Trans IAU*, **20B**, 169

Kurucz, R. L., 1991, *Stellar Atmospheres: Beyond Classical Models* (NATO ASI Ser. C.: Dordrect: Kluwer)

Kurucz, R. L., 1995, *Kurucz CD-ROM 23, Atomic Line Data*, Cambridge:SAO

Lamers, H. J. G. L. M. & Cassinelli, J. P., 1999

Lamers, H. J. G. L. M., Cerruti-Sola, M. & Perinotto, M., 1987, *ApJ*, **314**, 726

Lamers, H. J. G. L. M., Haser, S., de Koter, A. & Leitherer, C., 1999*a*, *ApJ*, **516**, 872

Lamers, H. J. G. L. M., Haser, S., de Koter, A. & Leitherer, C., 1999*b*, *ApJ*, **516**, 872

Lamers, H. J. G. L. M. & Leitherer, C., 1993, *ApJ*, **412**, 771

Lamers, H. J. G. L. M., Nota, A., Panagia, N., Smith, L. J. & Langer, N., 2001, *ApJ*, **551**, 764

Lamers, H. J. G. L. M., Snow, T. P. & Lindholm, D. M., 1995, *ApJ*, **455**, 269

Lanz, T.and Hubeny, I., 2003, *ApJS*, **146**, 417

Lennon, D. J., Dufton, P. L. & Fitzsimmons, A., 1992, *A&AS*, **94**, 569

Lesh, J. R., 1968, *ApJS*, **17**, 371

Lucy, L. B., 1982, *ApJ*, **255**, 278

Maeder, A. & Meynet, G., 2001, *A&A*, **373**, 555

Markova, N., Puls, J., Repolust, T. & Markov, H., 2004, *A&A*, **413**, 693

Markova, N., Puls, J., Scuderi, S. & Markov, H., 2005, *A&A*, **440**, 1133

Martins, F., Schaerer, D. & Hillier, D. J., 2002, *A&A*, **382**, 999

Martins, F., Schaerer, D. & Hillier, D. J., 2005, *A&A*, **436**, 1049

Martins, W. C., Sugar, J., Musgrove, A., Wiese, W. L. & Fuhr, J. R., 1999, *NIST Atomic Spectra Database*

Massa, D., 1989, *A&A*, **224**, 131

Massa, D., Fullerton, A. W., Nichols, J. S., Owocki, S. P., Prinja, R. K., St-Louis, N., Willis, A. J., Altner, B., Bolton, C. T., Cassinelli, J. P., Cohen, D., Cooper, R. G., Feldmeier, A., Gayley, K. G., Harries, T., Heap, S. R., Henriksen, R. N., Howarth, I. D., Hubeny, I., Kambe, E., Kaper, L., Koenigsberger, G., Marchenko, S., McCandliss, S. R., Moffat, A. F. J., Nugis, T., Puls, J., Robert, C., Schulte-Ladbeck, R. E., Smith, L. J., Smith, M. A., Waldron, W. L. & White, R. L., 1995*a*, *ApJL*, **452**, L53

Massa, D., Fullerton, A. W., Sonneborn, G. & Hutchings, J. B., 2003, *ApJ*, **586**, 996

Massa, D., Prinja, R. K. & Fullerton, A. W., 1995*b*, *ApJ*, **452**, 842

Massey, P., Bresolin, F., Kudritzki, R. P., Puls, J. & Pauldrach, A. W. A., 2004, *ApJ*, **608**, 1001

Massey, P., Puls, J., Pauldrach, A. W. A., Bresolin, F., Kudritzki, R. P. & Simon, T., 2005, *ApJ*, **627**, 477

Matteucci, F. & Calura, F., 2005, *MNRAS*, **360**, 447

Maund, J. R., Smartt, S. J. & Danziger, I. J., 2005, *MNRAS*, **364**, L33

McErlean, N. D., 1999, *Ph.D. Thesis*

McErLean, N. D., Lennon, D. & Dufton, P., 1999, *A&A*, **349**, 553

Meynet, G. & Maeder, A., 2000, *A&A*, **361**, 101

Meynet, G., Maeder, A., Schaller, G., Schaerer, D. & Charbonnel, C., 1994, *A&AS*, **103**, 97

Mihalas, D., 1978 (San Francisco:Freeman), 2nd edition

Moore, C. E., 1970, *Ionization Potentials and Ionisation Limits Derived from the Analyses of Optical Spectra*, Rep. NSRDS-NBS34; Washington, D. C.: US Dept. of Commerce

Morel, T., Marchenko, S. V., Pati, A. K., Kuppuswamy, K., Carini, M. T., Wood, E. & Zimmerman, R., 2004, *MNRAS*, **351**, 552

Morgan, W. W., Keenan, P. C. & Kellman, E., 1943, *An atlas of stellar spectra, with an outline of spectral classification* (Chicago, Ill., The University of Chicago press [1943])

Morton, D. C., 1991, *ApJS*, **77**, 119

Morton, D. C., 2003, *ApJS*, **149**, 205

Olson, G. L., Auer, L. H. & Buchler, J. R., 1986, *Journal of Quantitative Spectroscopy and Radiative Transfer*, **35**, 431

Owocki, S. P., Castor, J. I. & Rybicki, G. B., 1988, *ApJ*, **335**, 914

Owocki, S. P., Runacres, M. C. & Cohen, D. H., 2000, in H. Lamers & A. Sapar (eds.), *ASP Conf. Ser. 204: Thermal and Ionization Aspects of Flows from Hot Stars*, pp. 183–+

Panagia, N. & Felli, M., 1975, *A&A*, **39**, 1

Pauldrach, A. W. A., Hoffmann, T. L. & Lennon, M., 2001, *A&A*, **375**, 161

Pauldrach, A. W. A., Kudritzki, R. P., Puls, J., Butler, K. & Hunsinger, J., 1994, *A&A*, **283**, 525

Pauldrach, A. W. A. & Puls, J., 1990*a*, *A&A*, **237**, 409

Pauldrach, A. W. A. & Puls, J., 1990*b*, *A&A*, **237**, 409

Petrenz, P. & Puls, J., 1996, *A&A*, **312**, 195

Pradhan, A. K., Zhang, H. L., Nahar, S. N., Romano, P. & Baustista, M. A., 1996, *BAAS*, **189**, 72.11

Prinja, R. K., Fullerton, A. W. & Crowther, P. A., 1996, *A&A*, **311**, 264

Prinja, R. K., Markova, N., Scuderi, S. & Markov, H., 2006, *A&A*, submitted

Prinja, R. K. & Massa, D., 1998, in I. D. Howarth (ed.), *Boulder-Munich II: Properties of Hot, Luminous Stars*, volume 131 of *ASP Conference Series*, pp. 216–227

Prinja, R. K., Massa, D. & Fullerton, A. W., 2002, *A&A*, **388**, 587

Prinja, R. K., Massa, D. & Searle, S. C., 2005, *A&A*, **430**, L41

Prinja, R. K., Rivinius, T., Stahl, O., Kaufer, A., Foing, B. H., Cami, J. & Orlando, S., 2004, *A&A*, **418**, 727

Puls, J. & Hummer, D. G., 1988, *A&A*, **191**, 87

Puls, J., Kudritzki, R.-P., Herrero, A., Pauldrach, A. W. A., Haser, S. M., Lennon, D. J., Gabler, R., Voels, S. A., Vilchez, J. M., Wachter, S. & Feldmeier, A., 1996, *A&A*, **305**, 171

Puls, J., Markova, N., Scuderi, S., Stanghellini, C., Taranova, O. G., Burnley, A. W. & Howarth, I. D., 2006, *A&A*, submitted

Puls, J., Owocki, S. P. & Fullerton, A. W., 1993, *A&A*, **279**, 457

Puls, J., Urbaneja, M. A., Venero, R., Repolust, T., Springmann, U., Jokuthy, A. & Mokiem, M. R., 2005, *A&A*, **435**, 669

Repolust, T., Puls, J., Hanson, M. M., Kudritzki, R.-P. & Mokiem, M. R., 2005, *A&A*, **440**, 261

Repolust, T., Puls, J. & Herrero, A., 2004, *A&A*, **415**, 349

Rivinius, T., Stahl, O., Wolf, B., Kaufer, A., Gaeng, T., Gummersbach, C. A., Jankovics, I., Kovacs, J., Mandel, H., Peitz, J., Szeifert, T. & Lamers, H. J. G. L. M., 1997, *A&A*, **318**, 819

Runacres, M. C. & Blomme, R., 1996, *A&A*, **309**, 544

Runacres, M. C. & Owocki, S. P., 2002, *A&A*, **381**, 1015

Runacres, M. C. & Owocki, S. P., 2005, *A&A*, **429**, 323

Rusconi, L., Sedmak, G., Stalio, R. & Arpigny, C., 1980, *A&AS*, **42**, 347

Rybicki, G., 1972, 145

Santolaya-Rey, A. E. & Puls, J. & Herrero, A., 1997, *A&A*, **323**, 488

Scharmer, G., 1982, *ApJ*, **249**, 720

Scharmer, G. B., 1981, *ApJ*, **249**, 720

Schild, H., 1985, *A&A*, **146**, 113

Scuderi, S., Panagia, N., Stanghellini, C., Trigilio, C. & Umana, G., 1998, *A&A*, **332**, 251

Smartt, S. J., Lennon, D. J., Kudritzki, R. P., Rosales, F., Ryans, R. S. I. & Wright, N., 2002, *A&A*, **391**, 979

Sobolev, V. V., 1960

Team, T. O. P., 1995, *The Opacity Project* (Institute of Physics Publications, Bristol, UK)

Team, T. O. P., 1997, *The Opacity Project* (Institute of Physics Publications, Bristol, UK)

Townsend, R. H. D., 1997, *MNRAS*, **284**, 839

Trundle, C. & Lennon, D. J., 2005, *A&A*, **434**, 677

Trundle, C., Lennon, D. J., Puls, J. & Dufton, P. L., 2004, *A&A*, **417**, 217

Venn, K. A., 1995, *ApJ*, **449**, 839

Venn, K. A., 1999, *ApJ*, **518**, 405

Vink, J. S., de Koter, A. & Lamers, H. J. G. L. M., 1999, *A&A*, **350**, 181

Vink, J. S., de Koter, A. & Lamers, H. J. G. L. M., 2000, *A&A*, **362**, 295

Vink, J. S., de Koter, A. & Lamers, H. J. G. L. M., 2001, *A&A*, **369**, 574

Walborn, N. R., 1971, *ApJS*, **23**, 257

Walborn, N. R., 1972, *AJ*, **77**, 312

Walborn, N. R. & Fitzpatrick, E. L., 1990, *PASP*, **102**, 379

Walborn, N. R. & Fitzpatrick, E. L., 2000, *PASP*, **112**, 50

Walborn, N. R., Howarth, I. D., Lennon, D. J., Massey, P., Oey, M. S., Moffat, A. F. J., Skalkowski, G., Morrell, N. I., Drissen, L. & Parker, J. W., 2002, *AJ*, **123**, 2754

Walborn, N. R. & Nichols-Bohlin, J., 1987, *PASP*, **99**, 40

Walborn, N. R., Prevot, M. L., Prevot, L., Wamsteker, W., Gonzalez, R., Gilmozzi, R. & Fitzpatrick, E. L., 1989, *A&A*, **219**, 229

Walborn, N., R., 1971, *ibid*, **164**, L67

Walborn, Nolan, R., 1976, *ApJ*, **205**, 419

Werner, K., 1986, *A&A*, **161**, 177

Werner, K., 1987, *Numerical Radiative Transfer* (Cambridge: Cambrdige Univ. Press)

Werner, K., 1989, *A&A*, **226**, 265

Witherick, D., 2004, *Multi-Wavelength Studies of Wind Driven Cataclysmic Variables*, Ph.D. thesis, University College, London

Woosley, S. E. & Heger, A., 2006, *ApJ*, **637**, 914

Wright, A. E. & Barlow, M. J., 1975, *MNRAS*, **170**, 41